Progress Report

January 1, 1995 to June 30, 1995

NASA-UVA LIGHT AEROSPACE ALLOY AND STRUCTURES TECHNOLOGY PROGRAM (LA^{2}ST)

NASA-LaRC Grant NAG-1-745

Submitted to:

National Aeronautics and Space Administration
Langley Research Center
Hampton, Virginia 23681-0001

Attention:

Mr. Neil Price
Grants Officer
MS 126

For Review by:

Mr. Dennis L. Dicus
Grant Monitor
Metallic Materials Branch, MS 188A

Submitted by:

Richard P. Gangloff
Professor
and
Edgar A. Starke, Jr.
University Professor

Department of Materials Science and Engineering
School of Engineering and Applied Science
University of Virginia

Report No. UVA/528266/MS95/118
July 1995

SCHOOL OF
ENGINEERING
& APPLIED SCIENCE

University of Virginia
Thornton Hall
Charlottesville, VA 22903

UNIVERSITY OF VIRGINIA
School of Engineering and Applied Science

The University of Virginia's School of Engineering and Applied Science has an undergraduate enrollment of approximately 1,500 students with a graduate enrollment of approximately 600. There are 160 faculty members, a majority of whom conduct research in addition to teaching.

Research is a vital part of the educational program and interests parallel academic specialties. These range from the classical engineering disciplines of Chemical, Civil, Electrical, and Mechanical and Aerospace to newer, more specialized fields of Applied Mechanics, Biomedical Engineering, Systems Engineering, Materials Science, Nuclear Engineering and Engineering Physics, Applied Mathematics and Computer Science. Within these disciplines there are well equipped laboratories for conducting highly specialized research. All departments offer the doctorate; Biomedical and Materials Science grant only graduate degrees. In addition, courses in the humanities are offered within the School.

The University of Virginia (which includes approximately 2,000 faculty and a total of full-time student enrollment of about 17,000), also offers professional degrees under the schools of Architecture, Law, Medicine, Nursing, Commerce, Business Administration, and Education. In addition, the College of Arts and Sciences houses departments of Mathematics, Physics, Chemistry and others relevant to the engineering research program. The School of Engineering and Applied Science is an integral part of this University community which provides opportunities for interdisciplinary work in pursuit of the basic goals of education, research, and public service.

NASA-UVA LIGHT AEROSPACE ALLOY AND STRUCTURES TECHNOLOGY PROGRAM

LA^{2}ST

Program Directors:

Edgar A. Starke, Jr.
Richard P. Gangloff

Co-principal Investigators:

Carl T. Herakovich
John R. Scully
Gary J. Shiflet
Glenn E. Stoner
John A. Wert

NASA-LaRC Grant Monitor:

Dennis L. Dicus

Report No. UVA/528266/MS95/118

Copy No. ____

July 1995

TABLE OF CONTENTS

TABLE OF CONTENTS (continued)

NASA-UVa LIGHT AEROSPACE ALLOY AND STRUCTURES TECHNOLOGY PROGRAM

(LA^2ST)

EXECUTIVE SUMMARY

The NASA-UVa Light Aerospace Alloy and Structures Technology (LA^2ST) Program was initiated in 1986 and continues with a high level of activity. Projects are being conducted by graduate students and faculty advisors in the Department of Materials Science and Engineering, as well as in the Department of Civil Engineering and Applied Mechanics, at the University of Virginia. This work is funded by the NASA-Langley Research Center under Grant NAG-1-745. Here, we report on progress achieved between January 1 and June 30, 1995.

The objective of the LA^2ST Program is to conduct interdisciplinary graduate student research on the performance of next generation, light-weight aerospace alloys, composites and thermal gradient structures in collaboration with NASA-Langley researchers. Specific technical objectives are presented for each research project. We generally aim to produce relevant data and basic understanding of material mechanical response, environmental/corrosion behavior, and microstructure; new monolithic and composite alloys; advanced processing methods; new solid and fluid mechanics analyses; measurement and modeling advances; and a pool of educated graduate students for aerospace technologies.

The accomplishments presented in this report are summarized as follows.

- oo Three research areas are being actively investigated, including: (1) Mechanical and Environmental Degradation Mechanisms in Advanced Light Metals and Composites, (2) Aerospace Materials Science, and (3) Mechanics of Materials and Composites for Light Aerospace Structures.
- oo Eleven research projects are being conducted by 9 PhD and 3 MS level graduate students, with 7 faculty members from 2 departments in the School of Engineering and Applied Science at UVa. Each project is planned and executed in conjunction with a specific branch and technical monitor at NASA-LaRC.
- oo Two undergraduates are conducting research in the Metallic Materials Branch at NASA-LaRC during the Summer of 1995. No undergraduates are currently participating in LA^2ST research at UVa.

oo Collective accomplishments between January and June of 1995 include: 6 journal or proceedings publications, 1 NASA progress report, 9 presentations at national technical meetings, 1 MS thesis, and 1 PhD dissertation published. Two students graduated during this reporting period; 1 with the Masters of Science Degree in Materials Science and Engineering, and 1 with the Doctor of Philosophy Degree in Materials Science and Engineering at UVa. The LA^2ST totals since 1986 are 102 publications (60 archival journal or book publications), 20 PhD dissertations or MS theses, 109 external technical presentations, 17 NASA progress reports, and 4 NASA Contractor Reports. Since 1986, 33 graduate students, including 31 citizens of the United States, have been involved with LA^2ST research; 20 have received the MS or PhD degree. Five post-doctoral research associates have participated in LA^2ST research. A total of 13 different faculty have worked on the LA^2ST program.

oo ***Research on mechanisms of localized corrosion and environmental fracture in Al-Cu-Li-Mg-Ag alloy X2095 and compositional variations*** provides measurements of electrochemistry, occluded chemistry, fractography and environmental crack growth rates of UA and PA AA2095. The UA temper yields much higher crack growth rates, as well as film free and somewhat featureless fractography, consistent with an embrittlement mechanism. The PA temper yields high angle intergranular EAC type fractography with considerable corrosion product on the fracture surfaces, much slower crack growth rates, consistent with an EAC mechanism based on the anodic dissolution of T_1 and copper depleted zones. Cracking was observed in chromate inhibited environments, with samples polarized anodic to a critical electrochemical potential. (Project 4)

oo ***Research on hydrogen interactions with Al-Li alloys and hydrogen embrittlement of AA2090*** seeks to develop a fundamental understanding of the effects of internal lattice and trapped hydrogen on the mechanical properties of selected Al-Li-Cu-X alloys. Studies were performed on AA2090, an Al-Li-Cu-Zr alloy within the specified compositional range of AA2090, and model binary alloys. Mechanical properties were evaluated by constant extension rate testing of smooth tensile specimen and J-Integral testing of compact tension samples, both precharged with hydrogen. Degradation of mechanical properties with hydrogen was correlated with thermal desorption analysis of

hydrogen trapping and fractography. Results suggest that hydrogen embrittlement is a strong contributor to stress corrosion cracking of this class of alloys. (Project 5)

oo ***Research on the deformation and fracture of high strength titanium alloys*** demonstrates that predissolved hydrogen (500 to 700 wppm) causes stable crack growth at 75°C. This brittle cracking initiates at a stress intensity level that is about one-third of the plane strain fracture toughness for aged Beta-21S, and progresses by microscopic processes that are different compared to ductile fracture of as-received alloy without hydrogen. Work is progressing to develop procedures for reproducible electrochemical introduction of hydrogen, and slow-rate elevated temperature fracture resistance characterization; problems are associated with each procedure. Timet should deliver cold rolled sheet and hot rolled plate of Low Cost Beta. A single microstructure of LCB sheet, relevant to High Speed Civil Transport alloy development, will be examined to characterize and understand temperature-dependent internal hydrogen embrittlement of high strength β-titanium alloys. (Project 6a)

oo ***Research on the cryogenic fracture of Al-Cu-Li-In alloys*** demonstrates that the fracture toughness R-curve behavior of 2090-T81 plate is essentially constant in the temperature range from 25°C to about -150°C. Initiation and growth toughnesses increase substantially at -185°C, associated with numerous large delaminations. Delaminations occurred between grains, one of which was of the brass texture and in many cases the other was of the S texture. In contrast to the temperature dependence of fracture toughness; alloy yield strength, elastic modulus, work hardening exponent, and intrinsic fracture strain each increase monotonically with decreasing temperature from 25°C to -185°C. (Project 2)

oo ***Research on the fracture toughness of several Weldalite™ alloys*** demonstrates that the temperature dependence of initiation fracture toughness (K_{JIC}) is reasonably predicted by the critical strain controlled model of crack tip ductile fracture. For both AA2095 and AA2195, K_{JIC} is predicted to decline monotonically with decreasing temperature from 135°C to -185°C. This decline is controlled by the fact that; while alloy yield strength, work hardening, and elastic modulus increase with decreasing temperature; reduction in

area to fracture (a measure of intrinsic fracture resistance) decreases with decreasing temperature and dominates the fracture toughness temperature dependence. This prediction is consistent with measured fracture toughnesses for AA2095, however, results for AA2195 exhibit scatter that clouds the comparison between the model and experiment. (Project 3)

oo ***Research on the elevated temperature fracture toughness of advanced Al-Cu-Mg-Ag alloys*** establishes the importance of high resolution detection of fracture initiation in thin sheet precracked specimens. This method has provided extensive temperature-dependent fracture toughness data for a range of advanced aluminum alloys. A critical plastic strain controlled model successfully predicts these temperature dependencies of initiation toughness for ingot metallurgy and spray formed precipitation hardened alloys, as well as for submicron grain-size powder metallurgy alloys. It is hypothesized that intravoid strain localization governs the intrinsic fracture resistance ($\bar{\epsilon}_f^*$) in 2000-series alloys. As strain and strain rate localize and increase between growing microvoids, the material is strain and strain rate hardened, and dislocations promote void nucleation at dispersoids by accumulating at the particle/matrix interface. As temperature increases, the strain hardening rate decreases, the strain rate sensitivity increases, and the tendency for void nucleation at dispersoids decreases. The latter two are responsible for rising $\bar{\epsilon}_f^*$ with increasing temperature in AA2519. (Project 1)

oo ***Research on the precipitation hardening and microstructural stability of Al-Si-Ge-Cu alloys*** investigated the strengthening mechanisms in a recently developed Al-0.55Si-2.02Ge (wt.%) alloy and significantly improved the theoretical yield strength prediction for this ternary alloy as a function of aging time. Cavity nucleation in this ternary alloy was analyzed using finite element calculations; the results of these calculations are consistent with experimental measurements of the volume fraction of voids as a function of strain and precipitate diameter. (Project 8)

oo ***Research on the effect of tensile stress on nucleation and growth of precipitates in Al-Cu-Mg-Ag alloys*** shows that, in solution heat treated samples, Ω and Θ' precipitates are preferentially oriented parallel to the applied stress axis. This was not observed for

T6 samples which were further aged under stress. Therefore, it was concluded that nucleation of precipitates is strongly affected by stress. It was found that a threshold stress must be exceeded before this effect can be observed. (Project 9)

oo ***Research to evaluate wide-panel aluminum alloy extrusions*** produced accurate predictions of yield strength anisotropy in 2090 near net shape extrusions. These predictions were made using models constructed to predict strength variations due to texture, grain morphology, and precipitate orientation. (Project 7)

oo ***Research on damage evolution in polymeric composites*** will be reported apart from this grant review meeting and progress report. (Project 10)

oo ***Research to incorporate environmental effects into fracture mechanics fatigue life prediction codes such as NASA FLAGRO*** is nearing an initial stage of completion, with two MS thesis published on modeling environmental fatigue crack propagation in 7075-T6 (S-L) and Ti-6Al-4V (ELI) in aqueous NaCl solution. A Fortran 77 computer program, UVAFAS, has been written to incorporate linear superposition, interpolative, and multiple-power-law models of environmental fatigue crack growth rates. Simple linear superposition is of limited value due to the stress corrosion cracking resistance of these alloys in NaCl. Interpolative modeling provides reasonable descriptions of stress intensity, stress ratio and loading frequency effects on crack growth rates, however, the complexity of environmental fatigue and the lack of mechanistic models hinder the usefulness of this empirical approach. Corrosion fatigue crack growth rate data have been generated for 7075 and Ti-6-4 in aqueous to support these conclusions and to provide input for mechanistic modeling. (Project 11)

INTRODUCTION

Background

In 1986 the Metallic Materials Branch in the Materials Division of the NASA-Langley Research Center initiated sponsorship of graduate student engineering and scientific research in the Department of Materials Science and Engineering at the University of Virginia[1]. This work emphasized the mechanical and corrosion behavior of light aerospace alloys, particularly Al-Li-Cu based compositions, in aggressive aerospace environments[2-4].

In the Fall of 1988, the scope of this program increased to incorporate research on the development and processing of advanced aerospace materials[5]. Additional funding was provided by the Metallic Materials and Mechanics of Materials Branches at NASA-LaRC. In early 1989 the program was further enhanced to include interdisciplinary work on solid mechanics and thermal structures, with funding from several Divisions within the Structures Directorate at NASA-LaRC[6]. The Departments of Civil Engineering (Applied Mechanics Program) and Mechanical and Aerospace Engineering participated in this expanded program. With this growth, the NASA-UVa **L**ight **A**erospace **A**lloy and **S**tructures **T**echnology Program (or LA^{2}ST Program) was formed within the School of Engineering and Applied Science at UVa.

Since 1989, the LA2ST program has operated with full participation from 6 to 13 faculty and 10 to 15 graduate students, yearly, as outlined in the last ten progress reports[7-18] and five grant renewal proposals[19-24]. Five 2-day Grant Review Meetings have been held in July at the Langley Research Center, with over 25 faculty and graduate students from UVa participating at each meeting[9,11,13,15,17]. Since 1990, undergraduate engineering students have been involved in research projects at both NASA-LaRC and UVa.

In October of 1991, E.A. Starke proposed a substantial enhancement to the base LA^{2}ST Program[25,26]. The objective of this supplement was to involve UVa faculty with engineering scientists from aluminum alloy producers and airframe manufacturers in a broad research program to develop aluminum alloys and composites for elevated temperature High Speed Civil Transport applications. This research began in January of 1992 and the results are separately reported. The LA^{2}ST and HSCT activities were merged in 1995[23].

Problem and Needs

Future aerospace structures require high performance light alloys and metal matrix composites with associated processing and fabrication techniques; new structural design methods and concepts with experimental evaluations; component reliability/ durability/damage tolerance prediction procedures; and a pool of masters and doctoral level engineers and scientists. Work on advanced materials and structures must be interdisciplinary and integrated. The thermal and chemical effects of aerospace environments on light metals and composites are particularly important to material performance. Nationally, academic efforts in these areas are limited. The NASA-UVa LA^{2}ST Program addresses these needs.

LA^{2}ST Program

As detailed in the original proposal[6] and affirmed in the most recent renewal[24], faculty from the Departments of Materials Science and Engineering, Mechanical and Aerospace Engineering, and Civil Engineering and Applied Mechanics at UVa are participating in the LA^{2}ST research and education program focused on high performance, light weight, aerospace alloys and structures. We aim to develop long term and interdisciplinary collaborations between graduate students, UVa faculty, and NASA-Langley researchers.

Our research efforts are producing basic understanding of materials performance, new monolithic and composite alloys, advanced processing methods, solid and fluid mechanics analyses, measurement advances, and new methods for modeling material microstructure and properties. A major product of the LA^{2}ST program is graduate students with interdisciplinary education and research experience in materials science, mechanics and mathematics. These advances should enable various NASA technologies.

The scope of the LA^{2}ST Program is broad. Four research areas are being investigated, including:

- oo Mechanical and Environmental Degradation Mechanisms in Advanced Light Metals and Composites,
- oo Aerospace Materials Science,
- oo Mechanics of Materials and Composites for Light Aerospace Structures,

oo Thermal Gradient Structures.

Twelve research projects are currently ongoing within three of these four areas, and are reported here. These projects involve seven faculty, and twelve graduate students. Seventy-five pct of the graduate students are currently at the doctoral level (9 of 12), all but one are citizens of the United States, two are cosponsored by private industry, and two are conducting all research at the Langley Research Center. In each case the research provides the basis for the thesis or dissertation requirement of graduate studies at the University of Virginia. Each project is developed in conjunction with a specific LaRC researcher. Research is conducted at either UVa or LaRC, and under the guidance of UVa faculty and NASA staff. Participating students and faculty are closely identified with a NASA-LaRC branch.

Organization of Progress Report

This progress report first provides LA^{2}ST Program administrative information including statistics on the productivity of faculty and graduate student participants, a history of current and graduated students, refereed or archival publications, and a list of ongoing projects with NASA and UVa advisors.

Eleven sections summarize the technical accomplishments of each research project, emphasizing the period from January 1 to June 30, 1995. Each section contains a brief narrative of objective, recent progress, conclusions and immediate milestones; coupled with a set of visual aids presented at the Sixth Annual NASA-UVa LA^{2}ST Grant Review Meeting held at NASA-LaRC in July of 1995. The agenda of this meeting is presented in Appendix IV. Appendices I through III document grant-sponsored publications, conference participation and citations of all LA^{2}ST Progress Reports produced since 1986.

References

1. R.P. Gangloff, G.E. Stoner and M.R. Louthan, Jr., "Environment Assisted Degradation Mechanisms in Al-Li Alloys", University of Virginia, Proposal No. MS-NASA/LaRC-3545-87, October, 1986.

2. R.P. Gangloff, G.E. Stoner and R.E. Swanson, "Environment Assisted Degradation Mechanisms in Al-Li Alloys", University of Virginia, Report No. UVA/528266/MS88/101, January, 1988.

3. R.P. Gangloff, G.E. Stoner and R.E. Swanson, "Environment Assisted Degradation Mechanisms in Advanced Light Metals", University of Virginia, Report No. UVA/528266/MS88/102, June, 1988.

4. R.P. Gangloff, G.E. Stoner and R.E. Swanson, "Environment Assisted Degradation Mechanisms in Advanced Light Metals", University of Virginia, Report No. UVA/528266/MS89/103, January, 1989.

5. T.H. Courtney, R.P. Gangloff, G.E. Stoner and H.G.F. Wilsdorf, "The NASA-UVa Light Alloy Technology Program", University of Virginia, Proposal No. MS NASA/LaRC-3937-88, March, 1988.

6. R.P. Gangloff, "NASA-UVa Light Aerospace Alloy and Structures Technology Program", University of Virginia, Proposal No. MS NASA/LaRC-4278-89, January, 1989.

7. R.P. Gangloff, "NASA-UVa Light Aerospace Alloy and Structures Technology Program", University of Virginia, Report No. UVA/528266/MS90/104, August, 1989.

8. R.P. Gangloff, "NASA-UVa Light Aerospace Alloy and Structures Technology Program", University of Virginia, Report No. UVA/528266/MS90/105, December, 1989.

9. R.P. Gangloff, "NASA-UVa Light Aerospace Alloy and Structures Technology Program", UVa Report No. UVA/528266/MS90/106, June, 1990.

10. R.P. Gangloff, "NASA-UVa Light Aerospace Alloy and Structures Technology Program", UVa Report No. UVA/528266/MS91/107, January, 1991.

11. R.P. Gangloff, "NASA-UVa Light Aerospace Alloy and Structures Technology Program", UVa Report No. UVA/528266/MS91/108, July, 1991.

12. R.P. Gangloff, "NASA-UVa Light Aerospace Alloy and Structures Technology Program", UVa Report No. UVA/528266/MS92/109, January, 1992.

13. R.P. Gangloff, "NASA-UVa Light Aerospace Alloy and Structures Technology Program", UVa Report No. UVA/528266/MS93/111, July, 1992.

14. R.P. Gangloff, "NASA-UVa Light Aerospace Alloy and Structures Technology Program", UVa Report No. UVA/528266/MSE93/112, March, 1993.

15. R.P. Gangloff, "NASA-UVa Light Aerospace Alloy and Structures Technology Program", UVa Report No. UVA/528266/MSE93/113, July, 1993.

16. R.P. Gangloff, "NASA-UVa Light Aerospace Alloy and Structures Technology Program", UVa Report No. UVA/528266/MSE93/114, March, 1994.

17. R. P. Gangloff, "NASA-UVa Light Aerospace Alloy and Structures Technology Program," UVA Report No. UVA/528266/MSE94/116, July, 1994.

18. E.A. Starke, Jr. and R.P. Gangloff, "NASA-UVa Light Aerospace Alloy and Structures Technology Program", UVa Report No. UVA/528266/MSE94/117, March, 1995.

19. R.P. Gangloff, "NASA-UVa Light Aerospace Alloy and Structures Technology Program", University of Virginia, Proposal No. MS- NASA/LaRC-4512-90, November, 1989.

20. R.P. Gangloff, "NASA-UVa Light Aerospace Alloy and Structures Technology Program", University of Virginia, Proposal No. MS- NASA/LaRC-4841-91, September, 1990.

21. R.P. Gangloff, "NASA-UVa Light Aerospace Alloy and Structures Technology Program", University of Virginia, Proposal No. MS- NASA/LaRC-5219-92, October, 1991.

22. R.P. Gangloff, "NASA-UVa Light Aerospace Alloy and Structures Technology Program", University of Virginia, Proposal No. MSE- NASA/LaRC-5691-93, November, 1992.

23. R.P. Gangloff, "NASA-UVa Light Aerospace Alloy and Structures Technology Program", Proposal No. MSE-NASA/LaRC-6074-94, University of Virginia, Charlottesville, VA, November, 1993.

24. R. P. Gangloff and E. A. Starke, Jr., "NASA-UVa Light Aerospace Alloy and Structures Technology Program," Proposal No. MSE-NASA/LaRC-6478-95, University of Virginia, Charlottesville, VA, November, 1994.

25. R.P. Gangloff, E.A. Starke, Jr., J.M. Howe and F.E. Wawner, "NASA-UVa Light Aerospace Alloy and Structures Technology Program: Supplement on Aluminum Based Materials for High Speed Aircraft", University of Virginia, Proposal No. MS NASA/LaRC-5215-92, October, 1991.

26. R.P. Gangloff, E.A. Starke, Jr., J.M. Howe and F.E. Wawner, "NASA-UVa Light Aerospace Alloy and Structures Technology Program: Supplement on Aluminum Based Materials for High Speed Aircraft", University of Virginia, Proposal No. MSE NASA/LaRC-5691-93, November, 1992.

SUMMARY STATISTICS

Table I documents the numbers of students and faculty who have participated in the LA^{2}ST Program, both during this reporting period and since program inception in 1986. Academic and research accomplishments are indicated by the degrees awarded, publications and presentations. Graduate students and research associates who participated in the LA^{2}ST Program are named in Tables II and III, respectively.

TABLE I: LA^{2}ST Program Statistics

	Current 7/1/94 to 12/31/94	Cumulative 1986 to 12/31/94
PhD Students--UVa:	8	21
--NASA-LaRC:	1	1
MS Students--UVa:	2	9
--NASA:	1	1
--VPI:	0	1
Undergraduates--UVa:	0	9
--NASA-LaRC:	2	15
Faculty--UVa:	7	12
--VPI:	0	1
Research Associates--UVa:	1	5
PhD Awarded:	1	13
MS Awarded:	1	7
Employers--NASA:	1	3
--Federal:	1	4
--University:	0	1
--Industry:	1	6
--Next degree:	1	5

TABLE I: LA²ST Program Statistics (continued)

	Current 1/1/94 to 6/30/94	Cumulative 1986 to 6/30/94
Publications:	6	102
Presentations:	9	109
Dissertations/Theses:	2	20
NASA Reports:	1	21

TABLE II

GRADUATE STUDENT PARTICIPATION IN THE NASA-UVa LA^{2}ST PROGRAM
June, 1995

POS #	GRADUATE STUDENT EMPLOYER	ENTERED PROGRAM	DEGREE COMPLETED	LANGLEY RESIDENCY	RESEARCH TOPIC	UVa/NASA-LaRC ADVISORS
1.	R. S. Piascik NASA-Langley	6/86	Ph.D. 10/89		Damage Localization Mechanisms in Corrosion Fatigue of Aluminum-Lithium Alloys	R. P. Gangloff D. L. Dicus
2.	J. P. Moran NIST	9/88	Ph.D. 12/89		An Investigation of the Localized Corrosion and Stress Corrosion Cracking Behavior of Alloy 2090	G. E. Stoner W. B. Lisagor
3.	R. G. Buchheit Sandia National Laboratories	6/87	Ph.D. 12/90		Measurements and Mechanisms of Localized Aqueous Corrosion in Aluminum-Lithium Alloys	G. E. Stoner D. L. Dicus
4.	D. B. Gundel Ph.D.-UVa	9/88	M.S. 12/90		Investigation of the Reaction Kinetics Between SiC Fibers and Titanium Matrix Composites	F. E. Wawner W. B. Brewer
5.	F. Rivet (VPI)	9/88	M.S. 12/90		Deformation and Fracture of Aluminum-Lithium Alloys: The Effect of Dissolved Hydrogen	R. E. Swanson (VPI) D. L. Dicus
6.	C. Copper Ph.D.-UVa	4/89	M.S. 12/90		Design of Cryogenic Tanks for Space Vehicles	W. D. Pilkey J. K. Haviland D. R. Rummler M.J. Shuart
7.	J. A. Wagner NASA-Langley	6/87	Ph.D.	PhD Research @ LaRC	Temperature Effects on the Deformation and Fracture of Al-Li-Cu-In Alloys	R. P. Gangloff W. B. Lisagor J. C. Newman
8.	W. C. Porr, Jr. David Taylor Naval Ship R&DC	1/88	Ph.D. 6/92		Elevated Temperature Facture of an Advanced Powder Metallurgy Aluminum Alloy	R. P. Gangloff C. E. Harris
9.	J. B. Parse Consultant	9/88	Ph.D. 6/92		Quantitative Characterization of the Spatial Distribution of Particles in Materials	J. A. Wert D. R. Tenney

TABLE II (continued)

GRADUATE STUDENT PARTICIPATION IN THE NASA-UVa LA^{2}ST PROGRAM
(continued)

POS #	GRADUATE STUDENT EMPLOYER	ENTERED PROGRAM	DEGREE COMPLETED	LANGLEY RESIDENCY	RESEARCH TOPIC	UVa/NASA-LaRC ADVISORS
10.	D. C. Slavik Knolls Atomic Power Laboratory	9/89	Ph.D. 6/93		Environment Enhanced Fatigue of Advanced Aluminum Alloys and Composites	R. P. Gangloff D. L. Dicus
11.	C. L. Lach NASA-Langley	9/89	M.S.	MS Research @LaRC	Effect of Temperature on the Fracture Toughness of Weldalite™ 049	R. P. Gangloff W. B. Lisagor
12.	R. J. Kilmer General Motors	11/89	Ph.D. 9/93		Effect of Zn Additions on the Environmental Stability of Alloy 8090	G. E. Stoner W. B. Lisagor
13.	M. F. Coyle	12/89	Ph.D.		Visoplastic Response of High Temperature Structures	E. A. Thornton J. H. Starnes, Jr.
14.	C. J. Lissenden University of Kentucky; Engineering Mechanics	9/90	Ph.D. 6/93		Inelastic Response of Metal Matrix Composites Under Biaxial Loading	C. T. Herakovich M. J. Pindera W. S. Johnson
15.	C. Cooper AMP Incorporated	1/91	Ph.D. 6/93		Shell Structures Analytical Modeling	W. D. Pilkey J. K. Haviland M. Shuart J. Stroud
16.	Douglas Wall	4/91	Ph.D.		Measurements and Mechanisms of Localized Corrosion in Al-Li-Cu Alloys	G. E. Stoner D. L. Dicus
17.	S. W. Smith NASA-LaRC	4/91	Ph.D. 5/95		Hydrogen Interactions with Al-Li Alloys	J. R. Scully W. B. Lisagor
18.	D. B. Gundel Wright Laboratories US Air Force	4/91	Ph.D. 9/94		Effect of Thermal Exposure on the Mechanical Properties of Titanium/SiC Composites	F. E. Wawner W. B. Brewer
19.	K. McCarthy	5/91	M.S. 6/93 (Nonthesis)		Shell Structures Analytical Modeling	W. D. Pilkey M. J. Shuart J. Stroud

TABLE II (continued)

GRADUATE STUDENT PARTICIPATION IN THE NASA-UVa LA^{2}ST PROGRAM
(continued)

POS #	GRADUATE STUDENT EMPLOYER	ENTERED PROGRAM	DEGREE COMPLETED	LANGLEY RESIDENCY	RESEARCH TOPIC	UVa/NASA-LaRC ADVISORS
20.	M. Lyttle	12/91	M.S. 12/93		Superplasticity in Al-Li-Cu Alloys	J. A. Wert T. T. Bales
21.	T. Johnson NASA-LaRC	12/91	Ph.D. 6/93	(NASA Minority Grantee)	Shell Structures Analytical Modeling	W. D. Pilkey M. J. Shuart J. Stroud
22.	S. T. Pride Rohm and Haas	12/91	Ph.D. 6/94	(NASA Minority Grantee)	Metastable Pitting of Al Alloys	J. R. Scully D. L. Dicus
23.	M. A. Rowley	1/92	M.S. 12/93	(UVa AEP Sponsored)	Viscoplasticity of Metals	E. A. Thornton J. H. Starnes, Jr.
24.	M. J. Haynes	9/92	M.S./Ph.D.		Elevated Temperature Fracture of Advanced	R. P. Gangloff TBD
25.	M. Mason Allied Signal	9/92	M.S. 11/94		Environmental Effects in Fatigue Life Prediction	R. P. Gangloff R. S. Piascik
26.	H. J. Koenigsmann	6/93	Ph.D.		Precipitation Hardening and Microstructural Stability in Al-Si-Ge-Cu	E.A. Starke, Jr. W.B. Lisagor
27.	E. Richey	9/93	M.S. 5/95		Computer Modeling of Environmental Fatigue Crack Propagation	R.P. Gangloff R.S. Piascik
28.	M. Lyttle	1/94	Ph.D.		Wide-Panel Aluminum Alloy Extrusions	J.A. Wert W.B. Lisagor
29.	Z. Gasem	1/94	Ph.D.		Time-Dependent Environmental Fatigue in 7000-Series Al Alloys	R.P. Gangloff R.S. Piascik
30.	S. P. Hayes	9/94	Ph.D.		Temperature and Hydrogen-Effects on Fracture in Ti Alloys	R.P. Gangloff D.L. Dicus
31.	S. M. Kazanjian	12/94	M.S.		Temperature and Microstructure Effects on Fracture in Ti Alloys	E.A. Starke, Jr. D.L. Dicus
32.	R. D. Schroedter, III	6/93	Ph.D.		Damage Evolution in Polymeric Composites	C.T. Herakovich C.E. Harris

TABLE III

Post-Doctoral Research Associate Participation
in NASA-UVA LaRC-ST Program
June, 1995

Pos #	Research Assoc.	Tenure	Research	Supervisor
1.	Yang Leng	3/89 to 12/91	Elevated Temperature Deformation and Fracture of PM AL Alloys and Composites	R. P. Gangloff
2.	Farshad Mizadeh	7/89 to 12/91	Deformation of Metal Matrix Composites	C. T. Herakovich and Marek-Jerzy Pindera
3.	A. K. Mukhopadhyay	6/91 to 6/92	Aluminum Alloy Development	E. A. Starke, Jr.
4.	Sang-Shik Kim	12/91 to 2/94	Environmental Fatigue Life Prediction	R. P. Gangloff
5.	B. Skrotzki	1/95	Mechanical Property Anisotropy	E. A. Starke, Jr. and G. J. Shiflet

GRANT PUBLICATIONS: (REFEREED JOURNALS, ARCHIVAL VOLUMES AND NASA CONTRACTOR REPORTS)

The following papers are based on research conducted under LA^{2}ST Program support, and are published in the referred or archival literature.

60. B. Skrotzki, E. A. Starke and G. J. Shiflet, "The Effect of Stress on Nucleation and Growth of Precipitates in Al-Cu-Mg-X Alloys", Proc. of the 2nd International Conference on Microstructure and Mechanical Properties of Aging Materials, TMS-AIME, Warrendale, PA, in press (1995).

59. P.N. Kalu and J.A. Wagner, " A Microtexture Investigation of the Fracture Behavior of Al-Li Alloy 2090", Lightweight Alloys for Aerospace Applications III, TMS-AIME, Warrendale, PA, in press (1995).

58. Donald C. Slavik and Richard P. Gangloff, "Environment and Microstructure Effects on Fatigue Crack Facet Orientation in an Al-Li-Cu-Zr Alloy", Acta Metallurgica et Materialia, in review (1995).

57. S.T. Pride, J.R. Scully and J.L. Hudson, "Analysis of Electrochemical Noise from Metastable Pitting in Al, Aged Al-2%Cu and AA 2024-T3," in Electrochemical Noise Methods in Corrosion ASTM STP, ASTM, Philadelphia, PA, in review (1994).

56 R.G. Buchheit, G.E. Stoner and G.J. Shiflet, "Corrosion Properties of a Rapidly Solidified Al90Fe5Gd5 Alloy", J. Electrochem. Soc., in revision (1994).

55. C. J. Lissenden, B. A. Lerch, and C. T. Herakovich, "Response of SiC/Ti Tubes Under Combined Loading - Part III: Microstructural Evaluation", J. Composite Materials, in review (1994).

54. H.J. Koenigsmann and E.A. Starke, Jr., "Fracture Behavior in Al-Si-Ge Alloys", in Proceedings of the 2nd International Conference on Microstructures and Mechanical Properties of Aging Materials, TMS-AIME, Warrendale, PA, in press (1995).

53. S.S. Kim, M. J. Haynes and R.P. Gangloff, "Localized Deformation Control of Elevated Temperature Fracture in Submicron Grain Aluminum with Dispersoids", Materials Science and Engineering A, in press (1995).

52. R. S. Piascik and R. P. Gangloff, "Modeling Environment-Enhanced Fatigue Crack Growth in Al-Li-Cu-Zr," in Hydrogen Effects on Material Behavior, N. R. Moody and A. W. Thompson, eds., TMS-AIME, Warrendale, PA, in press (1995).

51. E.A. Thornton and J.D. Kolenski, "Viscoplastic Response of Structures with Intense Local Heating", Journal of Aerospace Engineering, in press (1995).

50. S. W. Smith and J. R. Scully, "Hydrogen Trapping and Its Correlation to the Hydrogen Embrittlement Susceptibility of Al-Li-Cu-Zr Alloys," in TMS Hydrogen Effects on Materials Behavior, N. R. Moody and A. W. Thompson, eds., TMS-AIME, Warrendale, PA, in press (1995).

49. C. J. Lissenden, C. T. Herakovich, and M-J. Pindera, "Response of SiC/Ti Tubes Under Combined Loading - Part II: Room Temperature Creep Effects", J. Composite Materials, in press (1995).

48. C. J. Lissenden, C. T. Herakovich, and M-J. Pindera, "Response of SiC/Ti Tubes Under Combined Loading - Part I: Theory and Experiment for Imperfect Bonding", J. Composite Materials, in press (1995).

47. E.A. Thornton, M.F. Coyle, and R.N. McLeod, "Experimental Study of Plate Buckling Induced by Spatial Temperature Gradients," Journal of Thermal Stresses, in press (1995).

46. C. J. Lissenden, C. T. Herakovich, and M-J. Pindera, "Inelastic Deformation of TMC Under Multiaxial Loading" in Life Prediction Methodology for Titanium Matrix Composites, ASTM STP, W.S. Johnson, ed., ASTM, Philadelphia, PA, in press (1995).

45. B. Skrotzki, E. A. Starke and G. J. Shiflet, "Effect of Texture and Precipitates on Mechanical Property Anisotropy of Al-Cu-Mg-X Alloys", Proc. of the 4th International Conference on Aluminum Alloys, Vol. II, EMAS, Warley Heath, UK p. 40 (1994).

44. R.G. Buchheit, F.D. Wall, G.E. Stoner and J.P. Moran, "Anodic Dissolution-Based Mechanism for the Rapid Cracking, Preexposure Phenomenon Demonstrated by Aluminum-Lithium-Copper Alloys", Corrosion, Vol. 51, pp. 417-428 (1995).

43. J. R. Scully, "Electrochemical Tests," in Manual on Corrosion Tests: Application and Interpretation, R. Baboian, ed., ASTM, Philadelphia, PA, pp. 75-90 (1995).

42. R.P. Gangloff, "Corrosion Fatigue Cracking", in Manual on Corrosion Tests: Application and Interpretation, R. Baboian, ed., ASTM, Philadelphia, PA, pp. 253-271 (1995).

41. M.E. Mason and R. P. Gangloff, "Modeling Time-Dependent Corrosion Fatigue Crack Propagation in 7000 Series Aluminum Alloys," in FAA/NASA International Symposium on Advanced Structural Integrity Methods for Airframe Durability and Damage Tolerance, C. E. Harris, ed., NASA Conference Publication 3274, Part 1, NASA-Langley Research Center, Hampton, VA, pp. 441-462 (1994).

40. J. M. Duva, J. Aboudi, and C. T. Herakovich, "A Probabilistic Micromechanics Model for Damaged Composites", Damage Mechanics in Composites, D. H. Allen and J. W. Ju, eds., ASME, AMD-Vol. 185, pp. 1-20 (1994).

39. S.T. Pride, J.R. Scully and J.L. Hudson, "Metastable Pitting of Aluminum and Criteria for the Transition to Stable Pit Growth," Journal of the Electrochemical Society, Vol. 141, No. 11, p. 3028 (1994).

38. C. J. Lissenden, C. T. Herakovich, and M-J. Pindera, "Damage Induced Room Temperature Creep of Titanium Matrix Composites", Durability of Composite Materials, R. C. Wetherhold, ed., ASME MD-Vol. 51, pp. 39-50 (1994).

37. H.J. Koenigsmann and E.A. Starke, Jr.,"Microstructural Stability and Fracture Behavior in Al-Si-Ge Alloys", Proceedings of the 4th International Conference on Aluminum Alloys - Their Physical and Mechanical Properties, T.H. Sanders, Jr. and E.A. Starke, Jr., eds., Atlanta, GA, Vol. II, pp. 24-31 (1994).

36. M.T. Lyttle and J.A. Wert, "Modeling of Continuous Recrystallization in Aluminum Alloys," Journal of Materials Science, Vol. 29, pp. 3342-3350 (1994).

35. Edward Richey, III, A.W. Wilson, J.M. Pope, and R.P. Gangloff, "Computer Modeling the Fatigue Crack Growth Rate Behavior of Metals in Corrosive Environments", NASA CR194982, NASA-Langley Research Center, Hampton, VA (1994).

34. R.G. Buchheit, J.P. Moran and G.E. Stoner, "The Electrochemical Behavior of the T1 (Al2CuLi) Intermetallic Compound and Its Role in Localized Corrosion of Al-3Cu-2Li Alloys", Corrosion, Vol. 50, pp. 120-130 (1994).

33. D. Gundel, P. Taylor and F. Wawner, "The Fabrication of Thin Oxide Coatings on Ceramic Fibers by a Sol-Gel Technique", Journal of Materials Science, Vol. 29, pp. 1795-1800 (1994).

32. M.T. Lyttle and J.A. Wert, "Simulative Modeling of Continuous Recrystallization of Aluminum Alloys", in Advances in Hot Deformation Textures and Microstructures, J.J. Jonas, T.R. Bieler and K.J. Bowman, eds., TMS-AIME, Warrendale, PA, pp. 373-383 (1994).

31. R.P. Gangloff, R.S. Piascik, D.L. Dicus and J.C. Newman, "Fatigue Crack Propagation in Aerospace Aluminum Alloys", Journal of Aircraft, Vol. 31, pp. 720-729 (1994).

30. W.C. Porr, Jr. and R.P. Gangloff, "Elevated Temperature Fracture of RS/PM Alloy 8009: Part I-Fracture Mechanics Behavior", Metall. Trans. A, Vol. 25A, pp. 365-379 (1994).

29. J. R. Scully, T. O. Knight, R. G. Buchheit, and D. E. Peebles, "Electrochemical Characteristics of the Al_2Cu, Al_3Ta and Al_3Zr Intermetallic Phases and Their Relevancy to the Localized Corrosion of Al Alloys," Corrosion Science, Vol. 35, pp. 185-195 (1993).

28. E.A. Thornton, "Thermal Buckling of Plates and Shells," Applied Mechanics Reviews, Vol. 46, No. 10, pp. 485-506 (1993).

27. R.P. Gangloff and Sang Shik Kim, "Environment Enhanced Fatigue Crack Propagation in Metals: Inputs to Fracture Mechanics Life Prediction", NASA CR-191538, NASA-Langley Research Center, Hampton, VA (1993).

26. R.S. Piascik and R.P. Gangloff, "Environmental Fatigue of an Al-Li-Cu Alloy: Part II - Microscopic Hydrogen Cracking Processes", Metall. Trans. A, Vol. 24A, pp. 2751-2762 (1993).

25. D.C. Slavik, J.A. Wert and R.P. Gangloff, "Determining Fracture Facet Crystallography Using Electron Back Scatter Patterns and Quantitative Tilt Fractography", Journal of Materials Research, Vol. 8, pp. 2482-2491 (1993).

24. D.C. Slavik, C.P. Blankenship, Jr., E.A. Starke, Jr. and R.P. Gangloff, "Intrinsic Fatigue Crack Growth Rates for Al-Li-Cu-Mg Alloys in Vacuum", Metall. Trans. A, Vol. 24A, pp. 1807-1817 (1993).

23. D. Gundel and F. Wawner, "The Influence of Defects on the Response of Titanium/SiC Fiber Composites to Thermal Exposure", Composites Engineering, Vol. 4, No. 1, pp. 47-65 (1993).

22. J.B. Parse and J.A. Wert, "A Geometrical Description of Particle Distributions in Materials", Modeling and Simulation in Materials Science and Engineering, Vol. 1, pp. 275-296 (1993).

21. D.C. Slavik and R.P. Gangloff, "Microscopic Processes of Environmental Fatigue Crack Propagation in Al-Li-Cu Alloy 2090", in Fatigue '93, Vol. II, J.-P. Bailon and J.I. Dickson, eds., EMAS, West Midlands, UK, pp. 757-765 (1993).

20. C.J. Lissenden, M-J. Pindera and C.T. Herakovich, "Response of SiC/Ti Tubes Under Biaxial Loading in the Presence of Damage," Damage Mechanics in Composites, D.H. Allen and D.C. Lagoudas, Eds., ASME- AMD-Vol. 150, pp. 73-90 (1992).

19. J.A. Wagner and R.P. Gangloff, "Fracture Toughness of Al-Li-Cu-In Alloys", Scripta Metallurgica et Materialia, Vol. 26, pp. 1779-1784 (1992).

18. R.G. Buchheit, Jr., J.P. Moran, F.D. Wall, and G.E. Stoner, "Rapid Anodic Dissolution Based SCC of 2090 (Al-Li-Cu) by Isolated Pit Solutions," Parkins Symposium on Fundamental Aspects of Stress Corrosion Cracking, S.M. Bruemmer, E.I. Meletis, R.H. Jones, W.W. Gerberich, F.P. Ford and R.W. Staehle, eds., TMS-AIME, Warrendale, PA, p. 141 (1992).

17. J.P. Moran, R.G. Buchheit, Jr., and G.E. Stoner, "Mechanisms of SCC of Alloy 2090 (Al-Li-Cu) - A Comparison of Interpretations from Static and Slow Strain Rate Techniques", Parkins Symposium on Fundamental Aspects of Stress Corrosion Cracking, S.M. Bruemmer, E.I. Meletis, R.H. Jones, W.W. Gerberich, F.P. Ford and R.W. Staehle, eds., TMS-AIME, Warrendale, PA, p. 159 (1992).

16. R.J. Kilmer, T.J. Witters and G.E. Stoner, "Effect of Zn Additions on the Precipitation Events and Implications to Stress Corrosion Cracking Behavior in Al-Li-Cu-Mg-Zn Alloys", Proceedings of the Sixth International Al-Li Conference, M. Peters and P.J. Winkler, eds., DGM Informationsgesellschaft, Verlag, pp. 755-760 (1992).

15. C.T. Herakovich and J.S. Hidde, "Response of Metal Matrix Composites with Imperfect Bonding", Ultramicroscopy, Vol. 40, pp. 215-228 (1992).

14. R.G. Buchheit, Jr., F.D. Wall, G.E. Stoner and J.P. Moran, "Stress Corrosion Cracking of Al-Li-Cu-Zr Alloy 2090 in Aqueous Cl- and Mixed Cl-/CO3-2 Environments", CORROSION/91, Paper No. 99, NACE, Houston, TX (1991).

13. R.P. Gangloff, D.C. Slavik, R.S. Piascik and R.H. Van Stone, "Direct Current Electrical Potential Measurement of the Growth of Small Fatigue Cracks", in Small Crack Test Methods, ASTM STP 1149, J.M. Larsen and J.E. Allison, eds., ASTM, Philadelphia, PA, pp. 116-168 (1992).

12. R.J. Kilmer and G.E. Stoner, "The Effect of Trace Additions of Zn on the Precipitation Behavior of Alloy 8090 During Artificial Aging", Proceedings, Light Weight Alloys for Aerospace Applications II, E.W. Lee, ed., TMS-AIME, Warrendale, PA, pp. 3-15, 1991.

11. W.C. Porr, Jr., Anthony Reynolds, Yang Leng and R.P. Gangloff, "Elevated Temperature Cracking of RSP Aluminum Alloy 8009: Characterization of the Environmental Effect", Scripta Metallurgica et Materialia, Vol. 25, pp. 2627-2632 (1991).

10. J. Aboudi, J.S. Hidde and C.T. Herakovich, "Thermo-mechanical Response Predictions for Metal Matrix Composites", in Mechanics of Composites at Elevated and Cryogenic Temperatures, S.N. Singhal, W.F. Jones and C.T. Herakovich, eds., ASME AMD, Vol. 118, pp. 1-18 (1991).

9. R.S. Piascik and R.P. Gangloff, "Environmental Fatigue of an Al-Li-Cu Alloy: Part I - Intrinsic Crack Propagation Kinetics in Hydrogenous Environments", Metallurgical Transactions A, Vol. 22A, pp. 2415-2428 (1991).

8. W.C. Porr, Jr., Y. Leng, and R.P. Gangloff, "Elevated Temperature Fracture Toughness of P/M Al-Fe-V-Si", in Low Density, High Temperature Powder Metallurgy Alloys, W.E. Frazier, M.J. Koczak, and P.W. Lee, eds., TMS- AIME, Warrendale, PA, pp. 129-155 (1991).

7. Yang Leng, William C. Porr, Jr. and Richard P. Gangloff, "Time Dependent Crack Growth in P/M Al-Fe-V-Si at Elevated Temperatures", Scripta Metallurgica et Materialia, Vol. 25, pp. 895-900 (1991).

6. R.J. Kilmer and G.E. Stoner, "Effect of Zn Additions on Precipitation During Aging of Alloy 8090", Scripta Metallurgica et Materialia, Vol. 25, pp. 243-248 (1991).

5. D.B. Gundel and F.E. Wawner, "Interfacial Reaction Kinetics of Coated SiC Fibers", Scripta Metallurgica et Materialia, Vol. 25, pp. 437-441 (1991).

4. R.G. Buchheit, Jr., J.P. Moran and G.E. Stoner, "Localized Corrosion Behavior of Alloy 2090-The Role of Microstructural Heterogeneity", Corrosion, Vol. 46, pp. 610-617 (1990).

3. Y. Leng, W.C. Porr, Jr. and R.P. Gangloff, "Tensile Deformation of 2618 and Al-Fe-Si-V Aluminum Alloys at Elevated Temperatures", Scripta Metallurgica et Materialia, Vol. 24, pp. 2163-2168 (1990).

2. R.P. Gangloff, "Corrosion Fatigue Crack Propagation in Metals", in Environment Induced Cracking of Metals, R.P. Gangloff and M.B. Ives, eds., NACE, Houston, TX, pp. 55-109 (1990).

1. R.S. Piascik and R.P. Gangloff, "Aqueous Environment Effects on Intrinsic Corrosion Fatigue Crack Propagation in an Al-Li-Cu Alloy", in Environment Induced Cracking of Metals, R.P. Gangloff and M.B. Ives, eds., NACE, Houston, TX, pp. 233-239 (1990).

COMPLETED PROJECTS: (1986 to present reporting period)

1. DAMAGE LOCALIZATION MECHANISMS IN CORROSION FATIGUE OF ALUMINUM-LITHIUM ALLOYS
   Faculty Investigator: R.P. Gangloff
   Graduate Student: Robert S. Piascik
   Degree: PhD
   UVa Department: Materials Science and Engineering (MS&E)
   NASA-LaRC Contact: D. L. Dicus (Metallic Materials)
   Start Date: June, 1986
   Completion Date: November, 1989
   Employment: NASA-Langley Research Center

2. AN INVESTIGATION OF THE LOCALIZED CORROSION AND STRESS CORROSION CRACKING BEHAVIOR OF ALLOY 2090 (Al-Li-Cu)
   Faculty Investigator: Glenn E. Stoner
   Graduate Student: James P. Moran
   Degree: PhD
   UVa Department: MS&E
   NASA-LaRC Contact: W.B. Lisagor (Metallic Materials)
   Start Date: September, 1988
   Completion Date: December, 1989
   Co-Sponsor: ALCOA
   Employment: ALCOA Laboratories

3. MECHANISMS OF LOCALIZED CORROSION IN AL-LI-CU ALLOY 2090
   Faculty Investigator: G.E. Stoner
   Graduate Student: R.G. Buchheit
   Degree: PhD
   UVa Department: MS&E
   NASA-LaRC Contact: D.L. Dicus (Metallic Materials)
   Start Date: June, 1987
   Completion Date: December, 1990
   Cosponsor: Alcoa
   Employment: Sandia National Laboratories

4. DEFORMATION AND FRACTURE OF ALUMINUM-LITHIUM ALLOYS: THE EFFECT OF DISSOLVED HYDROGEN

Faculty Investigator: R.E. Swanson (VPI)
Graduate Student: Frederic C. Rivet
Degree: MS
VPI Department: Materials Engineering
NASA-LaRC Contact: D.L. Dicus (Metallic Materials)
Start Date: September, 1988
Completion Date: December, 1990
Employment: Not determined

5. INVESTIGATION OF THE REACTION KINETICS BETWEEN SiC FIBERS AND SELECTIVELY ALLOYED TITANIUM MATRIX COMPOSITES AND DETERMINATION OF THEIR MECHANICAL PROPERTIES

Faculty Investigator: F.E. Wawner
Graduate Student: Douglas B. Gundel
Degree: MS
UVa Department: MS&E
NASA-LaRC Contact: D.L. Dicus and W.B. Brewer (Metallic Materials)
Start Date: January, 1989
Completion Date: December, 1990
Employment: Graduate School, University of Virginia; PhD candidate on LA^{2}ST Program; Department of Materials Science

6. DESIGN OF CRYOGENIC TANKS FOR SPACE VEHICLES

Faculty Investigators: W.D. Pilkey and J.K. Haviland
Graduate Student: Charles Copper
Degree: MS
UVa Department: Mechanical and Aerospace Engineering (MAE)
NASA-LaRC Contact: D.R. Rummler (Structural Mechanics Division), R.C. Davis and M.J. Shuart (Aircraft Structures)
Start Date: April, 1989
Completion Date: December, 1990
Employment: Graduate School, University of Virginia; PhD candidate on NASA-Headquarters sponsored program; Department of Mechanical and Aerospace Engineering

7. ELEVATED TEMPERATURE FRACTURE OF AN ADVANCED RAPIDLY SOLIDIFIED, POWDER METALLURGY ALUMINUM ALLOY

Faculty Investigator: R.P. Gangloff
Graduate Student: William C. Porr, Jr.
Degree: PhD
UVa Department: MS&E
NASA-LaRC Contact: C.E. Harris (Mechanics of Materials)
Start Date: January, 1988
Completion Date: June, 1992
Employment: David Taylor Naval Ship R&D Center

8. QUANTITATIVE CHARACTERIZATION OF THE SPATIAL DISTRIBUTION OF PARTICLES IN MATERIALS: APPLICATION TO MATERIALS PROCESSING

Faculty Investigator: John A. Wert
Graduate Student: Joseph Parse
Degree: PhD
UVa Department: MS&E
NASA-LaRC Contact: D.R. Tenney (Materials Division)
Start Date: September, 1988
Completion Date: June, 1992
Employment: Private Consultant

9. ENVIRONMENTAL FATIGUE CRACK GROWTH AND CRACKING MECHANISMS IN Al-Li-Cu Alloy 2090

Faculty Investigator: R.P. Gangloff
Graduate Student: Donald C. Slavik
Degree: PhD
UVa Department: MS&E
NASA-LaRC Contact: D.L. Dicus (Metallic Materials)
Start Date: September, 1989
Completion Date: June, 1993
Employment: Knolls Atomic Power Laboratory

10. INELASTIC DEFORMATION OF METAL MATRIX COMPOSITES UNDER BIAXIAL LOADING

Faculty Investigators: Carl T. Herakovich and Marek-Jerzy Pindera
Graduate Student: Mr. Clifford J. Lissenden
Degree: PhD
UVa Department: Civil Engineering and the Applied Mechanics Program
NASA-LaRC Contact: W.S. Johnson (Mechanics of Materials)
Start Date: September, 1990
Completion Date: June, 1993
Employment: University of Kentucky, Department of Engineering Mechanics

11. EFFECT OF TEMPERATURE ON THE RESPONSE OF METALLIC SHELL STRUCTURES

Faculty Investigators: W.D. Pilkey and J.K. Haviland
Graduate Student: Karen McCarthy
Degree: MS (non-thesis)
Graduate Student: Theodore Johnson (NASA Minority Grantee)
Degree: PhD
Employment: NASA-LaRC
Graduate Student: Charles Copper
Degree: PhD
Employment: AMP Incorporated
UVa Department: MAE
NASA-LaRC Contact: M.J. Shuart and Jeffrey Stroud (Aircraft Structures)
Start Date: April, 1991
Completion Date: May, 1993

12. EFFECTS OF Zn ADDITIONS ON THE PRECIPITATION AND STRESS CORROSION CRACKING BEHAVIOR OF ALLOY 8090

Faculty Investigator: Glenn E. Stoner
Graduate Student: Raymond J. Kilmer
Degree: PhD
Department: MS&E
NASA-LaRC Contact: W.B. Lisagor (Metallic Materials)
Start Date: September, 1989
Completion Date: September, 1993
Cosponsor: Alcoa
Employment: General Motors

13. PROCESSING AND SUPERPLASTIC PROPERTIES OF WELDALITETM SHEET

Faculty Investigator: John A. Wert
Graduate Student: Mark Lyttle
Degree: MS
Department: MS&E
NASA-LaRC Contact: T.T. Bales (Metallic Materials)
Start Date: September, 1991
Completion Date: December, 1993
Employment: Graduate School, University of Virginia; PhD Candidate in Materials Science and Engineering

14. METASTABLE PITTING OF Al ALLOYS AND CRITERIA FOR THE TRANSITION TO STABLE PITTING

Faculty Investigators: John R. Scully and J.L. Hudson
Graduate Student: Sheldon T. Pride
Degree: PhD
Department: Chemical Engineering
NASA-LaRC Contact: D.L. Dicus (Metallic Materials)
Start Date: September, 1991
Completion Date: May, 1994
Cosponsor: NASA Graduate Student Researchers Program; Under Represented Minority Emphasis
Employment: Rohm and Haas Chemical Company

15. THE EFFECT OF THERMAL EXPOSURE ON THE MECHANICAL PROPERTIES OF Ti-1100/SCS-6 COMPOSITES

Faculty Investigator: F.E. Wawner
Graduate Student: Douglas B. Gundel
Degree: PhD
UVa Department: MS&E
NASA-LaRC Contact: D.L. Dicus and W.B. Brewer (Metallic Materials)
Start Date: April, 1991
Completion Date: June, 1994
Employment: Wright Laboratories (WL/MLLM), US Air Force Materials Laboratory

16. ENVIRONMENTAL EFFECTS IN FATIGUE LIFE PREDICTION: MODELING ENVIRONMENTAL CRACK PROPAGATION IN LIGHT AEROSPACE ALLOYS

Faculty Investigator: R. P. Gangloff
Graduate Student: Mark E. Mason
Degree: MS
UVa Department: MS&E
NASA-LaRC Contact: R. S. Piascik (Mechanics of Materials)
Start Date: January, 1992
Completion Date: November, 1994
Employment: Allied-Signal; Hopewell, VA

17. ENVIRONMENTAL EFFECTS IN FATIGUE LIFE PREDICTION: MODELING ENVIRONMENTAL CRACK PROPAGATION IN LIGHT AEROSPACE ALLOYS

Faculty Investigator: R. P. Gangloff
Graduate Student: Edward Richey, III
Degree: MS
UVa Department: MANE
NASA-LaRC Contact: R. S. Piascik (Mechanics of Materials)
Start Date: September, 1993
Completion Date: May, 1995
Employment: Graduate School, University of Virginia; PhD Candidate in Materials Science and Engineering

18. HYDROGEN INTERACTIONS IN ALUMINUM-LITHIUM 2090 AND SELECTED MODEL ALLOYS

Faculty Investigator: John R. Scully
Graduate Student: Stephen W. Smith; PhD Candidate
UVa Department: MS&E
NASA-LaRC Contact: W.B. Lisagor and D.L. Dicus (Metallic Materials)
Start Date: April, 1991
Anticipated Completion Date: May, 1995
Cosponsor: Virginia CIT
Employment: NASA-LaRC

ADMINISTRATIVE PROGRESS

Faculty Participation

Professor G.J. Shiflet jointed the LA^{2}ST Program during this reporting period and will be collaborating with Professor Starke.

Graduate Student Recruitment

The LA^{2}ST Program has encountered no problems in recruiting the best graduate students entering the participating Departments at UVa, and in sufficient numbers to achieve our education and research objectives. Professor Scully recently recruited Mr. Keith Eklund, currently completing his MS degree in Materials Science at the Pennsylvania State University. His LA^{2}ST research will focus on mechanisms of stress corrosion crack initiation and growth in advanced ingot metallurgy aluminum alloys.

Undergraduate Research Participation

In April of 1990, the LA^{2}ST Program was increased in scope to include undergraduate engineering students. Four students worked at NASA-LaRC during the Summer of 1990, none were recruited for the 1991 program, and seven were successfully recruited to work at NASA-LaRC during the Summer of 1992. Each student was a rising senior in an engineering or science major closely related to aerospace materials and mechanics. Represented universities have included Harvard, Georgia Institute of Technology, Virginia Polytechnic Institute, Duke, the University of Missouri, California Polytechnical Institute, and North Carolina State University.

Professor Glenn E. Stoner assumed responsibility for the 1993 Summer Undergraduate Program. During the past reporting period, he recruited two students from the Pennsylvania State University and North Carolina State University. These students are working in the Metallic Materials Branch at NASA-LaRC for the Summer of 1995.

CURRENT PROJECTS

MECHANICAL AND ENVIRONMENTAL DEGRADATION MECHANISMS IN ADVANCED LIGHT METALS AND COMPOSITES

1. TIME-TEMPERATURE DEPENDENT FRACTURE IN ADVANCED WROUGHT INGOT METALLURGY, AND SPRAY DEPOSITED ALUMINUM ALLOYS

   Faculty Investigator: R.P. Gangloff
   Graduate Student: Michael J. Haynes; PhD (direct) candidate
   UVa Department: MS&E
   NASA-LaRC Contact: A. P. Reynolds (Metallic Materials)
   Start Date: September, 1992
   Completion Date: September, 1996
   Project #1

2. CRYOGENIC TEMPERATURE EFFECTS ON THE DEFORMATION AND FRACTURE OF Al-Li-Cu-In ALLOYS

   Faculty Investigator: R.P. Gangloff
   Graduate Student: John A. Wagner; PhD candidate and NASA-LaRC employee
   UVa Department: MS&E
   NASA-LaRC Contacts: W.B. Lisagor (Metallic Materials) and J.C. Newman (Mechanics of Materials)
   Start Date: June, 1987
   Anticipated Completion Date: December, 1995
   Project #2

3. EFFECTS OF AGING AND TEMPERATURE ON THE DUCTILE FRACTURE OF AA2095 AND AA2195

   Faculty Investigator: R.P. Gangloff
   Graduate Student: Cynthia L. Lach; MS candidate and NASA- LaRC employee
   UVa Department: MS&E
   NASA-LaRC Contacts: W.B. Lisagor (Metallic Materials)
   Start Date: August, 1990
   Anticipated Completion Date: December, 1995
   Project #3

4. MECHANISMS OF LOCALIZED CORROSION IN 2090 AND X2095

Faculty Investigator: G.E. Stoner
Graduate Student: Douglas Wall; PhD candidate
UVa Department: MS&E
NASA-LaRC Contact: M.S. Domack (Metallic Materials)
Start Date: April, 1991
Completion Date: December, 1995
Cosponsor: Reynolds Metals Company (A. Cho)
Project #4

5. HYDROGEN INTERACTIONS IN ALUMINUM-LITHIUM 2090 AND SELECTED MODEL ALLOYS

Faculty Investigator: John R. Scully
Graduate Student: Stephen W. Smith; PhD Candidate
UVa Department: MS&E
NASA-LaRC Contact: W.B. Lisagor and D.L. Dicus (Metallic Materials)
Start Date: April, 1991
Anticipated Completion Date: May, 1995
Cosponsor: Virginia CIT
Project #5

6a. MECHANISMS OF DEFORMATION AND FRACTURE IN HIGH STRENGTH TITANIUM ALLOYS: EFFECTS OF TEMPERATURE AND DISSOLVED HYDROGEN

Faculty Investigators: R. P. Gangloff
Graduate Student: Sean P. Hayes; PhD Candidate
UVa Department: MS&E
NASA-LaRC Contact: To be determined (Metallic Materials)
Start Date: September, 1994
Completion Date: September, 1997
Project #6a

6b. MECHANISMS OF DEFORMATION AND FRACTURE IN HIGH STRENGTH TITANIUM ALLOYS: EFFECTS OF TEMPERATURE AND MICROSTRUCTURE

Faculty Investigators: E. A. Starke, Jr.
Graduate Student: Susan M. Kazanjian, MS Candidate
UVa Department: MS&E
NASA-LaRC Contact: To be determined (Metallic Materials)
Start Date: December, 1994
Completion Date: To be determined
Project #6b

AEROSPACE MATERIALS SCIENCE

7. EVALUATION OF WIDE-PANEL ALUMINUM ALLOY EXTRUSIONS
   Faculty Investigator: John A. Wert
   Graduate Student: Mark T. Lyttle, Ph.D. Candidate
   UVa Department: Materials Science and Engineering
   NASA-LaRC Contact: T. T. Bales (Metallic Materials)
   Start Date: January, 1994
   Completion Date: September, 1996
   Project #7

8. Al-Si-Ge-Cu ALLOY DEVELOPMENT
   Faculty Investigator: E.A. Starke, Jr.
   Graduate Student: H.J. Koenigsmann, Ph.D. Candidate
   UVa Department: Materials Science and Engineering
   NASA-LaRC Contact: W.B. Lisagor
   Start Date: September, 1993
   Completion Date: To be determined
   Project #8.

9. EFFECTS OF TEXTURE AND PRECIPITATES ON MECHANICAL PROPERTY ANISOTROPY OF Al-Cu-Mg-X ALLOYS
   Faculty Investigators: E.A. Starke, Jr. and G.J. Shiflet
   Graduate Student: None
   Post Doctoral Research Associate: B. Skrotzki
   UVa Department: Materials Science and Engineering
   NASA-LaRC Contact: W.B. Lisagor
   Start Date: January, 1995
   Completion Date: To be determined
   Project #9.

MECHANICS OF MATERIALS FOR LIGHT AEROSPACE STRUCTURES

10. DAMAGE EVOLUTION IN POLYMERIC COMPOSITES
    Faculty Investigator: C. T. Herakovich
    Graduate Student: R. D. Schroedter III, MS Candidate
    UVa Department: Civil Engineering & Applied Mechanics
    NASA-LaRC Contact: C. E. Harris & T. Gates
    Start Date: September 1993
    Completion Date: December, 1995
    Project #10

11. ENVIRONMENTAL EFFECTS IN FATIGUE LIFE PREDICTION: MODELING ENVIRONMENTAL CRACK PROPAGATION IN LIGHT AEROSPACE ALLOYS

Faculty Investigator: R.P. Gangloff
Graduate Students: Zuhair Gasem; PhD Candidate
Edward Richey III; MS Candidate (Mechanical and Aerospace Engineering)
UVa Department: MS&E
NASA-LaRC Contact: R.S. Piascik (Mechanics of Materials)
Start Date: January, 1992
Anticipated Completion Date: June, 1995 (Richey)
December, 1996 (Gasem)
Project #11

THERMAL GRADIENT STRUCTURES

None

RESEARCH PROGRESS AND PLANS (January 1 to June 30, 1995)

Research progress, recorded during the period from January 1, 1995 to June 30, 1995, is summarized for each project in the following sections. The standard format includes the program objective, recent progress, conclusions, and immediate milestones; coupled with a set of visual aids given in graduate student presentations at the Seventh Annual NASA-UVa LA^{2}ST Grant Review Meeting held at NASA-LaRC in July of 1995. The agenda of this meeting is presented in Appendix IV.

Project #1 Time-Temperature Dependent Fracture in Advanced Wrought Ingot Metallurgy and Spray Deposited Aluminum Alloys

Michael J. Haynes and Richard P. Gangloff

Objective

The objective of this study is to quantitatively characterize plane strain initiation (K_{JICi}) and plane stress growth toughnesses of advanced Al-Cu-Mg-Ag alloys as a function of temperature. The effect of temperature on K_{JICi} is micromechanically modeled, employing temperature dependent measurements of elastic modulus, intrinsic fracture strain, yield strength, and work hardening, coupled with an estimate of the critical microstructural distance relevant to dimpled rupture. Metallurgical aspects of elevated temperature microvoid fracture; including second phase particle distributions, shear localization during coalescence, and dynamic recovery; are identified and incorporated into explanations of time-temperature dependent fracture processes.

Recent Findings

Direct current potential difference crack length monitoring, coupled with J-integral fracture mechanics, successfully characterizes initiation and growth toughness of thin sheet compact tension [C(T)] specimens. Rising load experiments on AA2650-T6, for C(T) thicknesses of 3.2 mm and 6.0 mm, demonstrate that K_{JICi} from DCPD detected initiation is nearly identical for the two thicknesses ($K_{JICi} \approx 28.0$ MPa$\sqrt{m}$). In contrast measured fracture

toughness (K_{JC}) from a 0.2 mm offset blunting line definition of fracture initiation (ASTM E813) is 30% higher for the 3.2 mm thick C(T) specimen. The 0.2 mm offset in Δa corresponds to a significant amount of process zone damage and a substantial loss in plane strain constraint. The R-curve rises rapidly in the low Δa regime, resulting in the inflated K_{JC}. For the 6.0 mm thick specimen the plane strain constraint is maintained and K_{JC} approaches K_{JCi}.

Ambient and elevated temperature initiation (K_{JCi}) and growth (K_J^{2mm}) fracture toughnesses have been characterized for a commercial aluminum alloy (AA2024), a low Fe and Ni version of AA2618 (AA2650), and three Ag bearing, 2519-type alloys (AA2519+Mg+Ag, C416, and spray formed N203). AA2519+Mg+Ag and C416 display superior initiation and growth fracture toughness at ambient temperature. Both alloys maintain their initiation toughness to elevated temperatures, and C416 displays the highest K_{JCi} and K_J^{2mm} at elevated temperatures. Spray formed N203, with a 1 to 5 μm grain size, does not display the elevated temperature ductility and fracture toughness degradations seen in submicron grain-size aluminum alloys such as AA8009 and high purity cryogenically milled aluminum.

The critical plastic strain-controlled model successfully predicts the temperature dependency of initiation fracture toughness for a wide variety of advanced aluminum alloys, including AA2519+Mg+Ag, AA2618, AA2095, AA2195, spray formed N203, AA8009, and cryogenically milled aluminum. Predictions can be reasonably based on smooth bar tensile properties and an estimate of the reduction in smooth bar strain to failure ($\bar{\varepsilon}_f^p$) to a triaxial-stress-state constraint corresponding to the crack tip. Temperature insensitive K_{JCi} is predicted and observed for precipitation hardened 2000 series alloys, while a degradation of K_{JCi} is correctly modelled in submicron grain size alloys. The temperature dependencies of K_{JCi} are traceable to the interplay between thermally sensitive process zone fracture resistance ($\bar{\varepsilon}_f^*$) and the temperature-dependent crack tip strain field (dependent on σ_{ys}, E, and N). Both components are necessary to successfully predict temperature insensitive initiation toughness in precipitation hardened alloys, where $\bar{\varepsilon}_f^*$ rises with temperature and σ_{ys}, E, and N decline.

The critical distance (l^*), calculated from the model by equating measured and predicted fracture toughness at ambient temperature, correlates with the nearest neighbor particle spacing in a volume for a variety of aluminum and steel alloys. The data are divided into two correlations, based on whether the alloy contains a unimodal or bimodal size distribution of void

nucleating particles. For a bimodal distribution of particles, the linear fit suggests that the critical fracture initiation event occurs over roughly one particle spacing. For a unimodal distribution, a linear fit suggests that the critical fracture event occurs over 4 to 5 particle spacings. These results are preliminary.

Strain localization between growing microvoids ("Intravoid Strain Localization" or ISL) is hypothesized to have a large influence on the intrinsic fracture resistance (alloy ductility) since subsequent void sheeting truncates primary void growth, which would otherwise dissipate a large amount of strain energy prior to coalescence by impingement. The progression or abatement of ISL depends on the competition between intravoid flow hardening (from strain and strain rate hardening) and intravoid flow softening (partly from void nucleation at dispersoids within an ISL band). As temperature increases, the work hardening exponent (N from $\sigma = K\epsilon^N$) declines, the strain rate hardening exponent (m from $\sigma = K\dot{\epsilon}^m$) increases, and the propensity for void nucleation at dispersoids decreases. Competition between these three variables (in promoting or retarding ISL) results in reduced ISL and void sheeting at elevated temperatures, and an associated rise in $\bar{\epsilon}_f^*$.

Milestones

Two manuscripts, prepared for submittal to *Metallurgical Transactions A* and an ASTM *Special Technical Publication* (STP), have been written and are currently in the revision process. These papers should be completed by September. Another paper, on characterization of initiation toughness and J-Δa behavior will be written for submittal to the ASTM *Journal of Testing and Evaluation.* Mr. Haynes successfully completed the research proposal for his PhD program.

In the next reporting period, we will study intravoid strain localization in AA2519+Mg+Ag and spray formed N203. Stress relaxation tests will be employed to characterize strain rate hardening over a wide range of strain rate and temperature. Smooth and notched tensile bars will be interrupted at various damage levels (as detected by DCPD monitoring) and sectioned for microstructural observation of the microvoid failure processes. Ultra-sensitive density measurements will be employed to quantify void damage.

Presentation Captions

1. Title.

2. Project objectives.

3. Can one accurately characterize initiation (K_{JICi}) and growth (K_J^{2mm}) fracture toughnesses using specimens of reduced width and thickness?

4. Chemical compositions of precipitation hardened alloys (AA2519+Mg+Ag, C416, N203, AA2650, AA2024) characterized for initiation and growth fracture toughness.

5. Photograph illustrating the experimental set up for fracture toughness testing of thin sheet C(T) specimens with buckling restraints. Load, crack length from electrical potential and crack mouth opening displacement are digitally recorded for input to the calculation of J versus Δa.

6. Plane strain character of crack initiation in a thin sheet C(T) specimen and the subsequent transition to plane stress fracture as the crack extends.

7. K_J versus Δa for two thicknesses of C(T) specimens of AA2650 at 25°C, showing: (1) the sensitivity of the offset blunting line (ASTM E813) measurement of initiation toughness (K_{JIC}) to C(T) specimen thickness, and (2) the insensitivity of direct current potential difference (DCPD) detected initiation toughness to specimen thickness. Each C(T) specimen was machined from the central portion of thick plate AA2650.

8. K_{JICi} versus temperature for a variety of precipitation hardened alloys (AA2024, AA2650, AA2519+Mg+Ag, C416, and N203).

9. Summary bar chart of ambient temperature growth toughness (K_J^{2mm}) for precipitation hardened alloys AA2650, N203, AA2024, C416, AA2519+Mg+Ag, and AA2519+Mg, displaying the superior growth toughness of the 2519-type ingot metallurgy alloys (AA2519+Mg, AA2519+Mg+Ag, and C416).

10. Summary bar chart of ambient and elevated temperature K_J^{2mm} for precipitation hardened alloys AA2519+Mg, AA2650, AA2519+Mg+Ag, and C416, displaying the superior elevated temperature K_J^{2mm} for Ag-bearing C416.

11. Can one quantitatively predict the temperature dependence of K_{JICi} in ingot metallurgy, spray formed, and submicron grain size powder metallurgy aluminum alloys?

12. Chemical compositions of aluminum alloys that were micromechanically modelled to predict initiation toughness.

13. Schematic representation of the critical plastic strain-controlled model depicting three model elements: (1) the effective plastic strain field ahead of a crack tip ($\bar{\varepsilon}^p$), (2) the intrinsic fracture resistance relevant to a high stress state triaxiality ($\bar{\varepsilon}_f^*$), and (3) the fracture criterion of $\bar{\varepsilon}^p$ exceeding $\bar{\varepsilon}_f^*$ over a critical microstructural distance (l^*). By combining these three elements, K_{JICi} is predicted as a composite property dependent on yield strength, modulus, work hardening, constituent particle spacing, and fracture ductility (reduction in area). Each of these latter material properties depends on temperature.

14. Temperature-dependent tensile properties (σ_{ys} and %RA) of AA2519+Mg+Ag and spray formed N203. AA2519+Mg+Ag possesses superior yield strength and ductility.

15. Temperature dependent work hardening exponent (N) for spray formed N203 and AA2519+Mg+Ag, showing superior work hardening capacity of lower strength N203.

16. Micromechanical model predictions of temperature dependent K_{JICi} for AA2519+Mg+Ag compared to experimental measurements. Two sets of predictions were produced, based on reduction in area measurements of smooth and notched round tensile bars.

17. Micromechanical model predictions of temperature dependent K_{JICi} for spray formed N203 and AA2618 compared to experimental measurements.

18. Micromechanical model predictions of cryogenic to elevated temperature K_{JICi} for AA2095 and AA2195 compared to experimental measurements.

19. Elevated temperature dependence of normalized intrinsic fracture strain for AA2519+Mg+Ag, cryogenically milled aluminum, and AA8009.

20. Micromechanical model predictions of temperature dependent K_{JICi} for AA8009 and cryogenically milled aluminum, compared to experimental measurements.

21. Correlation between l^* and the nearest neighbor spacing of void nucleating constituents in a volume for aluminum alloys and steels, subdivided into unimodal and bimodal particle size distribution classes.

22. Hypothesis: the intrinsic fracture resistance of 2000 series aluminum alloys increases with increasing temperature due to a decreasing tendency for Intravoid Strain Localization (ISL) and a decreased tendency for the associated plastic shear instability between growing microvoids.

23. Experimental evidence of retarded ISL behavior at elevated temperature, obtained from crack tip profiles of AA2519+Mg+Ag.

24. List of continuum and microstructural variables governing ISL.

25. Schematic representation of ISL between two growing microvoids (nucleated at constituent particles), illustrating important features such as: (1) stress and strain rate amplification within the band, and (2) flow hardening in the band due to local strain and strain rate hardening as well as flow softening due to void nucleation at submicron dispersoids.

26. Fractographs displaying the role of constituent particle distribution in influencing ISL behavior.

27. Explanation of retarded void sheeting and enhanced %RA at elevated temperature in AA2519+Mg+Ag. At ambient temperature, intravoid flow hardening due to strain and strain rate hardening is insufficient to overcome intravoid flow softening (partly from void nucleation at dispersoids). ISL and void sheeting is prevalent. At elevated temperatures, intravoid flow hardening is substantial and sufficient to delay the onset of ISL and void sheeting, due to enhanced strain rate hardening and reduced void nucleation at dispersoids. Fracture ductility increases due to enhanced stable growth of primary microvoids.

28. Correlation between strain rate sensitivity, m, and $\bar{\varepsilon}_f^*$ for AA2519+Mg+Ag and AA2618. m was calculated from creep data for AA2219 and AA2618, while $\bar{\varepsilon}_f^*$ was calculated from %RA.

29. Conclusions.

Elevated Temperature Fracture of Advanced Aluminum Alloys

Michael J. Haynes and Richard P. Gangloff

July 17, 1995

Funded by NASA Langley Research Center
W.B. Lisagor, Project Monitor

Objectives of Elevated Temperature Fracture Studies

- Characterize the initiation and growth fracture toughness of advanced aluminum alloys as a function of temperature.
- Micromechanically model initiation fracture toughness (K_{JICi}) as a function of temperature.
- Identify metallurgical and continuum aspects of temperature dependent microvoid fracture.

CAN ONE ACCURATELY CHARACTERIZE INITIATION (K_{JICI}) AND GROWTH (K_J^{2mm}) FRACTURE TOUGHNESSES USING SPECIMENS OF REDUCED WIDTH AND THICKNESS ?

Chemical Compositions of Characterized Alloys (Wt%)

Alloy Designation	Cu	Mg	Ag	Mn	Zr	V	Fe	Si	Ti (Ni)
AA2519-T87+Mg+Ag	5.75	0.52	0.50	0.3	.16	.09	.05	0.04	---
C416-T8	5.40	0.50	0.50	0.3	.13	---	.06	.04	---
N203-T6	4.90	0.50	0.40	0.50	0.40	0.22	---	---	0.19
AA2650-T6	2.71	1.64	---	---	---	---	0.20	0.21	(.21)
AA2024-T3	4.4	1.5	---	---	---	---	---	---	---

AA2519+Mg+Ag, C416: Ingot metallurgy sheet (0.125" and 0.090" thick), Ω precipitate strengthened

N203: Spray formed (SF), precipitation hardened extrusion (1")- Ω strengthened

AA2650: Ingot metallurgy plate (0.250" thick), S' and θ' precipitate strengthened

AA2024: Ingot metallurgy sheet (0.125" thick), Naturally Aged (θ' precipitates)

Thickness is 0.125" for C(T) specimens of AA2519+Mg+Ag, N203, AA2650, and AA2024

Thickness is 0.090" for C(T) specimens of C416

C(T) Specimen Detail for Thin Sheet J-Δa Determination

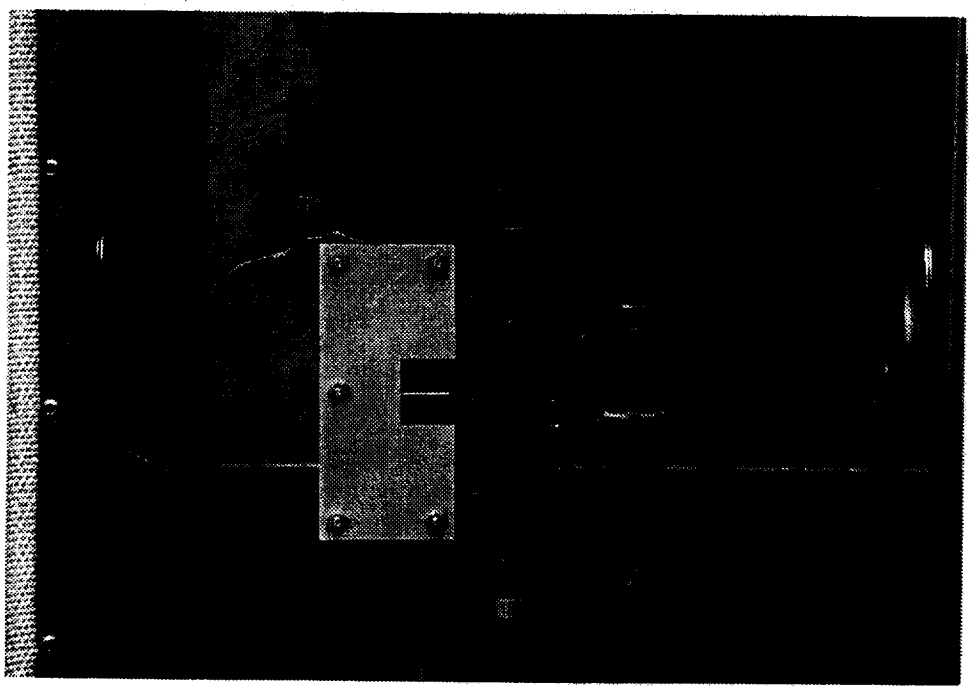

- Low magnification SEM fractograph of a 2519-T87 (+Mg+Ag) fracture surface produced at 25•C showing the plane strain flat fracture and transition to plane stress cracking. The shear lip - flat fracture interface is indicated by arrows, with the fatigue precrack just visible parallel to the bottom edge of the photo.

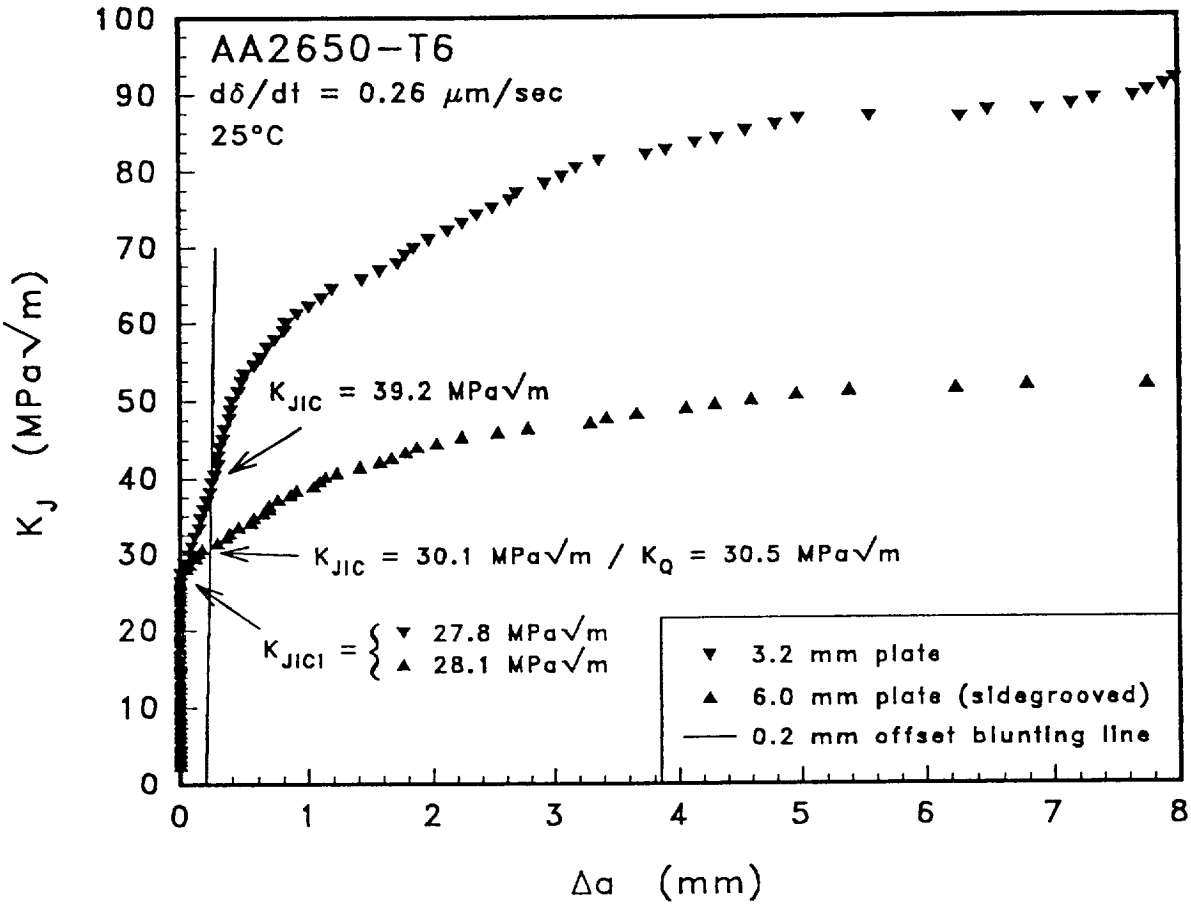
AA2650-T6
dδ/dt = 0.26 μm/sec
25°C
K_JIC = 39.2 MPa√m
K_JIC = 30.1 MPa√m / K_Q = 30.5 MPa√m
K_JIC1 = 27.8 MPa√m
28.1 MPa√m
3.2 mm plate
6.0 mm plate (sidegrooved)
0.2 mm offset blunting line
K_J (MPa√m)
Δa (mm)
0
10
20
30
40
50
60
70
80
90
100
0
1
2
3
4
5
6
7
8

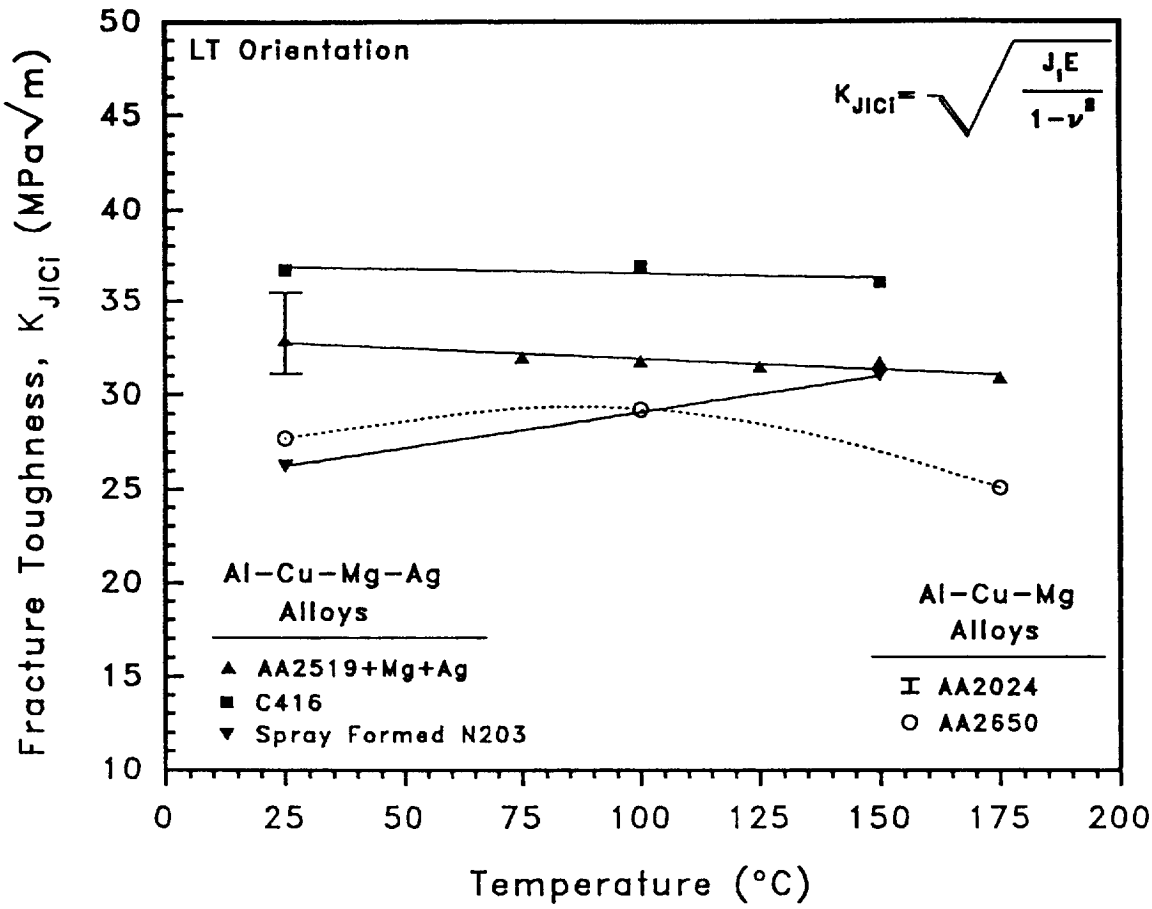
LT Orientation
$K_{JICi} = \sqrt{\frac{J_i E}{1-\nu^2}}$
Fracture Toughness, K_{JICi} (MPa√m)
Temperature (°C)
50
45
40
35
30
25
20
15
10
0
25
50
75
100
125
150
175
200
Al–Cu–Mg–Ag Alloys
▲ AA2519+Mg+Ag
■ C416
▼ Spray Formed N203
Al–Cu–Mg Alloys
I AA2024
○ AA2650

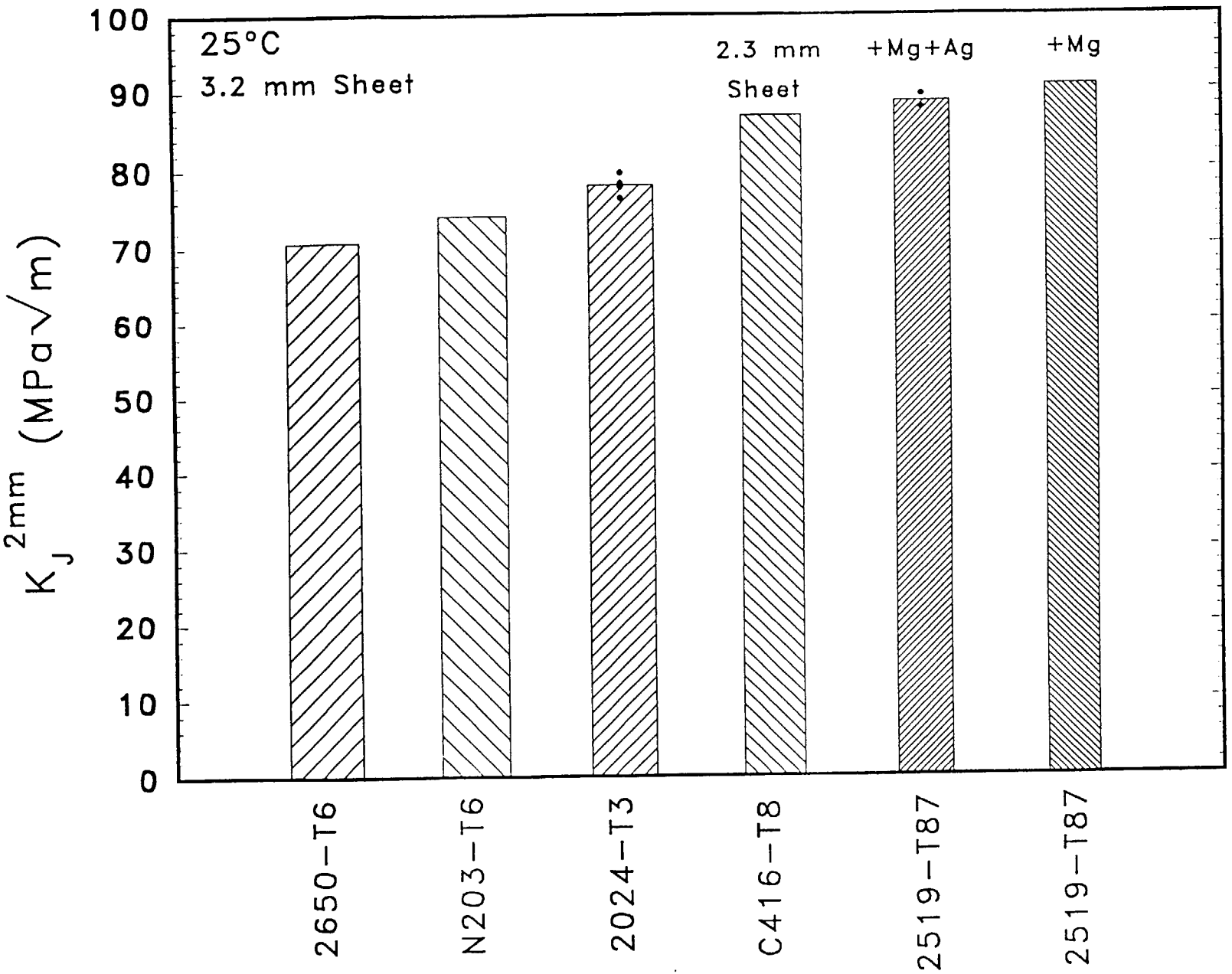
25°C
3.2 mm Sheet
2.3 mm Sheet
+Mg+Ag
+Mg
K_J^{2mm} (MPa√m)
100
90
80
70
60
50
40
30
20
10
0
2650-T6
N203-T6
2024-T3
C416-T8
2519-T87
2519-T87

$K_{J_{2mm}}$ (MPa$\sqrt{m}$)
130
120
110
100
90
80
70
60
50
40
30
20
10
0
3.2 mm Sheet
$\dot{\delta}$ = 0.26 μm/sec
2519-T87
(+Mg)
25°C
100°C
175°C
2650-T6
25°C
100°C
175°C
2519-T87
(+Mg+Ag)
25°C
100°C
150°C
175°C
C416-T8
(2.3 mm
Sheet)
25°C
100°C
150°C

CAN ONE QUANTITATIVELY PREDICT THE TEMPERATURE DEPENDENCE OF K_{JICi} IN INGOT METALLURGY, SPRAY FORMED, AND SUBMICRON GRAIN SIZE (PM) ALLOYS ?

Chemical Compositions of Ingot Metallugy, Spray Formed, Ultra-Fine Grain Size, and Metal Matrix Composite Alloys for Modelling

Alloy Designation	Alloy Class	Product Form	Nominal Alloy Composition (weight %)
AA2095-T6	I/M	Plate	Al-4.6Cu-1.5Li-0.35Ag-0.4Mg-0.15Zr
AA2195-T6	I/M	Plate	Al-4.0Cu-1.0Li-0.35Ag-0.4Mg-0.15Zr
AA2618-T851	I/M	Plate	Al-2.6Cu-1.6Mg-1.0Fe-1.2Ni-0.2Si
AA2519-T87(+Mg+Ag)	I/M	Sheet	Al-5.75Cu-0.5Mg-0.5Ag-0.3Mn-0.15Zr-0.1V
N203-T6	SF	Extrusion	Al-5.0Cu-0.5Mg-0.5Mn-0.4Zr-0.4Ag-0.2Ti-0.2V
CM Al	SM/GS	Extrusion	Al + 2.5 vol%Al_2O_3
AA8009	SM/GS	Extrusion	Al-8.5Fe-1.3V-1.7Si
2009/SiC/20p-T6	MMC	Plate	Al-3.6Cu-1.3Mg + 19.5 vol% SiC

Critical Plastic Strain Controlled Model

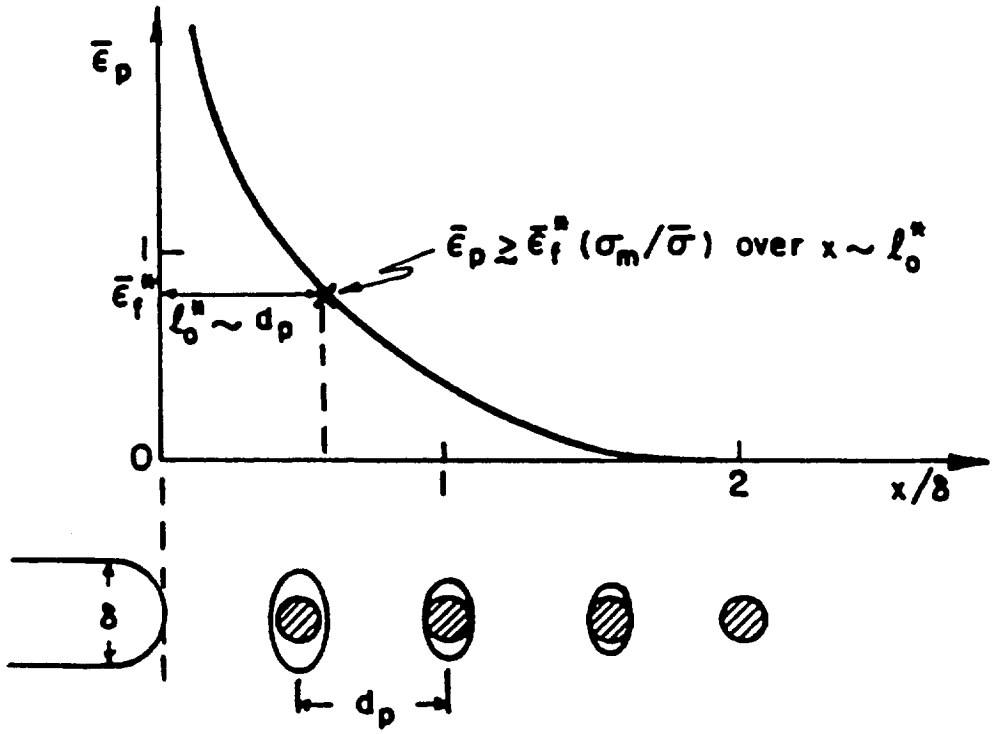

$$K_{JICi} = \sqrt{\frac{\sigma_{ys} E I^*}{(1-\nu^2) d_n} \left(\frac{\bar{\epsilon}_f^*}{C1} \right)^{\frac{1}{C2}}}$$

$$\bar{\epsilon}_f^* = (1/\gamma)\ (-\ln(1-\%RA))$$

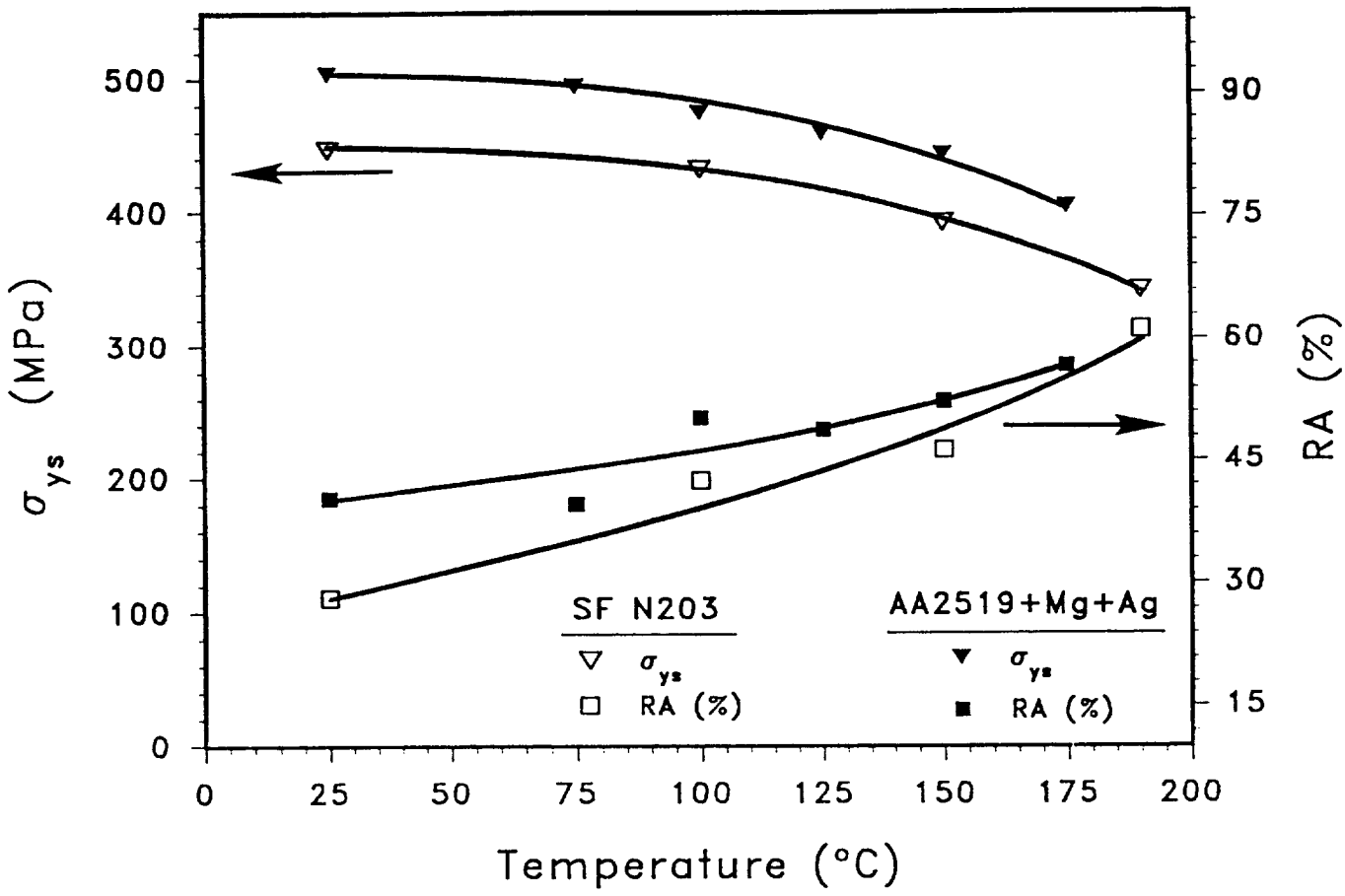
500
400
300
200
100
0
σ_{ys} (MPa)
90
75
60
45
30
15
RA (%)
0
25
50
75
100
125
150
175
200
Temperature (°C)
SF N203
σ_{ys}
RA (%)
AA2519+Mg+Ag
σ_{ys}
RA (%)

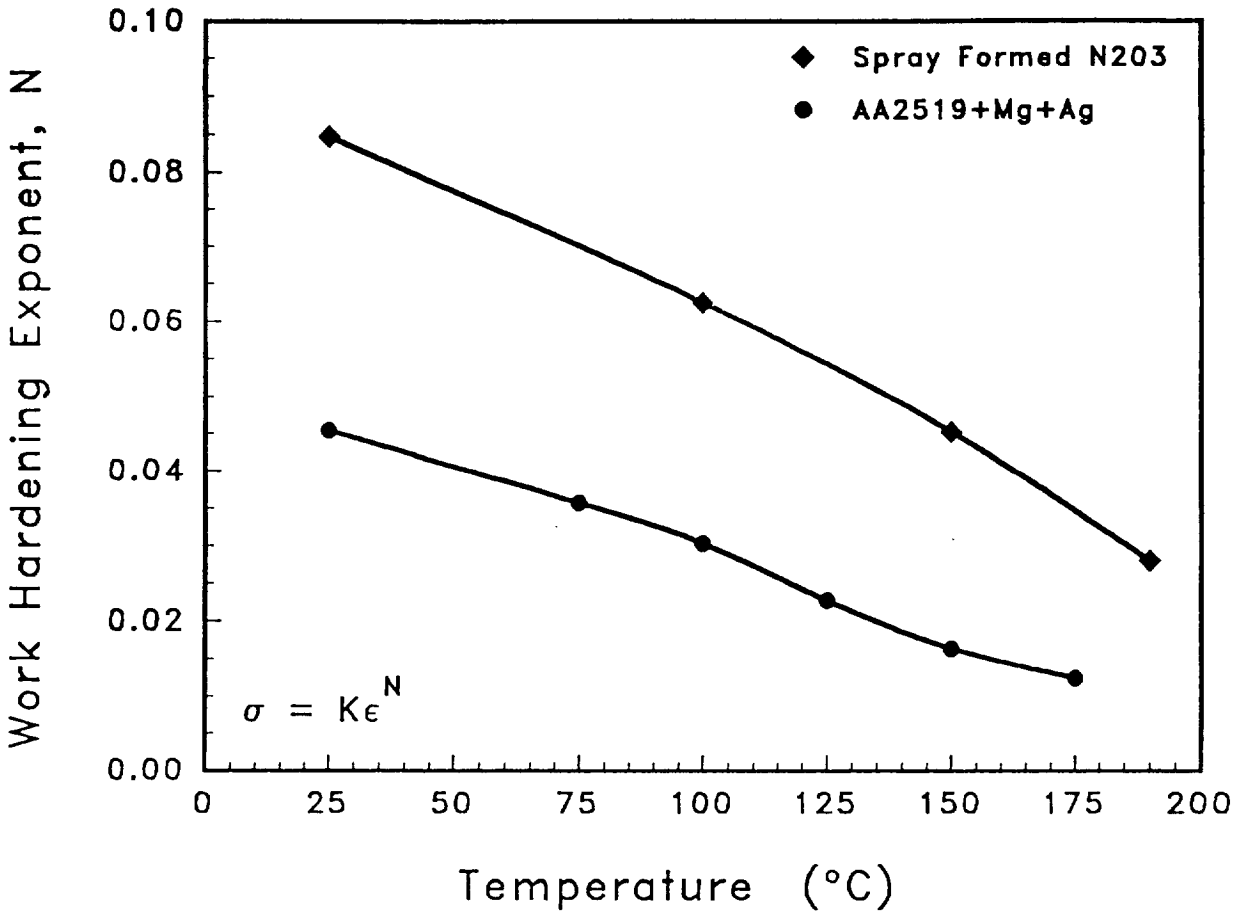
Work Hardening Exponent, N
0.10
0.08
0.06
0.04
0.02
0.00
0
25
50
75
100
125
150
175
200
Temperature (°C)
Spray Formed N203
AA2519+Mg+Ag
$\sigma = K\epsilon^N$

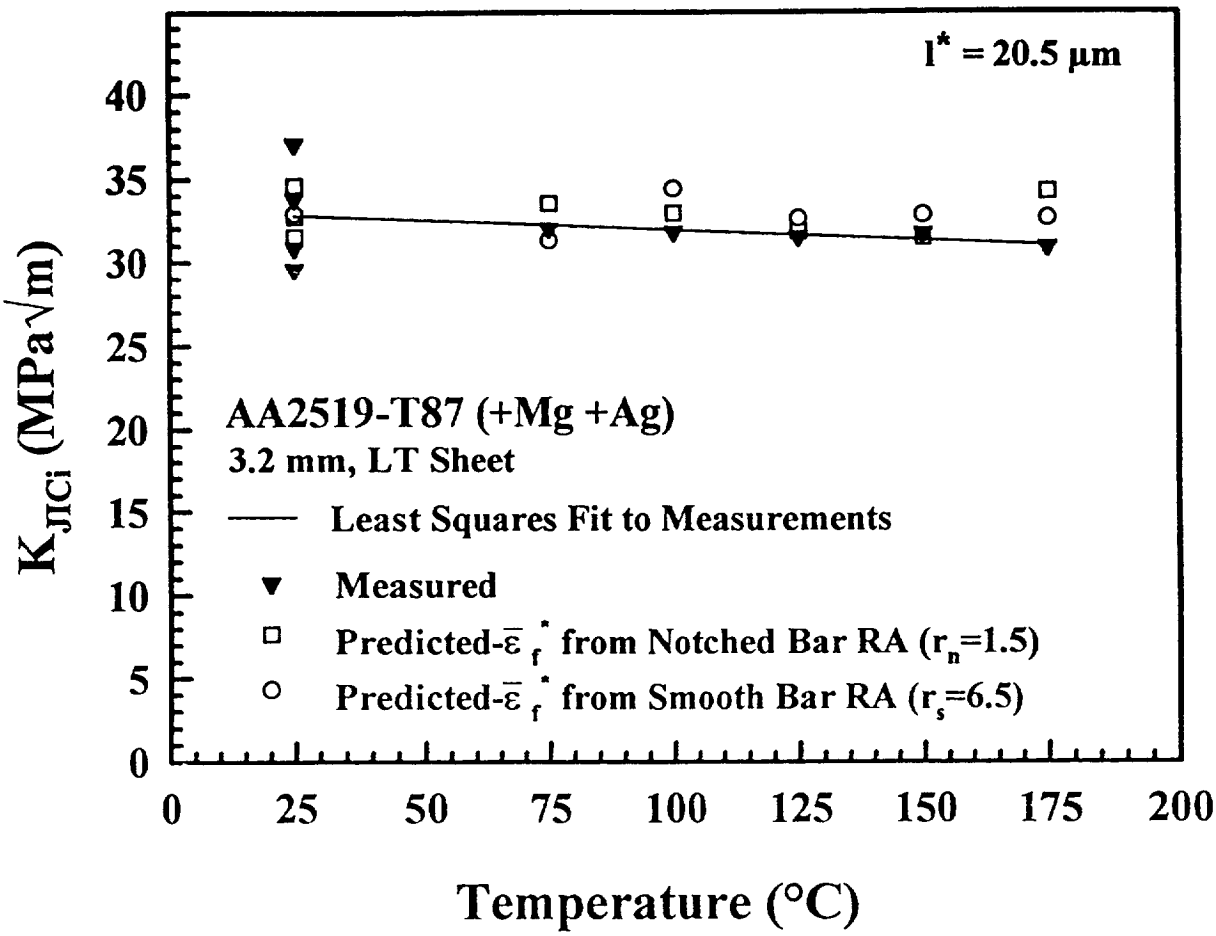
l* = 20.5 µm
AA2519-T87 (+Mg +Ag)
3.2 mm, LT Sheet
Least Squares Fit to Measurements
Measured
Predicted-$\bar{\varepsilon}_f^*$ from Notched Bar RA (r_n=1.5)
Predicted-$\bar{\varepsilon}_f^*$ from Smooth Bar RA (r_s=6.5)
K_{JICi} (MPa$\sqrt{m}$)
0
5
10
15
20
25
30
35
40
0
25
50
75
100
125
150
175
200
Temperature (°C)

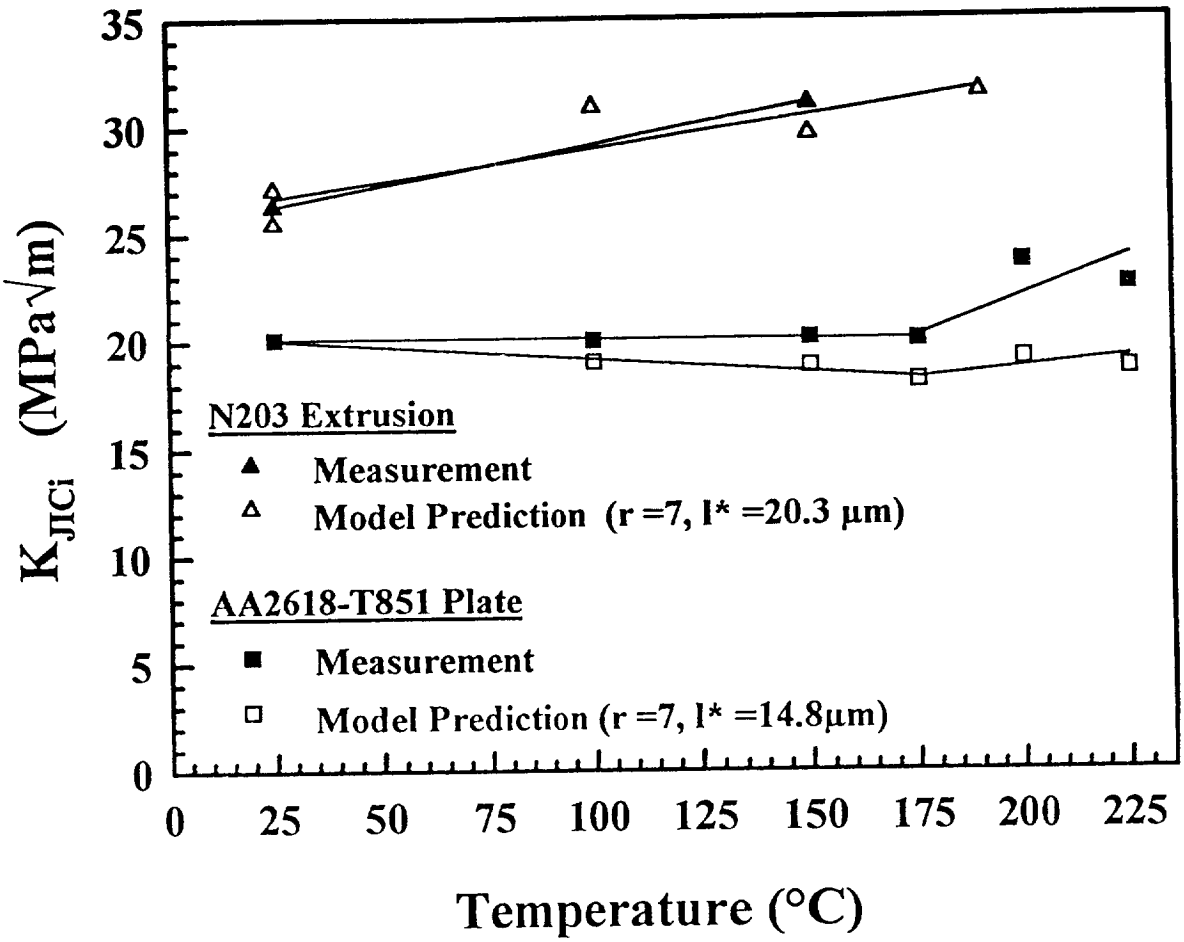
35
30
25
20
15
10
5
0
K_{JICi} (MPa√m)
N203 Extrusion
Measurement
Model Prediction (r =7, l* =20.3 μm)
AA2618-T851 Plate
Measurement
Model Prediction (r =7, l* =14.8μm)
0
25
50
75
100
125
150
175
200
225
Temperature (°C)

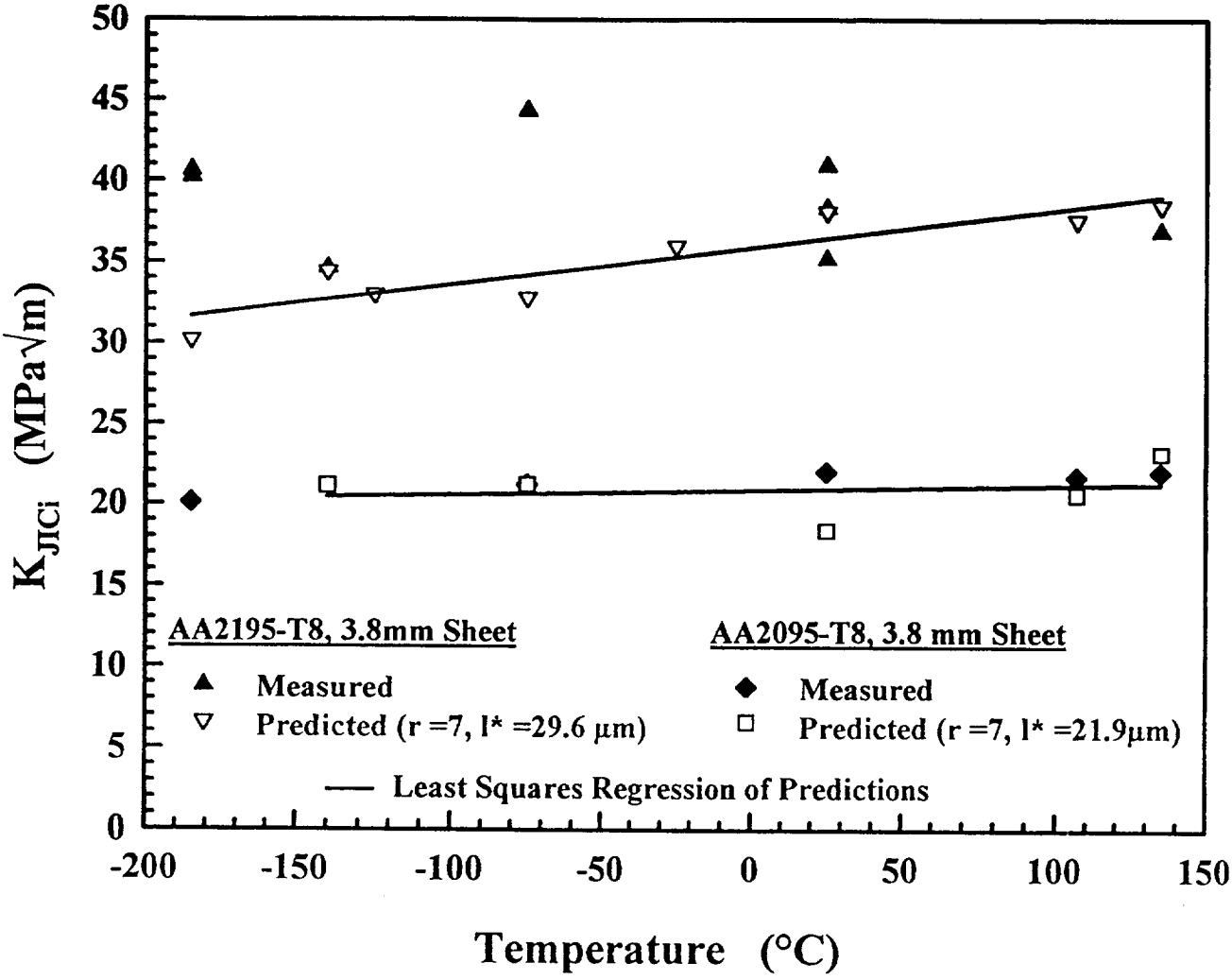
50
45
40
35
30
25
20
15
10
5
0
K_{JICi} (MPa√m)
AA2195-T8, 3.8mm Sheet
Measured
Predicted (r =7, l* =29.6 μm)
AA2095-T8, 3.8 mm Sheet
Measured
Predicted (r =7, l* =21.9μm)
Least Squares Regression of Predictions
-200
-150
-100
-50
0
50
100
150
Temperature (°C)

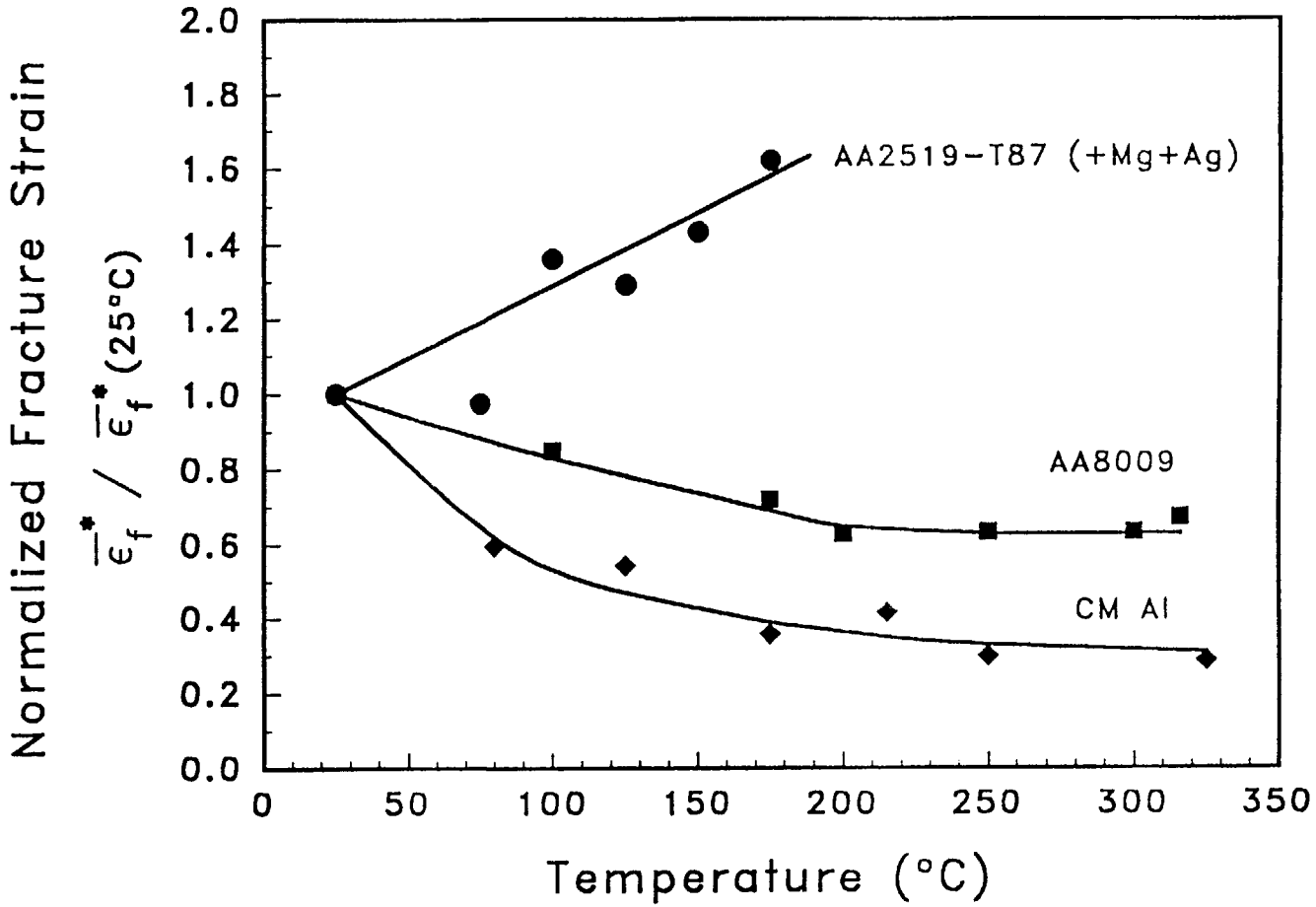
Normalized Fracture Strain
$\overline{\epsilon_f^*}$ / $\overline{\epsilon_f^*}$(25°C)
2.0
1.8
1.6
1.4
1.2
1.0
0.8
0.6
0.4
0.2
0.0
0
50
100
150
200
250
300
350
Temperature (°C)
AA2519-T87 (+Mg+Ag)
AA8009
CM Al

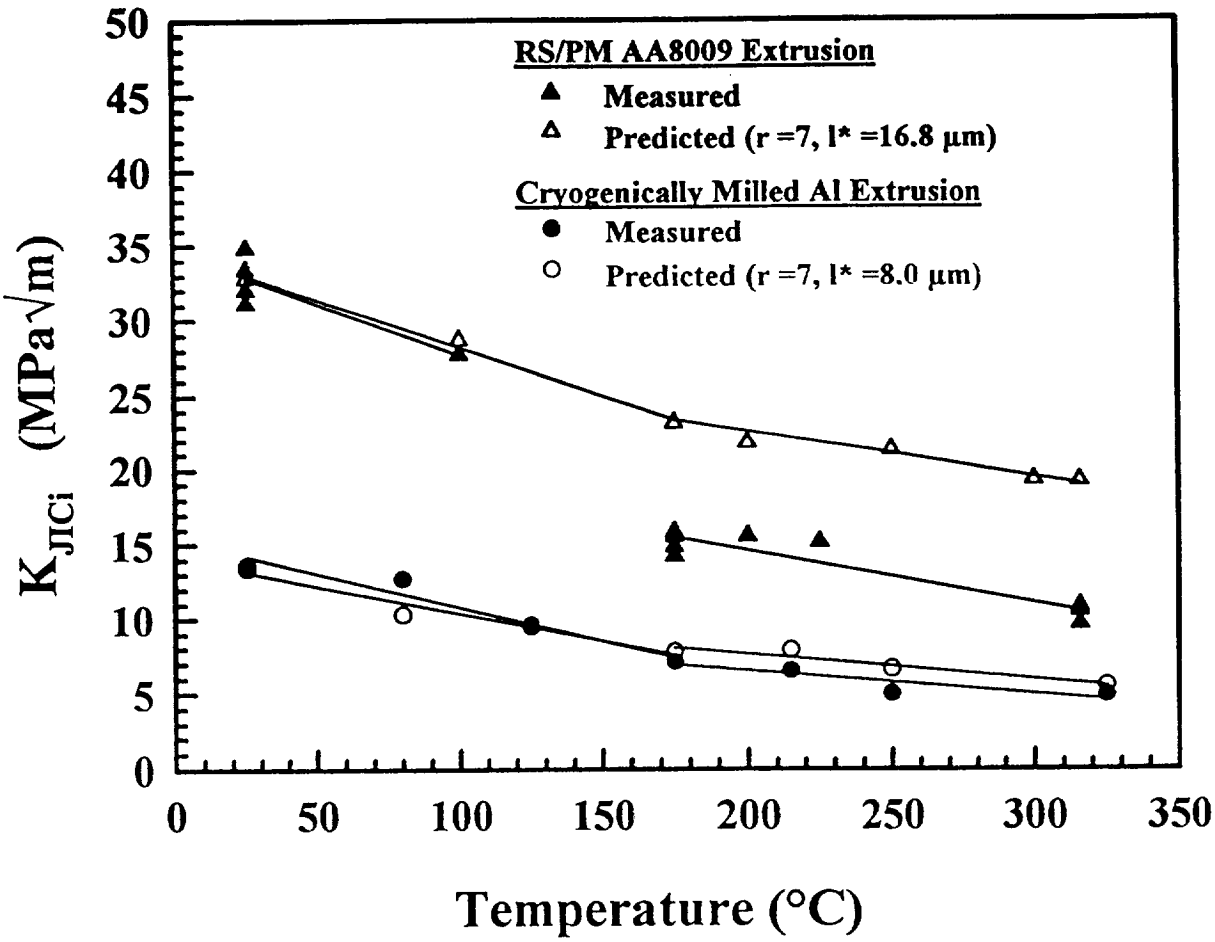
RS/PM AA8009 Extrusion
Measured
Predicted (r =7, l* =16.8 μm)
Cryogenically Milled Al Extrusion
Measured
Predicted (r =7, l* =8.0 μm)
K_{JICi} (MPa√m)
Temperature (°C)
0
5
10
15
20
25
30
35
40
45
50
0
50
100
150
200
250
300
350

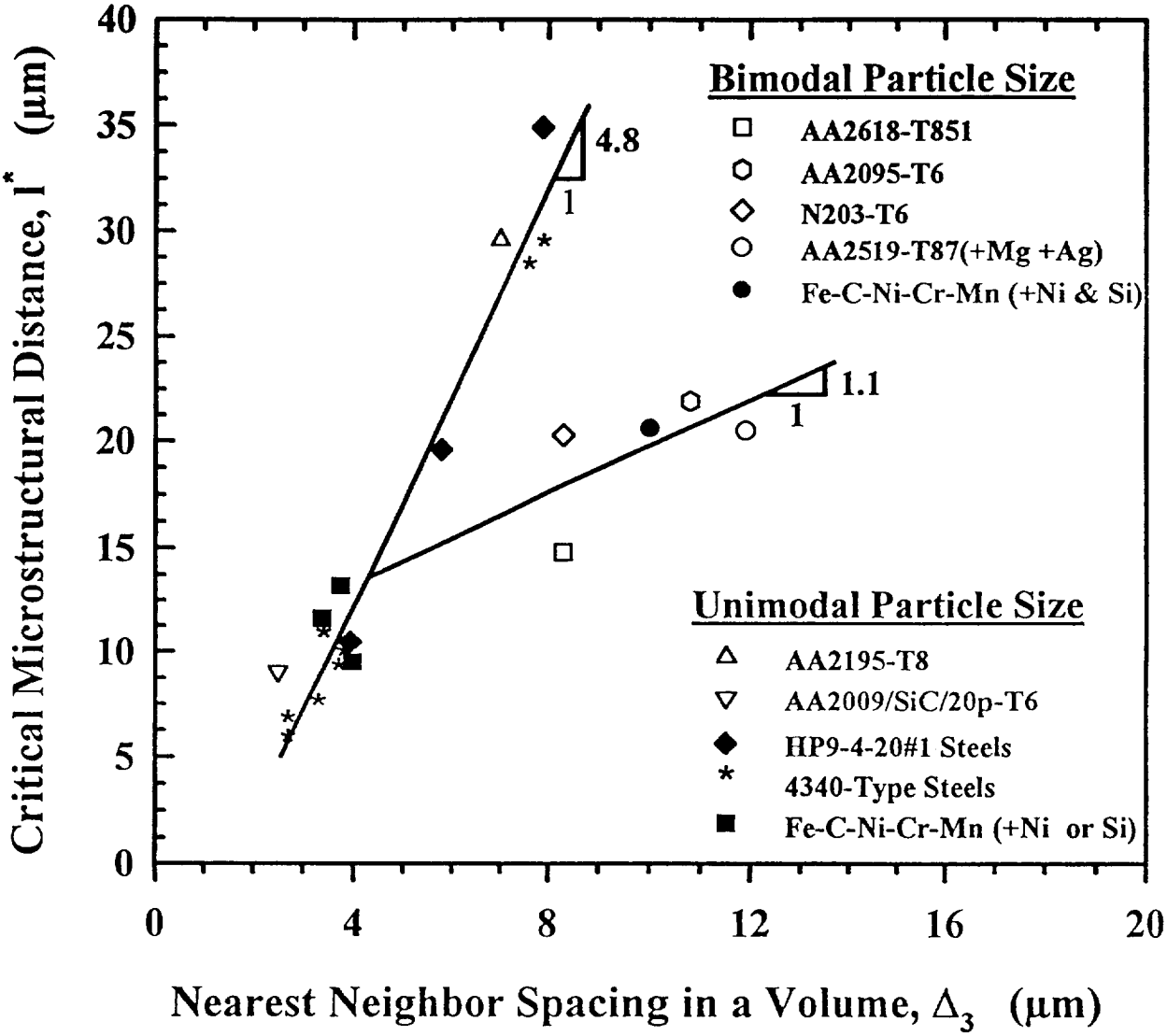
Critical Microstructural Distance, l* (μm)
Nearest Neighbor Spacing in a Volume, Δ3 (μm)
0
5
10
15
20
25
30
35
40
0
4
8
12
16
20
Bimodal Particle Size
AA2618-T851
AA2095-T6
N203-T6
AA2519-T87(+Mg +Ag)
Fe-C-Ni-Cr-Mn (+Ni & Si)
4.8
1
1.1
1
Unimodal Particle Size
AA2195-T8
AA2009/SiC/20p-T6
HP9-4-20#1 Steels
4340-Type Steels
Fe-C-Ni-Cr-Mn (+Ni or Si)

HYPOTHESIS

The intrinsic fracture resistance of 2000 series aluminum alloys increases with increasing temperature due to a decreasing tendency for Intravoid Strain Localization (ISL) and a decreased tendency for the associated plastic shear instability between growing microvoids.

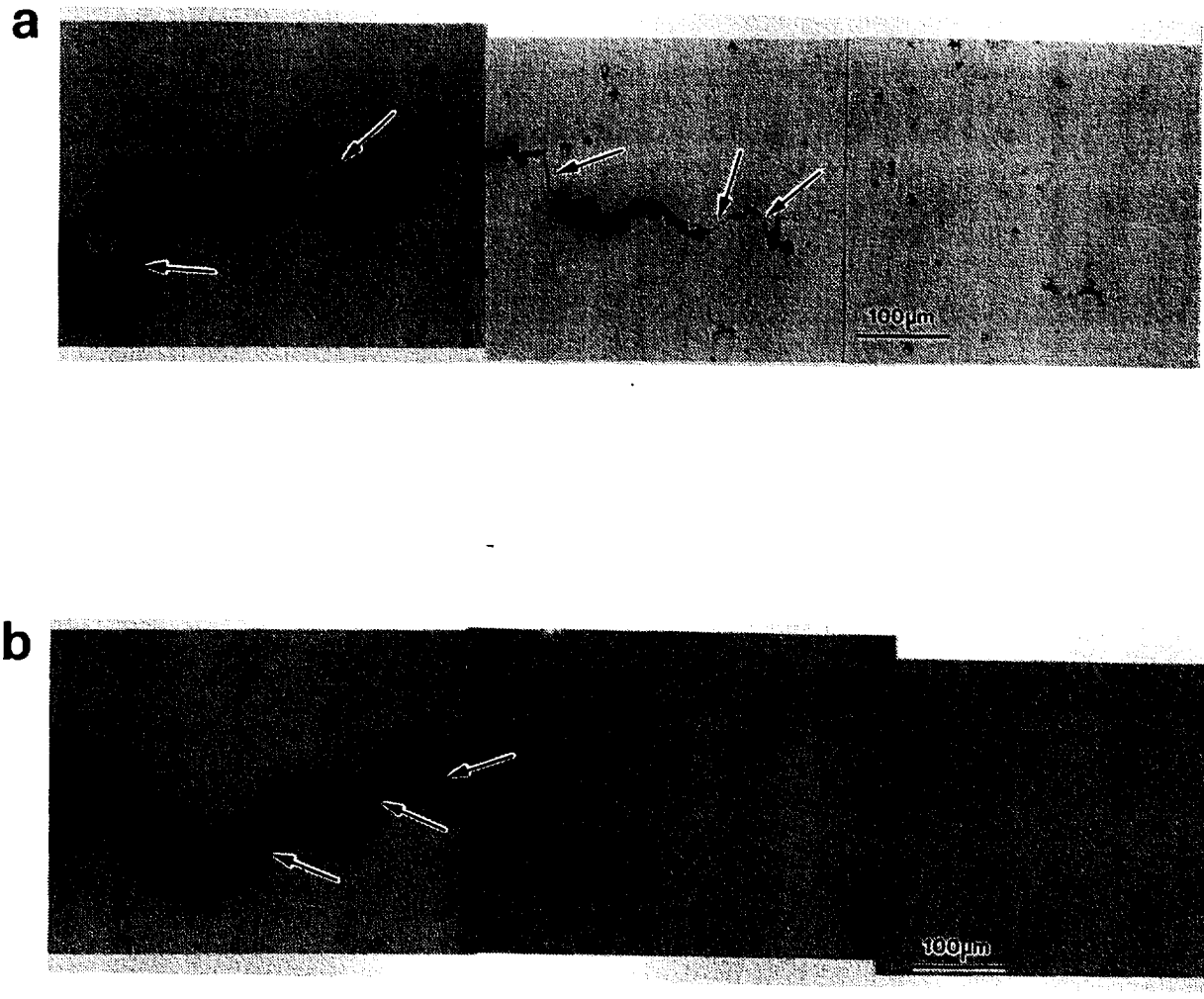

Crack tip profiles from midplane of C(T) specimens fractured at: (a) 25°C and (b) 150°C; load-line displacement rate = 0.26 μm/sec. Arrows indicate void sheeting.

CONTINUUM AND MICROSTRUCTURAL VARIABLES GOVERNING ISL

Microstructural Variables

1. Spatial Distribution of Primary or Large Voids
2. Primary Void Shape (Projected Area Normal to Stress)
3.[1] Void Nucleation at Small Second Phase Particles (Dispersoids)
4.[2] Slip Mode

Continuum Variables

1. Global Stress State Triaxiality
2.[1] Strain Hardening
3.[1] Strain Rate Hardening

[1] **Strongly Temperature Dependent**

[2] **May be Temperature Dependent Depending on Alloy System**

INTRAVOID STRAIN LOCALIZATION SCHEMATIC

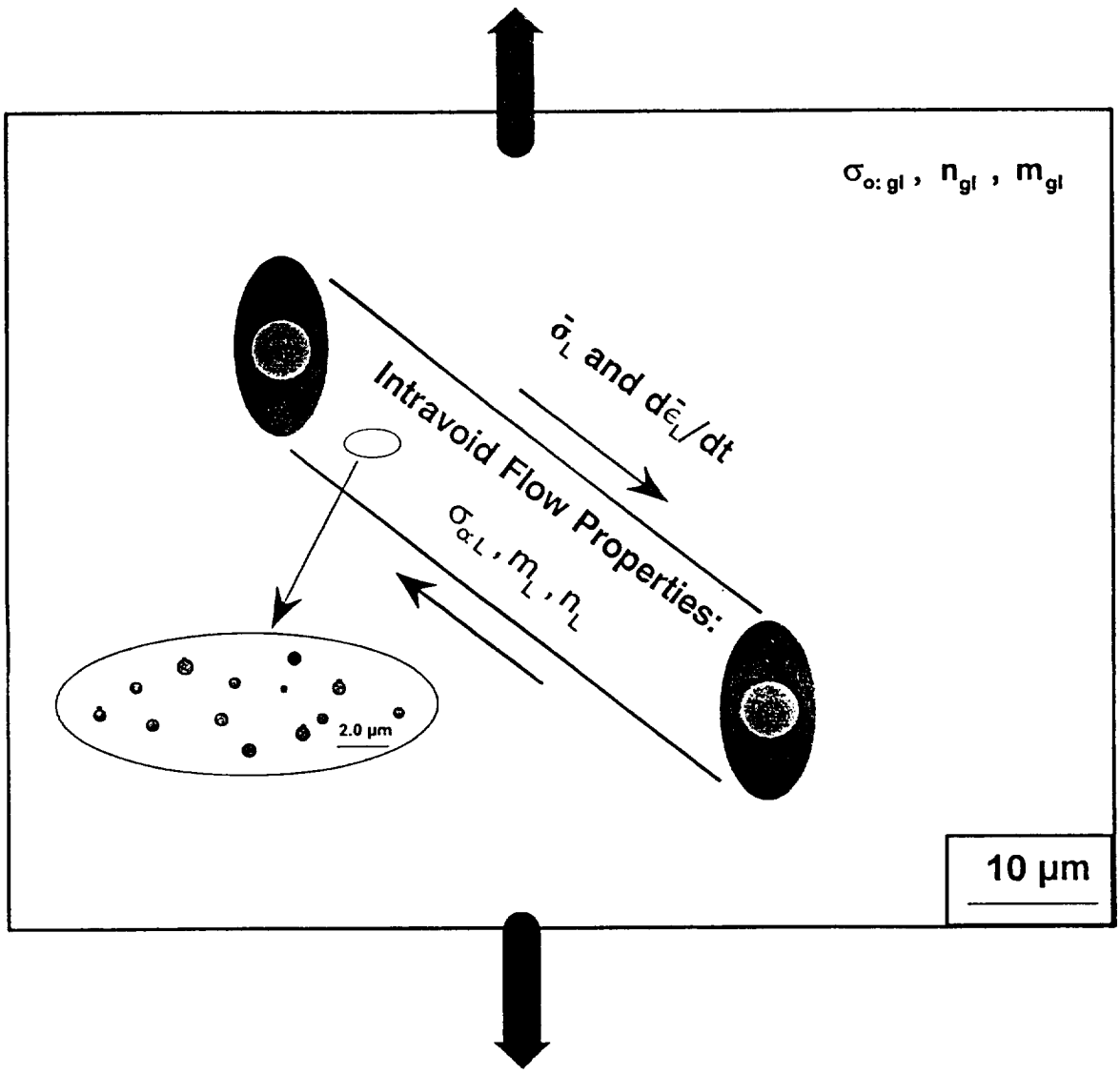

Role of Undissolved θ Constituent in ISI

25° C

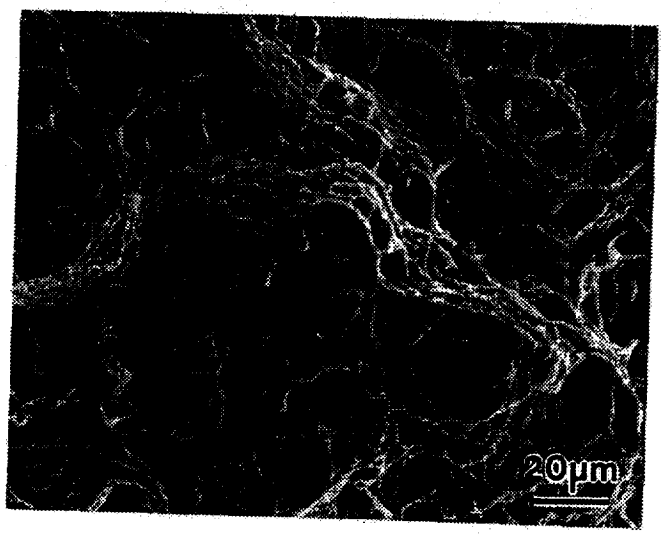

25° C

150° C

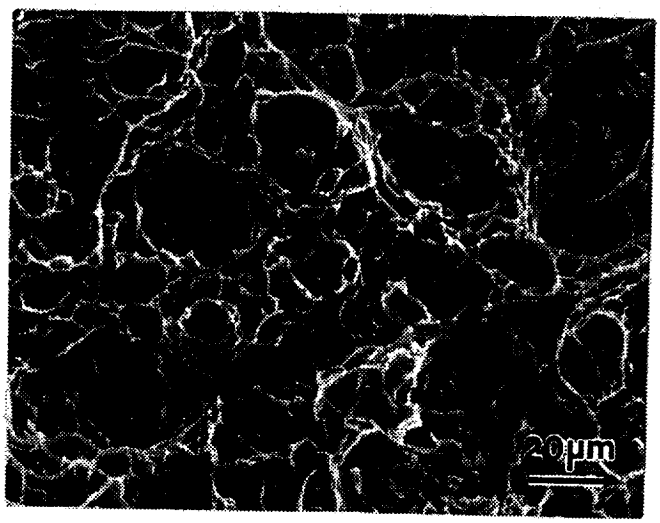

150° C

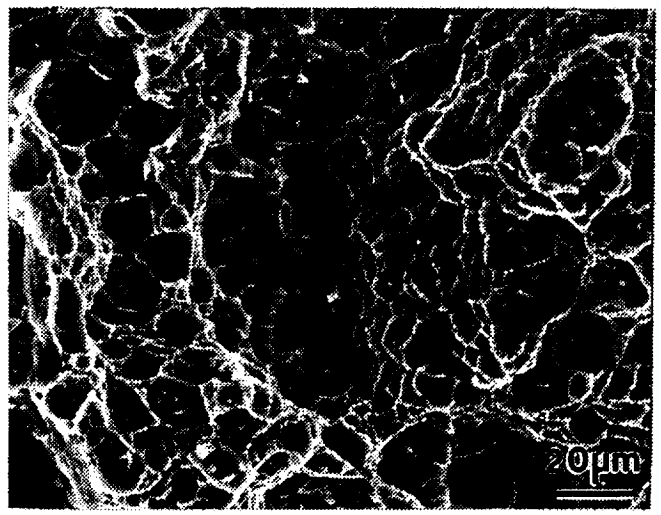

2519-T87(+Mg+Ag)

High V_f of Undissolved θ

C416-T8

Low V_f of Undissolved θ

INTRAVOID STRAIN LOCALIZATION

Void sheeting is retarded (and $\bar{\epsilon}_f^*$ increases) at elevated temperatures because:

At ambient temperature:

- Intravoid flow softening is substantial, due to void initiation and growth at submicrometer dispersoids.
- Strain and strain rate hardening are low; thus intravoid flow hardening is relatively low.
- Flow hardening is insufficient to delay the onset of ISL. Relative to elevated temperatures, void sheeting is prevalent and the extent of stable void growth and $\bar{\epsilon}_f^*$ are low.

As temperature is increased:

- Intravoid flow softening is reduced, due to dislocation bypassing of dispersoids by climb.
- Strain hardening decreases, but strain rate hardening increases; intravoid flow hardening remains constant or increases.
- Intravoid flow hardening is substantial enough to delay the onset of ISL. Void sheeting is reduced, the extent of stable void growth increases and $\bar{\epsilon}_f^*$ increases.

NEED: *Quantify the roles of m, N, and intravoid flow softening on the onset of strain localized coalescence.*

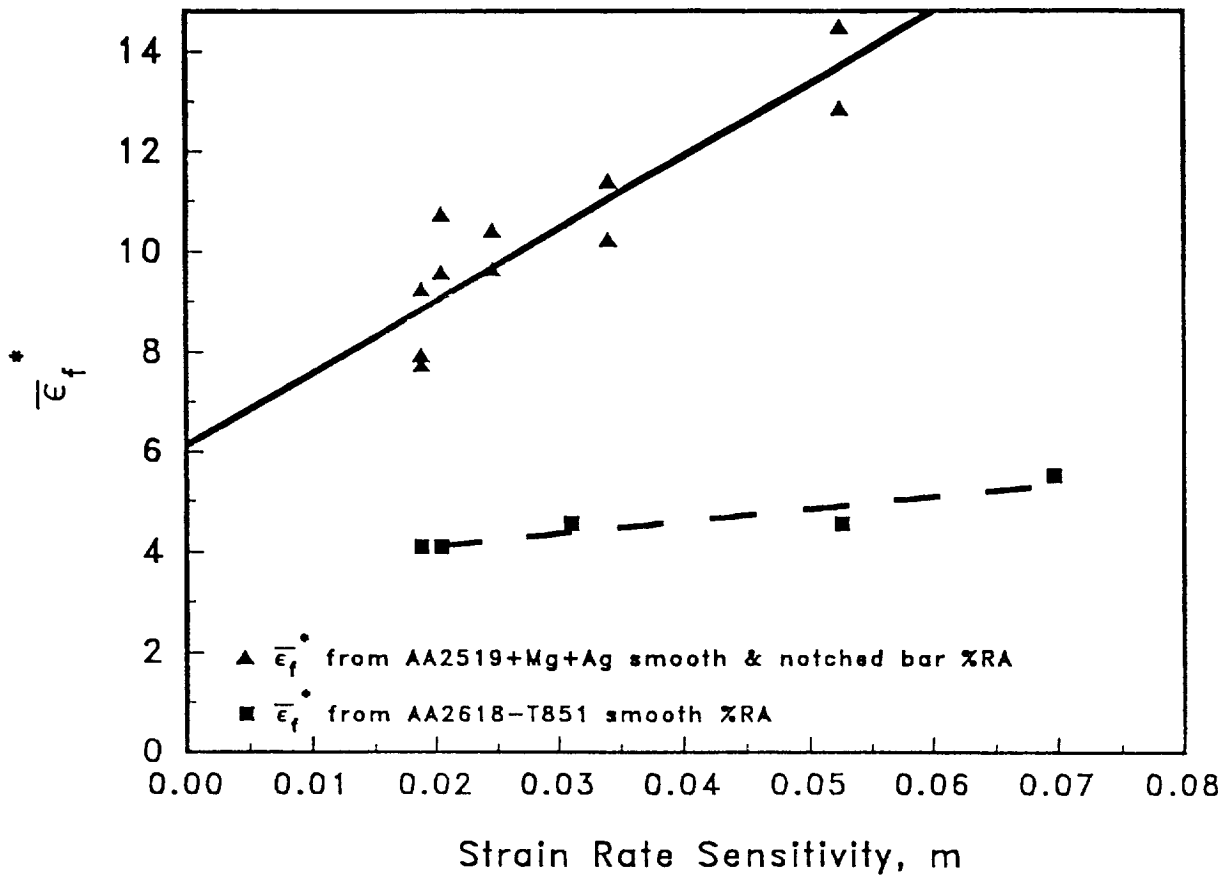

Correlations between strain rate sensitivity, m, and $\bar{\epsilon}_f^*$ for 2519-T87 (+Mg+Ag) and 2618-T851. $\bar{\epsilon}_f^*$ values are derived from smooth and notched tensile specimen reduction in areas by employing Eq. [6]; $r_n = 1.53$ for notched bars and $r_s = 6.5$ for smooth bars.

Conclusions

- Initiation (K_{JICi}) and growth (K_J^{2mm}) are characterized accurately by a J-integral fracture mechanics method and direct current potential difference crack length monitoring, with potential for small-specimen experiments.

- The offset blunting line definition of initiation toughness from ASTM E813 overestimates the initiation toughness of thin sheet aluminum alloys (despite satisfying the thickness criterion), due to a sharply rising R-curve associated with a loss in plane strain constraint. The DCPD method detects fracture initiation closer to the fatigue crack tip and appears to be insensitive to specimen thickness, at least down to a 1/8" gage.

- At ambient temperature, the 2519-type alloy sheets display superior plane stress toughness (K_J^{2mm}) over 2024-T3, 2650-T6, and spray formed N203-T6.

- At elevated temperatures, C416-T8 shows the best plane stress toughness (K_J^{2mm}) compared to 2519-T87(+Mg+Ag), 2519-T87(+Mg), and 2650-T6.

- The magnitude and temperature dependence of K_{JICi} is accurately predicted for a variety of advanced aluminum alloys by a strain-based micromechanical model of microvoid fracture.

- Initiation fracture toughness is a composite property, composed of temperature dependent intrinsic alloy flow (σ_{ys}, E, N) and fracture ($\bar{\epsilon}_f^*$, %RA) properties.

- l^* correlates to the nearest neighbor spacing of void nucleating constituents in a volume for aluminum alloys and steels.

- The intrinsic fracture strain, $\bar{\epsilon}_f^*$, is strongly influenced by ISL (strain localization between primary voids nucleated at constituents). The prevalence of ISL at ambient versus elevated temperatures depends directly on the propensity for void nucleation at dispersoids and is inversely related to the levels of strain and strain rate hardening at these temperatures.

Project #2 **Cryogenic Temperature Effects on the Deformation and Fracture of Al-Li-Cu and Al-Li-Cu-In Alloys:** ***Microtexture and Temperature Dependent Fracture of AA2090***

John A. Wagner and R.P. Gangloff

Objective

The objective of this Ph.D. research is to characterize and optimize the crack initiation and growth fracture resistance Al-Li-Cu (alloy 2090) and Al-Li-Cu-In (alloy 2090+In) for cryogenic tank applications. The program aims to understand microscopic fracture events; as influenced by ambient to cryogenic temperatures, stress state and microstructure. The specific goal is to determine the mechanisms associated with delamination and transgranular shear (TGS) fracture.

Status

The current work in this project has been focusing on the details of the mechanisms associated with fracture of 2090-T81 at intermediate temperatures in the range 25°C to -185°C and on the microtexture of fracture. Previous work has focused on the fracture behavior at the two extreme temperatures. To gain a better understanding of the mechanisms of fracture tensile, notched tensile and toughness tests were conducted at intermediate temperatures. In addition, microtexture studies were conducted using the Electron Backscattered Pattern (EBSP) technique.

Recent Results

Fracture toughness R-curve behavior was determined at intermediate temperatures using 12.0 mm thick side-grooved compact tension (CT) specimens in the LT orientation. The largest increase in toughness, as determined by R-curve behavior, was observed to occur from -155°C to -185°C. Associated with the increase in toughness at -185°C was an increase in the occurrence of large delaminations. In addition, long range transgranular shear in which numerous grains are traversed by a single shear crack, as observed at ambient temperature, tends to "break-up" as the test temperature decreases.

Transverse uniaxial tensile specimens and longitudinal notched tensile specimens were machined from the plate midplane and tested in the temperature range 25°C to -185°C. There was

a fairly linear increase in uniaxial yield strength with a decrease in temperature typical of 2090 in the T81 condition. There also was an increase in the work hardening exponent, n, with a decrease in temperature. The largest change in n was observed to occur at the lowest temperature and is probably related to more homogenous deformation at -185°C. Similarly, effective plastic strain to failure (ϵ_{pf}) increased with decreasing temperature.

Grain orientation of individual (sub)grains was determined using the EBSP technique. A typical microtexture analysis around the area adjacent to a delamination involved obtaining an EBSP pattern across a 300 μm linear region. EBSP {111} pole figures around delaminations at the midplane were similar to the X-ray pole figure. Results of EBSP analysis indicate that delaminations typically occur along high angle boundaries (27° to 40°). In addition, it was observed that one grain adjacent a given delamination was within 15° of the ideal brass orientation. In some cases, the second grain had an orientation close to the S orientation.

Milestones

In the next six months, a fourth publication will be completed and published. Significant progress will be made toward the completion of the PhD dissertation.

Presentation Graphics Captions

1. Title.
2. Problem statement and program objective.
3. Current program emphasis.
4. Backscattered SEM images of the through thickness microstructure of 2090 in the near peak aged condition.
5. R-curve fracture toughness behavior increases with decreasing temperature with the largest increase between -155°C and -185°C.
6. K_{JIci} was determined from the intersection the power law regression line of the J-Δa data and the 0.1 mm offset of the blunting line. In the temperature range 25° to -155°C, K_{JIci} remains almost constant, but increases between -155°C and -185°C.

7. Both yield strength and work hardening exponent increased with decreasing temperature typical of 2090-T81 plate.

8. Effective plastic strain to failure increased with decreasing temperature presumably due to more homogeneous deformation at the cryogenic temperature.

9. Increase in fracture toughness at -185°C was associated with an increase in delamination fracture.

10. Higher magnification of delaminations associated with fracture at -185°C.

11. Schematic of instrumentation employed for EBSP studies of boundary misorientation and microtexture analysis.

12. L-S section of a compact tension specimen tested at -185°C showing typical delaminations examined using the EBSP technique.

13. (Sub)grain boundary misorientation indicating that delaminations occur at high angle boundaries with a misorientation of approximately 27° to 40°.

14. X-ray {111} pole figure at the midplane of 2090-T81 plate indicating a strong deformation brass texture.

15. EBSP {111} pole figure at the midplane of 2090-T81 plate around a delamination showing good agreement with the X-ray pole figure.

16. Backscattered images of interrupted notch tensile test showing delaminations occurred at boundaries with significant amounts of precipitation.

17. Summary.

FRACTURE OF Al-Li ALLOYS 2090 AND 2090+In AT CRYOGENIC TEMPERATURES

FRACTURE AND MICROTEXTURE OF Al-Li ALLOY 2090

John A. Wagner and Richard P. Gangloff

LA²ST Program Review
NASA Langley Research Center
July 17-18, 1995

PROGRAM PROBLEM STATEMENT AND OBJECTIVE

Fracture of 2090 and 2090+In Alloys

Problem

- No systematic investigation conducted to determine the interactive effects of:
  - Temperature
  - Delamination
  - Indium addition
  - Microstructure

  on the fracture of 2090-based alloys.

Objective

- Determine the influences of microstructure, stress state and temperature on the occurrence of various fracture modes in Al-Li-Cu-X alloys. Understand the mechanism(s) associated with delamination and transgranular shear fracture.

FRACTURE OF 2090 AND 2090+In ALLOYS

Current Program Emphasis

- Understand the fracture mode transition of 2090-T81 at various temperatures in the range 25°C to -185°C.

- Examine boundary misorientation and microtexture associated with delamination and transgranular shear fracture.

Backscattered Electron Micrograph Showing the Through-Thickness Microstructure of 2090-T81

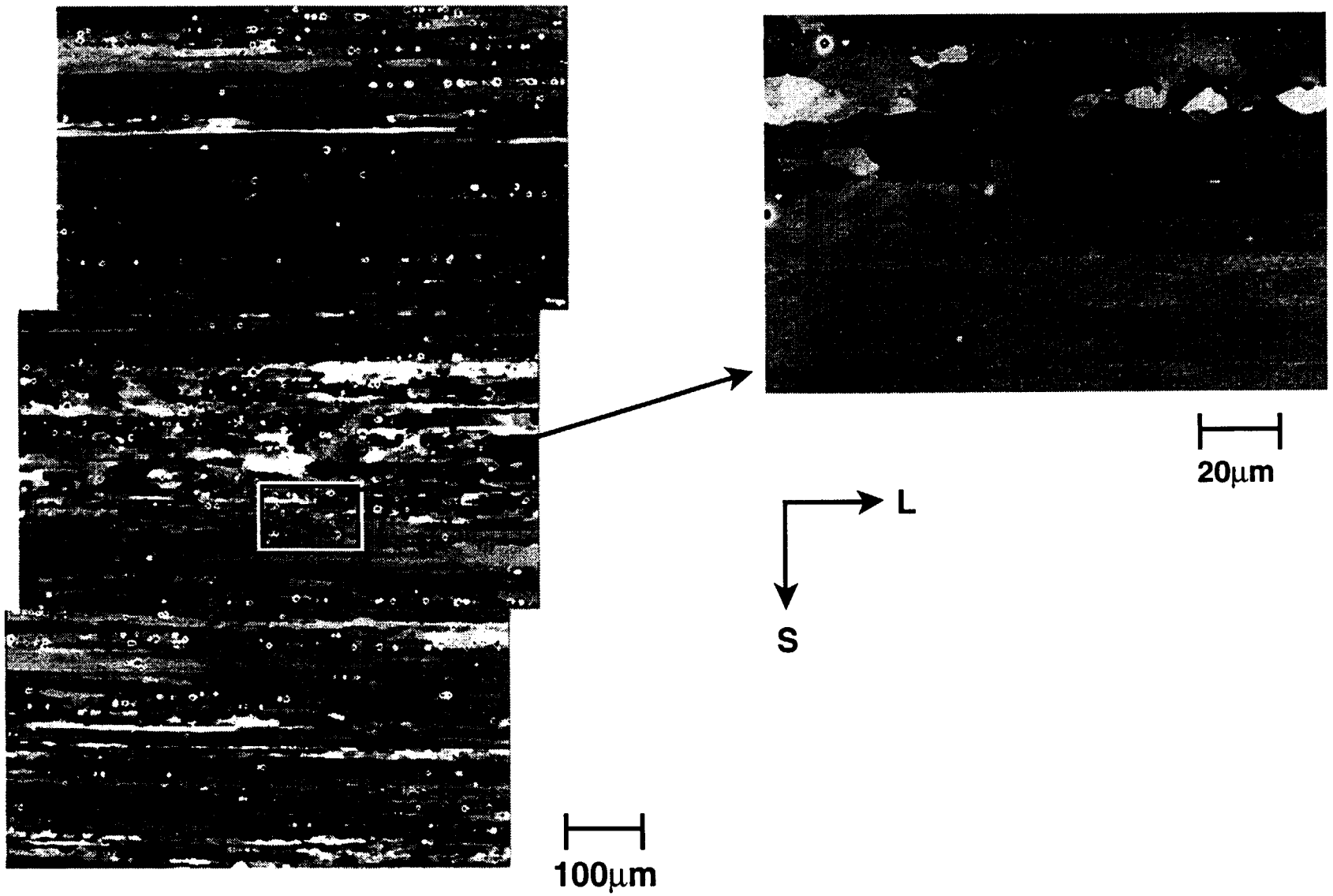

R-curves of 12mm thick specimens at -185°C to 25°C.

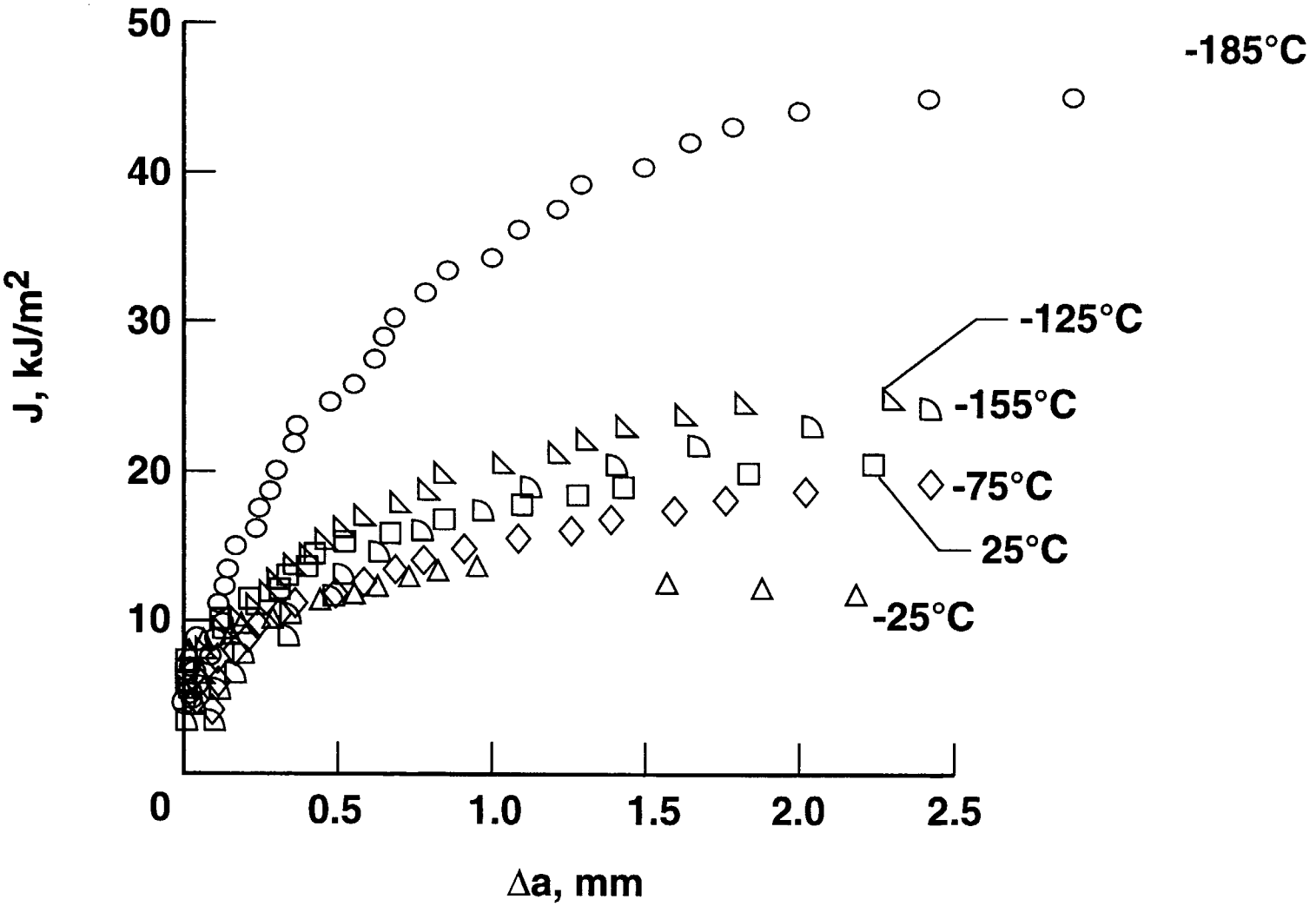

Fracture Toughness, K_{JIci}, of 12mm Thick 2090-T81 as a Function of Temperature

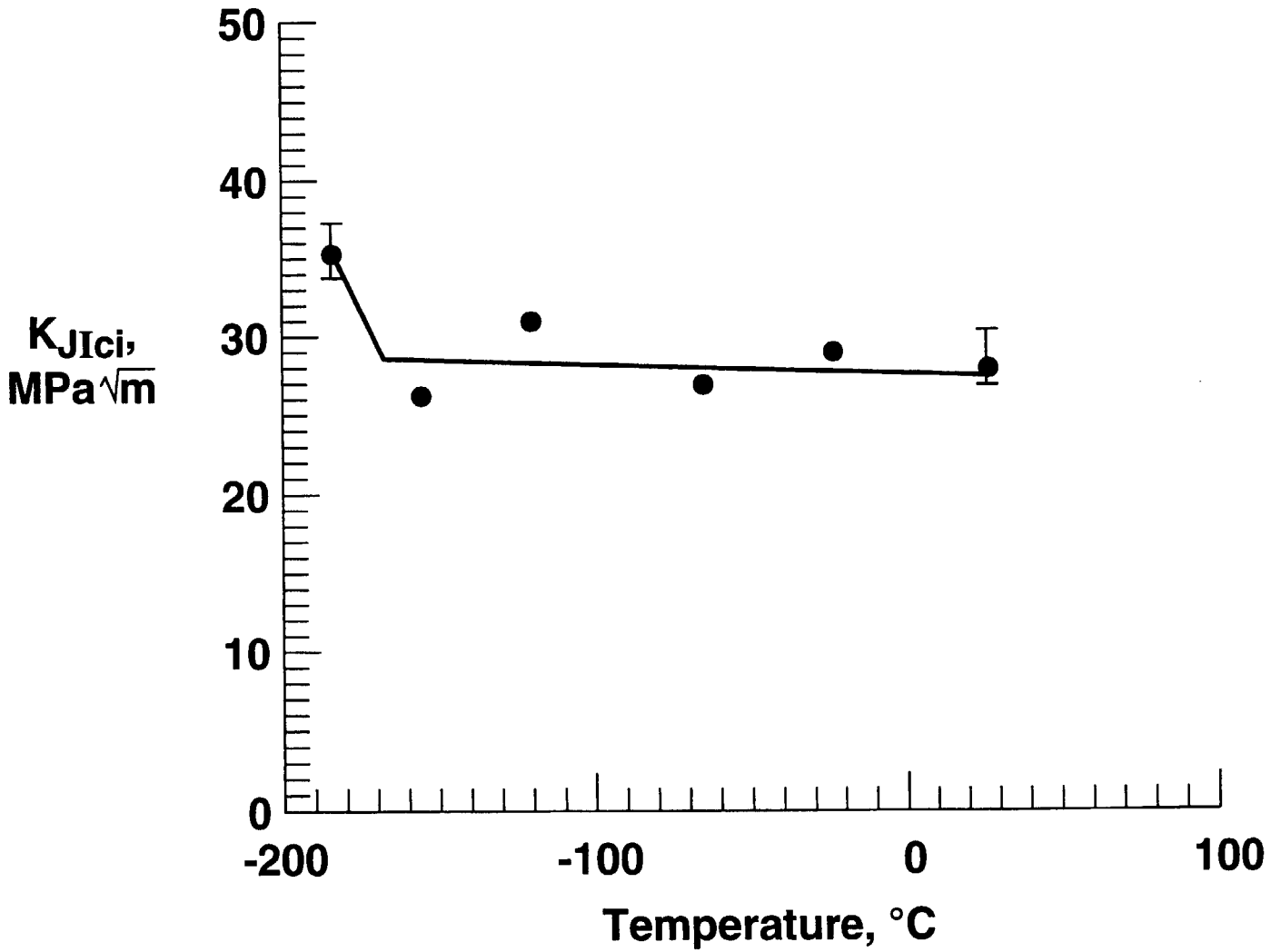

Yield Strength and Work Hardening Coefficient of 2090-T81 as a Function of Temperature

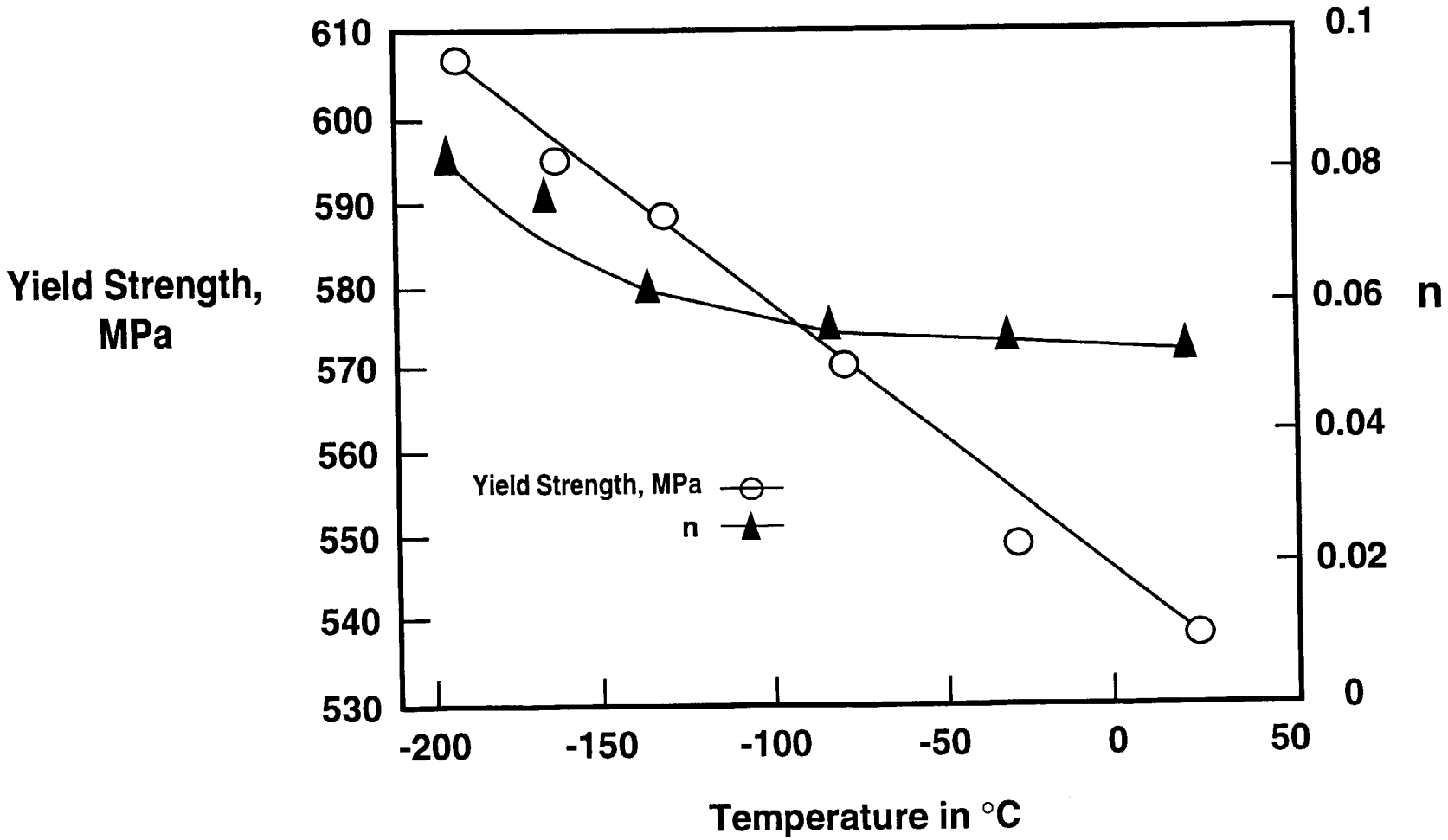

Effective Plastic Strain To Failure of 2090-T81 As A Function Of Temperature ($\sigma_m/\bar{\sigma}$=1.03)

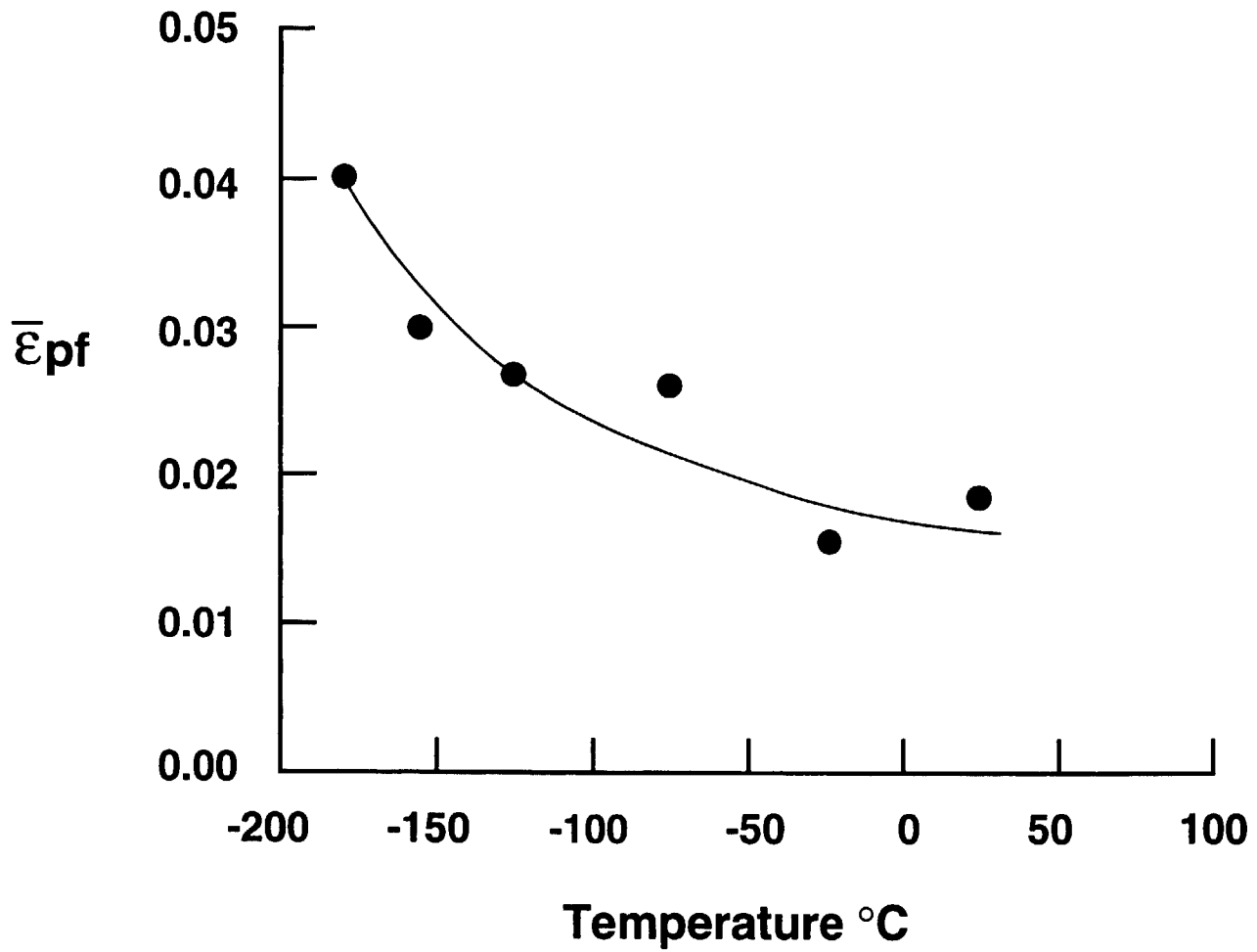

Fracture surface cross section of 2090-T81 as a function of temperature.

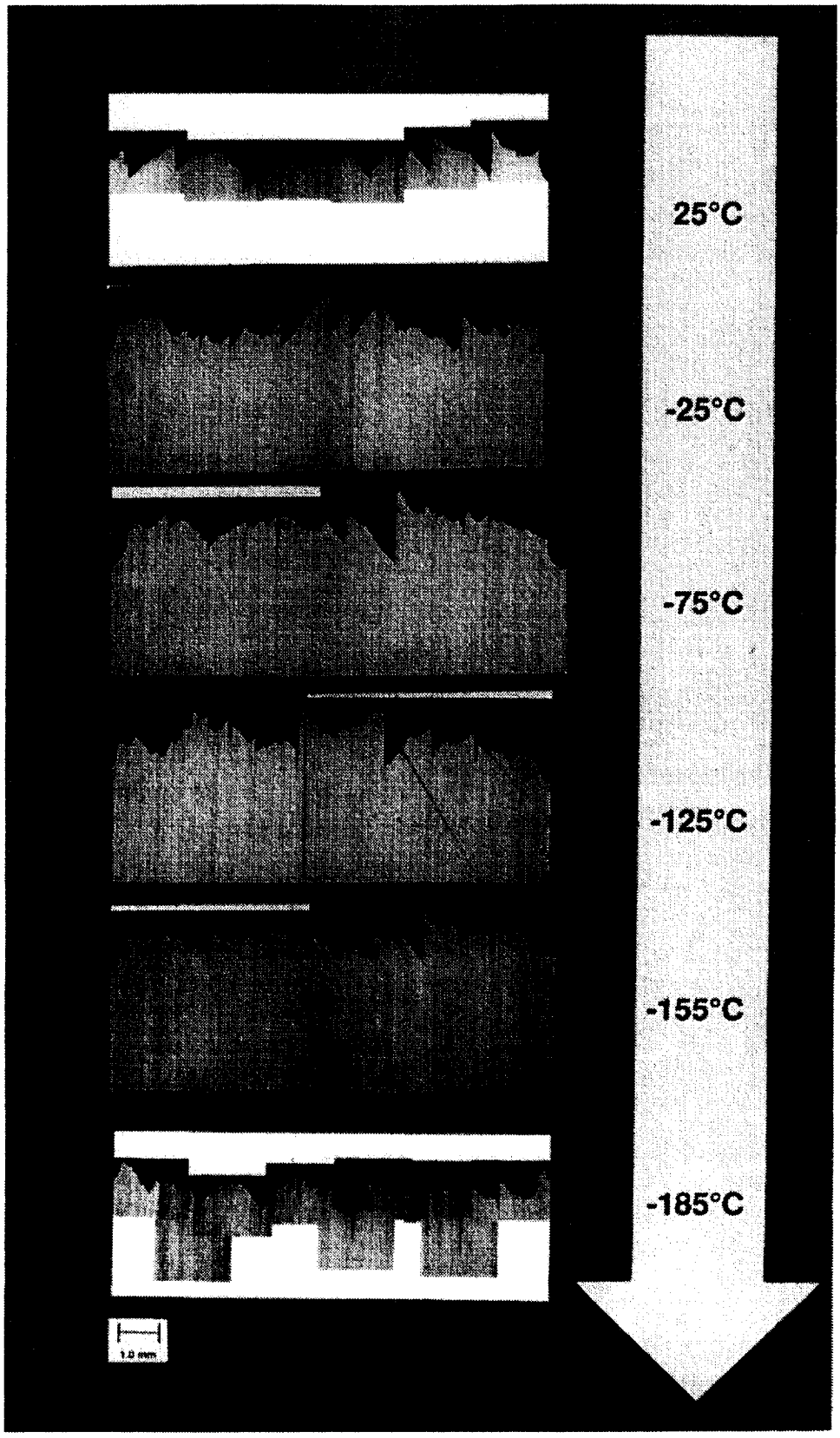

Optical L-S Section of the Fracture Surface of a 2090-T81 Specimen Tested at -185°C

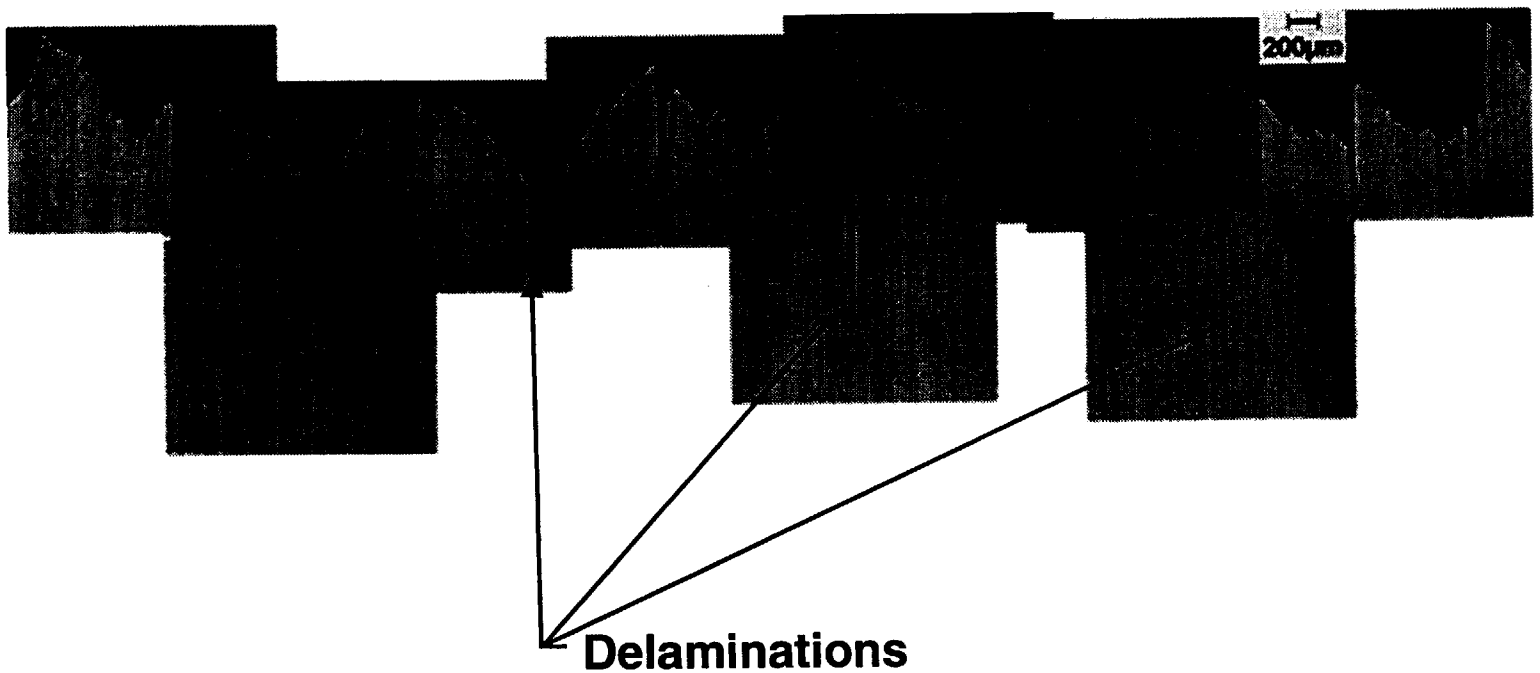

Schematic Representation of the Setup Used for the Electron Backscattered Pattern (EBSP) Technique

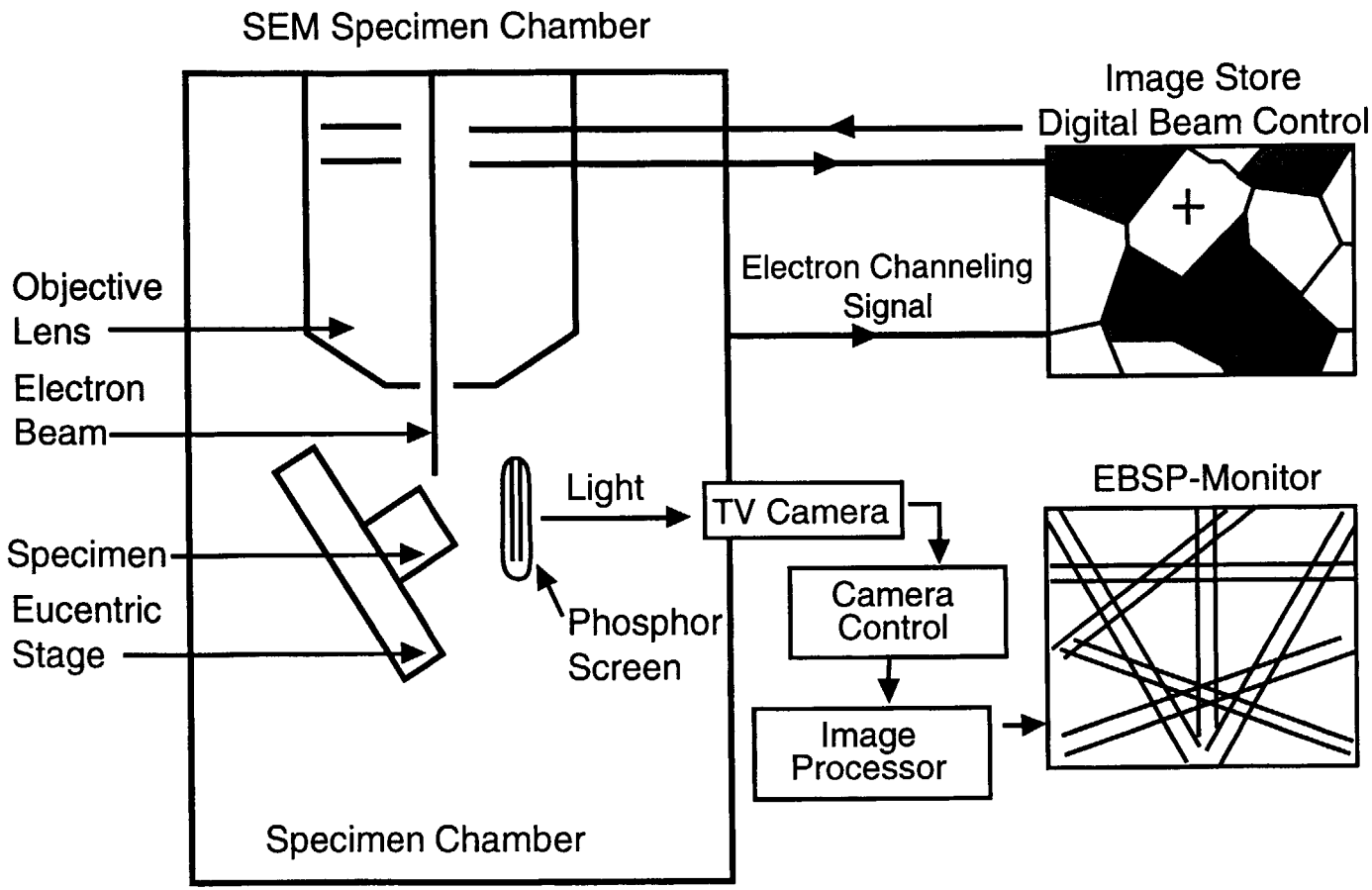

sr

OPTICAL MICROGRAPH IN POLARIZED LIGHT OF AN L-S SECTION OF SAMPLE TESTED AT - 185°C

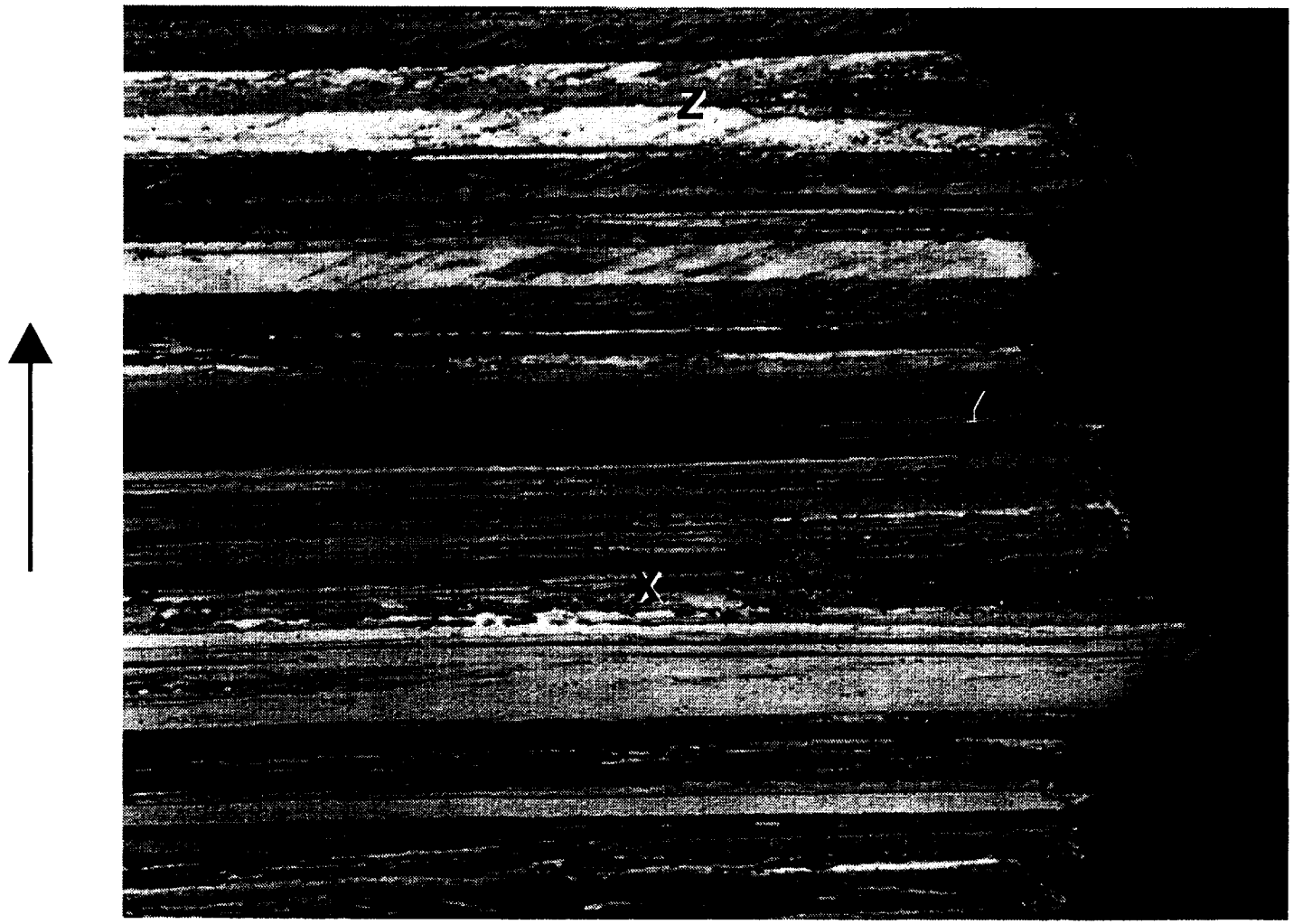

400 µm

OM POL

MISORIENTATION ANGLE AS A FUNCTION OF THE (SUB)GRAIN NUMBER, ALONG ND

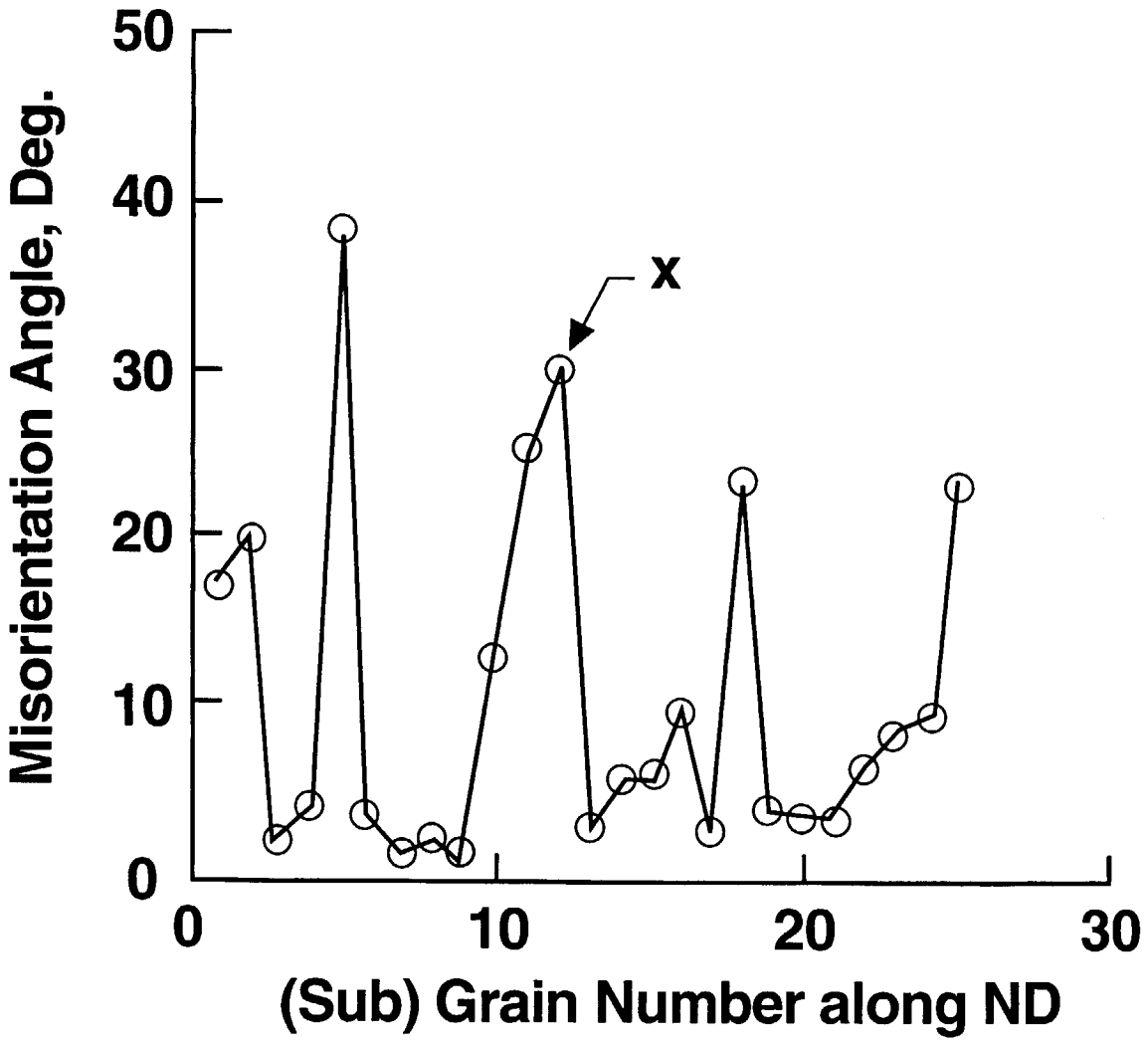

MISOR

X-ray {111} Pole Figure at T/2 for 2090-T81

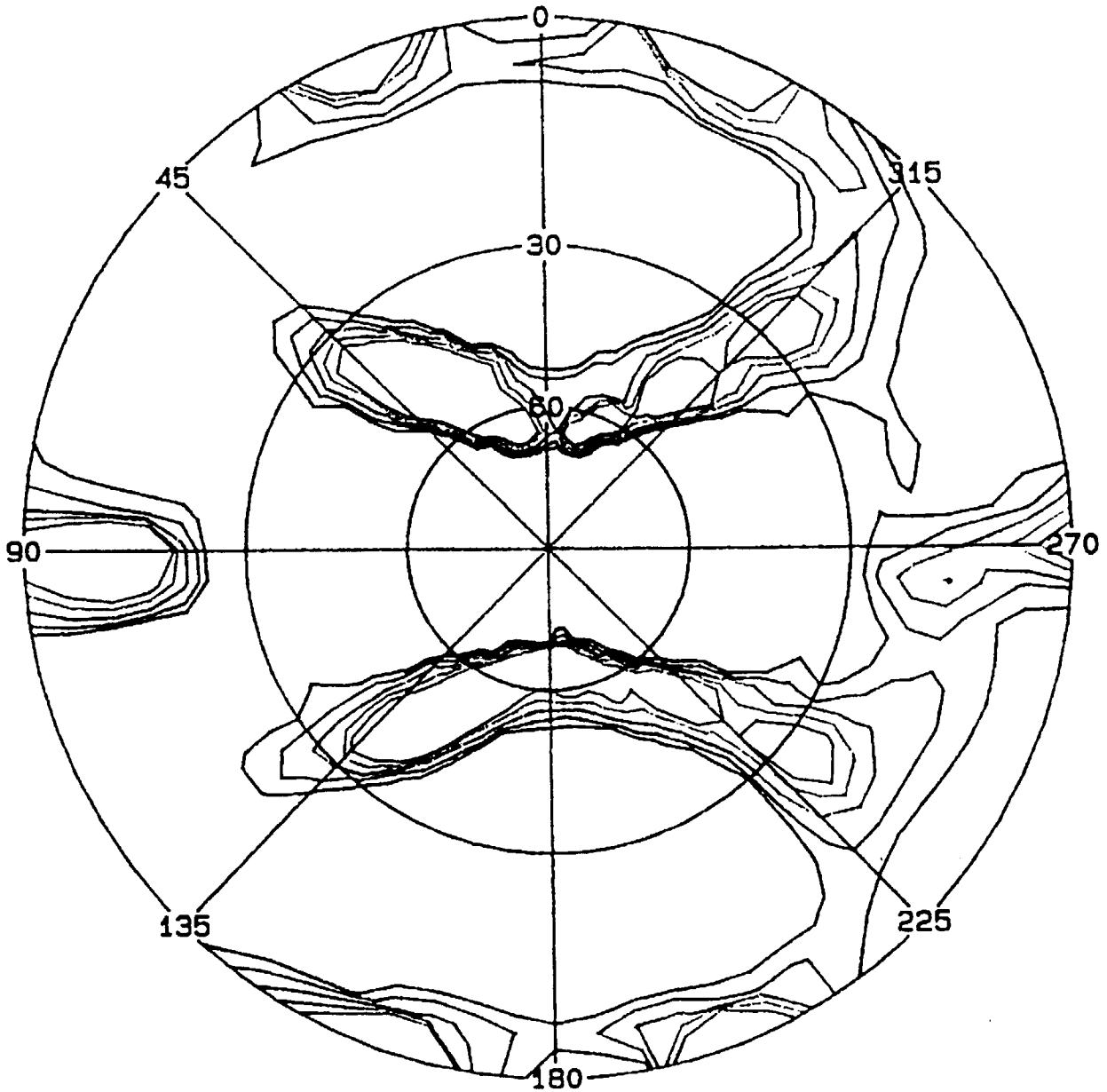

x-ray

EBSP {111} Pole Figure of a Region Around Delamination

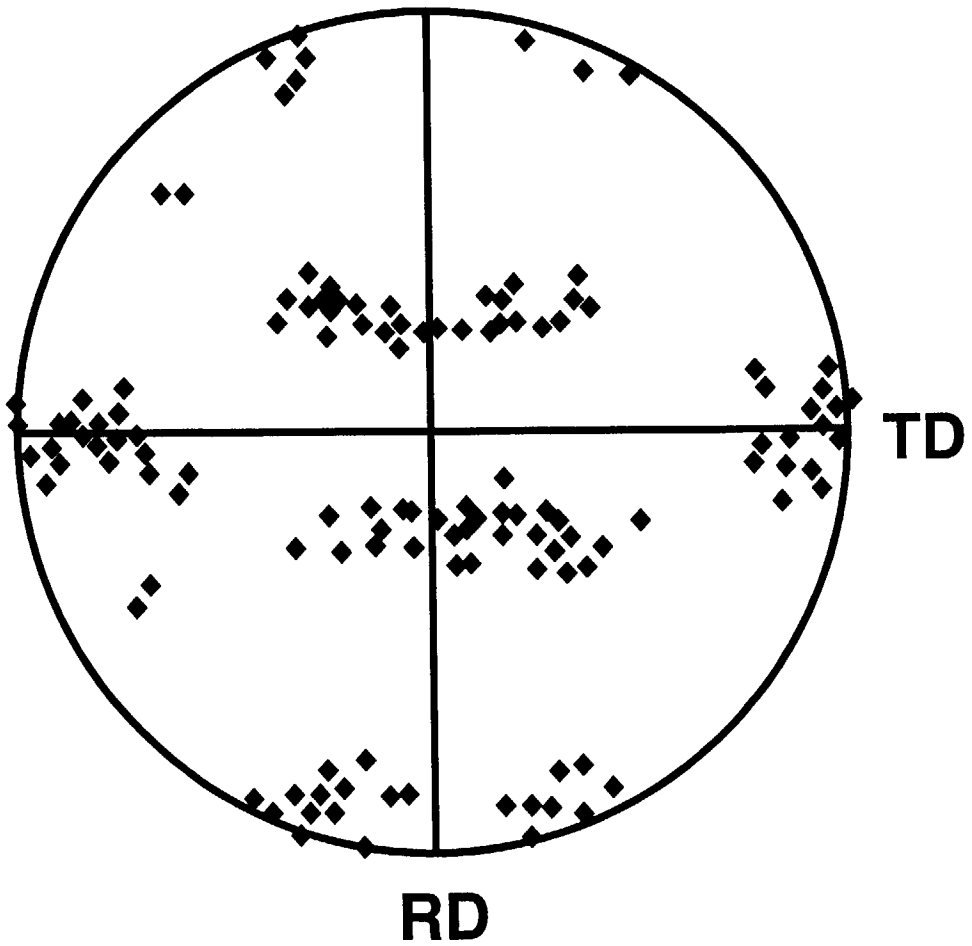

ebsp

BACK SCATTERED IMAGES OF THE MIDPLANE OF INTERUPTED NOTCH TENSILE

TEST AT -185°C

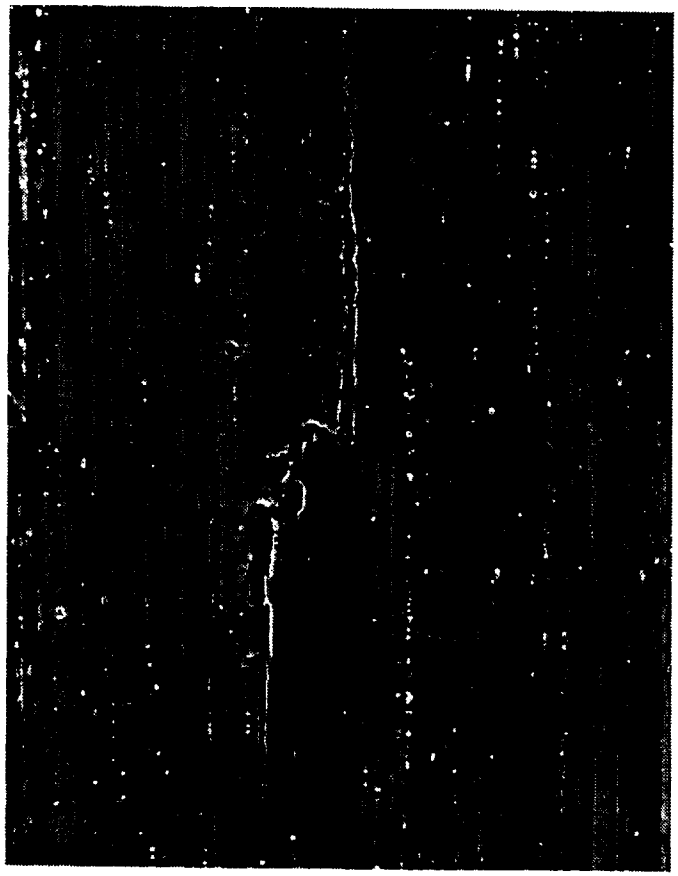

200μm

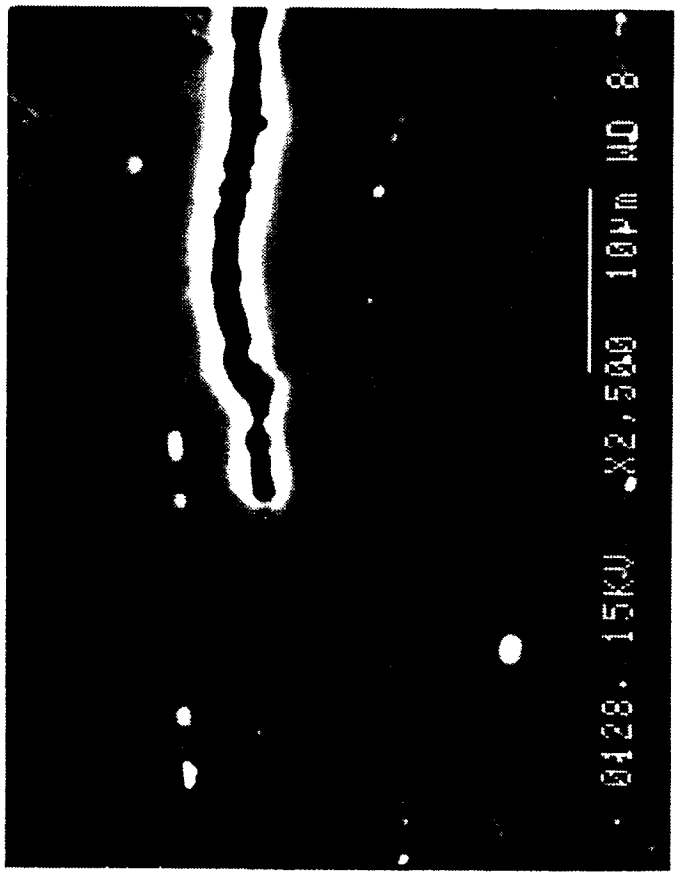

10μm

ptcl & bck scttrd mgs/uva

FRACTURE AND MICROTEXTURE OF Al-Li ALLOY 2090

Summary

- Fracture toughness R-curve behavior increased with decreasing temperature with the largest increase between -155°C to -185°C.

- Fracture at -185°C was associated with large delaminations which occured at high angle boundaries (27° - 40°).

- High angle boundaries where delaminations occured were in some cases bounded by one grain of the brass texture and one of the S texture.

Project #3 EFFECTS OF AGING AND TEMPERATURE ON THE DUCTILE FRACTURE OF AA2095 AND AA2195

Cynthia L. Lach and Richard P. Gangloff

Objective

The objective of this research is to characterize the effect of cryogenic to mildly elevated temperature on the tensile deformation and fracture toughness of an emerging composition of Weldalite™-type alloys. We will determine quantitative stress versus strain data, and initiation and growth fracture toughnesses, as well as the associated microscopic fracture mechanisms, and conduct micromechanical modeling in order to understand temperature-dependent fracture.

Status

Two Weldalite™ compositions were selected for study to examine the limits of the Cu and Li levels for the alloy registered as AA2095. Specifically, a high Cu-Li alloy (Al-4.64Cu-1.53Li-0.34Ag-0.37Mg-0.17Zr; wt%) at the upper extreme of the AA2095 specification, and a low copper alloy (Al-4.04Cu-1.00Li-0.37Ag-0.36Mg-0.15Zr; wt%) at the low end of the AA2095 composition specification, and in the middle of the AA2195 specification, were chosen for evaluation. Uniaxial tensile stress-strain relationships and J-Integral based crack initiation and growth fracture toughnesses were determined as a function of temperature for AA2195 (aged for 30 hours at 143°C). Selected tests were conducted on AA2095 aged for 20 hours at 143°C for comparison purposes.

The following experiments were conducted on the alloy variants during this reporting period: ICP chemical analysis at various locations through the thickness of the plate, an extended aging study, precision modulus tests at -180°C and 25°C, and uniaxial tensile and fracture toughness tests from -185°C to 135°C.

Recent Results

The results of the chemical analyses of all of the alloys suggest a significant level of Cu segregation, as indicated by the consistently low Cu content at the mid-plane (t/2) location. The

least amount of Cu segregation with respect to the mid-plane was observed for X2095 (AA2095), while the greatest was observed for the X2095 (AA2195) alloy.

The high Cu-Li alloy variant (AA2095) did not overage at 143°C in 768 hours, while the low Cu-Li variant (AA2195) began overaging between 100 and 198 hours.

The modulus of AA2195 (aged for 30 hours at 143°C) increases by approximately 6% from ambient to cryogenic temperatures (-185°C). Increased yield strength and work hardening are observed for each alloy with decreasing temperature to cryogenic levels. For a given yield strength, the fracture toughness values were significantly lower for the high Cu-Li alloy variant at both test temperatures. This result was supported by the presence of a large volume fraction of undissolved particles in the high Cu-Li variant because its composition exceeds solid solubility at the solution treatment temperature that was employed, as discussed in previous progress reports.

Milestones

Fracture surfaces will be examined by SEM to detect temperature dependent changes in the details of the microvoid-based fracture process.

The critical plastic strain-controlled model developed by Ritchie and coworkers will be employed to predict the temperature dependence of K_{JC} based on measured tensile properties for the initial aging study that was conducted on both alloys.

Presentation Graphics Captions

1. Title.

2. Objective.

3. Approach.

4. The table displays the registered compositional limits of Weldalite™ 049 alloys. The original lean and rich chemistries were chosen to reflect the upper and lower limits of the X2095 alloy. The lean variant (4.wt%Cu-1.0wt%Li) also falls in the middle of the AA2195 specification.

5&6. Previous work has shown that AA2195 had variations, through the plate thickness, with respect to texture and microstructure. Alloy AA2095 exhibited only texture variations

through the thickness. Thus, standard inductively coupled plasma (ICP) chemical analysis was conducted on samples, in the form of shavings, which were dry milled from various locations through the thickness (t/8, t/4, t/2, 3t/4 and 7t/8) of the 12.7 mm plates. The values plotted in this figure represent the averages of triplicate analyses. The data appear well behaved and exhibit very little scatter.

The upper and lower limits the registered composition limits of AA2095 and AA2195 are shown as horizontal lines. The results of the chemical analyses suggest a significant level of Cu segregation, as indicated by the consistently low Cu content at the mid-plane (t/2) location. The least amount of Cu segregation with respect to the mid-plane was observed for AA2095, while the greatest was observed for AA2195 alloy. AA2095 has an average through-the-thickness (bulk) chemistry of 4.64wt%Cu which is outside of the registered composition specification (3.9-4.6wt%). For AA2195, the bulk chemistry is 4.04wt%Cu which falls within the specification of (3.7-4.3wt%); however the midplane chemistry is 3.58wt%Cu, which is outside of the composition specification.

7. An aging study was conducted at 143°C for the two X2095 alloy variants to characterize more completely the age hardening response of this alloy. Originally, the aging study was conducted up to 100 hours, as depicted by the open symbols in the figure, however, neither alloy overaged in that time frame. Results of an extended aging study (24, 72, 100, 198, 334, 408, 502, and 768 hours) are shown as filled symbols in the figure. The high Cu-AA2095 with high Cu-to-Li was stable with respect to hardness throughout the 768 hour time frame. No evidence of overaging was observed, as a hardness of 92.0 +/- 0.4 HRB was maintained from 100 to 768 hours. AA2195 with low Cu-to-Li began to overage between 100 and 200 hours, which was followed by a hardness plateau through 502 hours, before significantly overaging. The overall hardness results of the extended aging study were approximately 2 Rockwell B scale (HRB) points lower than the original study; however, incremental hardness changes with corresponding time changes for 24, 72 and 100 hours, resulted in the same relative change in hardness for the two heat treat runs.

8. Tensile results from the initial aging study resulted in a selection of 20 and 30 hour ages at 143°C for AA2095 and AA2195, respectively. This peak-aging "-T8" condition attempted to optimize the strength and fracture of toughness of these alloy variants. Another factor in selecting this aging condition was that the tensile properties of the two variants were quite similar from ambient to cryogenic test temperatures.

9&10. Tensile precision modulus tests were conducted on the X2095 (AA2195) alloy variant aged for 30 hours at 143°C. Specimens were machined from the mid-plane of the plate in the longitudinal orientation. The tests were conducted in accordance to ASTM E111, the Standard Test Method for Young's Modulus, Tangent Modulus, and Chord Modulus at 25°C and -185°C. An average modulus was determined from three runs per specimen at each test condition. The modulus of AA2195 (aged for 30 hours at 143°C) increased by approximately 6% from ambient to cryogenic temperatures (-185°C). The critical

alignment criteria was met for all of the tests while the coefficient of variation was twice as good as expected for aluminum alloys.

11&
12. Uniaxial tensile deformation behavior of AA2195-T8 was determined as a function of temperature (-185, -140, -125, -75, -25, 25, 107, and 135°C). Selected tests were conducted on AA2095-T8 for comparison purposes. Yield strength and ultimate strengths increased with decreasing temperature.

13&
14. The effect of temperature on the percent elongation (25.4 mm gage) is shown for both alloy variants. The percent elongation of AA2095 decreases to a minimum as temperatures decrease to around 20°C. The increase in percent elongation, about the minimum, appears to be approximately the same magnitude for both high and low temperatures. The minimum elongation for AA2195 is not as clear due to the wide scatter in data. However, the percent elongation minimum for AA2195 is shifted slightly to the left of AA2095's minimum, to approximately -25 to -125°C. AA2195 is more sensitive to changes in temperature as the percent elongation decreases more rapidly than for AA2095.

15. Work hardening exponents are observed to increase for each alloy with decreasing temperature to cryogenic levels. An absence of work hardening (as calculated between the yield strength and the ultimate strength) was observed at 135°C for both alloys, and at 107°C for AA2195 where the yield strength equaled the ultimate strength.

16. The intrinsic fracture resistance (reduction of area) of each alloy decreases with decreasing temperature to cryogenic levels, with a particularly strong sensitivity noted for the low Cu-low Li composition, AA2195-T8.

17. Tearing modulus, which is used to assess the materials resistance to stable crack growth after crack initiation was determined for both alloys as a function of temperature. Tearing modulus decreased with decreasing temperature for both alloys. The largest increase in T_R occurred for AA2195 for the temperature interval from 25°C to 135°C. T_R increased from 11.3 at 25°C to 24.0 at 135°C.

18. Initiation fracture toughness, K_{JIC}, decreases slightly with decreasing temperature for AA2095. The wide scatter in the AA2195 fracture data makes it difficult to determine if a slight increase in K_{JIC} occurs at cryogenic temperatures. For all temperatures, AA2195 has superior fracture toughness compared to AA2095.

19. For AA2095, as yield strength increases, a decrease in K_{JIC} is observed. The reverse trend is suggested for AA2195.

20. The tensile and microstructural data for AA2095 and AA2195 were input into the critical plastic strain-controlled model, presented by Haynes in Project #1, to predict the

temperature dependence of K_{JIC} for these alloys. The experimental K_{JIC} results for AA2195 and AA2095 are compared to the model predictions in this figure. The model accurately predicted the effect of temperature on K_{JIC} for AA2095. Due to the wide scatter in K_{JIC} experimental data and the smaller "constituent" particle size for AA2195, it is more difficult to assess the accuracy of the model predictions. Given the well-behaved temperature dependencies of modulus, yield strength, work hardening and intrinsic fracture resistance for this alloy, however, it is reasonable to speculate that the predicted mildly declining initiation toughness with decreasing temperature is accurate. Experiments are required to test this hypothesis.

21. Future Work.

22. Conclusions.

EFFECTS OF AGING AND TEMPERATURE ON THE DUCTILE FRACTURE OF AA2095 AND AA2195

C. L. Lach and Richard P. Gangloff

LA^2 ST Program Review

NASA Langley Research Center

July 17-18, 1995

OBJECTIVE

To characterize the effects of aging, temperature, and alloy composition on the deformation and fracture behavior of AA2095 and AA2195 from elevated to cryogenic temperatures.

APPROACH

2095-T3
2195-T3

{X2095·Vintage 1990}

6% Stretch
12.5 mm plate

Material Characterization:

- o Chemistry (ICP)
- o Optical Microscopy
- o PPt Image Analysis
- o Texture Analysis

Aging Study:

- o Preliminary Study 0-100hrs at 143°C
- o Extended Study 0-600 hrs at 143°C

Tensile Tests: at 25°C and -185°C

- o 2095 (10, 20 & 72 hrs at 143°C)
- o 2195 (10, 20, 30 & 72 hrs at 143°C)

Fracture Toughness J-Integral Tests: at 25°C and -185°C

- o 2095(10,20 & 72 hrs at 143°C)
- o 2195(10,20,30 & 72 hrs at 143°C)

Aged Alloys to -T8:

- o 2095-T8 (20 hrs at 143°C)
- o 2195-T8 (30 hrs at 143°C)

Tensile Tests: at -185°C to 135°C

- o 2095-T8
- o 2195-T8

Fracture Toughness J-Integral Tests: at -185° to 135°C

- o 2095-T8
- o 2195-T8

CHEMICAL COMPOSITIONS

Registered Composition limits of Weldalite™049 Alloys

ELEMENTS	AA2094	AA2095	AA2195	Lean Variant	Rich Variant
Cu	4.4-5.2	**3.9-4.6**	**3.7-4.3**	**4.04**	**4.64**
Li	.70-1.4	**.70-1.5**	**.80-1.2**	**1.00**	**1.53**
Mg	.25-.80	.25-.80	.25-.80	0.36	0.37
Ag	.25-.60	.25-.60	.25-.60	0.37	0.35
Zr	.04-.18	.04-.18	.08-.16	0.15	0.17
Mn	.25 max	.25 max	.25 max	.25 max	.25 max
Zn	.25 max	.25 max	.25 max	.25 max	.25 max
Fe	.15 max	.15 max	.15 max	.15 max	.15 max
Si	.12 max	.12 max	.12 max	.12 max	.12 max
Ti	.10 max	.10 max	.10 max	.10 max	.10 max
Other, Each	.05 max	.05 max	.05 max	.05 max	.05 max
Other, Total	.15 max	.15 max	.15 max	.15 max	.15 max
Al	Remainder	Remainder	Remainder	Remainder	Remainder

CHEMICAL ANALYSIS

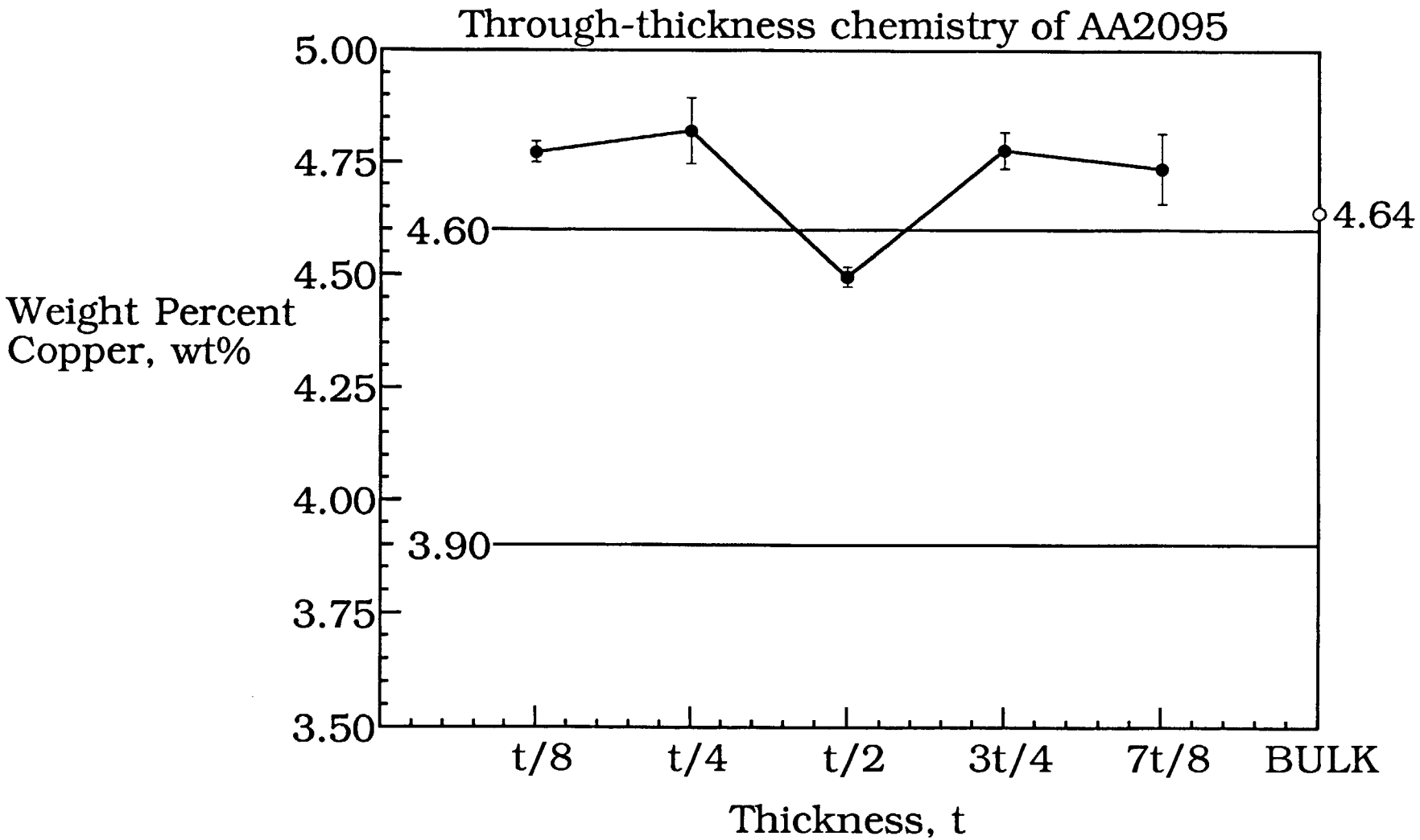

CHEMICAL ANALYSIS

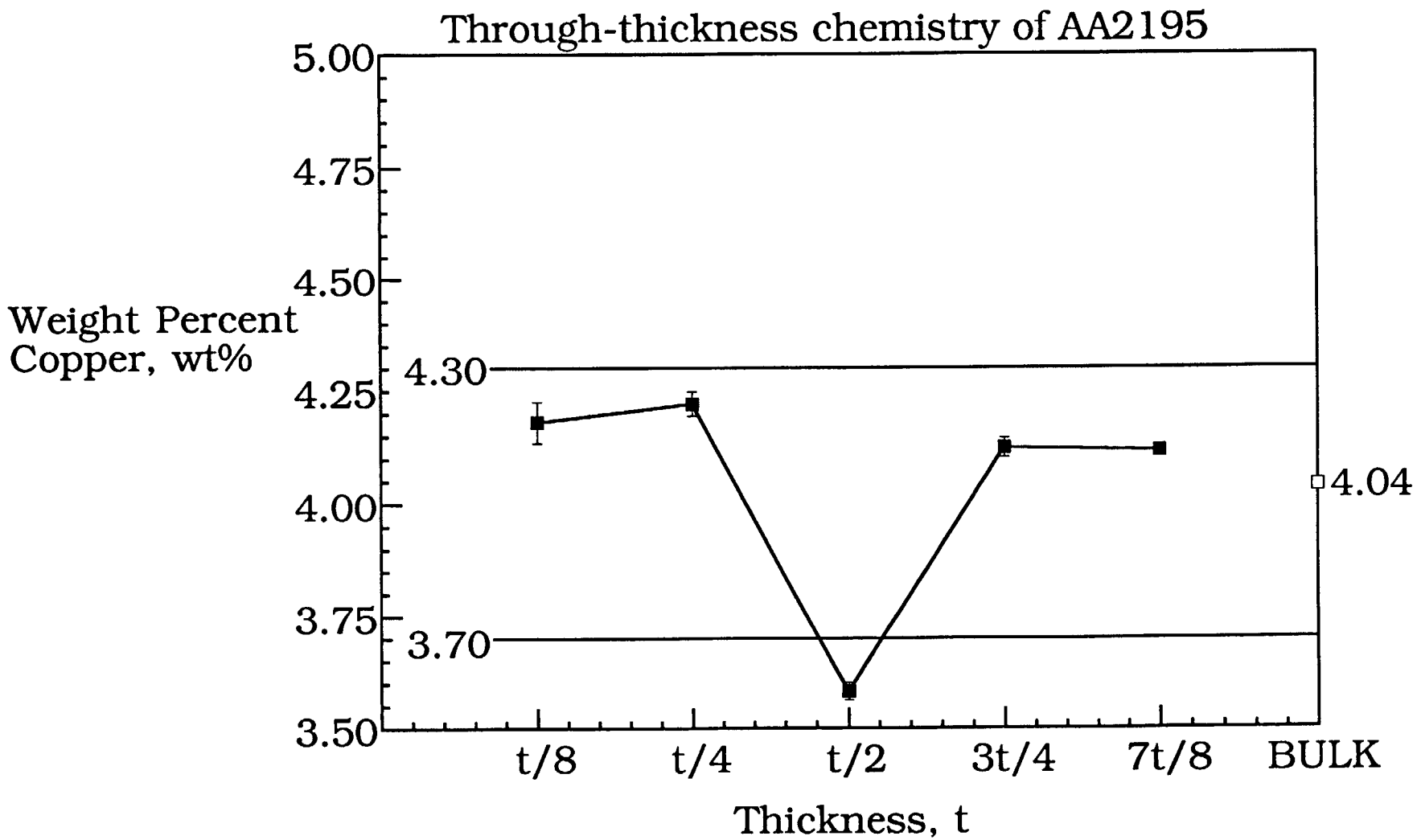

MECHANICAL PROPERTIES

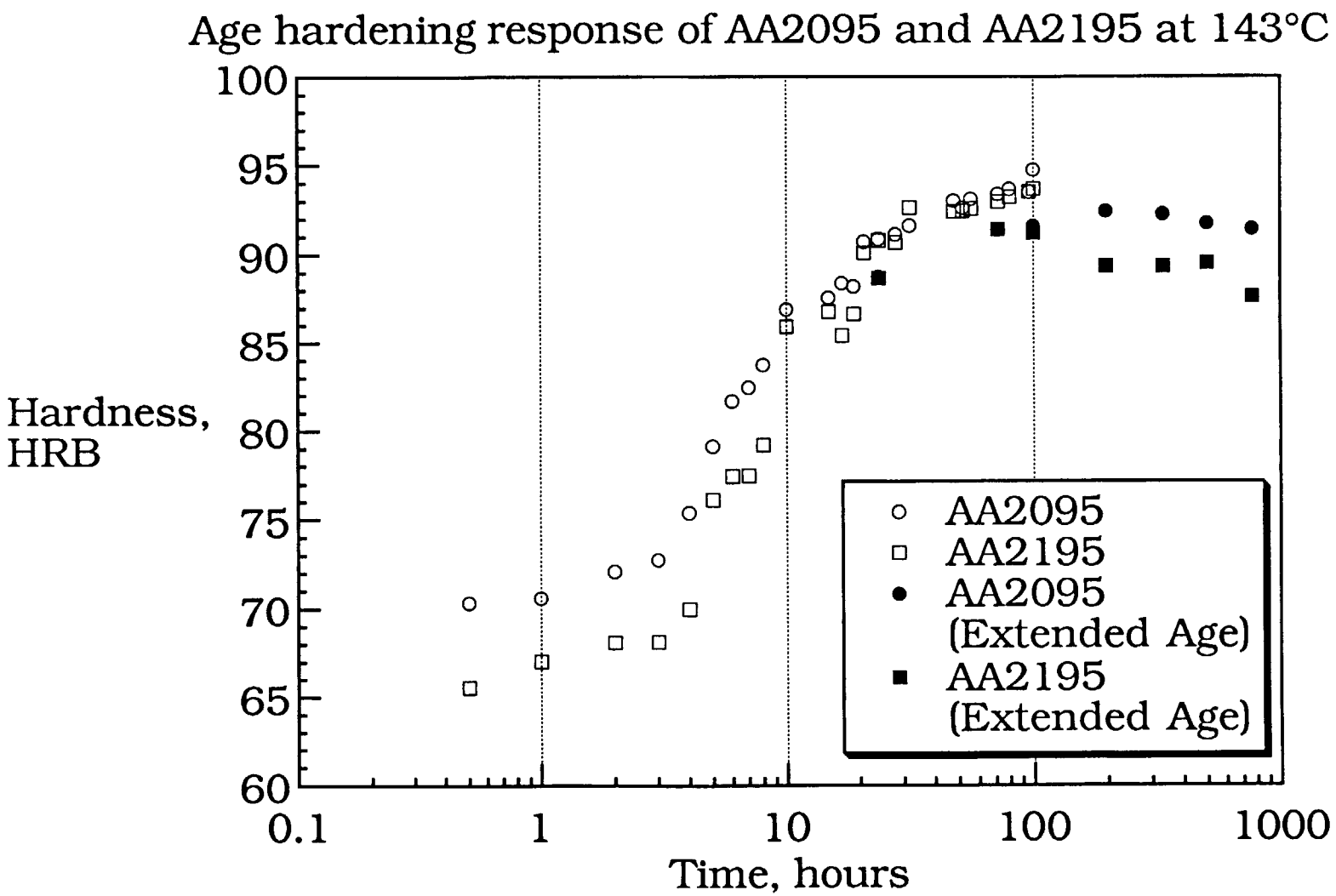

MECHANICAL PROPERTIES

Constant aging condition selected for -T8 property characterization

Alloy	143°C Age, hours	Temp., °C	YS, MPa	ULT, MPa	% elongation 25.4mm gage	Strain hardening exponent, η	E, GPa	RA, %
AA2195-T8 (Avg. of 3 tests)	30	25	577	602	11.1	0.046	72.4	27.5*
AA2095-T8 (single tests)	20	25	572	600	6.8	0.050	74.5	-
AA2195-T8 (Avg. of 3 tests)	30	-185	690	745	10.2	0.067	83.2	22.5*
A2095-T8 (single tests)	20	-185	676	731	8.2	0.061	84.1	-

MECHANICAL PROPERTIES

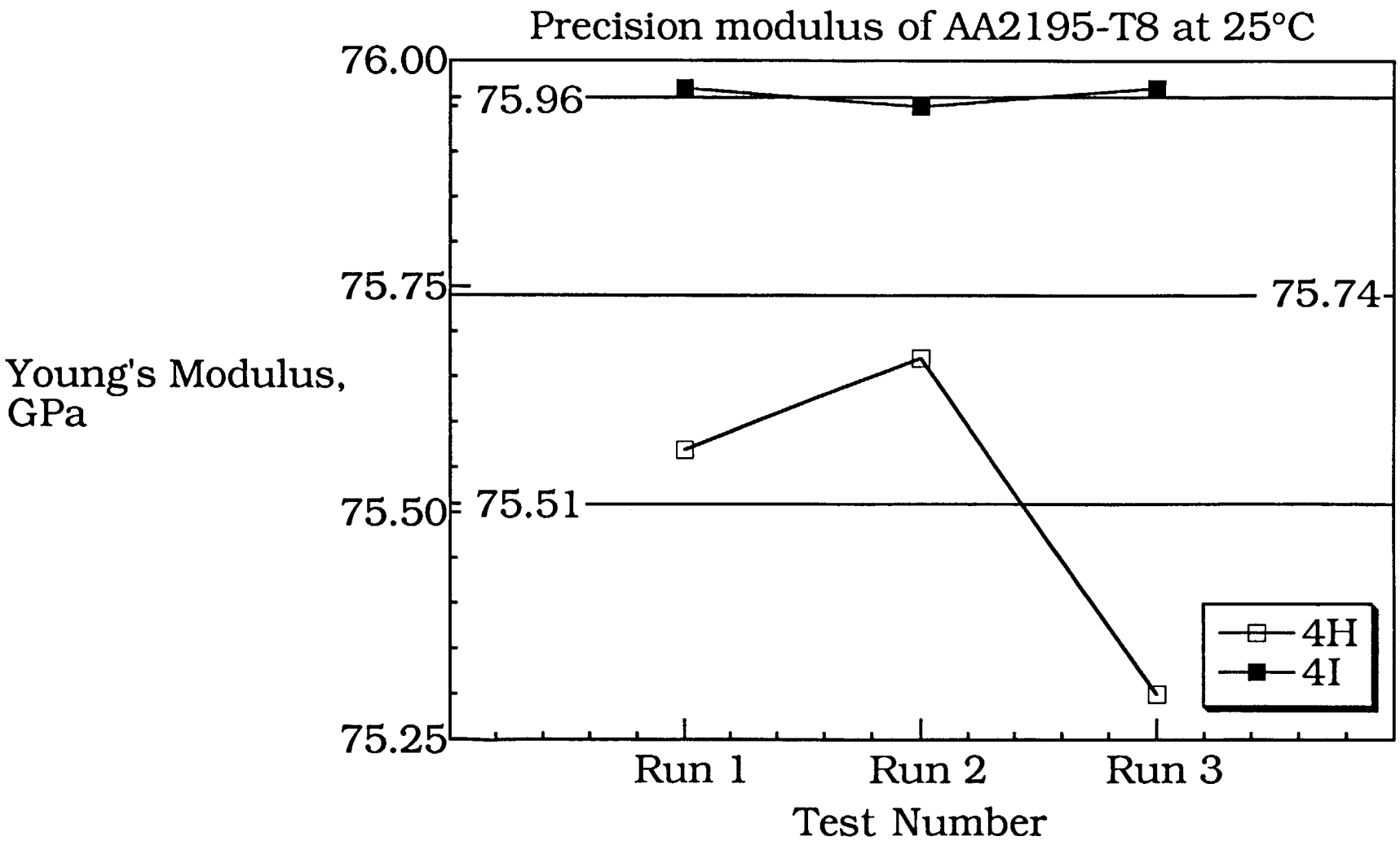

MECHANICAL PROPERTIES

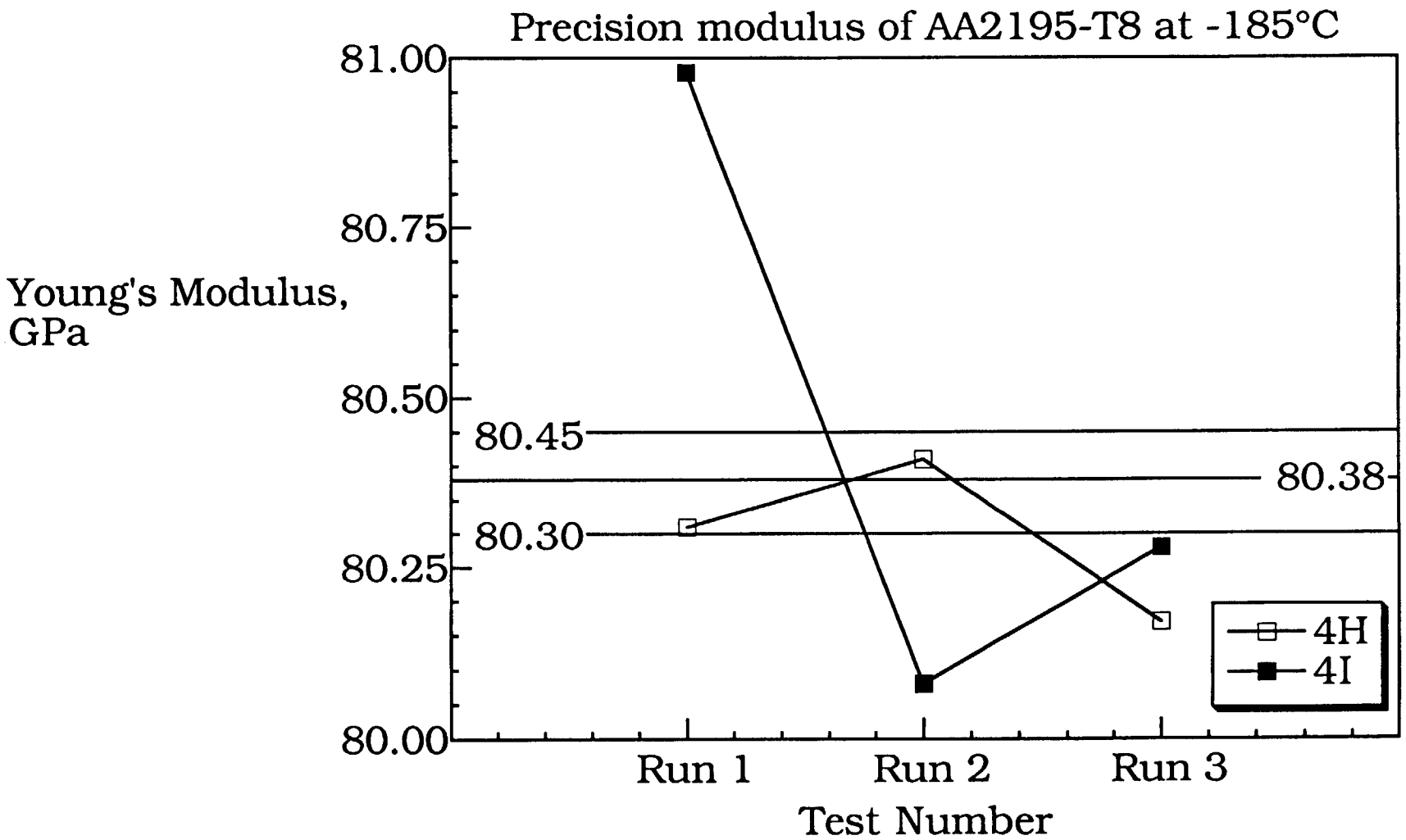

MECHANICAL PROPERTIES

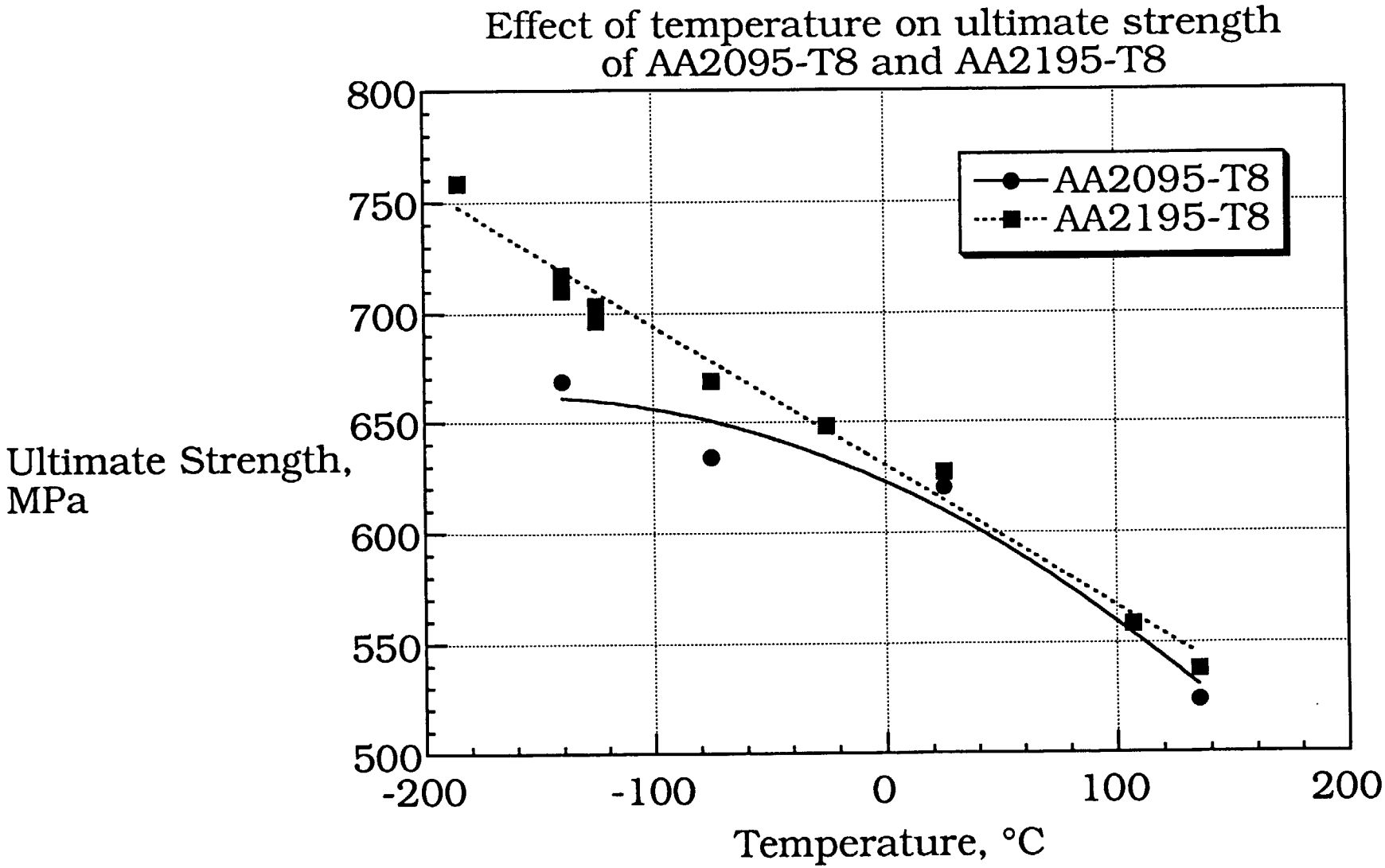

MECHANICAL PROPERTIES

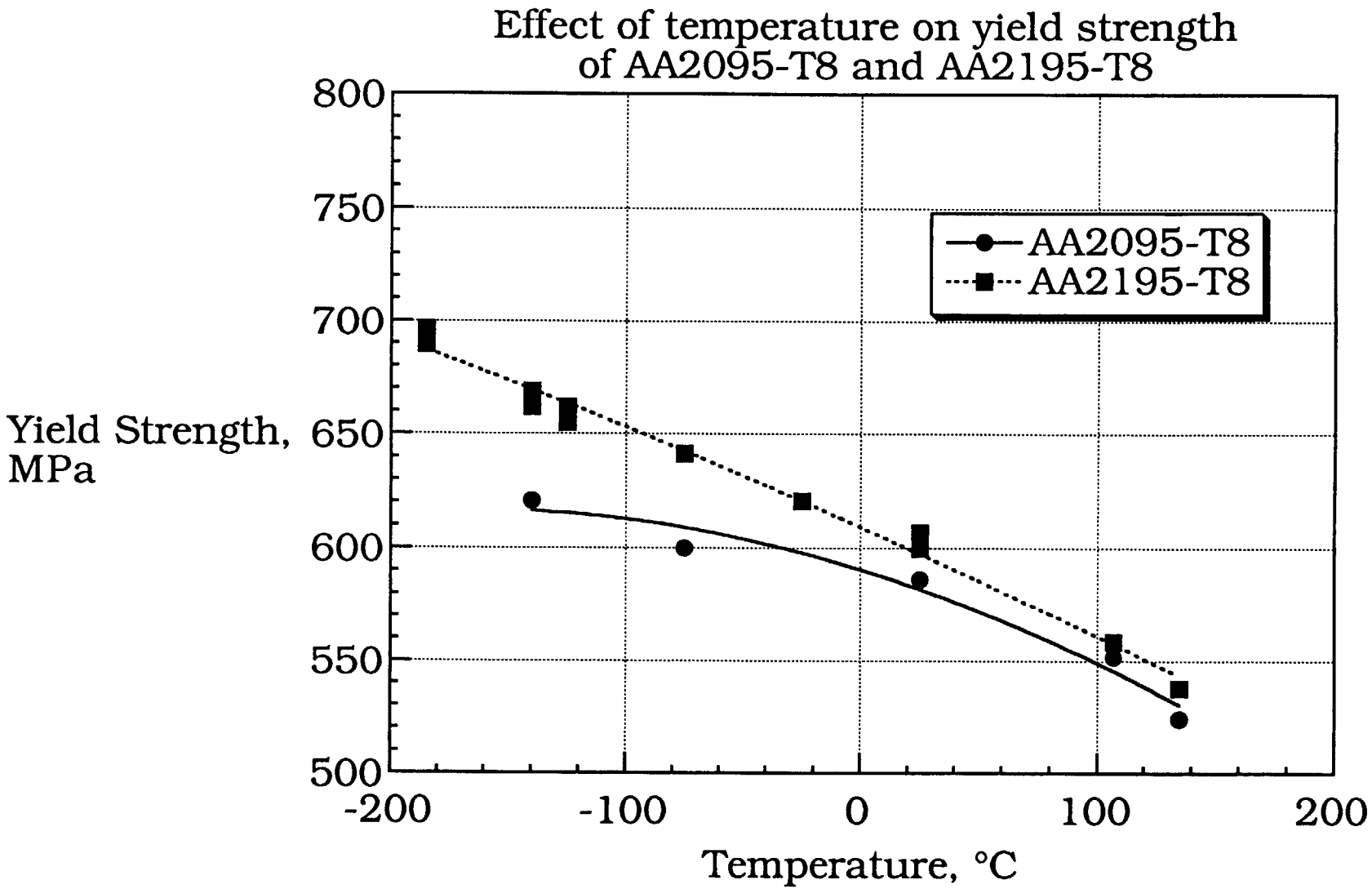

MECHANICAL PROPERTIES

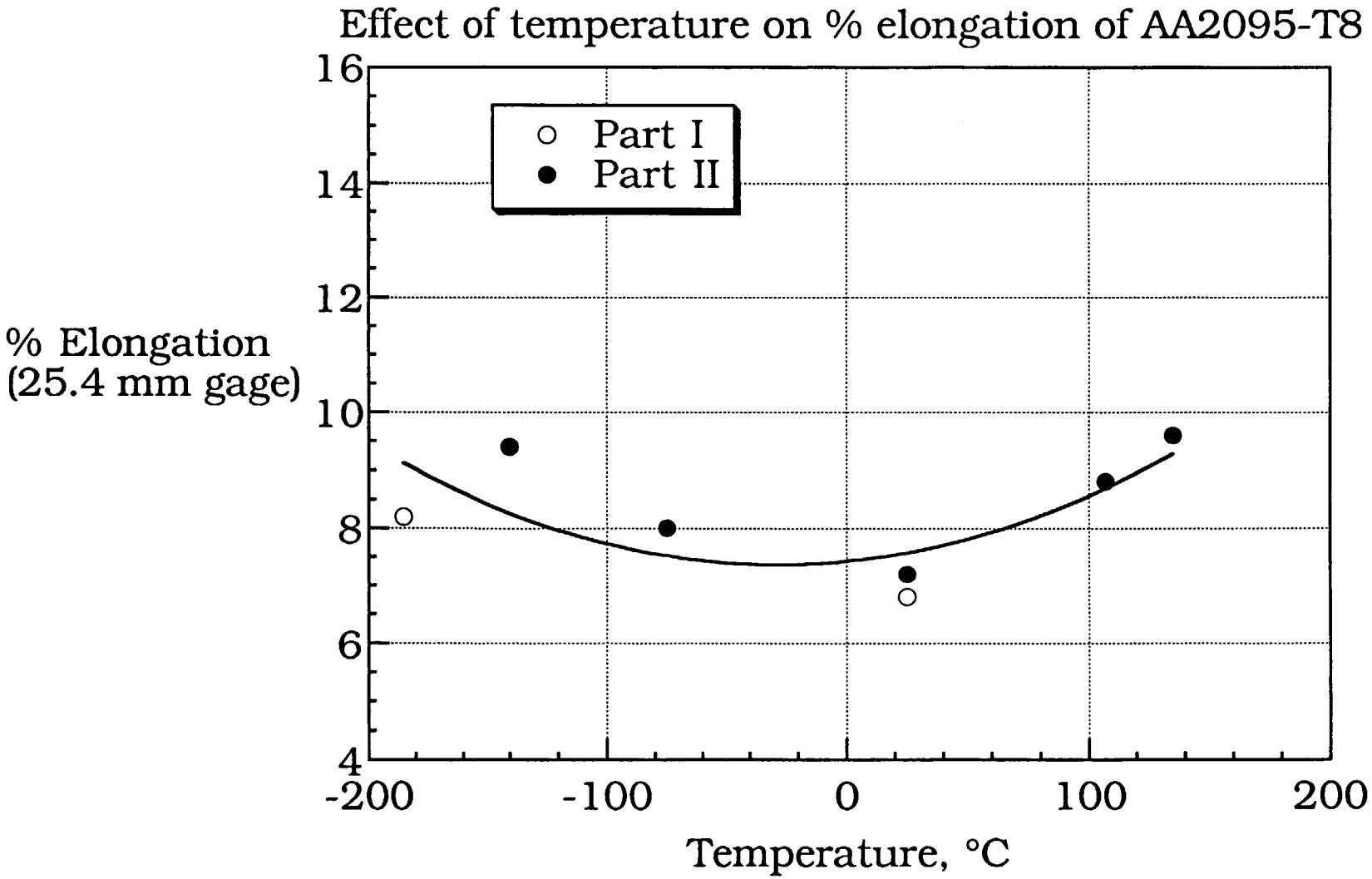

MECHANICAL PROPERTIES

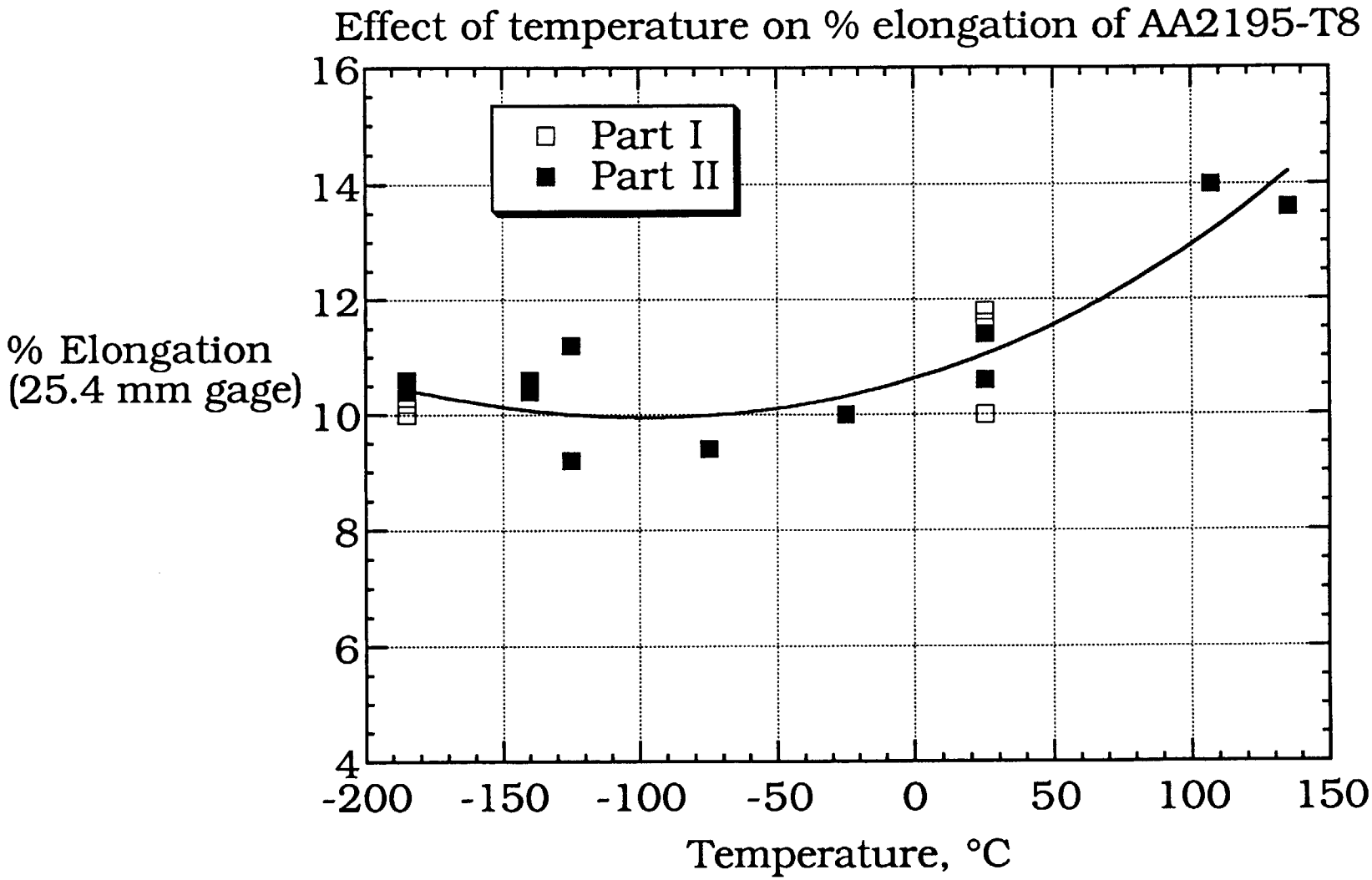

MECHANICAL PROPERTIES

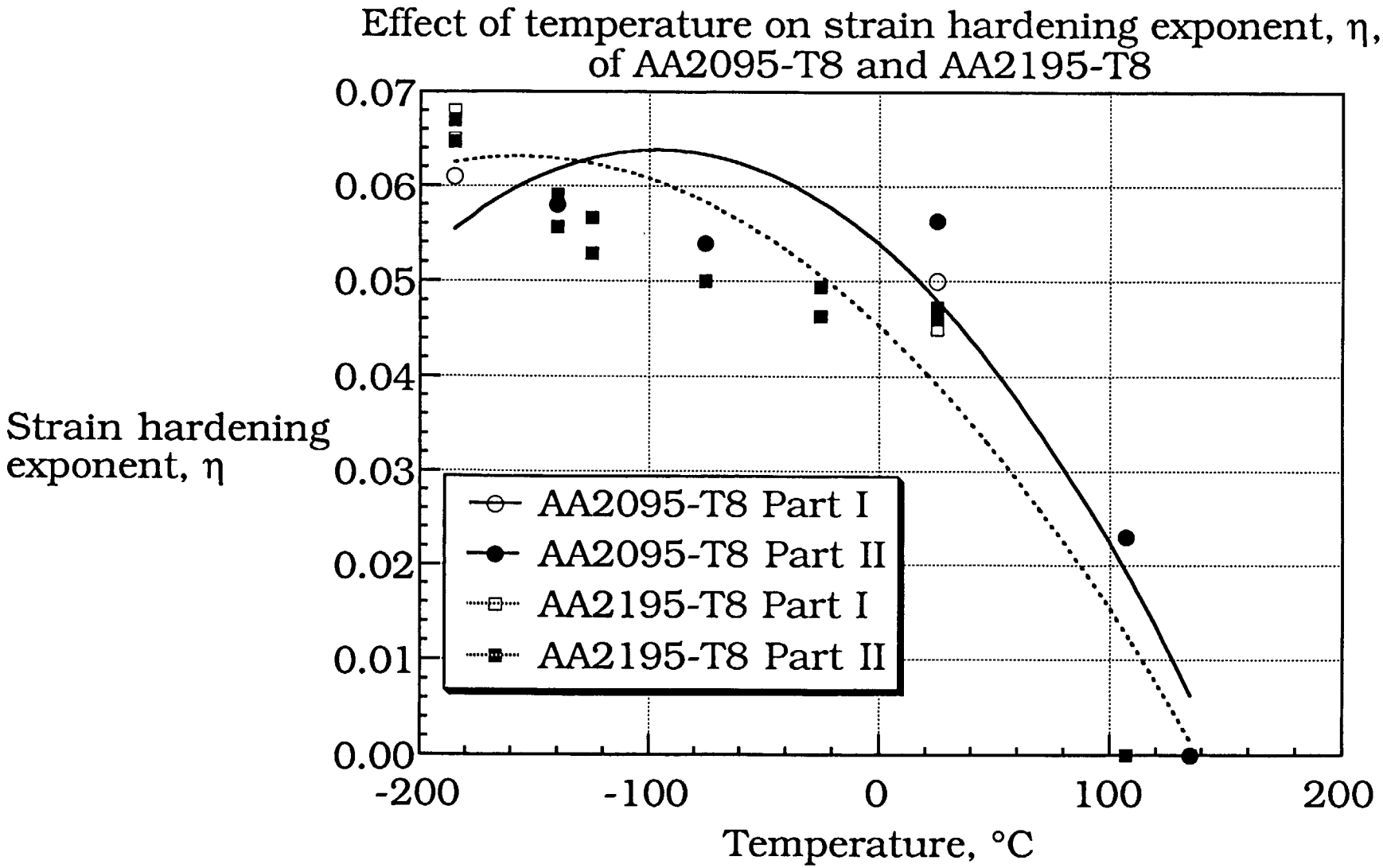

MECHANICAL PROPERTIES

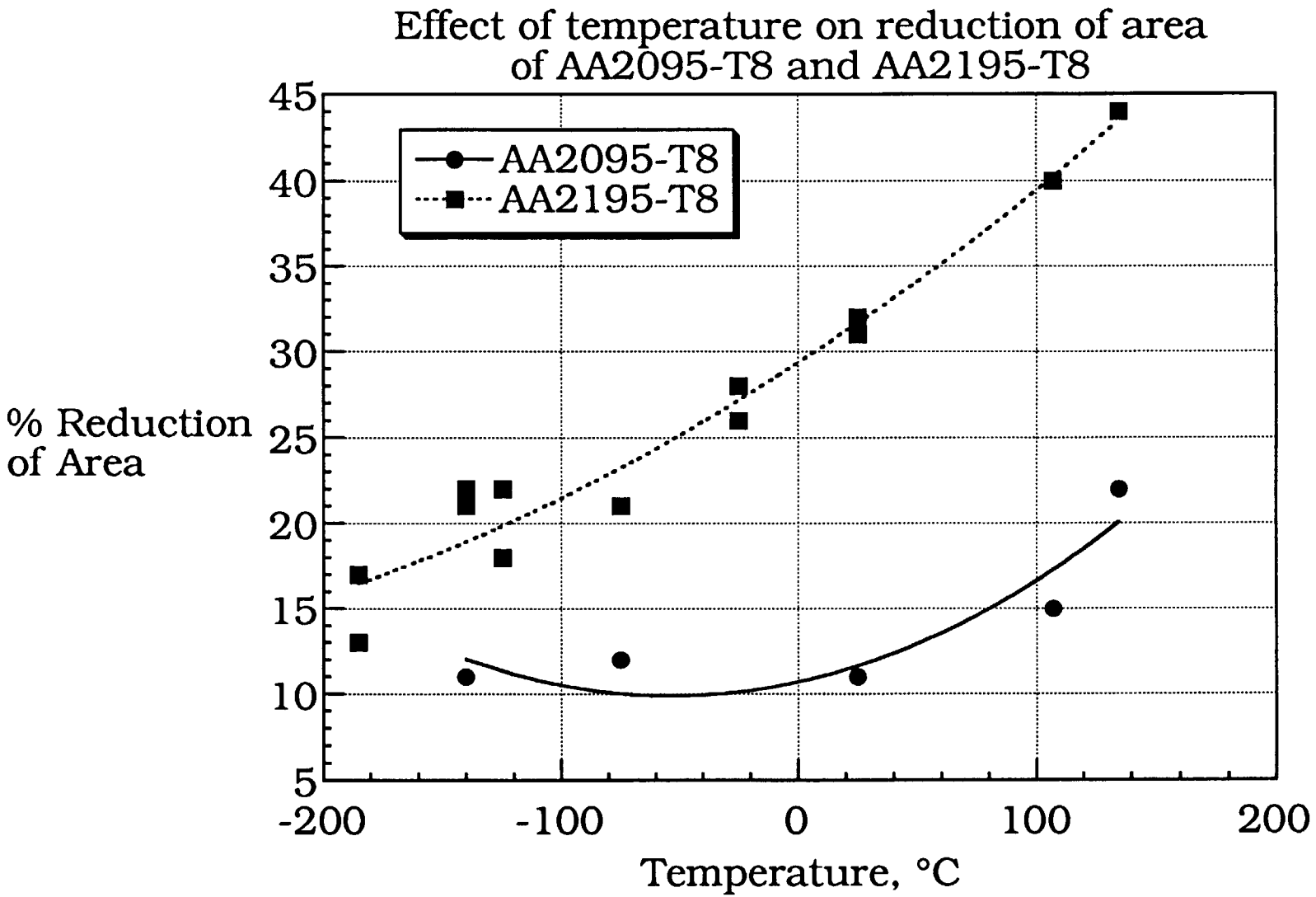

MECHANICAL PROPERTIES

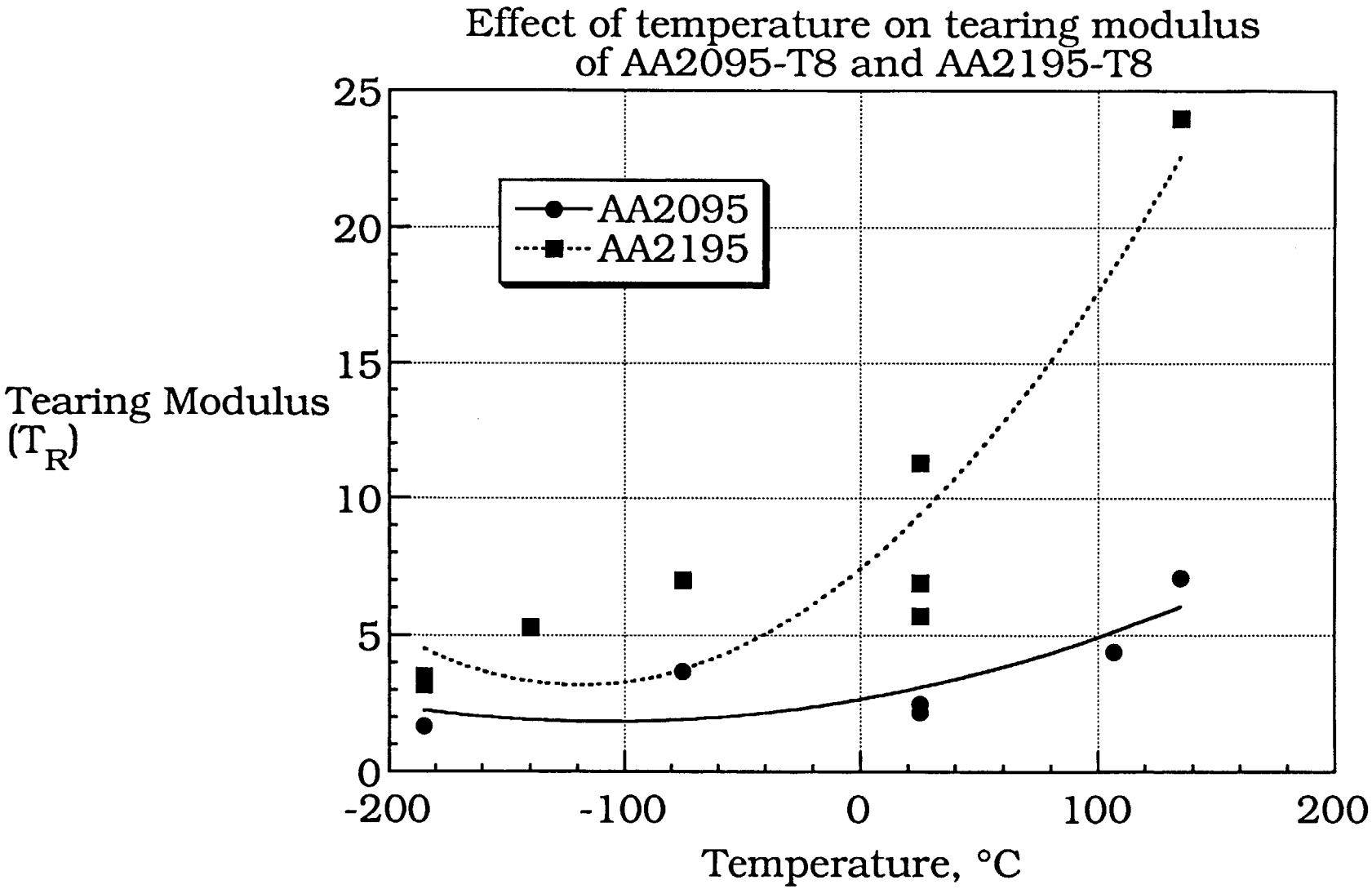

MECHANICAL PROPERTIES

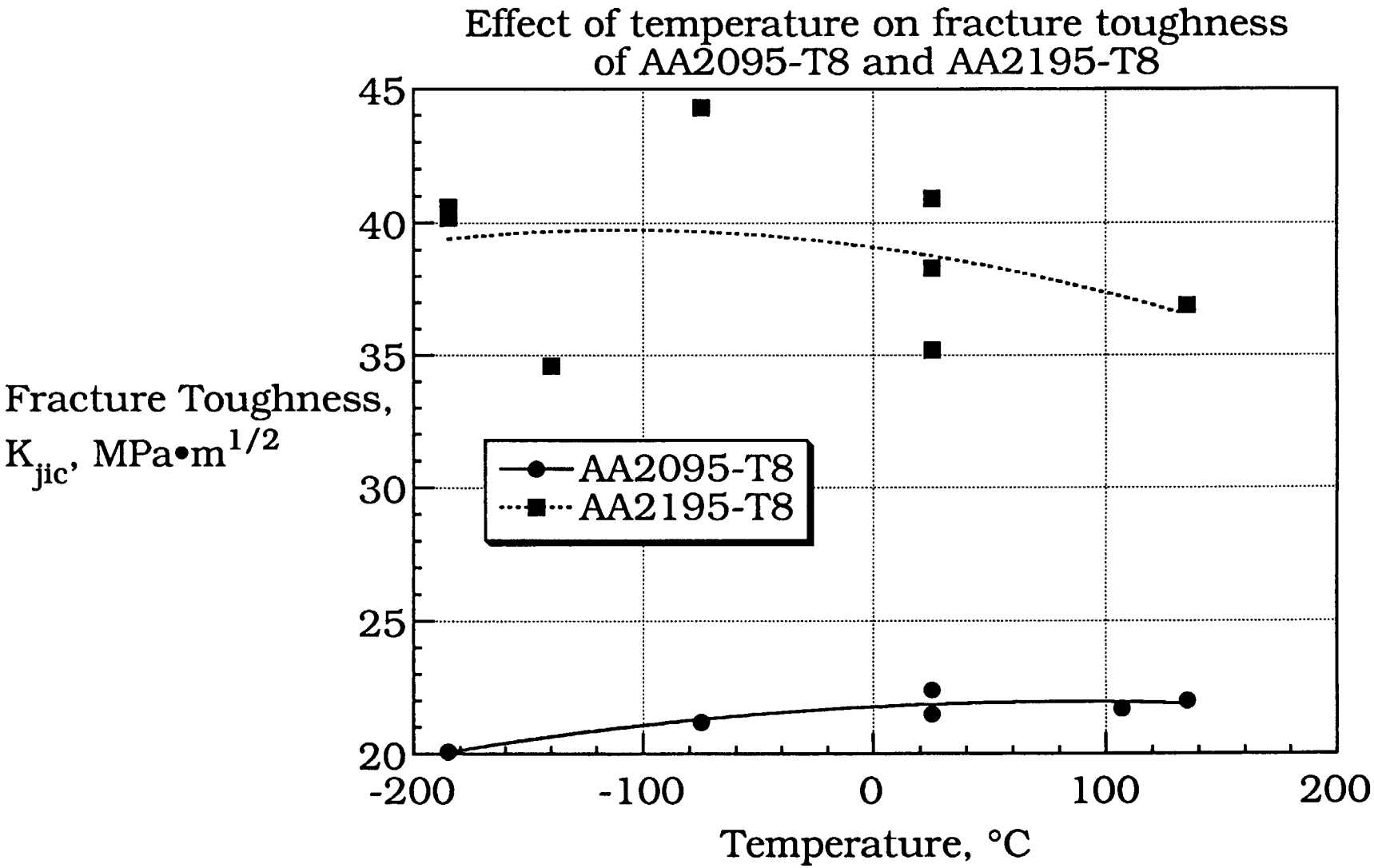

MECHANICAL PROPERTIES

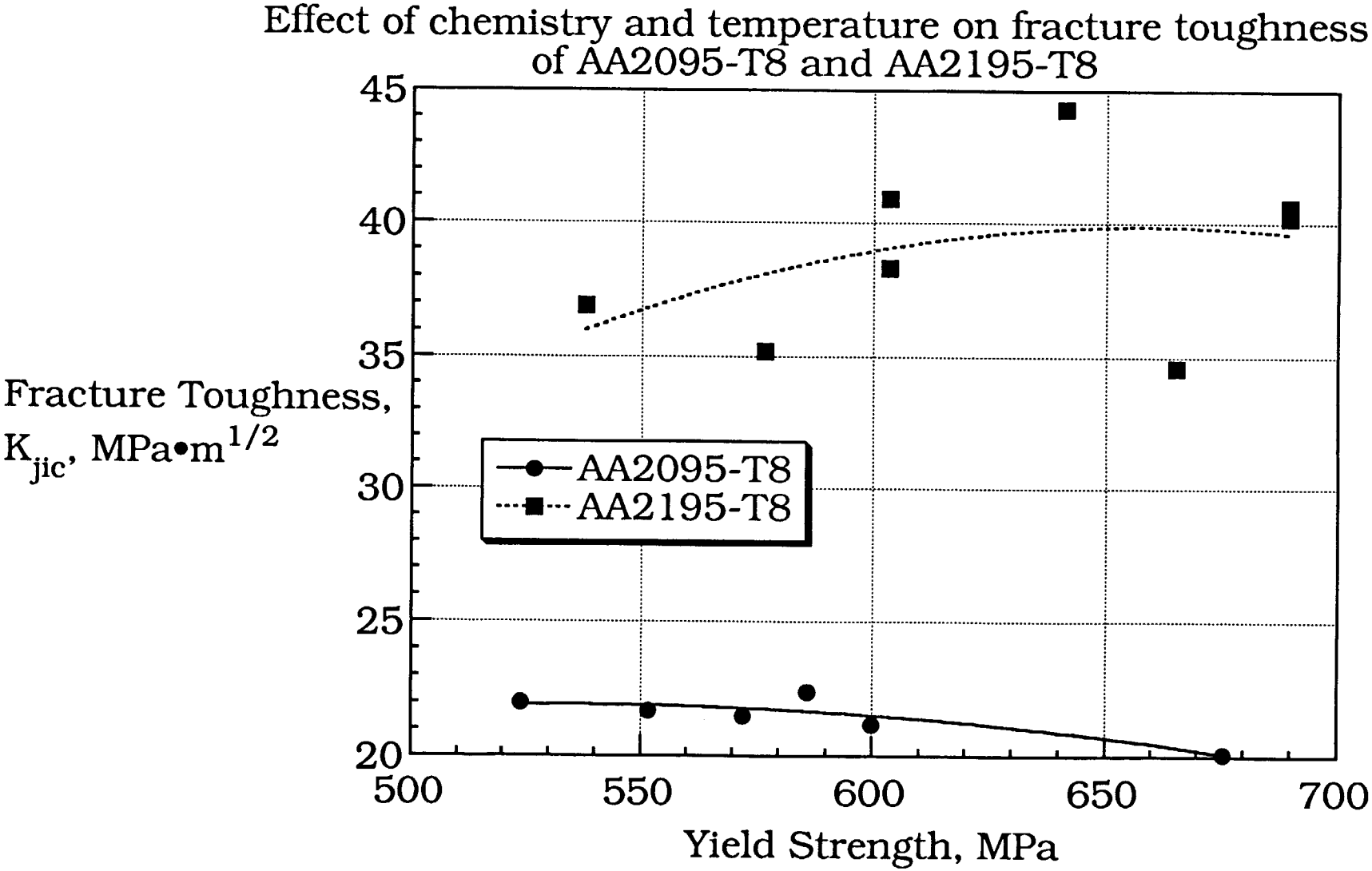

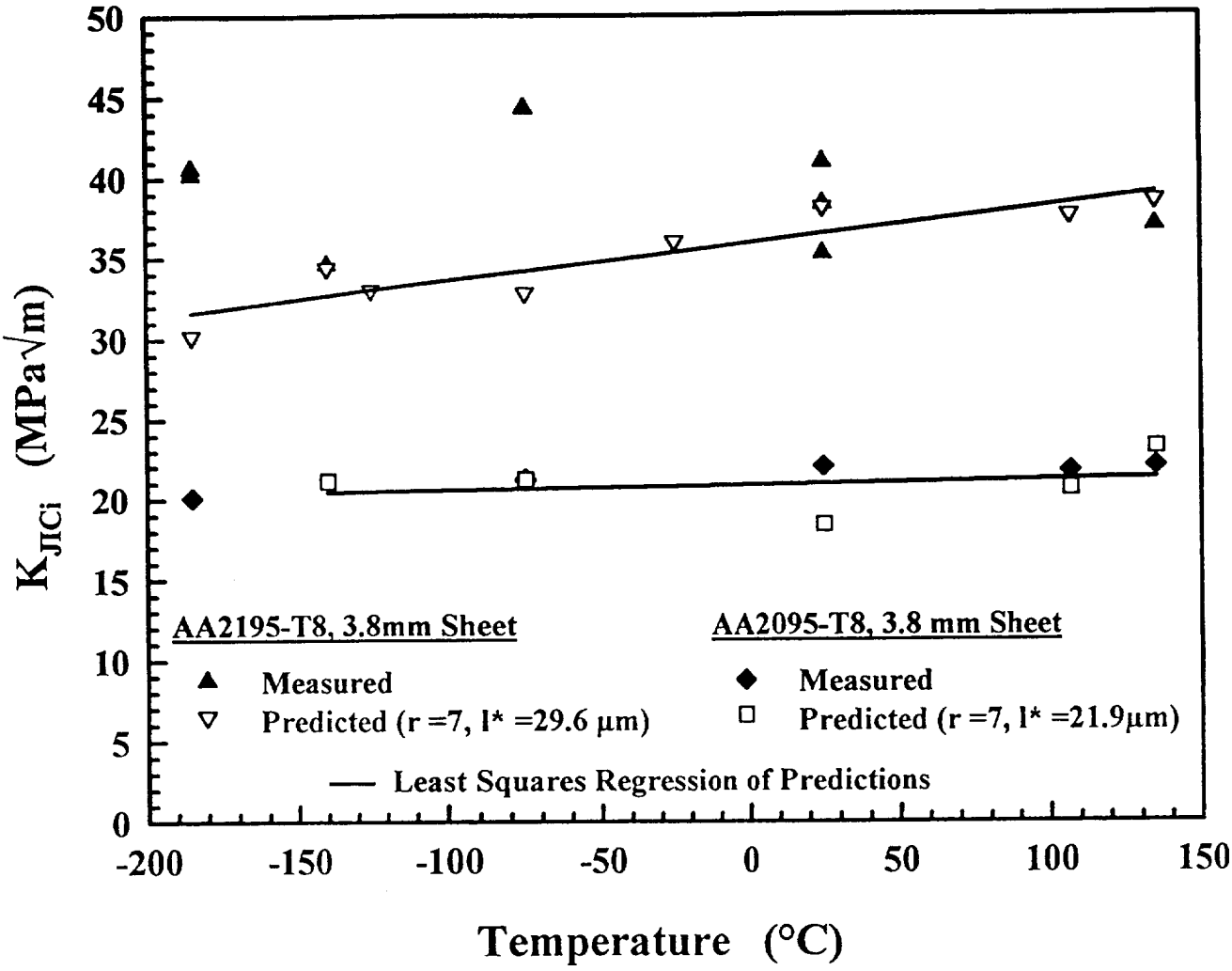
50
45
40
35
30
25
20
15
10
5
0
K_{JCi} (MPa√m)
AA2195-T8, 3.8mm Sheet
Measured
Predicted (r =7, l* =29.6 μm)
AA2095-T8, 3.8 mm Sheet
Measured
Predicted (r =7, l* =21.9μm)
Least Squares Regression of Predictions
-200
-150
-100
-50
0
50
100
150
Temperature (°C)

CONCLUSIONS

- o A significant level of Cu segregation through-the-thickness occurred for both alloys.
- o AA2095 did not overage at 143°C in 768 hours while AA2195 began overaging between 100-200 hours.
- o The modulus of AA2195-T8 increased by 6% from ambient to cryogenic (-185°C) temperatures.
- o Tensile and microstructural data were sufficient to predict the temperature dependence of the plane strain initiation fracture toughness of these alloys using a critical plastic strain-controlled model.

FUTURE WORK

- Characterize the effect of temperature on the microvoid-based fracture process.

- Predict the temperature dependence of plane strain initiation fracture toughness, as a function of aging at 143°C, for AA2095 and AA2195.

Project #4 **A Study of Environmentally Assisted Cracking in Al-Li-Cu Alloys 2090 and 2095**

F. Douglas Wall and G.E. Stoner

Project Objective:

The objectives of this research project are to define the conditions sufficient to cause cracking in Al-Li-Cu alloys, to identify microstructural features which may contribute to anodic dissolution based cracking in PA tempers; to describe the critical solution chemistry changes associated with cracking under alternate immersion conditions in chloride solution; to develop an in-situ technique for quantifying EC propagation rates; and to investigate the influence of material temper, sample orientation, stress intensity level, applied external electrochemical potential and bulk aqueous environment on the environmental cracking of Al-Li-Cu alloys.

Current Status:

The experimental phase of this research project is approaching completion and efforts are beginning to focus on data analysis, compilation of a dissertation and publication of findings.

Recent Findings:

Progress this reporting period has been concentrated in the areas of solution chemistry analysis and crack propagation rate studies.

Solution analysis

Initial experiments in this area were intended to simulate the chemistry which develops in an isolated pit during the dry cycle of alternate immersion testing in aqueous NaCl. Exposure of large material surface areas to low solution volumes resulted in the solutions with alkaline pH's (8-11) and significant dissolved lithium concentrations. This data is in agreement with the literature for research performed on other Al-Li-Cu alloys. However, the extrapolation of these data to propagating environmental cracks is not suitable due to the extreme depth to height ratios of cracks and the subsequent separation of anodic and cathodic reactions.

Recently samples having more restricted geometries have been exposed to alternate immersion in NaCl solution with real-time monitoring of pH as well as post-test pH determination via freezing and sampling with broad range pH paper. Additionally, post test analysis has been attempted on DCB specimens of Al-Li-Cu alloys. All data indicates that deep cracks/ crevices are acidic in nature with a pH in the range of 2 to 4.

Spatially resolved solution chemistry analysis of DCB specimens has been attempted using a frozen ball sampling technique. In this procedure 12 μl droplets are deposited on a frozen DCB fracture surface after the sample has undergone alternate immersion exposure. The droplets freeze into the ice layer of the specimen thus sampling the solution chemistry. The droplets are removed, melted and analyzed using capillary electrophoresis. Although the sampling efficiency is sufficient to allow identification of Al and Li ions the technique lacks the reproducibility required to gain spatial knowledge of ion concentrations.

A new technique has been developed which relies on physical isolation of a "patch" of frozen solution followed by sampling. Initial results indicate that this system may have sufficient reproducibility and sampling efficiency to allow new insights into the occluded chemistry which develops during alternate immersion testing of Al-Li-Cu alloys.

Environmental Cracking

The technique for growing and monitoring in-situ environmental cracks in Al-Li-Cu alloys has been refined and used to investigate the influence of several experimental variables on crack rates and fracture surface morphology.

The base-line experiment which is used as a control consists of SL-PA 2095 exposed to 0.1M NaCl + 0.1M Na_2CrO_4 solution, polarized to -0.547 V_{SCE} and stressed such that the crack tip stress intensity falls between 10 and 20 MPa-$m^{1/2}$. Under these conditions the crack growth rates are approximately 10^{-5}mm/sec. The environmental fracture surfaces have significant tortuosity, evidence of ductile features and are covered with extensive corrosion products.

Ramping the applied potential in the cathodic direction once the test has initiated does not result in cessation of cracking until after net cathodic currents have been measured. Smooth specimens exhibit a critical EAC potential below which cracking will not occur. This recent data suggests that the macroscopic experimental conditions for crack propagation are different than

for initiation. It is likely that IR drop down the crack has caused a loss of "communication" between the potentiostat and crack front.

Low stress intensity levels have been investigated in an attempt to define a K_{IEAC} for the system being studied. However, to this point no lower bound of applied stress intensity has been clearly defined at which environmental cracks will not propagate. Low stress intensity levels (K_{APPL} < 6 MPa-$m^{1/2}$) have resulted in a change in fracture morphology from the control experiment. Crack fracture surfaces appear flat with loss of ductile features. This observation has not been interpreted at this time.

Material temper has been shown to have an enormous effect on propagation rate. Aging 2095 from 4 to 20 hours at 160°C results in a 15X change in crack propagation rates. Additionally the fracture morphology for the UA samples is relatively featureless, is sparingly decorated with corrosion products and has been shown to have matching features on opposite sample halves. These observations indicate the possibility of an embrittlement mechanism dominating the cracking of the UA materials.

Testing in a bulk environment of NaCl without the presence of an inhibiting specie does not result in environmental cracking for an applied potential of -0.7 V_{SCE} (anodic to E_{OC}). Fractography indicates that overload failure ensues at the end of the fatigue precrack for a large portion of the central crack front. However, along the edges of the sample extensive attack is evident stemming from the end of the fatigue crack. Even though this attack was resolvable via DCPD measurements during the test, it appears to be gross pitting caused by polarization near the pitting potential.

Future Work:

During the next month the experimental stage of this project will be completed. Emphasis will be on calibration and implementation of a technique for gaining improved knowledge on the solution chemistries associated with propagating environmental cracks in specimens alternately exposed to NaCl solution and ambient air. The following months (9/95 through 12/95) will be used for completion of a dissertation and publication of findings.

Explanatory Text for Viewgraphs:

1. Title slide.

2. Objectives.

3. Microstructural features considered for anodic dissolution based cracking of PA Al-Li-Cu alloys. TEM micrograph shows boundary in PA 2095 decorated with T_1 particles. Lower graph is data on Cu depletion taken from Kumai. Our model for a boundary is a high density of T_1 phase surrounded by a region of diminished copper content.

4. This slide lists the materials used to simulate the electrochemical behavior of relevant boundary phases. The T_1 phase was cast as a bulk ingot by Rudy Bucheit (Sandia Labs). Al-Cu binaries are used to map out the electrochemical behavior of Al as a function of Cu content. The experimental techniques used to investigate the electrochemical behavior are also listed. In general, attempts were made to determine electrochemical potentials which resulted in a change in material corrosion current. These values were then compared to potentials which result in a change in material environmental cracking response for the same environment.

5. These are the relevant data in a $NaCl/Na_2CrO_4$ environment for the simulated T_1 phase (upper left), Al with varying Cu content (upper right), TTF of PA 2095 as a function of applied potential (lower left), and critical potentials associated with an abrupt change in TTF for various Al-Cu-X alloys (lower right).

6. An overview of occluded chemistry analysis is presented.

7. A list of the techniques used to improve understanding of localized chemistry during propagation of environmental cracks.

8. Experimental set-up used to simulate a long propagating environmental crack and resulting data from AI exposure to NaCl environment.

9. One of the techniques used in an attempt to gain spatial knowledge of crack chemistries associated with DCB specimens under AI conditions.

10. An example of the data obtained using the technique summarized in slide #9. Although sampling efficiency is adequate, reproducibility remains a problem with this technique.

11. Improved device for obtaining local solution chemistry samples. This rig relies on physical isolation of solution followed by sampling and analysis. Initial testing indicates a high sampling efficiency and reasonable reproducibility.

12. Summary of solution analysis findings.

13. Overview of approach and variables examined in environmental cracking study.

14. Control experiment for environmental cracking study. Conditions for this test were derived from electrochemical characterization of model boundary features and results of TTF testing of smooth bar specimens under constant immersion conditions.

15. Results of testing in NaCl without an inhibiting specie present. Although crack extension is indicated by DCPD data, SEM fractography indicates that gross pitting and not EAC caused the change in the potential signal.

16-17. Effect of changing the applied external potential on the crack growth rate and resulting environmental cracking fractography. Although the potential is lowered cathodic to the material critical EAC potential the crack continues to propagate. Optical microscopy and SEM indicate that this crack developed a very deep front. This is most likely due to the loss of external electrochemical driving force. It is possible that the crack sides may have even been cathodically protected to some extent. As the overpotential was shifted in the cathodic direction the fracture surface morphology changed from an appearance consistent with the control experiment (slide#14) to a relatively featureless surface. A mechanistic interpretation of this phenomena has not been developed at this time.

18. This slide shows the crack length vs. time data typical of a test carried out at an elevated stress intensity ($K > 24$ MPa-$m^{1/2}$). Crack bursting events are indicated by DCPD as well as corrosion current data. These bursts may be due to either an embrittlement phenomena or ligament failure lagging the crack front. It is interesting to note that at these stress intensities the crack front is under plain stress conditions.

19-20. The effect of low stress intensity ($K < 6$ MPa-$m^{1/2}$) on environmental cracking is shown in these two slides. Experimentation at low K levels was carried out in order to determine a K_{IEAC} value for these experimental conditions; however, no limit was conclusively determined below which a crack would not propagate. Similar to the case for reduced electrochemical driving force, reduced stress intensity results in a change of fracture morphology from that associated with the control (slide#14) to a relatively featureless surface.

21-23. These slides examine the cracking behavior of 2095 and 2090 as a function of thermomechanical processing. A strong correlation exists between crack growth rates and material temper. UA materials have been observed to crack at rates between 15 and 1000 times faster than PA materials. Additionally, differences in fracture morphology suggests that cracking of PA materials in accompanied by extensive materials dissolution while cracking of UA materials appears to be due to brittle failure.

24-25. A UA 2095 sample was tested in the LT orientation in order to determine if the high crack velocities associated with this temper were a high angle boundary phenomenon. Crack growth rate data indicates several orders of magnitude change in velocity with changing orientation. Post test failure of the specimen resulted in cracking along a direction

perpendicular to the fatigue crack plane. Fractography suggests the embrittlement of high angle boundaries.

26. This slide shows the misorientation of material along opposite sides of an environmental crack grown under control conditions (slide#14). Kikuchi patterns were generated and indexed in order to determine misorientations. Cracking under these conditions follows high angle grain boundaries.

27. General summary and conclusions of presented research.

A Study of Environmentally Assisted Cracking in Al-Li-Cu Alloys 2090 and 2095

F.D. Wall
G.E. Stoner

Department of Materials Science and Engineering
University of Virginia
Charlottesville, Virginia 22903

NASA - LaRC Contact : Marsha Domac

Additional Support:
Reynolds Metals Corporation
Waters Corporation

Objectives

Determine if the grain boundaries can provide a pathway for anodic dissolution based environmental cracking. What microstructural feature defines the active path?

Analyze the occluded chemistries that develop in an isolated pit and in a propagating environmental crack. Determine conditions (pH, ions present) which are necessary for crack initiation and crack propagation.

Develop a technique for growing and monitoring cracks in Al-Li-Cu alloys under constant immersion conditions. Use the technique to examine the effect of E_{APPL}, K_{APPL}, material temper and bulk aqueous environment on crack propagation rates.

Knowledge to be gained by meeting objectives

Conditions sufficient to cause in-situ environmental cracking.

Environmental factors associated with cracking during Al exposure in aqueous NaCl.

Effects of changing macroscopic variables on EC of alloy 2095.

Al-Li-Cu Boundary Microstructure

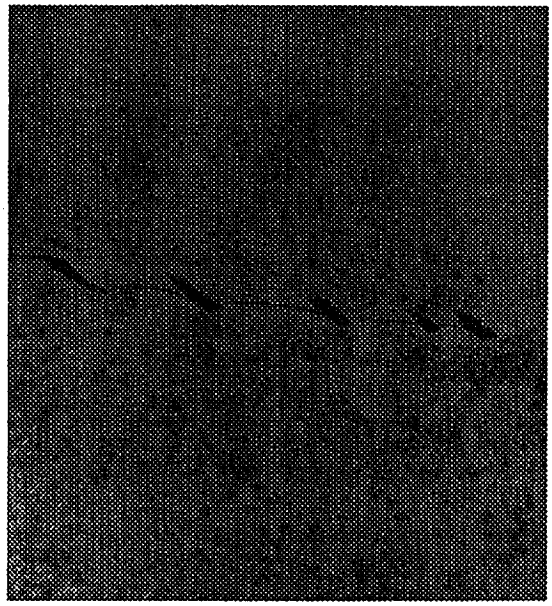

2095-B (PA) Boundary

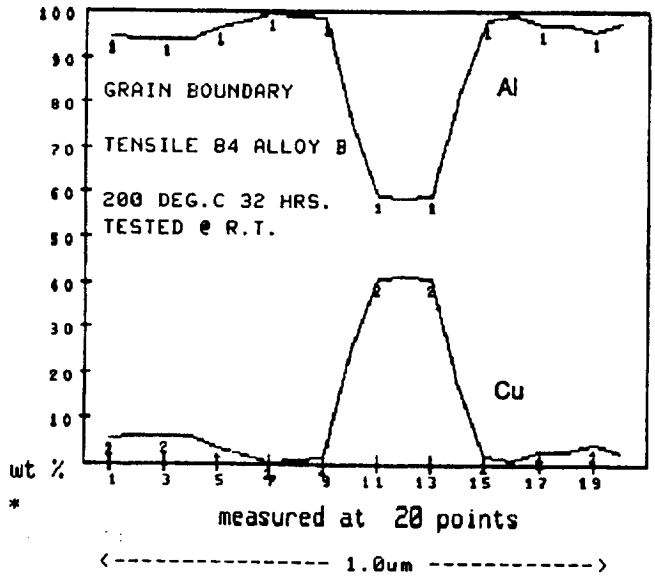

Cu-depletion across grain boundary in Al-Li-Cu 2090
(from Kumai, Corrosion Science, V45, No. 4, p 300)

Electrochemical Behavior of Model GB Features and EAC Behavior of Tempered Alloys

Materials used to model GB features:

T_1 phase (Al_2CuLi)	: bulk ingot casting of 2Al : 1Cu : 1Li
Al with varying Cu content	: 99.99 Al Al-0.10 Cu Al-0.98 Cu Al-3.96 Cu

Techniques used to assess behavior of GB features:

Cast T_1 : potentiodynamic polarization $\longrightarrow$ E_{BR} (E_{PIT})

Al-Cu : scratching electrode experiments $\longrightarrow$ E_{RP}

Technique for assessing EAC Behavior of Tempered Al-Li-Cu alloys:

Constant extension / scratching electrode experiment $\longrightarrow$ $E_{CRIT\text{-}EAC}$

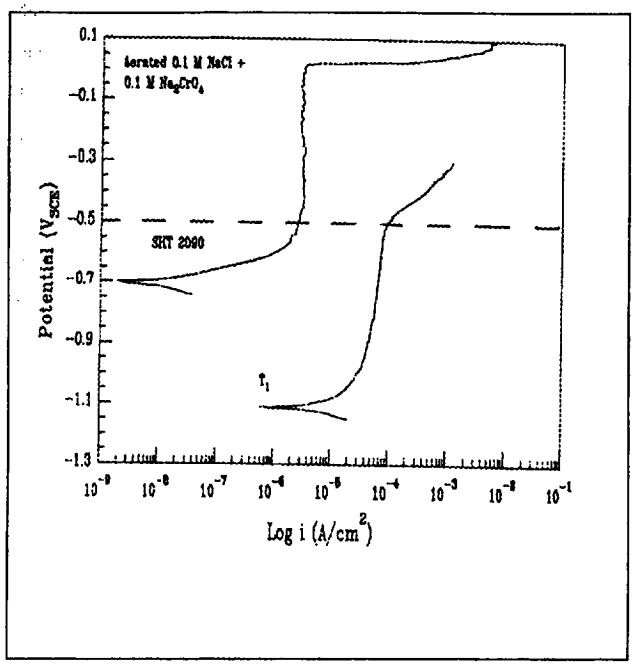
Aerated 0.1 M NaCl +
0.1 M Na2CrO4
SHT 2090
Potential (VSCE)
Log i (A/cm2)

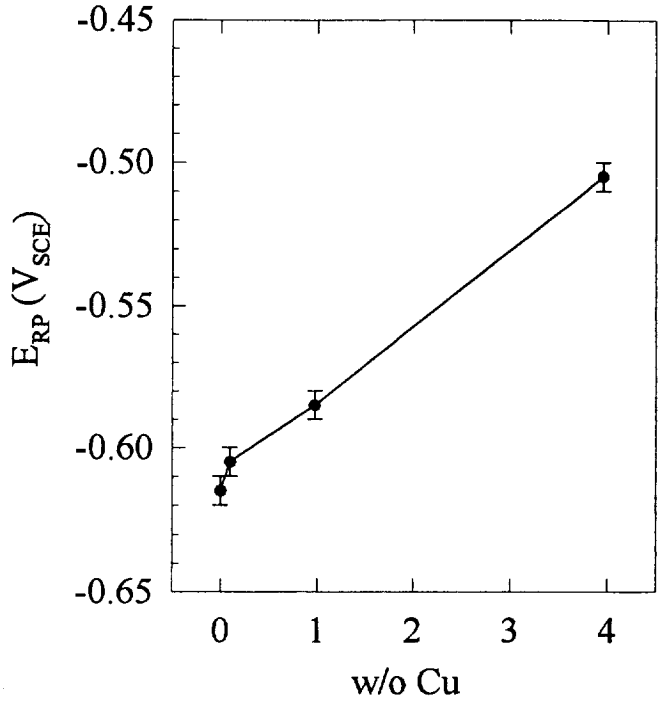
ERP (VSCE)
w/o Cu

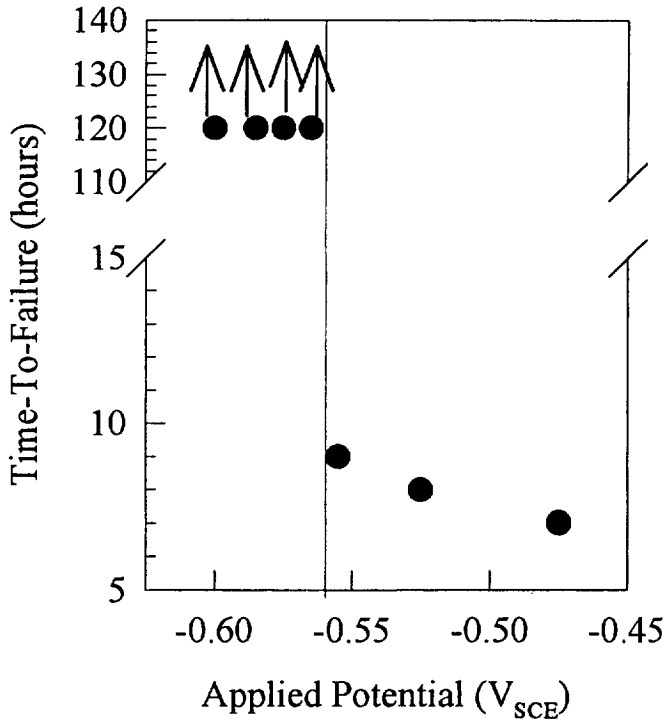
Time-To-Failure (hours)
Applied Potential (VSCE)

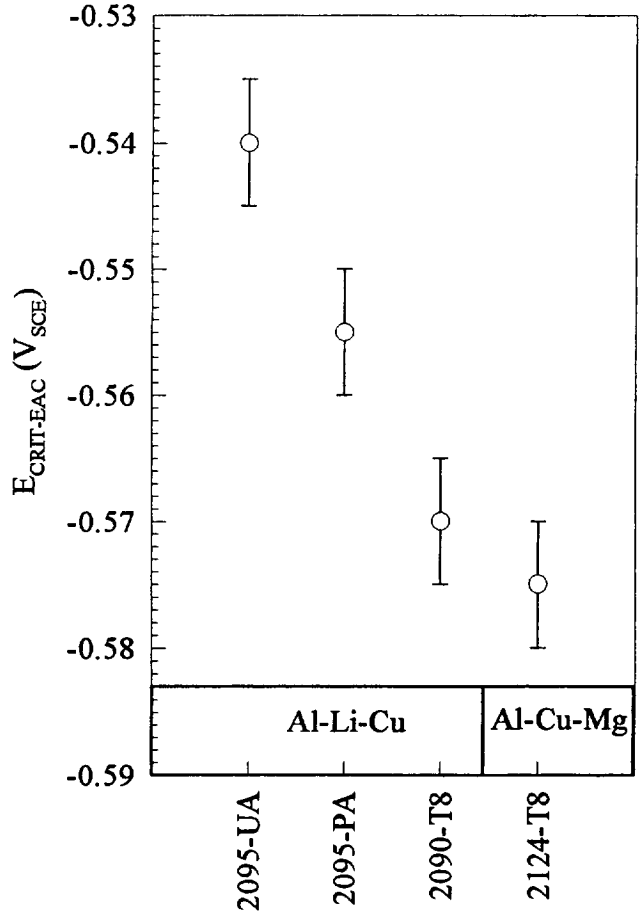
ECRIT-EAC (VSCE)
Al-Li-Cu
Al-Cu-Mg
2095-UA
2095-PA
2090-T8
2124-T8

Occluded Chemistry Analysis

Stressed samples of Al-Li-Cu alloys generally do not fail during constant immersion in aqueous chloride environments but rapidly fail during alternate immersion testing in the same environment.

What happens to the pit chemistry when the sample is removed from the bulk aqueous environment?

The pH and ionic makeup of solution within an isolated pit has been experimentally modeled by exposure of large areas of material surface to small volumes of chloride solution.

pH microelectrode ⟶ alkaline pH : 9-11

capillary electrophoresis ⟶ significant $[Li^+]$: mMol

Hypothesis

Under constant immersion conditions the pit chemistry is too aggressive and a sharp crack cannot be initiated/maintained.

Removal of a pitted sample to ambient air results in the development of an alkaline pH, absorption of CO_2 and the subsequent formation of a specie causing passivation of crack walls.

Next Question

Is this chemistry maintained as the crack propagates away from the initiation site? What pH and solution makeup are associated with a propagating EAC crack?

Techniques for examining solution chemistries associated with crack propagation

Alternate immersion in aqueous NaCl:

pre-cracked DCB specimens

model crevice

pH measurements

micro-electrode mounted in center of model crevice (real-time)

pH paper used to investigate frozen surfaces (post exposure)

Solution analysis

Isolation of solution from DCB samples followed by speciation and quantification using capillary electrophoresis

Solution pH measured under alternate immersion conditions in aqueous NaCl for restricted geometry intended to model a propagating environmental crack.

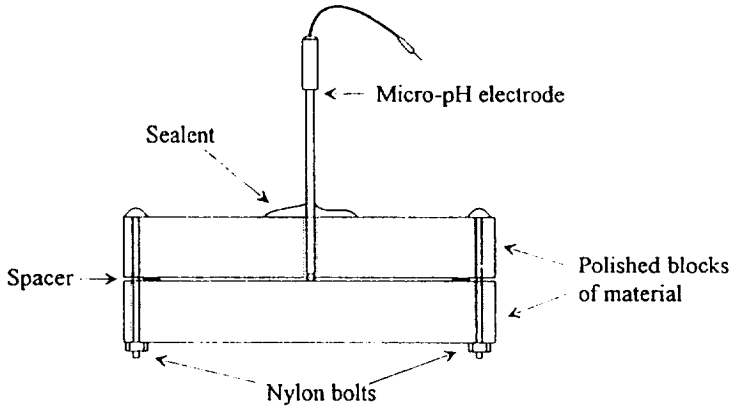

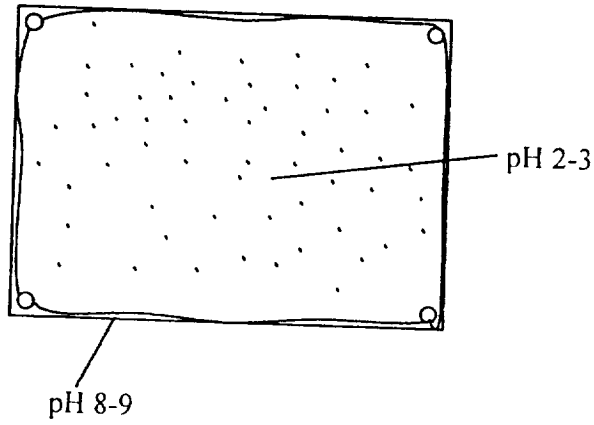

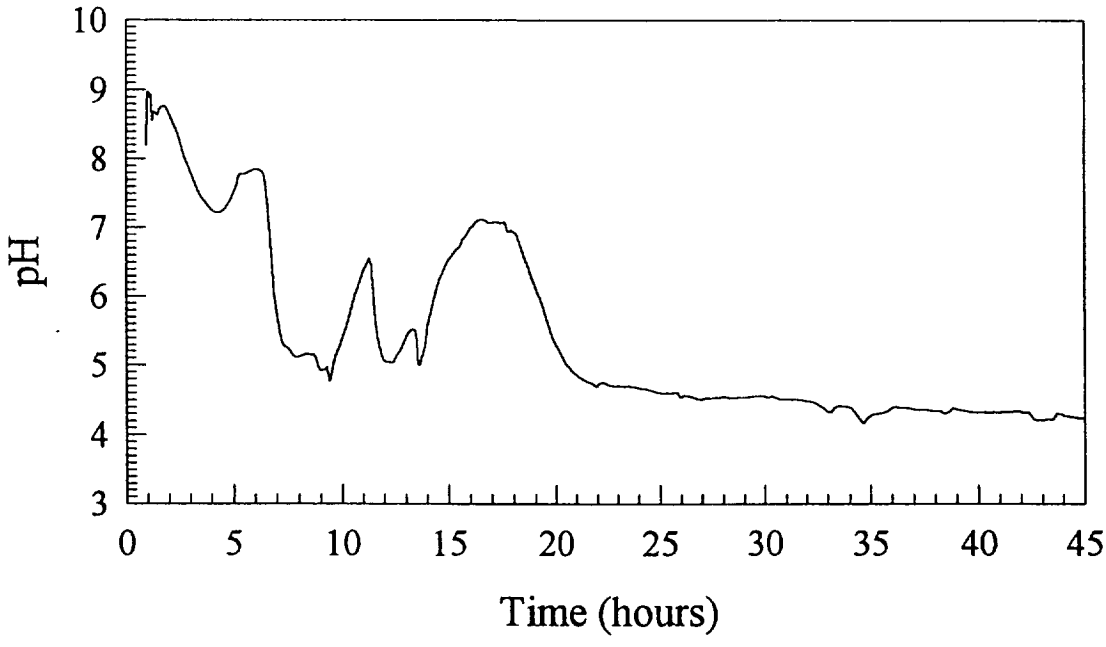

Methodology:

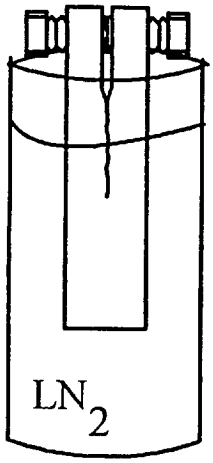

1. Freeze sample in liquid nitrogen.

2. Remove from LN_2 and load to failure.

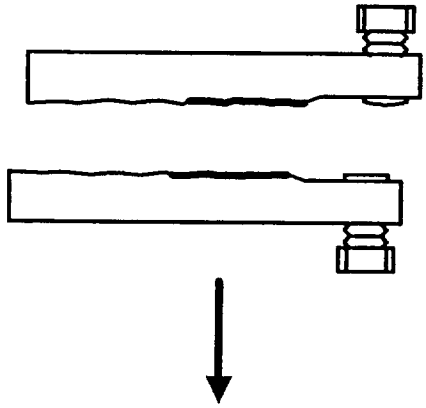

3. Place sample in tub of LN_2 to maintain temperature and provide N_2 blanket.

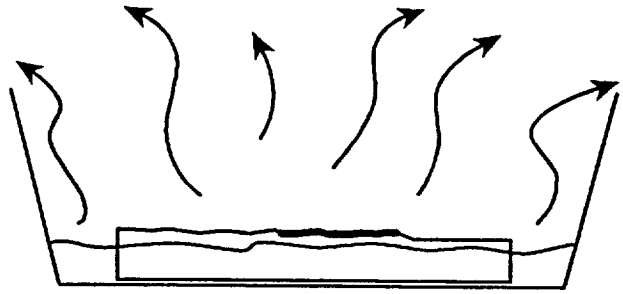

4. Deposit 12ul droplets of sampling solution onto specimen fracture surface.

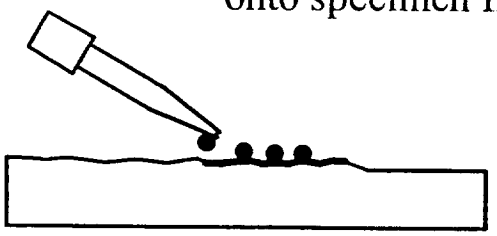

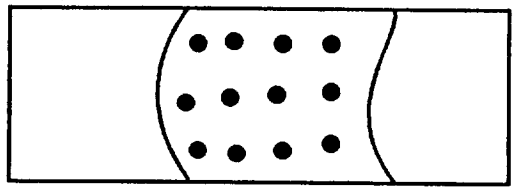

5. Place frozen samples into vials to thaw.

6. Analyze samples using capillary electrophoresis.

Analysis of solution removed from 2095 DCB specimen following alternate immersion exposure in 0.1M NaCl.

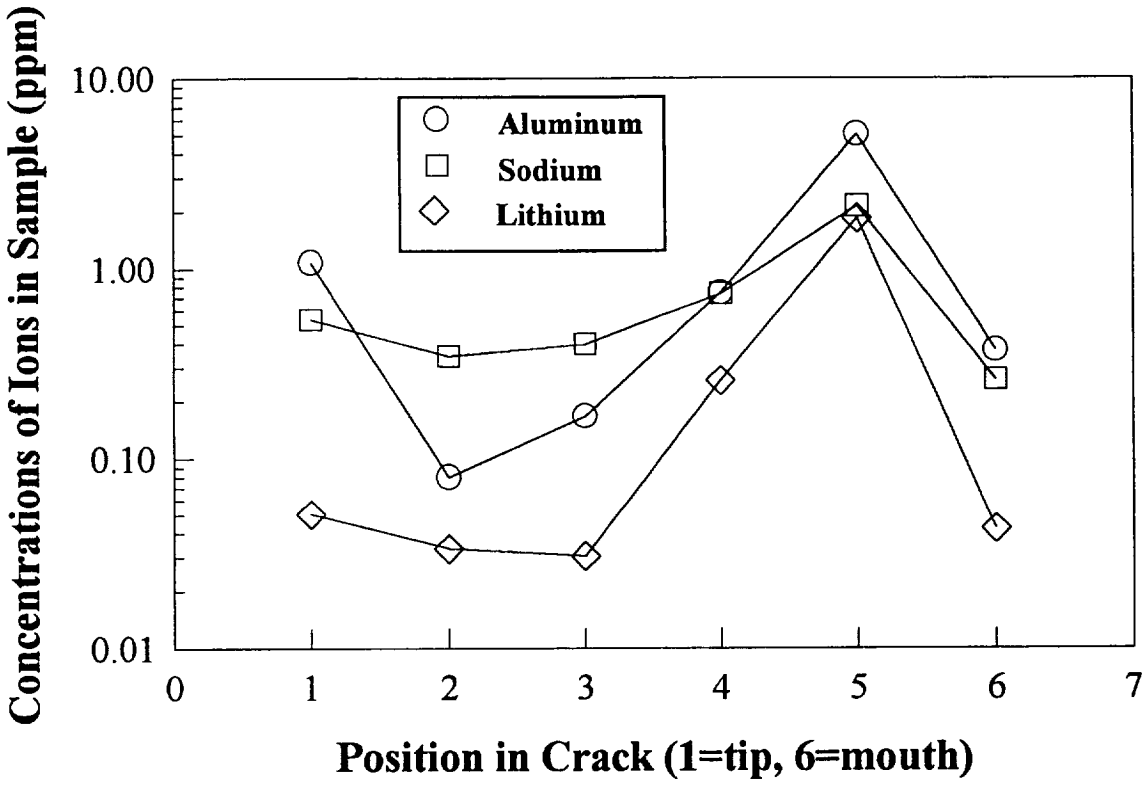

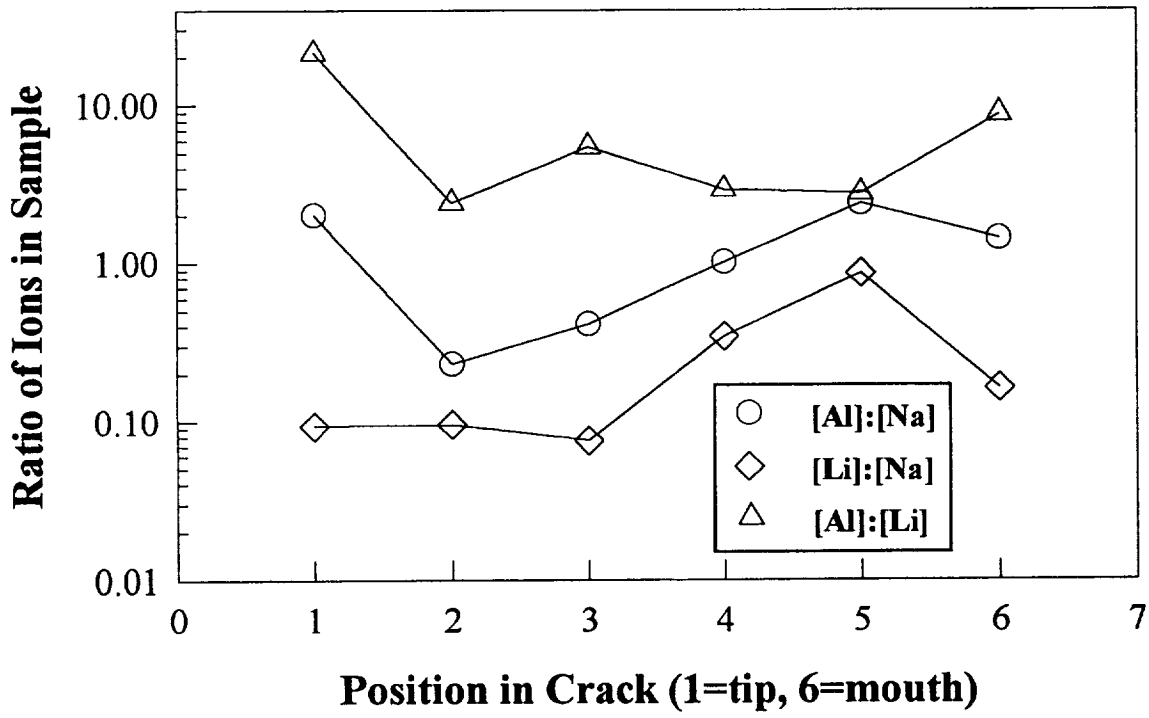

Technique of physical isolation for obtaining spacially resolved samples of solution of known volume

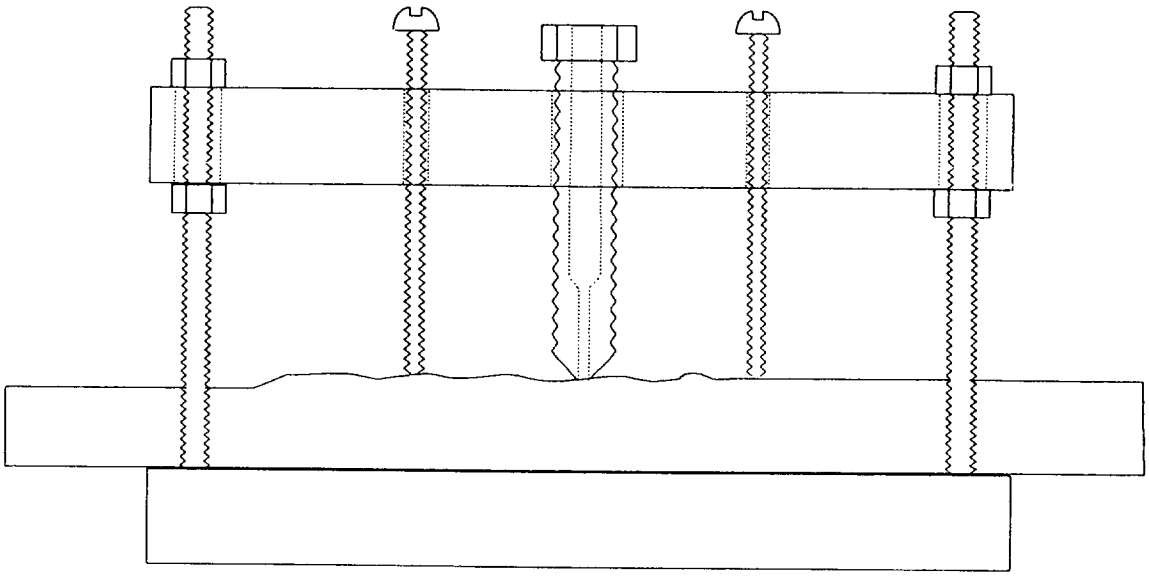

Sampling efficiency of solution isolation rig for 0.05 M K_2MoO_4 +0.05 M $MgSO_4$ extracted from an artificial 0.060 mm crevice:

trial#	Efficiency
1	70%
2	60%
3	73%
3+4	95%

Summary of solution analysis

Model experiments indicate that the solution in an isolated pit is likely to develop an alkaline pH and a significant Li^+ concentration during the dry cycle of an AI experiment in NaCl solutions. This environment may be critical in the initiation of environmental cracks.

Model crevices in AI exposures develop an acidic pH which remains acidic independent of wet or dry cycle. This condition is representative of a long environmental crack and suggests that an acidic pH dominates crack tip chemistry during propagation.

Techniques such as the frozen ball method and the solution isolation rig are promising for broadening knowledge of spatially resolved crack tip chemistries.

Examination of Variables affecting Environmental Cracking Behavior

Approach

Use knowledge of boundary feature electrochemistry and TTF behavior of statically loaded smooth bar specimens to select environmental and electrochemical conditions likely to result in crack initiation under constant immersion conditions.

Change variables to deviate from this base-line condition and examine effects on EC behavior in terms of crack propagation rates (quantitative) and crack path fractography (qualitative).

Variables examined

Bulk solution chemistry : $NaCl + Na_2CrO_4$ vs. NaCl

Applied overpotential : constant vs. ramp towards cathodic

Stress intensity : low, intermediate, high (2-5, 10-20, 24-26 $MPa\text{-}m^{1/2}$)

Material temper : UA vs. PA

Crack path : high or low angle, SL vs. LT

EC Behavior of PA 2095 Under Base-Line Conditions

Temper : PA 2095 (SHT+CWQ+6%STR+30hrs@143°C)

Sample orientation : SL

Sample geometry : WOL (a_o= 9.11mm; b = 3.175mm; w = 36.58mm)

Bulk environment : 0.1M NaCl + 0.1M Na_2CrO_4

Applied potential : $E_{APPL,AVE}$ = -0.547 V_{SCE}

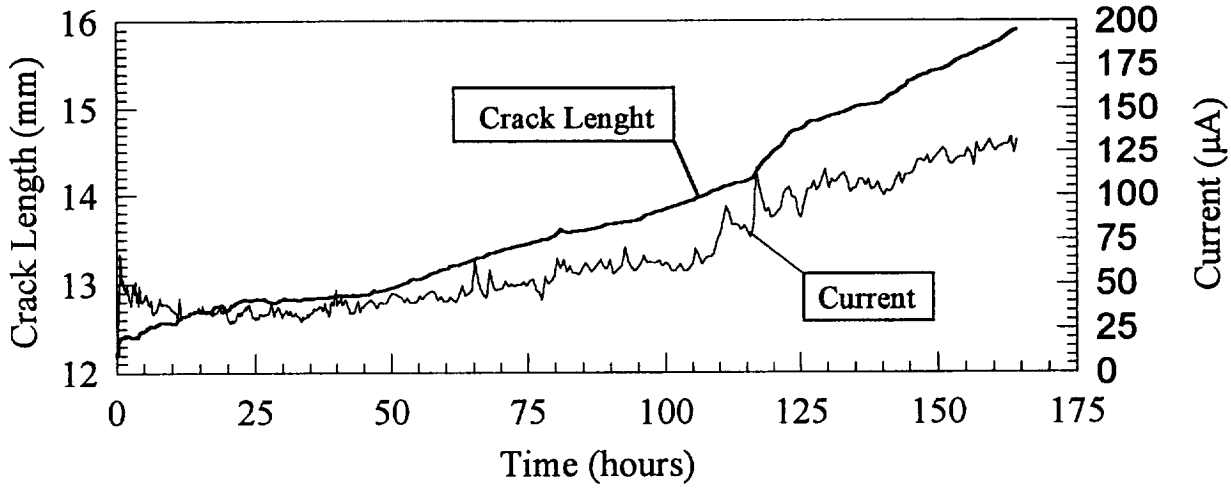

Target stress intensity : 18 MPa-$m^{1/2}$

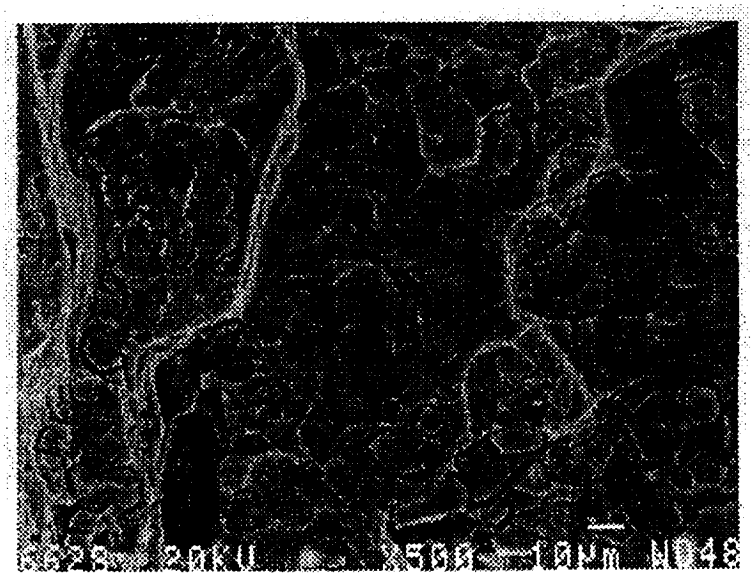

Average crack growth rate = 10^{-5} mm/sec

Typical morphology for EC region under listed conditions.

Effect of testing in aqueous chloride without the presence of an inhibiting specie

Temper : 2095 (SHT+CWQ+6.5%STR+20hrs@143°C)

Sample orientation : SL

Sample geometry : WOL (a_o= 9.11mm; b = 3.175mm; w = 36.58mm)

Bulk environment : **0.6 M NaCl (aerated)**

Applied potential : $E_{APPL,AVE}$ = -0.700 V_{SCE}

Target stress intensity : 16.5 MPa-$m^{1/2}$

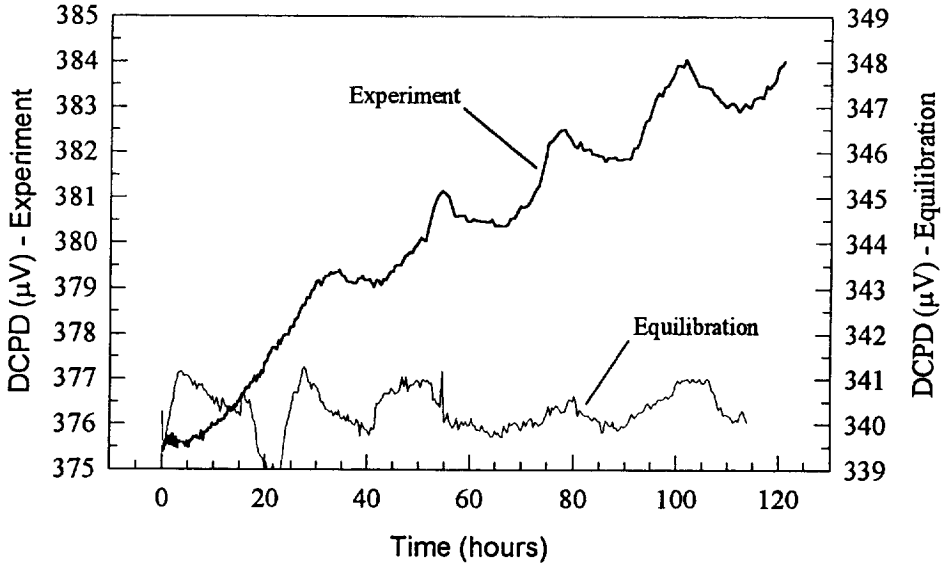

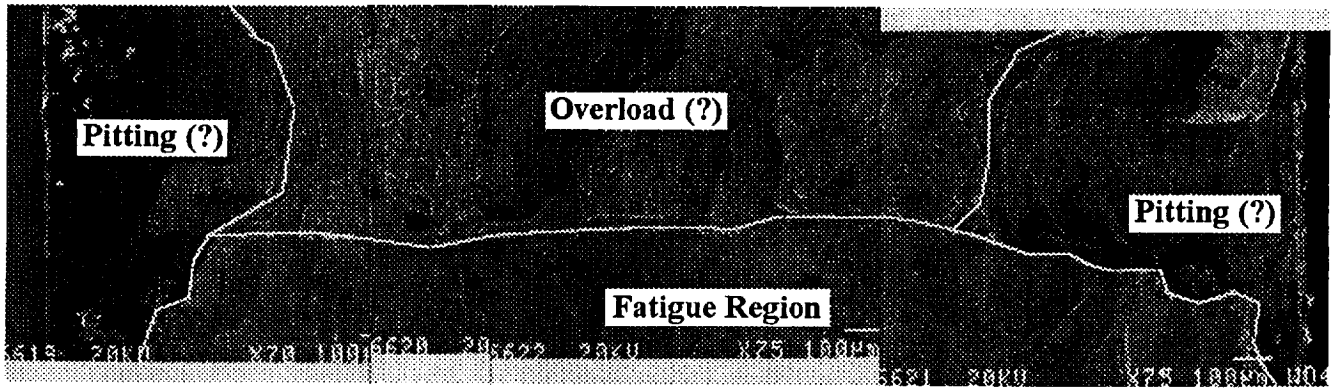

Effect of overpotential on a propagating environmental crack

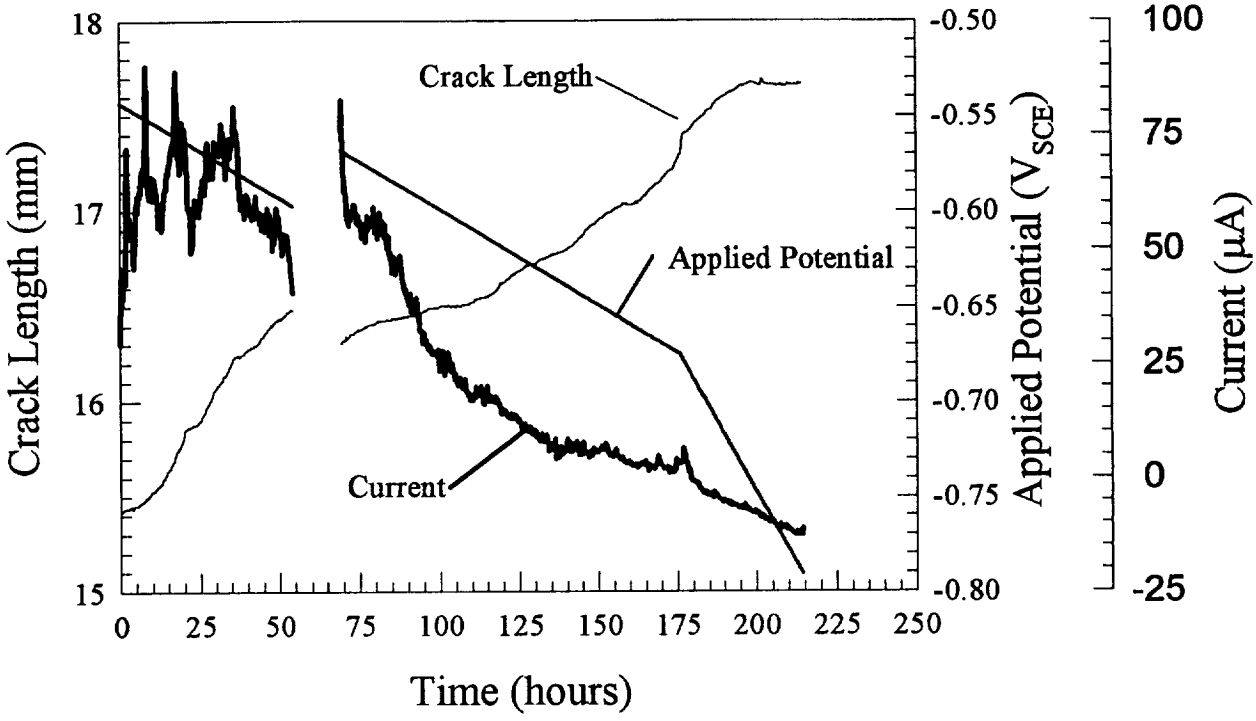

PA 2095 loaded to 18 MPa-$m^{1/2}$ in $NaCl/Na_2CrO_4$

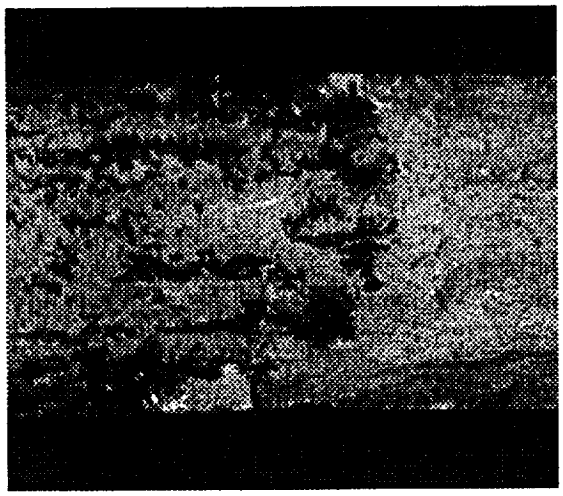

E_{APPL} = -0.547 V_{SCE}

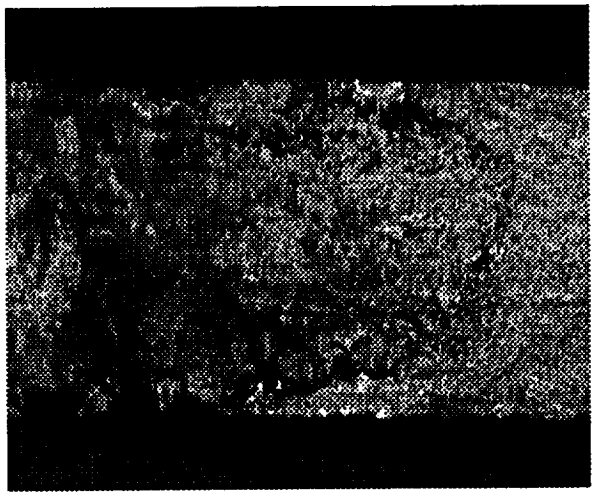

E_{APPL} ramped from -0.547 to -0.790 V_{SCE}

Change in fractography associated with cathodic ramp of applied potential

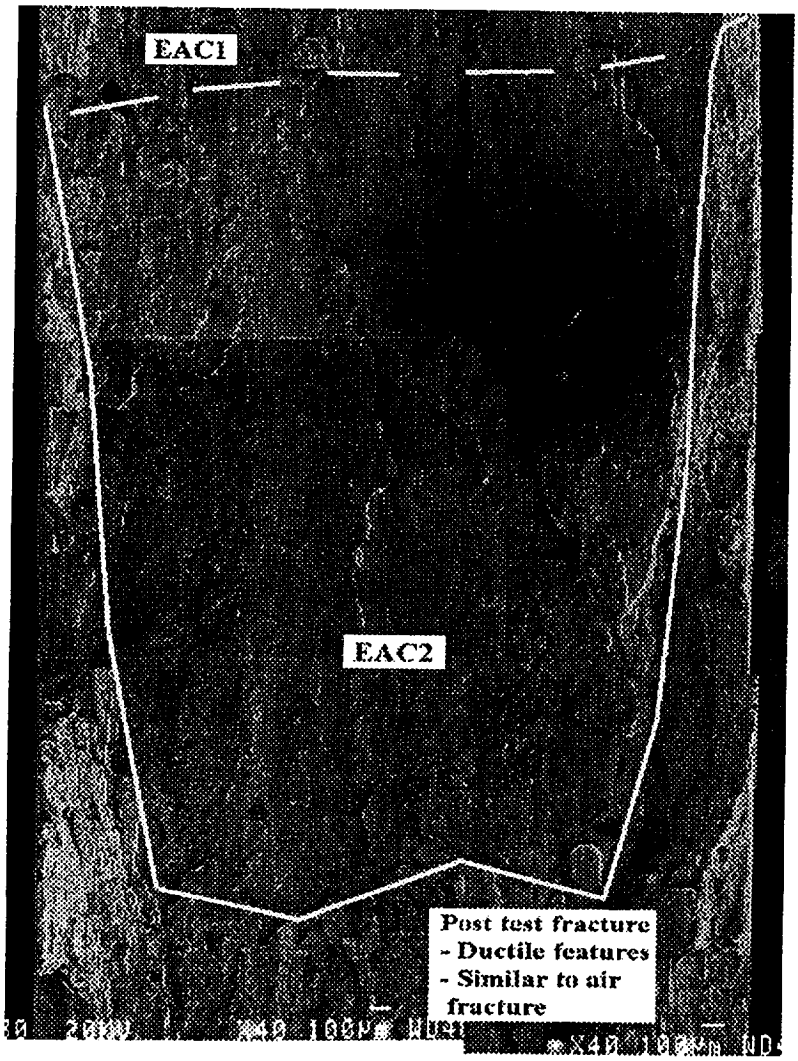

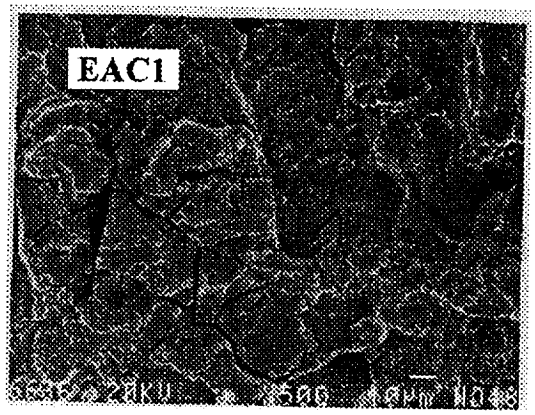

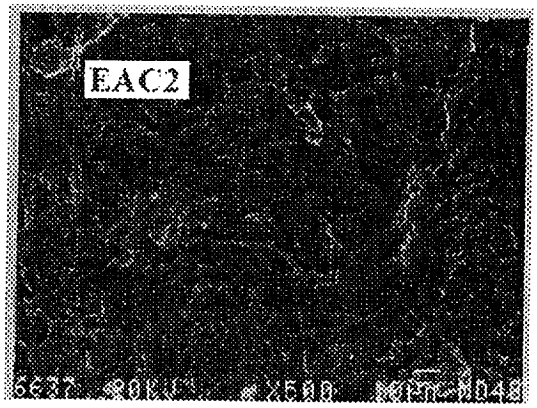

Effect of elevated applied stress intensity on cracking behavior : $2R_P^* > 0.12$ b

Temper : PA 2095 (SHT+CWQ+6%STR+30hrs@143°C)

Sample orientation : SL

Sample geometry : WOL (a_o= 9.11mm; b = 3.175mm; w = 36.58mm)

Bulk environment : 0.1M NaCl + 0.1M Na_2CrO_4 (aerated)

Applied potential : $E_{APPL,AVE}$ = -0.547 V_{SCE}

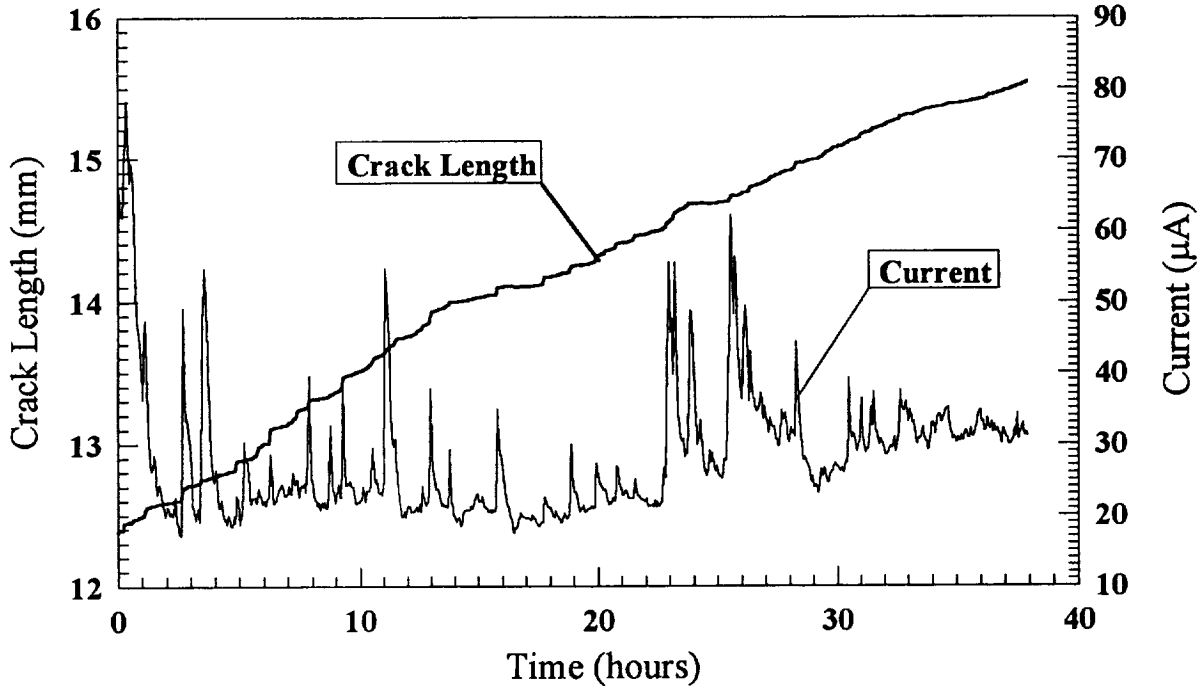

Target stress intensity : **24 MPa-m$^{1/2}$**

Average crack velocity : 2x10^{-5} mm/sec

Crack bursting **not** observed for samples loaded between 4 and 20 MPa-m$^{1/2}$. Bursting events can be accounted for by either **embrittlement** at the crack tip causing local resistance to crack growth to fall below applied mechanical driving force, or by **failure of ligaments** lagging the average crack front.

Effect of reduced stress intensity on environmental cracking

Temper : PA 2095 (SHT+CWQ+6%STR+30hrs@143°C)

Sample orientation : SL

Sample geometry : WOL (a_o= 9.11mm; b = 3.175mm; w = 36.58mm)

Bulk environment : 0.1M NaCl + 0.1M Na_2CrO_4 (aerated)

Applied potential : $E_{APPL,AVE}$ = -0.547 V_{SCE}

Target stress intensity : **4 MPa-m$^{1/2}$**

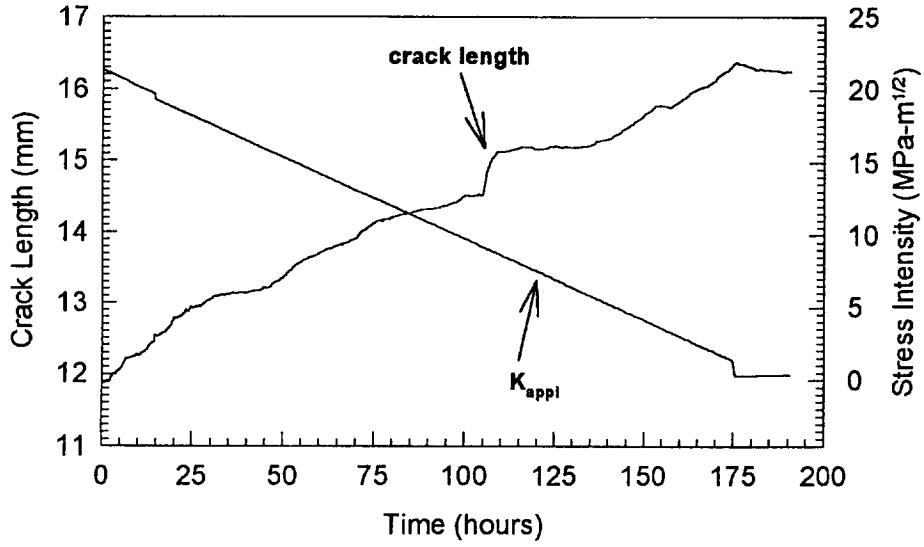

average da/dt
$7x10^{-6}$ mm/sec

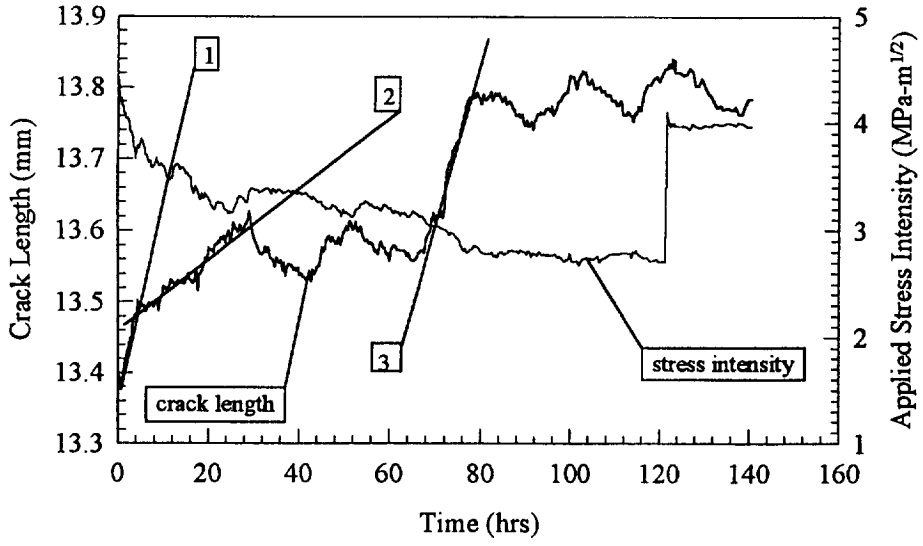

da/dt (mm/sec)
[1] $1x10^{-5}$
[2] $1x10^{-6}$
[3] $5x10^{-6}$

Effect of low K on crack fractography

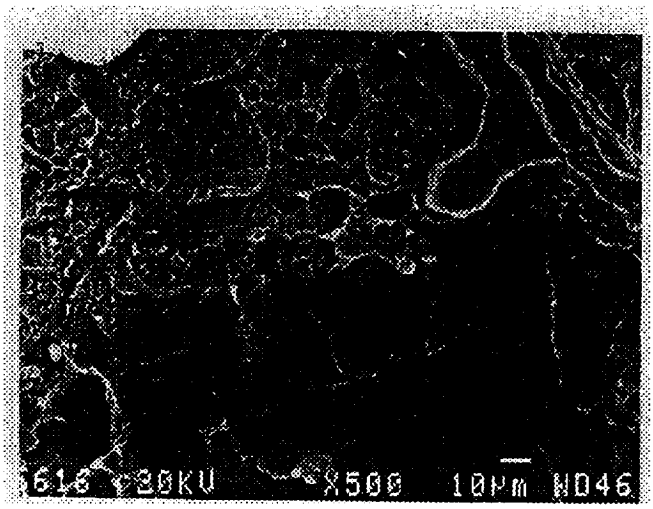

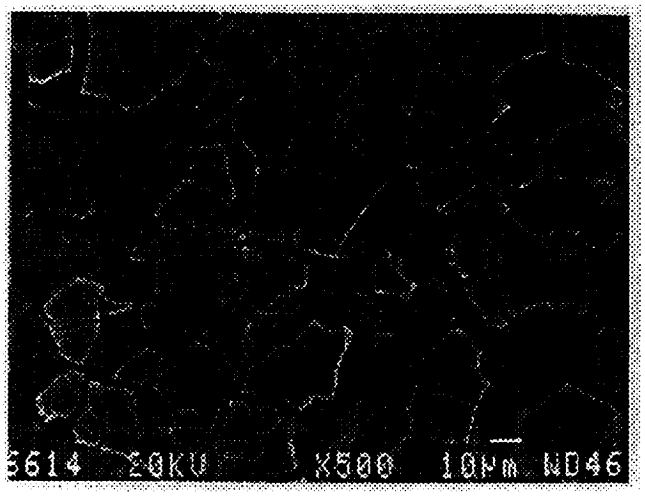

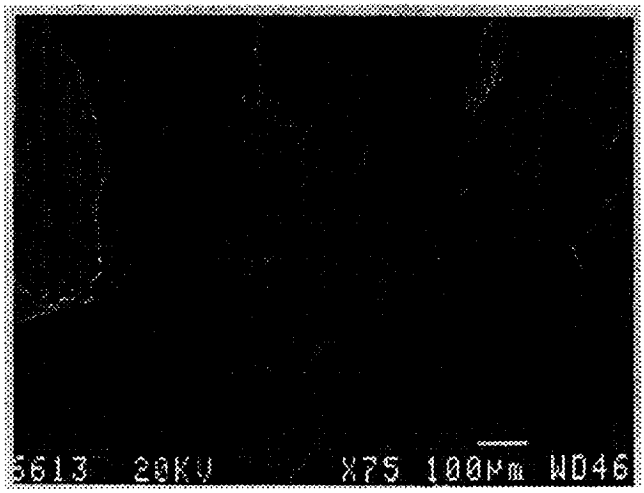

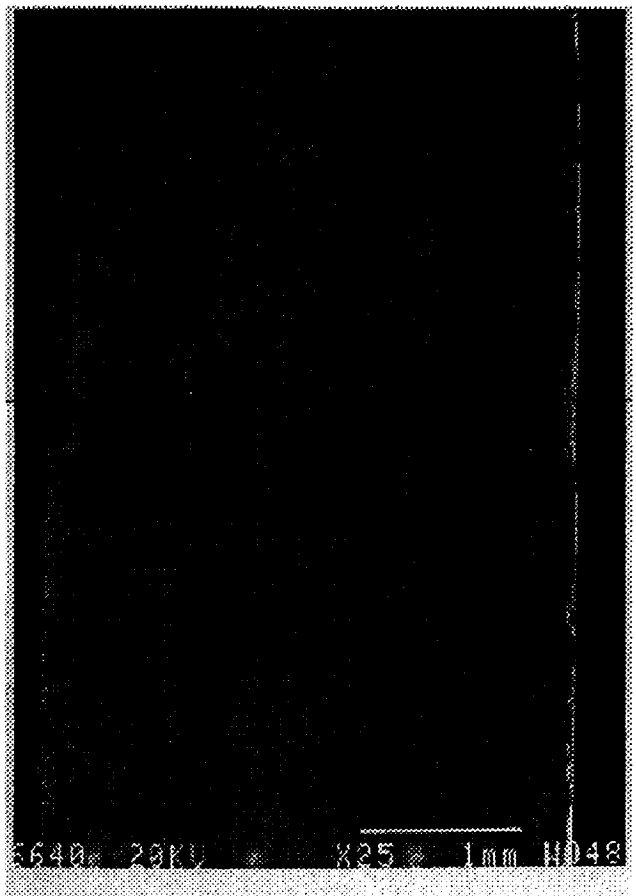

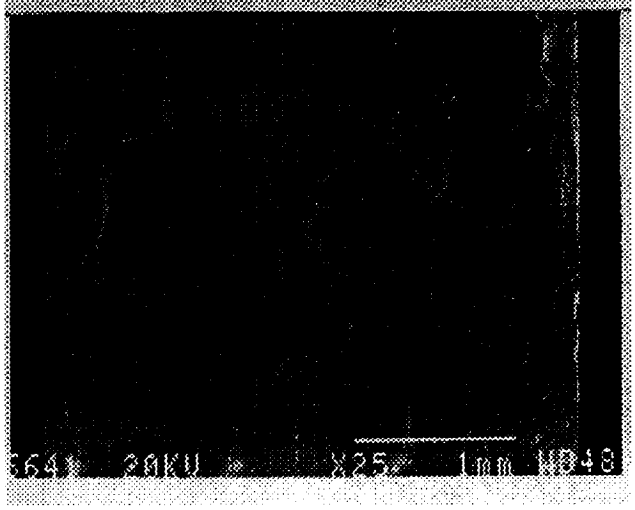

Effect of thermomechanical treatment on environmental cracking propagation rates

Sample orientation : SL

Sample geometry : WOL (a_o= 9.11mm; b = 3.175mm; w = 36.58mm)

Bulk environment : 0.1M NaCl + 0.1M Na_2CrO_4 (aerated)

Applied Potential : $E_{APPL} < E_{CRIT\text{-}EAC}$ (-0.515...-0.547 V_{SCE})

Alloy	Stretch	Aging [t(hrs)@T(°C)]	da/dt (mm/sec)
2095	6%	20 @ 143	$1x10^{-5}$
2095	6.5%	30 @ 143	$1x10^{-5}$
2095	0%	5 @ 143	$5x10^{-4}$
2095	0%	14 @ 143	$8x10^{-4}$
2095	0%	25 @ 143	$3x10^{-4}$
2095	0%	35 @ 143	$7x10^{-4}$
2095	0%	45 @ 143	$3x10^{-4}$
2095	0%	20 @ 160	$2x10^{-5}$
2095	0%	4 @ 160	$5x10^{-4}$
2090	3.5%	14 @ 160	$1x10^{-5}$
2090	0%	3 @ 160	$2x10^{-3}$

Many of the 0%stretch UA alloys exhibited growth rates greater than $1x10^{-3}$ mm/sec for significant periods. The listed numbers indicate the longest sustained continuous growth rates.

Effect of aging time on crack propagation rates

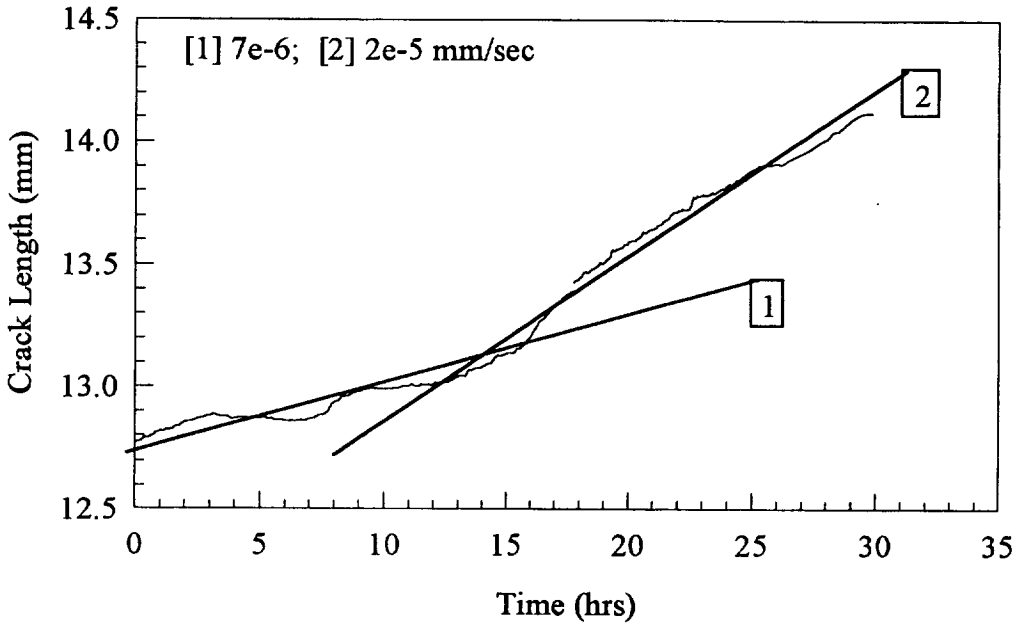

2095 (20 hrs @ 160°C)

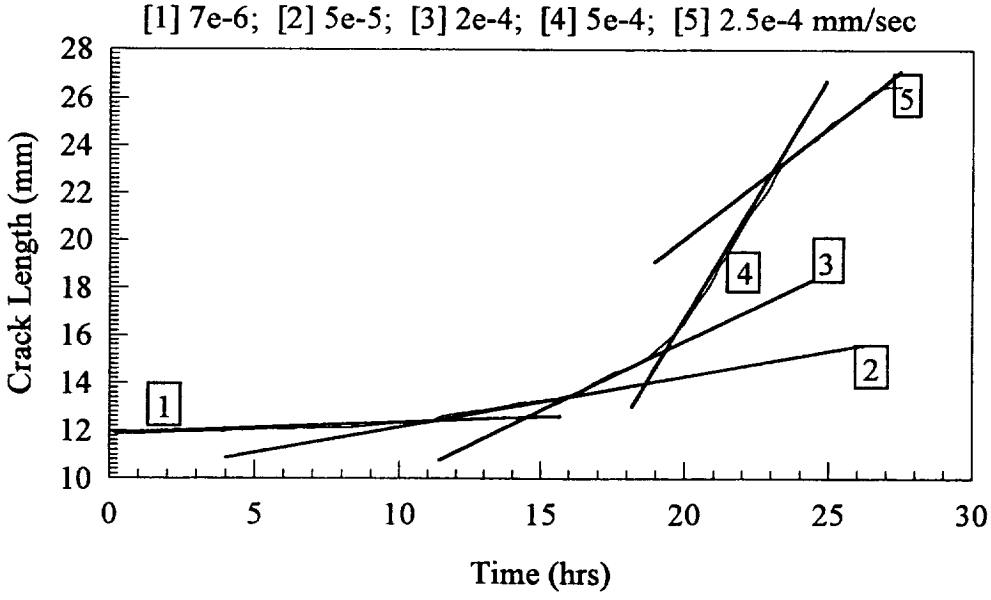

2095 (4 hrs @ 160°C)

Comparison of EC behavior for anodically polarized 2095-D (UA) and 2095-B (PA) in $NaCl/Na_2CrO_4$

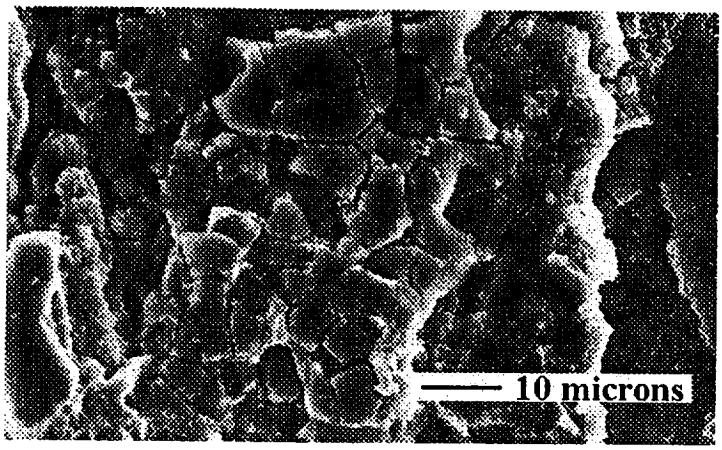

2095-B-PA : Copious corrosion products, heavily attacked fracture surface.

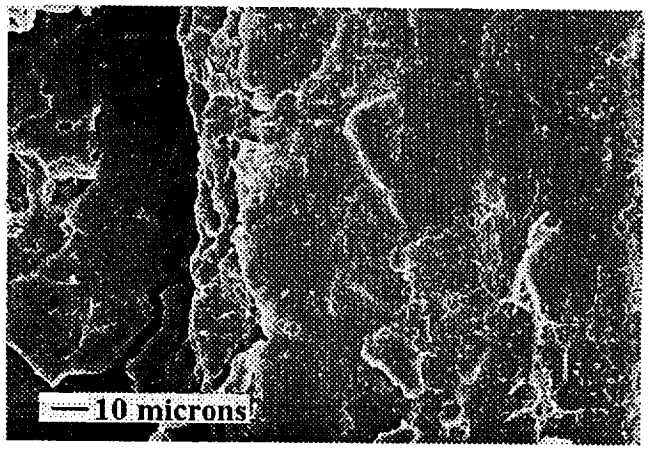

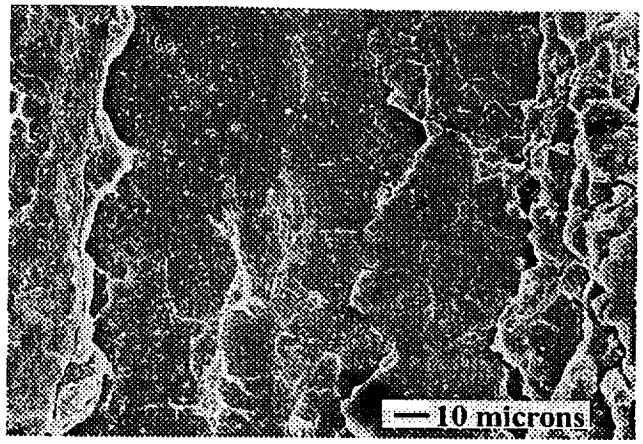

2095-D-UA : Less corrosion evident compared to PA, matching fracture surfaces indicative of brittle failure.

Effect of sample orientation on EC behavior of UA 2095 (SHT+CWQ+0%STR+5 hrs@ 143°C)

Temper UA 2095 (SHT+CWQ+0%STR+5 hrs@143°C)

Sample orientation : SL / LT

Sample geometry : WOL (a_o= 9.11mm; b = 3.175mm; w = 36.58mm)

Bulk environment : 0.1M NaCl + 0.1M Na_2CrO_4 (aerated)

Applied potential : $E_{APPL,AVE}$ = -0.520 V_{SCE}

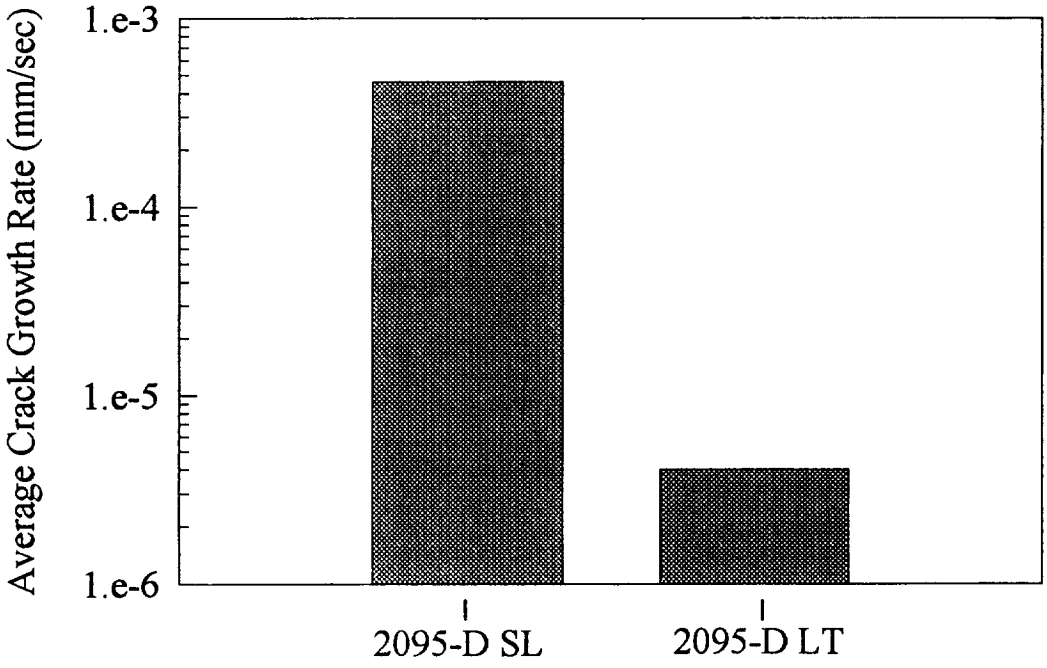

Effect of sample orientation on EC behavior of UA 2095 (SHT+CWQ+0%STR+5 hrs@ 143°C)

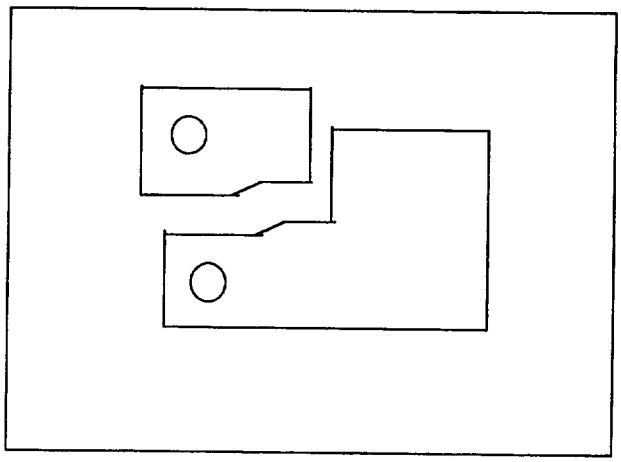

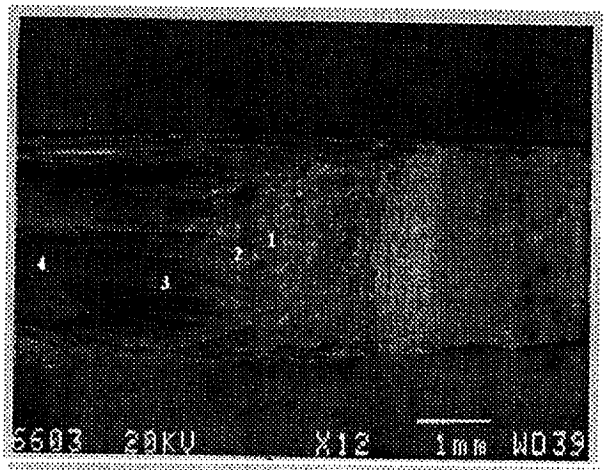

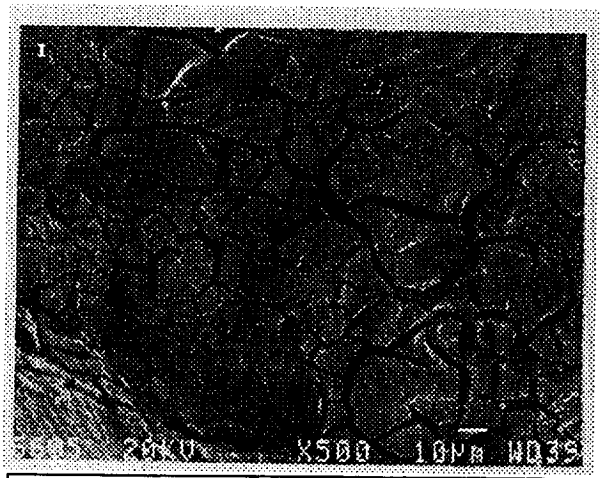

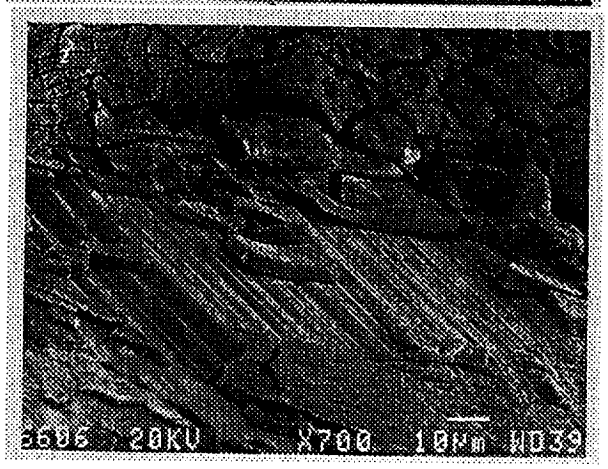

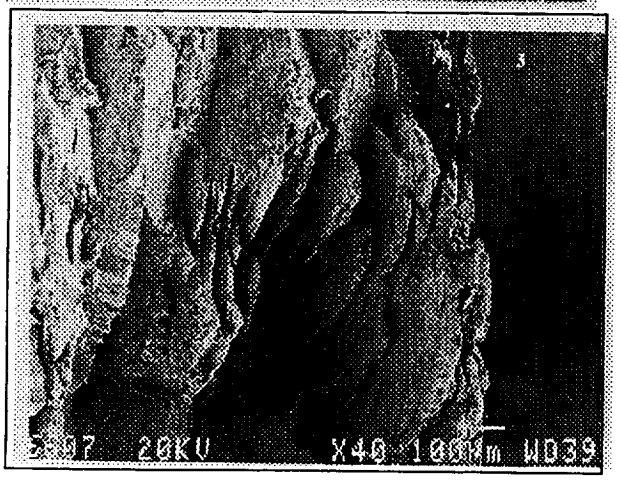

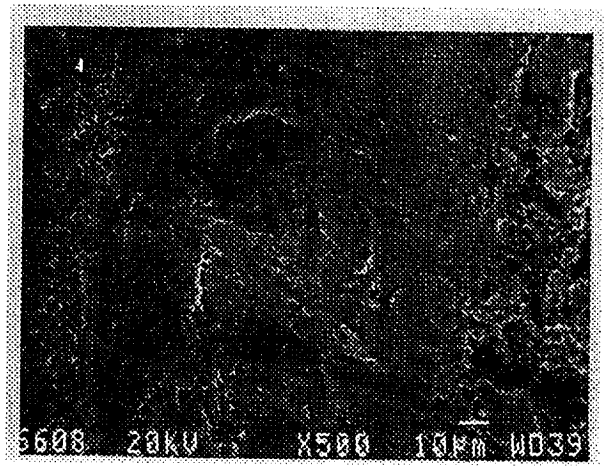

Crack path for PA 2095

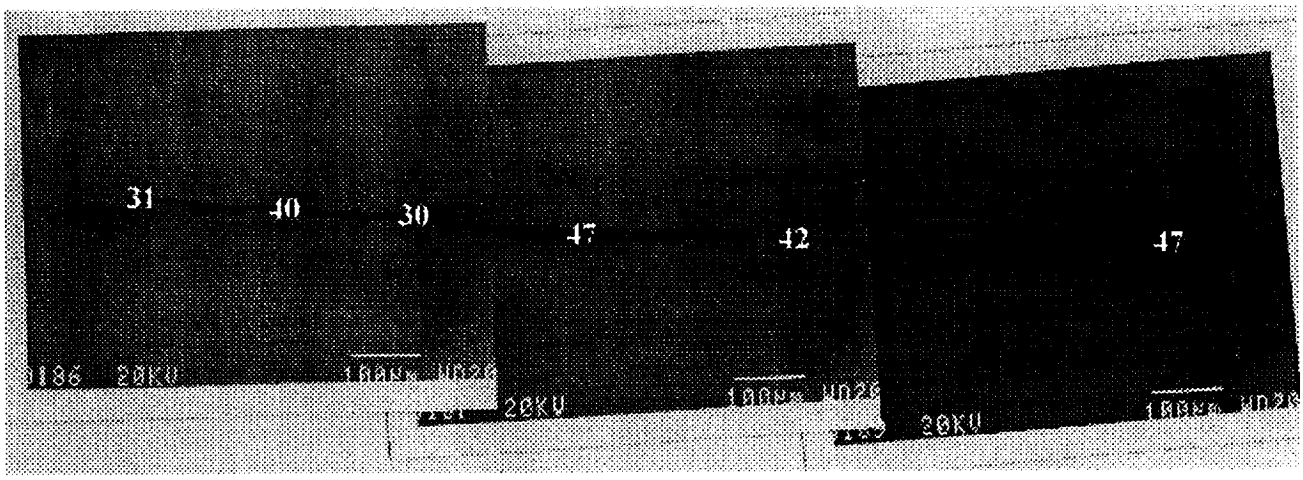

Summary/ Conclusions

AD based cracking along boundaries in Al-Li-Cu alloys

* The T_1 phase and Cu depleted Al may contribute to defining an active pathway.

* The electrochemical behavior of Cu depleted Al appears to define the critical EAC potentials under the conditions investigated.

Occluded solution chemistry analysis

* Models for isolated pits suggest an alkaline environment and passivating specie are necessary for EC initiation under AI conditions in aqueous NaCl.

* Models for deep cracks indicate the development of an acidic pH during crack propagation.

* Techniques for spacially resolving crack tip chemistries are being developed.

Crack propagation studies

* Conditions have been defined under which environmental cracks can be studied in-situ for Al-Li-Cu alloys in constant immersion.

* Cracking has not been observed under constant immersion in NaCl solution without the presence of an inhibiting specie.

* Propagating environmental cracks did not arrest when the externally applied potential was reduced below $E_{CRIT-EAC}$

* Reduction of crack driving forces such as applied potential and stress intensity resulted in a change in crack morphology.

* EC behavior is a strong function of material temper. UA tempers of 2090 and 2095 exhibit accelerated growth rates and flat, matching fracture surfaces with little corrosion product build-up.

* Cracking occurs along high angle grain boundaries for the conditions investigated.

Project #5 **Hydrogen Trapping and its Correlation with the Hydrogen Embrittlement Susceptibility of Al-Li-Cu-Zr Alloys**

Stephen W. Smith and John R. Scully

Research Objectives:

The goal of this project was to develop a fundamental understanding of the effects of internal lattice and trapped hydrogen on the mechanical properties of selected Al-Li-Cu-X alloys. The program focused on unrecrystallized alloy 2090, an Al-Li-Cu-Zr alloy within the specified compositional range of AA2090 which has been recrystallized to varying grain sizes, and complimentary model alloys. We proposed to: (a) distinguish HEAC from aqueous dissolution controlled EAC by using a novel precharging procedure, (b) correlate hydrogen induced EAC with mobile and trapped hydrogen concentrations, (c) identify significant trap sites and hydride phases (if any) through utilization of model alloys and phases. Following identification of relevant hydrogen trap sites, the emphasis during the last 2 quarters has centered on comparing hydrogen concentrations produced from the novel precharging procedure to hydrogen levels produced during conventional aqueous alternate immersion exposure and straining electrode testing. Additionally, the role of dynamic straining in promoting hydrogen uptake and repartitioning was investigated during the last reporting period. This program ended in the spring of 1995

Current Status

This project has been completed and a Ph.D. degree has been awarded to Mr. Steven W. Smith. Dr. Smith has accepted an NRC Post-Doctoral Research Position with R. S. Piascik at the NASA- Langley Research Center.

Project Findings

A novel method was successfully utilized to unambiguously separate the competitive roles of anodic dissolution and absorbed hydrogen in an Al-Li-Cu-Zr alloy (AA 2090) that is susceptible to environmentally assisted cracking. Specifically, a nickel-coating procedure was utilized to cathodically pre-charge alloys with hydrogen without damage due to corrosion. Pre-

charged samples were tested in air, exploiting the strong hydrogen permeation barrier of the native Al oxide film to retain internal hydrogen. Aqueous stress corrosion was thereby completely decoupled from hydrogen embrittlement phenomena. The decoupled effects of internal hydrogen on environmental fracture were evaluated by studying commercial unrecrystallized AA2090 sheet as well as a model recrystallized Al-Li-Cu-Zr alloy with a composition within the specified range of AA 2090. The model recrystallized alloy was fabricated in three different grain sizes and tested in the underaged (UA) and peak aged (PA) tempers. Unrecrystallized AA2090 in the LT and TL orientations was studied in the T3, UA, and PA tempers. The anisotropic nature of the AA2090 microstructure and the range of recrystallized grain sizes relative to expected plastic zone dimensions were exploited in an attempt to examine hydrogen embrittlement, if operative, on either (a) sub-grain boundaries, (b) transgranular slip planes, or (c) high angle grain boundaries. Continuous extension rate testing (CERT) of smooth tensile specimens and J-integral resistance curve testing of pre-cracked specimens at slow actuator displacement rates were employed to assess the effects of internally dissolved and trapped hydrogen on ductility and fracture initiation toughness.

Hydrogen operated in two primary ways to induce embrittlement under the limited conditions investigated. Hydrogen promoted high angle grain boundary crack initiation when such boundaries presented a favorably oriented hydrogen assisted cracking path and stress concentration was sufficient. This occurred in J-integral fracture toughness testing of the fine grain recrystallized material (UA and PA) and to a lessor extent in commercial AA2090 in the TL orientation (UA and PA). Hydrogen also promoted the localization of shear deformation into less numerous, narrower bands. This was observed in CERT test results on unrecrystallized AA 2090 particularly in the T3 and UA tempers. A decrease in K_i for unrecrystallized AA 2090 was also observed for material in the T3 condition that was linked to the presence of finer, more numerous microvoids on transgranular fracture initiation surfaces. In no cases was intersubgranular cracking observed even though this cracking path would have been favorable in both the LT and TL orientations of unrecrystallized AA2090.

Embrittlement trends were correlated with hydrogen-metal defect interactions using thermal desorption spectroscopy (TDS). Trapping analysis was conducted after performing the same hydrogen charging procedure as utilized for CERT and fracture toughness testing. Six

metallurgical trapping states have been identified. Lower binding energy hydrogen trap sites included solid solution lithium and δ′. Higher energy states were correlated with dislocations, T_1, T_2 or T_B particles, and high angle boundaries. Trapping at subgrain boundaries was not observed when comparing unrecrystallized to recrystallized materials.

The tendency for high angle grain boundaries (containing T_1 , T_2 and/or T_B particles) to provide a favorable hydrogen assisted cracking path correlated with the observation that high angle boundaries and T particle are strong hydrogen trap sites. Hydrogen trapping at dislocations is consistent with the notion of hydrogen enhanced slip localization. This effect is due to trapped hydrogen as a dislocation atmosphere lowering the interaction energy between dislocations; thereby lowering the shear stress required to sweep dislocations through a lattice containing other dislocations. However, modelling to date on dislocation interaction energies has only dealt with a limited number of dislocations. It is unclear whether such results would apply to a more complicated situation involving heavily deformed structures containing planar slip bands as well as shear deformation bands across multiple high angle boundaries in Al-Li-Cu alloys. The fact that subgrain boundaries were not an observed cracking path can be rationalized in the context of a low energy dislocation structure which does not trap hydrogen. However, the presence of hydrogen trapping T_1 particles on such boundaries would seem to make them an eligible cracking path. It could be argued that the decohesion forces required are significantly higher at subgrain boundaries compared to high angle boundaries.

TDS analysis has also produced direct evidence of significant hydrogen absorption during aqueous alternate immersion exposure testing and either enhanced uptake or transport of hydrogen via dislocations during straining electrode testing in aqueous full immersion or moist air. Enhanced hydrogen absorption occurs during conventional stress corrosion cracking testing of Al-Li-Cu-Zr alloys compared to the nickel coated precharging procedure. Moreover, hydrogen transport via dislocations was implicated as the cause of the internal redistribution of hydrogen from sites of lower binding energy to sites of higher binding energy.

Future Plans

A follow-on project emphasizing localized corrosion, and the transition to stress corrosion cracking initiation and SCC propagation will investigate two advanced aerospace Al-Li-Cu

alloys. The alloys of interest are AA 2096 and C155 which have nearly identical Cu/Li ratios. One alloy contains Ag as a precipitation promotor while the other contains Mn. These compositions present an interesting scientific opportunity in terms of linking composition and microstructure to localized corrosion, SCC and hydrogen trapping. (See additional information below for objective, approach and expected payoffs).

List of Presentation Overheads

1. Title.

2. Proposed EAC mechanisms for Al-Li-Cu-Zr alloys existing in the literature.

3. Project objectives.

4. Procedures utilized for introducing pre-dissolved hydrogen in Al-Li-Cu-Zr Alloys.

5. Absorbed hydrogen concentrations measured for AA2090 after several testing conditions. SET= straining electrode test, AI = alternate immersion.

6. Mechanical properties data for the unrecrystallized AA2090 and the three variants of the recrystallized Al-Li-Cu-Zr alloy used for mechanical testing.

7. Continuous extension rate test results for smooth AA2090 specimen tested with absorbed hydrogen. All testing was performed at a strain rate of 2.5×10^{-6} sec^{-1}.

8. J-integral results indicating the stress intensity at initiation for fatigue precracked AA2090 tested with absorbed hydrogen using the nickel coated charging procedure.

9. J-integral results indicating the stress intensity at initiation for fatigue precracked recrystallized Al-Li-Cu-Zr tested with absorbed hydrogen using the nickel coated charging procedure.

10. Summary of findings from mechanical testing of Al-Li-Cu-Zr alloys.

11. Relevant questions to be investigated developed from mechanical testing .

12. Deconvolution of hydrogen desorption rate data from AA2090-UA and the identification of major trapping states. (precharged using the nickel coated charging procedure).

13. Hydrogen desorption rate vs. time data for an Al-3% Li binary alloy tested in the solution heat treated (SHT), SHT + 5 hrs. @ 160°C, and SHT + 25 hrs. @ 160°C tempers.

14. Hydrogen partitioning data for AA2090 and the Al-3% Li binary as a function of aging condition. This plot shows that a lower fraction of the total internal hydrogen concentration is trapped at Li in solid solution (peaks 1 and 2) with aging in accordance with the expectation that Li is depleted from solid solution with aging. Conversely, the fraction of hydrogen partitioned at T particles (peaks 5 and 6) and high angle boundaries is increased with aging.

15. Hydrogen desorption spectra and hydrogen partitioning data for AA2090-UA. Data identified as being prestrained 3% represents specimens that were strained at a constant cross head displacement of 2×10^{-6} sec^{-1} to a total strain of 3% before being charged. An enhancement of hydrogen trapped at dislocations results.

16. Hydrogen desorption spectra and hydrogen partitioning data for a fine and large grained recrystallized Al-Li-Cu-Zr alloy. A lower fraction of hydrogen is observed on high angle boundary and T sites (peaks 5 and 6) in accordance with a lower density of grain boundary sites in the coarse grained material.

17. Summary of the trap site identification methodologies.

18. Hydrogen desorption spectra and hydrogen partitioning data for AA2090. Data identified as being strained to 3% represents a specimen that was cathodically charged then strained at a constant cross head displacement rate of 2×10^{-6} sec^{-1} to a total strain of 3 %. A fixed internal amount of hydrogen exists and some of it is shown to repartition from δ' sites (peak 3) to dislocations (peak 4).

19. Hydrogen desorption spectra for AA2090 specimens cathodically charged under a straining electrode test. The specimens were preloaded to 75% σ_{ys} and strained at a constant cross head displacement rate of 2×10^{-6} sec^{-1} while being polarized at -2 V_{SCE} in a pH 1 HCl solution. An increase in the amount of hydrogen at dislocation traps is observed indicative of enhance hydrogen absorption during dynamic straining as well as dynamic trap site formation during straining.

20. Hydrogen desorption "difference" spectra for AA2090 specimens following fracture toughness testing. The desorption rate data from a sample cut far from the plastic zone was subtracted from the spectra of a specimen containing the fracture process zone. The results indicated that dynamic strain enhances hydrogen absorption and trapping at dislocations even in moist lab air.

21. Summary of plausible hydrogen transport processes.

22. Conclusions.

23. Conclusions (cont.)

24. Summary of Conclusions.

HYDROGEN INTERACTIONS AND THEIR CORRELATION TO THE HYDROGEN EMBRITTLEMENT SUSCEPTIBILITY OF Al-Li-Cu-Zr ALLOYS

Stephen W. Smith

and

John R. Scully

University of Virginia

Department of Materials Science and Engineering

Center for Electrochemical Sciences and Engineering

Charlottesville, VA 22903

Sponsors:

NASA Langley Research Center

Virginia Center for Innovative Technology

Alcoa Technical Center

Proposed EAC Mechanisms for Al-Li-Cu-Zr Alloys

- Aqueous dissolution
  - Preferential T_1 dissolution at boundaries [Buis 92, Buchheit 90, Colvin 86, Bavarian 89]
    - T_1 has been shown to be electrochemically active with respect to the matrix.
    - T_1 does not provide a continuous active path for dissolution.
    - T_1 does not precipitate exclusively at high angle grain boundaries.
    - T_1 is just as prevalent, if not more so, along subgrains and dislocations.

- Hydrogen Embrittlement
  - Pre-dissolved hydrogen has been shown to affect IG cracking [Shin 89, Shin 90]
  - Pre-dissolved hydrogen has been shown to affect TGS [Meletis 89]

    Hydrogen effects have not been adequately decoupled from AD.
    Evidence for hydrogen interactions are circumstantial.

  - A hydride phase ($AlLiH_4$) has been observed during concurrent straining and cathodic charging [Balasubramaniam 91, 91a].
    The microstructure used to promote the hydride formation is not characteristic of a commercial microstructure.

Objectives

- **Distinguish hydrogen induced EAC from aqueous dissolution controlled EAC**
  - **Mechanical Testing of pre-charged specimens**
    Continuous Extension Rate Testing (CERT)
    J-Integral R-Curve Testing

- **Identify significant hydrogen trap sites and hydride phases (if any), present in selected Al-Li-Cu-Zr alloys**
  - **Characterized hydrogen partitioning as a function of microstructural features and aging condition**
    Thermal Desorption Spectroscopy (TDS)

- **Correlate internal hydrogen embrittlement (IHE) with mobile and trapped hydrogen concentrations and operative trap sites**

Procedures Utilized for Introducing Pre-dissolved Hydrogen in Al-Li-Cu-Zr Alloys

1.Cathodic polarization of Ni-coated alloys

Sputter etch native Al_2O_3 under high vacuum → deposit 400Å nickel coating → cathodic polarization in buffered solution for 28 days → mechanical testing / TDS

2.Straining electrode test (SET)

Straining of flat tensile electrode at eng. strain rate of $2x10^{-6}$ sec^{-1} in a pH 1 HCl solution at $-2V_{SCE}$, for approx. 4 hrs. to a total strain of 3% → TDS (after J. Albrecht, I.M. Bernstein, A.W. Thompson, Met. Trans. 13A, 1982)

3.Alternate immersion (AI) aqueous exposure

AI in 3.5 wt.% NaCl/moist air, at 70% yield strength (UA) or 80% yield strength (PA) for 84 days → TDS / metallographic observation

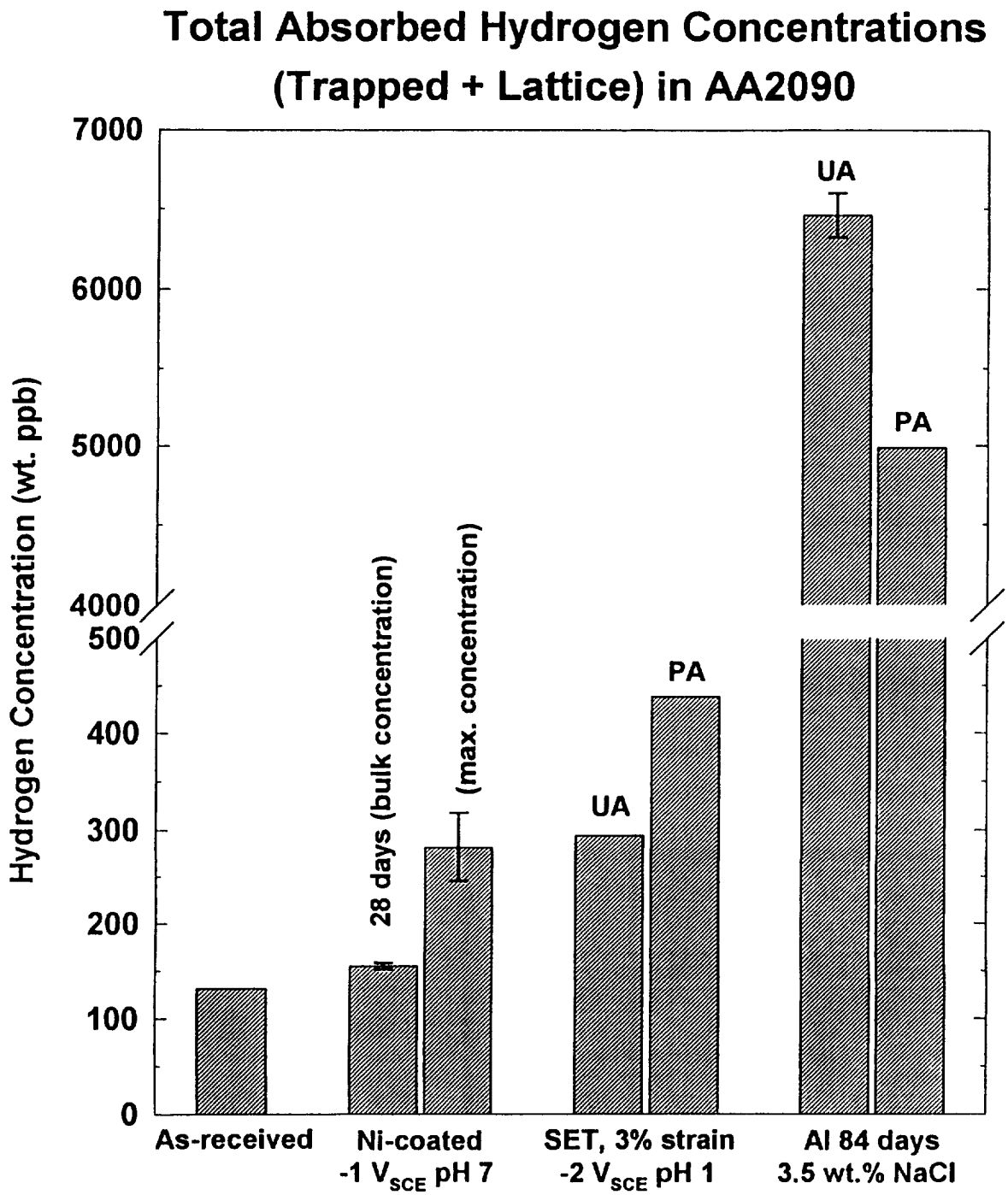
Total Absorbed Hydrogen Concentrations
(Trapped + Lattice) in AA2090
Hydrogen Concentration (wt. ppb)
7000
6000
5000
4000
500
400
300
200
100
0
28 days (bulk concentration)
(max. concentration)
UA
PA
UA
PA
As-received
Ni-coated
-1 V_SCE pH 7
SET, 3% strain
-2 V_SCE pH 1
Al 84 days
3.5 wt.% NaCl

Materials

Commercial AA2090 - unrecrystallized:

Al - 2.15Li - 2.56Cu - 0.12Zr, wt.%
4400 μm x 600 μm x 10 μm grain size, 5-10 μm subgrains

T3: solutionized and cold worked	σ_{ys} = 255 MPa;	σ_{UTS} = 303 MPa
Underaged (UA): T3 + 5 hrs. @ 160°C	σ_{ys} = 296 MPa;	σ_{UTS} = 476 MPa
Peak aged (PA): T3 + 25 hrs. @ 160°C	σ_{ys} = 434 MPa;	σ_{UTS} = 572 MPa

Recrystallized Al-Li-Cu-Zr:

Al - 2.05Li - 2.27Cu - 0.09Zr, wt.%

30 μm equiaxed grains (FGR)		
Underaged (UA): T3 + 5 hrs. @ 160°C	σ_{ys} = 303 MPa;	σ_{UTS} = 421 MPa
Peak aged (PA): T3 + 25 hrs. @ 160°C	σ_{ys} = 400 MPa;	σ_{UTS} = 496 MPa
800 x 800 x 100 μm (MGR)		
Underaged (UA): T3 + 5 hrs. @ 160°C	σ_{ys} = 241 MPa;	σ_{UTS} = 379 MPa
Peak aged (PA): T3 + 25 hrs. @ 160°C	σ_{ys} = 400 MPa;	σ_{UTS} = 490 MPa
1200 x 1100 x 250 μm (LGR)		
Underaged (UA): T3 + 5 hrs. @ 160°C	σ_{ys} = 296 MPa;	σ_{UTS} = 393 MPa
Peak aged (PA): T3 + 25 hrs. @ 160°C	σ_{ys} = 379 MPa;	σ_{UTS} = 434 MPa

tensile properties for L oriented flat tensile specimens tested in lab air

CERT RESULTS
Unrecrystallized AA2090

Temper	Orientation	Charging Condition	Reduction in Area (% loss)	Fracture Mode
T3	T	Uncharged	27.98#	transgranular shear
		28 days @ $-1V_{SCE}$	17.49#	TGS + intersubgranular
T3	L	Uncharged	19.97#	transgranular shear
		28 days @$-1V_{SCE}$	9.63#	hydrogen affected TGS
UA	T	Uncharged	20.68*	transgranular shear
		28 days @$-1V_{SCE}$	13.85*	TGS + intersubgranular
UA	L	Uncharged	13.35*	transgranular shear
		28 days @$-1V_{SCE}$	11.94*	hydrogen affected TGS
PA	T	Uncharged	32.27#	transgranular shear
		28 days @$-1V_{SCE}$	38.40#	transgranular shear
PA	L	Uncharged	16.30#	transgranular shear
		28 days @$-1V_{SCE}$	14.85#	transgranular shear

All specimens charged in 0.25 M Na_2SO_4 buffered to pH 7.

- average of 3 specimens
* - single specimen tested

Effect of Hydrogen Pre-charging on the Mechanical Behavior of Unrecrystallized AA2090

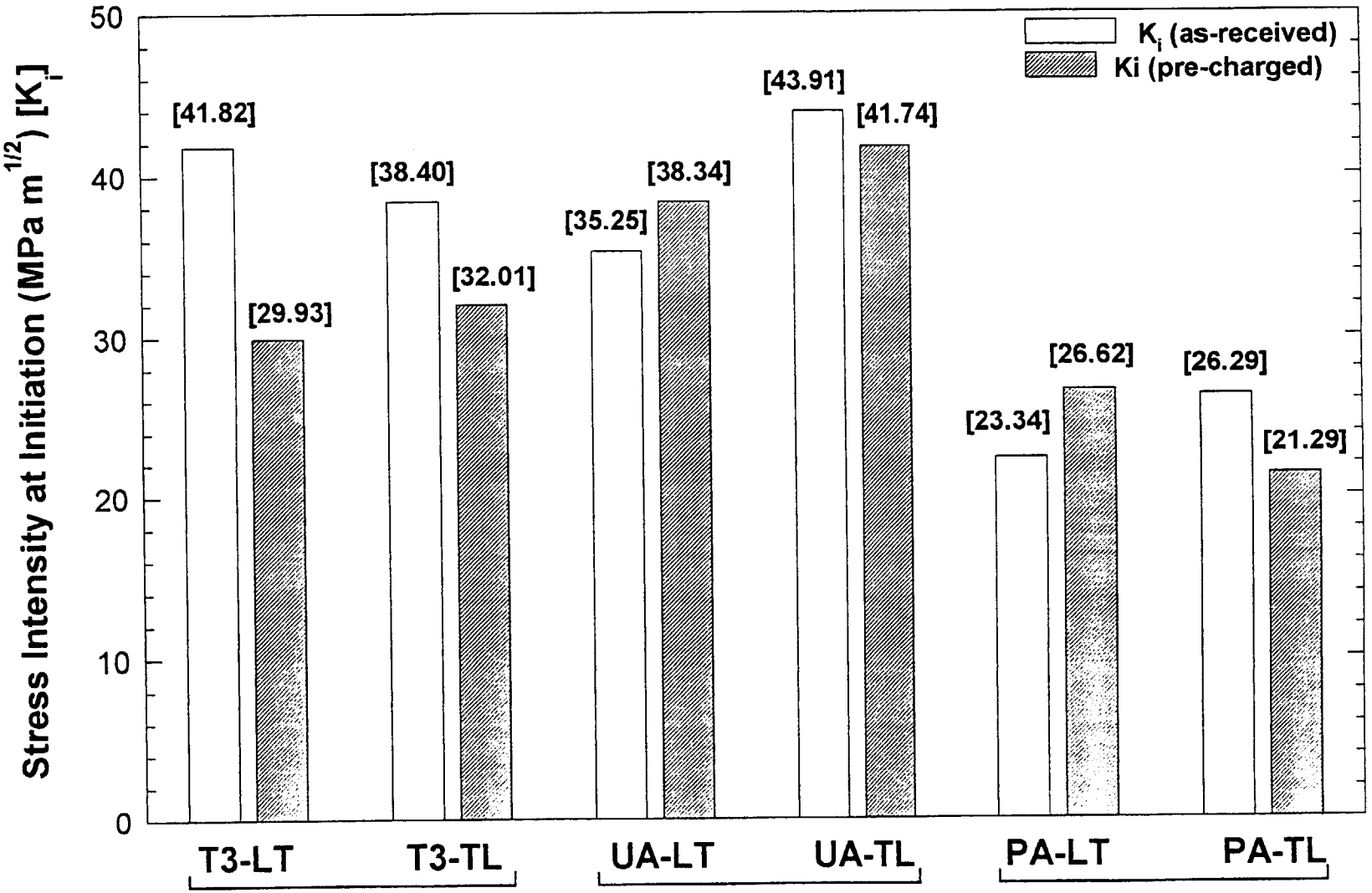

All specimens pre-charged at -1V_{SCE} in pH 7 solution for 28 days

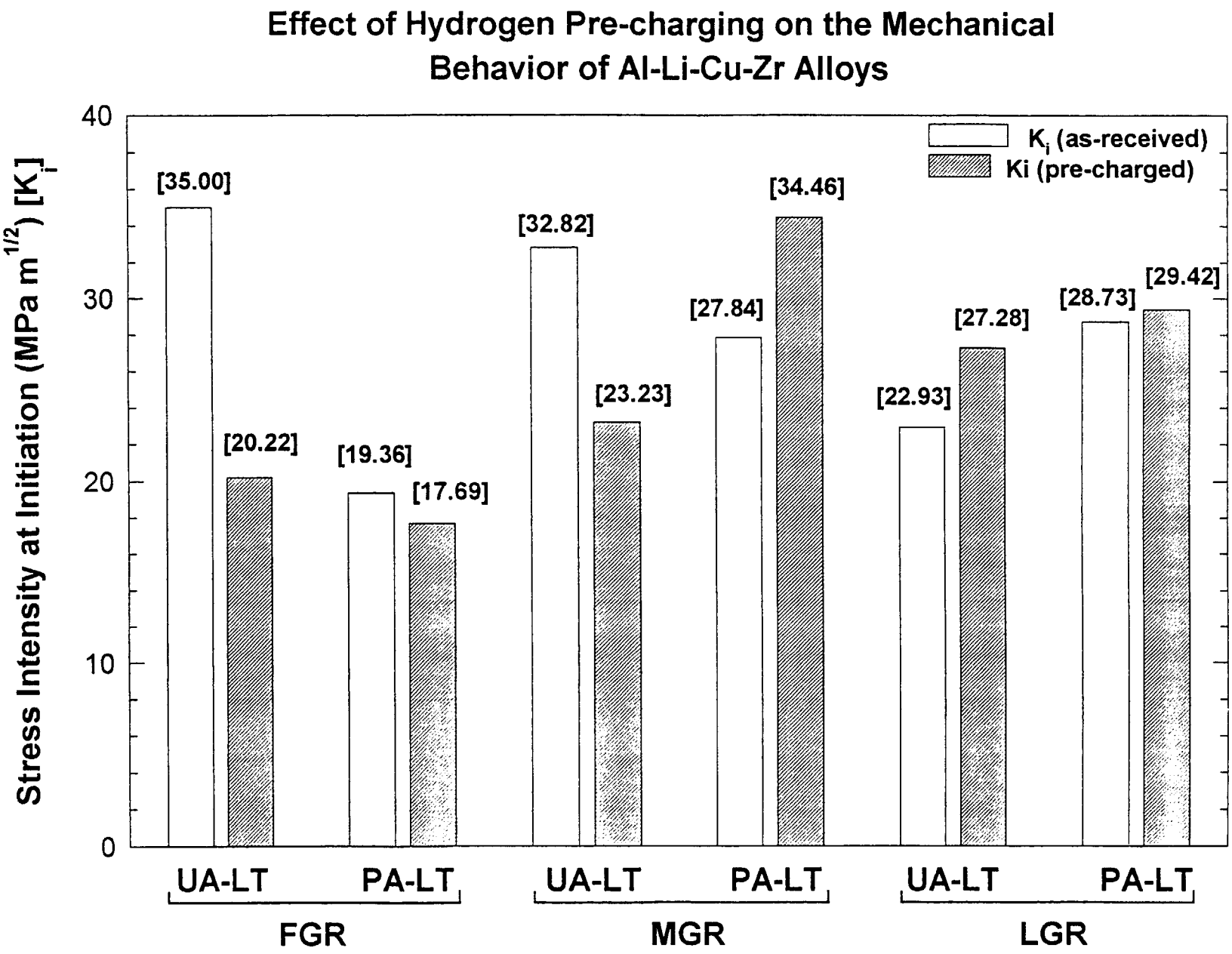
Effect of Hydrogen Pre-charging on the Mechanical Behavior of Al-Li-Cu-Zr Alloys
Stress Intensity at Initiation (MPa m^1/2) [K_i]
40
30
20
10
0
K_i (as-received)
Ki (pre-charged)
[35.00]
[20.22]
[19.36]
[17.69]
[32.82]
[23.23]
[27.84]
[34.46]
[22.93]
[27.28]
[28.73]
[29.42]
UA-LT
PA-LT
UA-LT
PA-LT
UA-LT
PA-LT
FGR
MGR
LGR
All specimens pre-charged at -1V_SCE in pH 7 solution for 28 days

Summary: Mechanical Testing

- Elevated levels of pre-dissolved hydrogen have been shown to result in the HE of Al-Li-Cu-Zr alloys in the T3, UA, and PA tempers. This HE has been observed by fracture toughness and CERT testing of pre-charged samples for a limited combination of strain rate and pre-dissolved hydrogen level.

- Pre-dissolved hydrogen alters transgranular shear in Al-Li-Cu-Zr alloys. This effect is most obvious in the T3 temper for CERT and fracture toughness testing. Absorbed hydrogen has been shown to enhance slip localization.

- Pre-dissolved hydrogen enhances intergranular cracking in Al-Li-Cu-Zr when high angle grain boundaries are oriented favorably with respect to the tensile stress and a sufficiently high tensile stress is developed.

- The favorable orientation of subgrain boundaries does not result in a significant fraction of intersubgranular cracking under the combinations of strain rate and hydrogen concentrations investigated.

Questions Developed From Mechanical Testing

- How many trapping states exist in AA2090 and what microstructural features are they associated with?
- How does aging affect trapping and can this explain IHE behavior?
- Is hydrogen absorption during AI/SCC or concurrent polarization/straining dominated by dislocation transport or mechanical destabilization of passive films coupled with locally high hydrogen fugacities?
- Can a fixed concentration of internal hydrogen repartition during straining?

Trap Site Identification
AA2090 - UA, 10°C/min

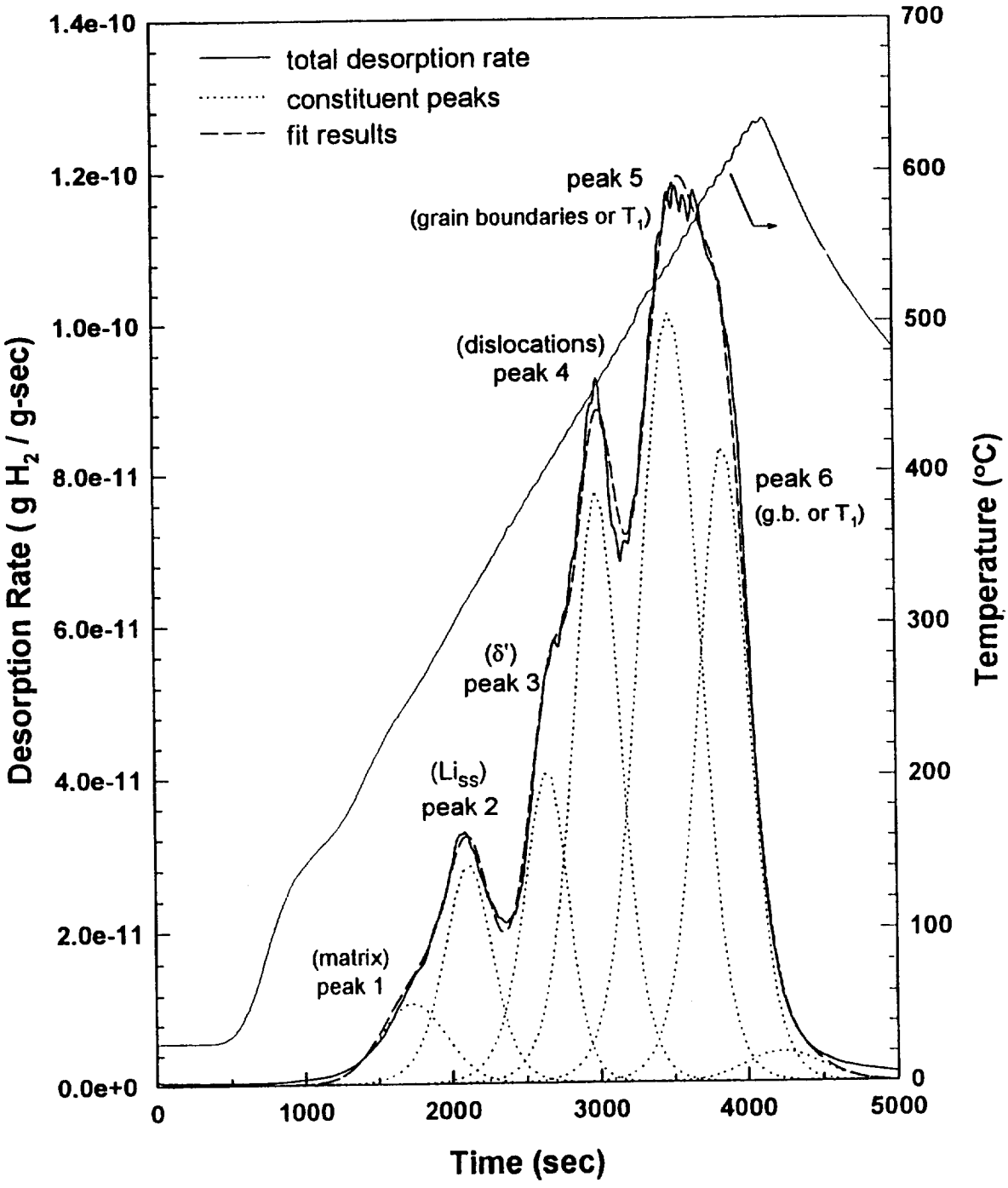

Desorption Spectra
Al - 3 wt. % Li, 10°C/min

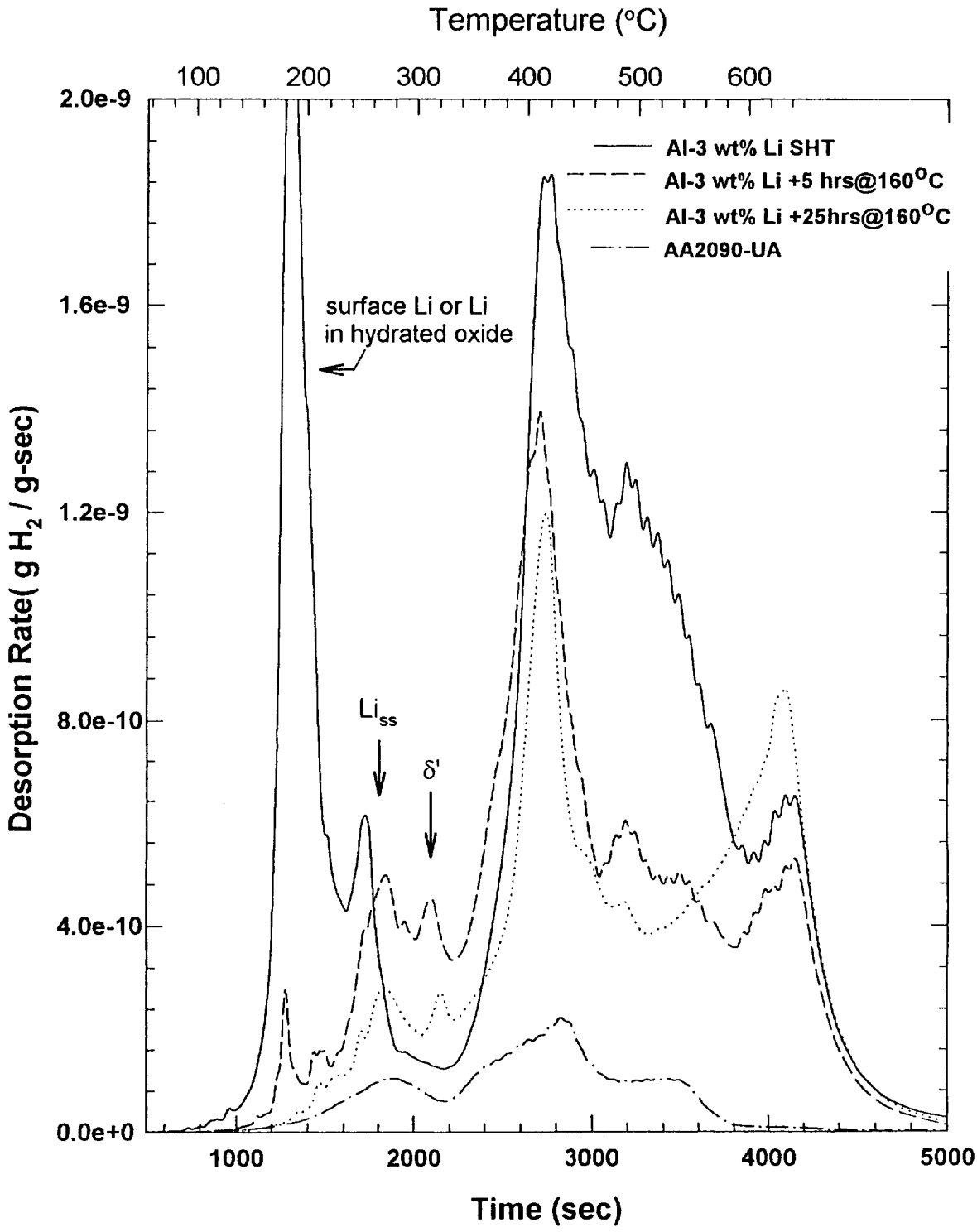

Hydrogen Partitioning for AA2090 and Al- 3 wt. % Li

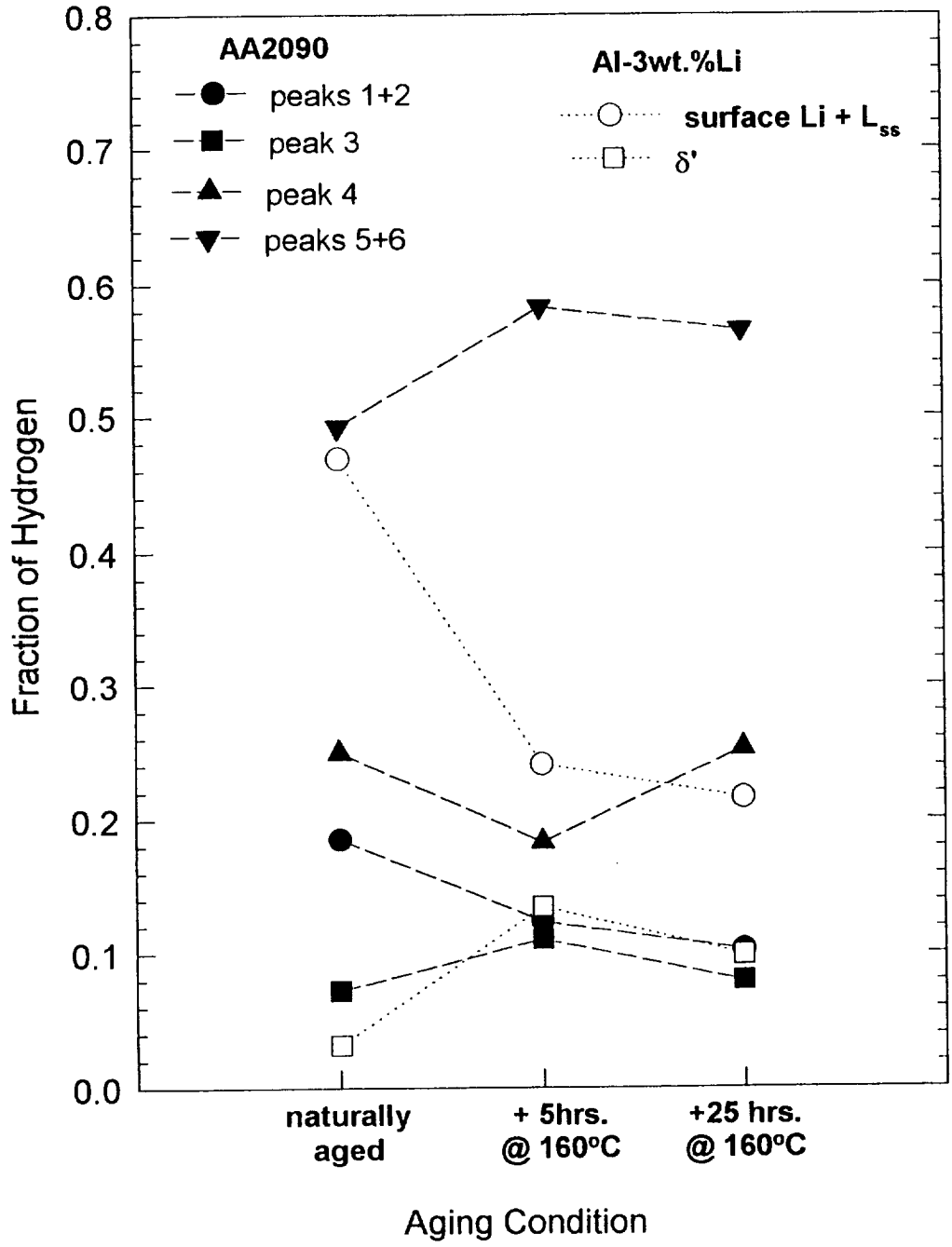

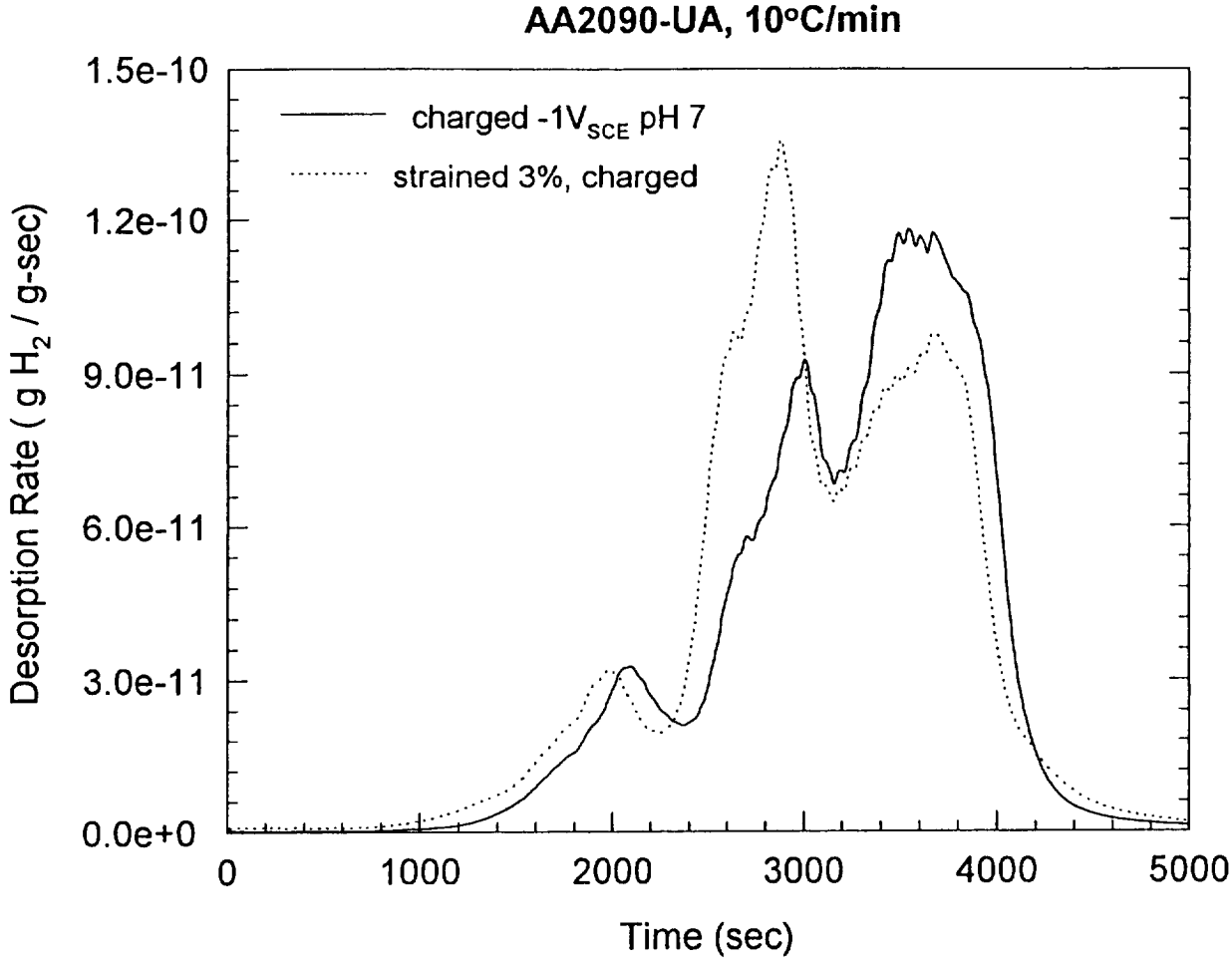
AA2090-UA, 10°C/min
charged -1V$_{SCE}$ pH 7
strained 3%, charged
Desorption Rate (g H$_2$ / g-sec)
1.5e-10
1.2e-10
9.0e-11
6.0e-11
3.0e-11
0.0e+0
0
1000
2000
3000
4000
5000
Time (sec)

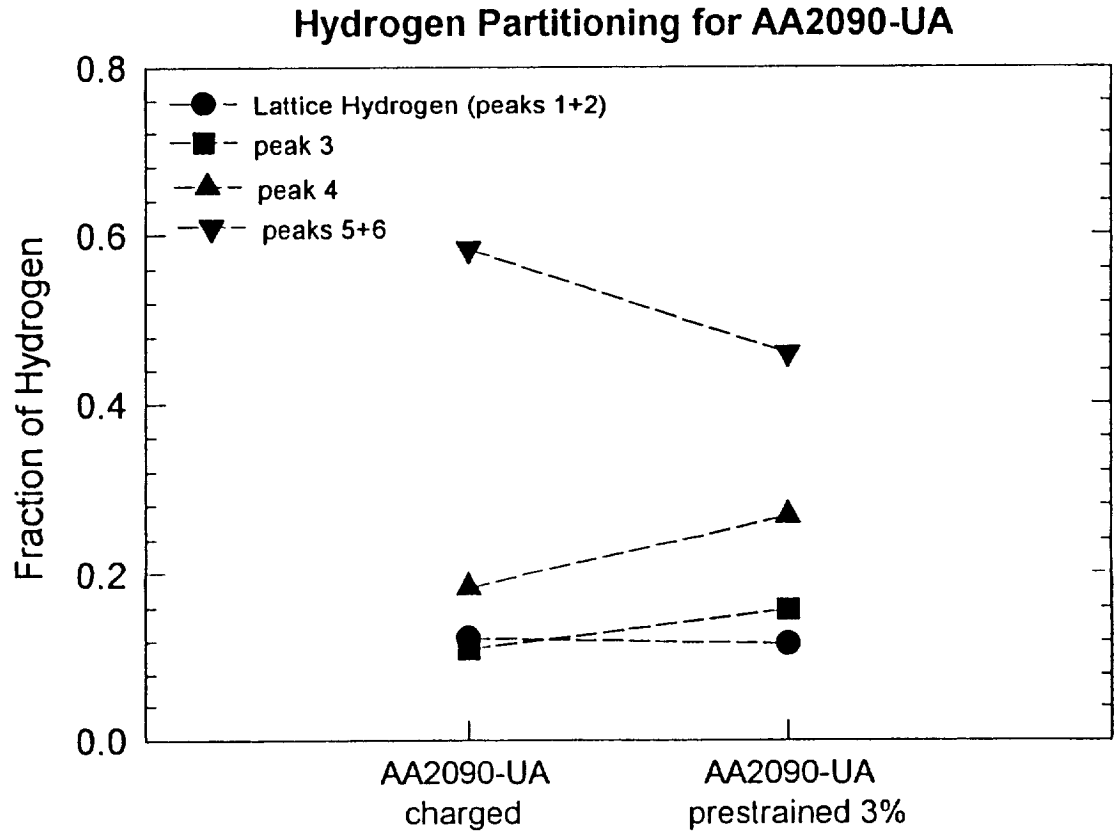
Hydrogen Partitioning for AA2090-UA
Lattice Hydrogen (peaks 1+2)
peak 3
peak 4
peaks 5+6
Fraction of Hydrogen
0.8
0.6
0.4
0.2
0.0
AA2090-UA
charged
AA2090-UA
prestrained 3%

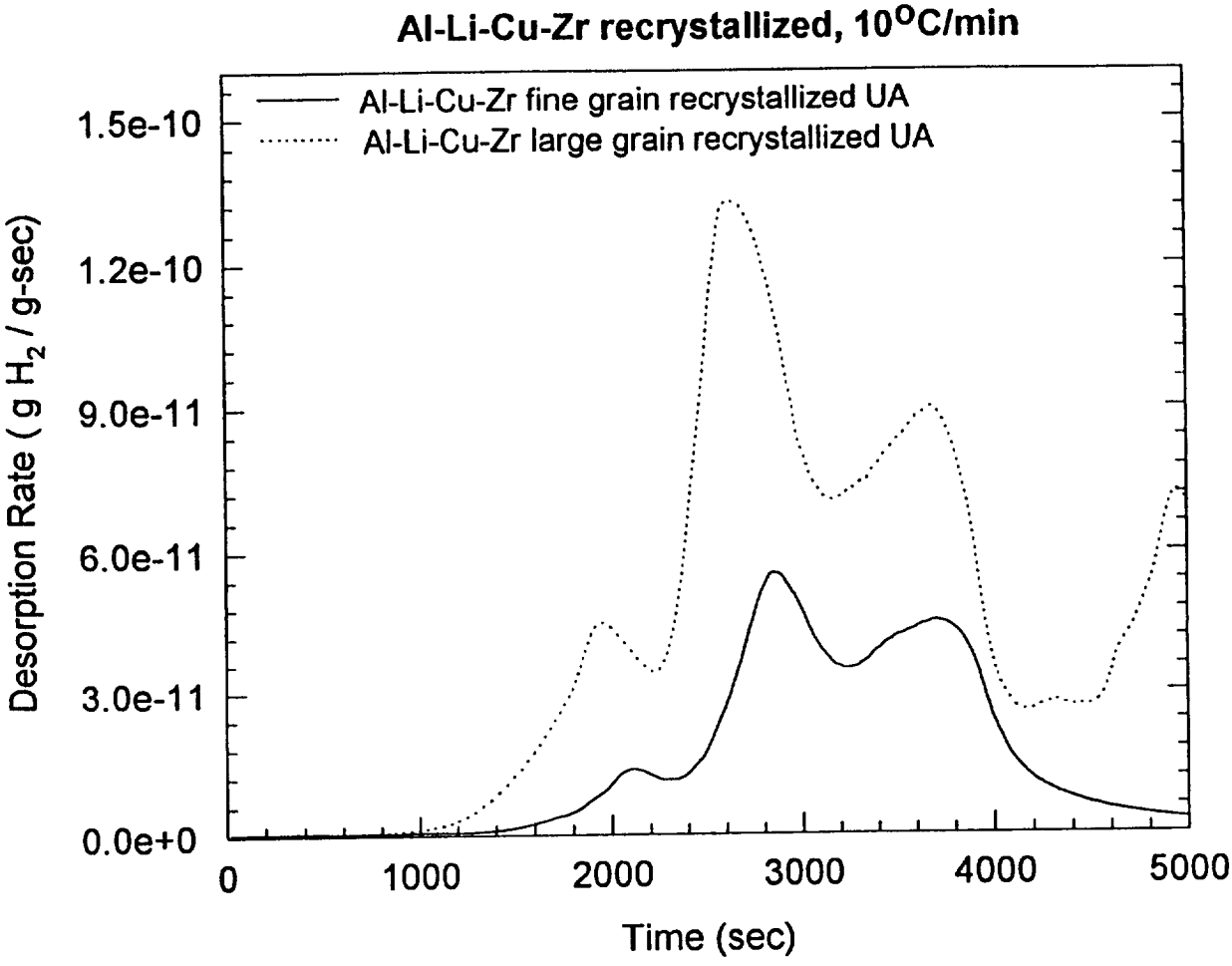
Al-Li-Cu-Zr recrystallized, 10°C/min
Al-Li-Cu-Zr fine grain recrystallized UA
Al-Li-Cu-Zr large grain recrystallized UA
Desorption Rate (g H2 / g-sec)
1.5e-10
1.2e-10
9.0e-11
6.0e-11
3.0e-11
0.0e+0
0
1000
2000
3000
4000
5000
Time (sec)

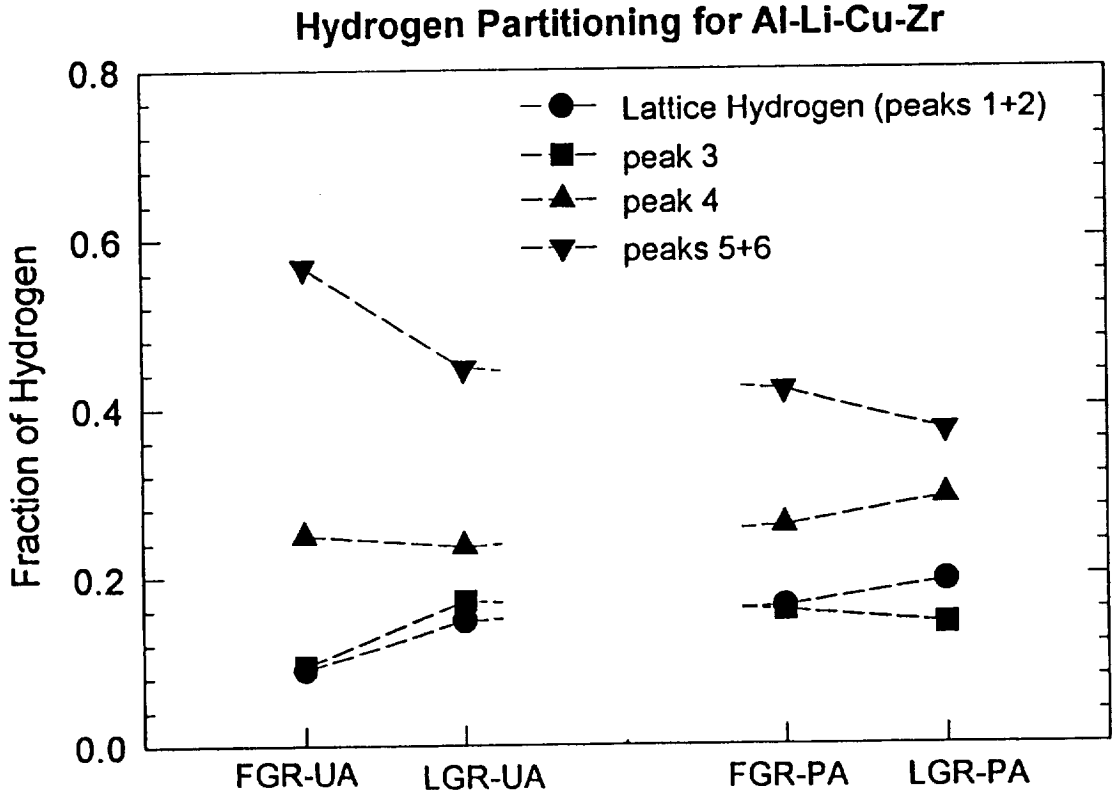
Hydrogen Partitioning for Al-Li-Cu-Zr
Lattice Hydrogen (peaks 1+2)
peak 3
peak 4
peaks 5+6
Fraction of Hydrogen
0.8
0.6
0.4
0.2
0.0
FGR-UA
LGR-UA
FGR-PA
LGR-PA

Summary: Trap Site Identification

- Solution heat treated and aged Al-3%Li was used to identify hydrogen trapped at: Li_{ss} and δ' (Al_3Li)

- Variation of aging times for AA2090 aided in the identification of hydrogen associated with Li_{ss}, δ' (Al_3Li) and T_1(Al_2CuLi).

- Plastic straining of AA2090 was exploited to identify trapping at dislocations.

- Variation of recrystallized grain size followed by aging was utilized to identify trapping at high angle boundaries with T_1.

- Comparison of AA2090 and recrystallized Al-Li-Cu-Zr aided in establishing whether hydrogen was trapped at subgrain boundaries.

- Solution heat treated and aged Al-1% and Al-4%Cu were utilized to identify hydrogen trapping at: Cu_{ss}, GP_{zones}, θ'', θ', and θ (Al_2Cu).

- By a process of elimination trapping state 1 was identified as interstitial hydrogen and trapping at T_1 particles was determined to be trapping state 5 or 6.

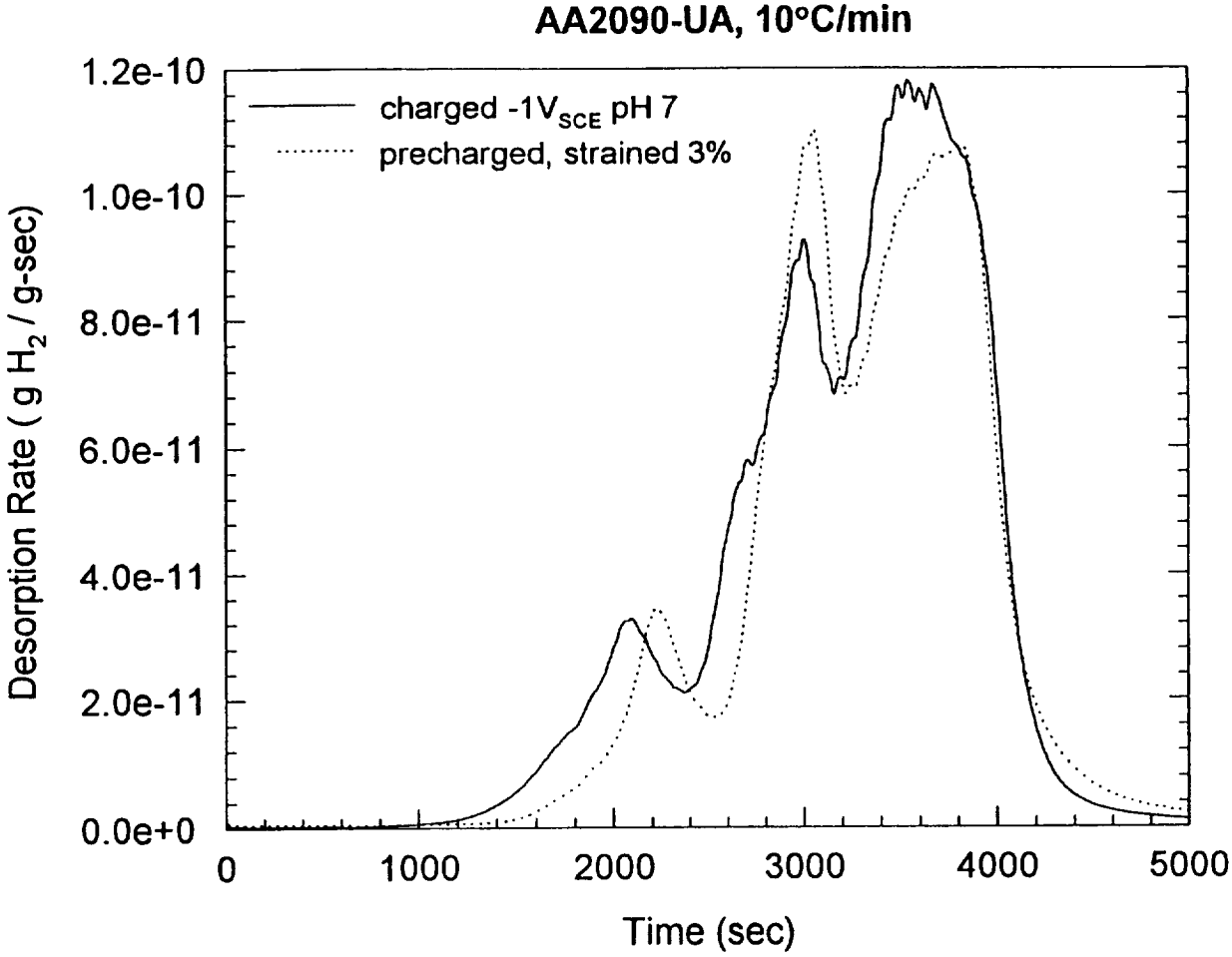
AA2090-UA, 10°C/min
charged -1V$_{SCE}$ pH 7
precharged, strained 3%
Desorption Rate (g H$_2$ / g-sec)
1.2e-10
1.0e-10
8.0e-11
6.0e-11
4.0e-11
2.0e-11
0.0e+0
0
1000
2000
3000
4000
5000
Time (sec)

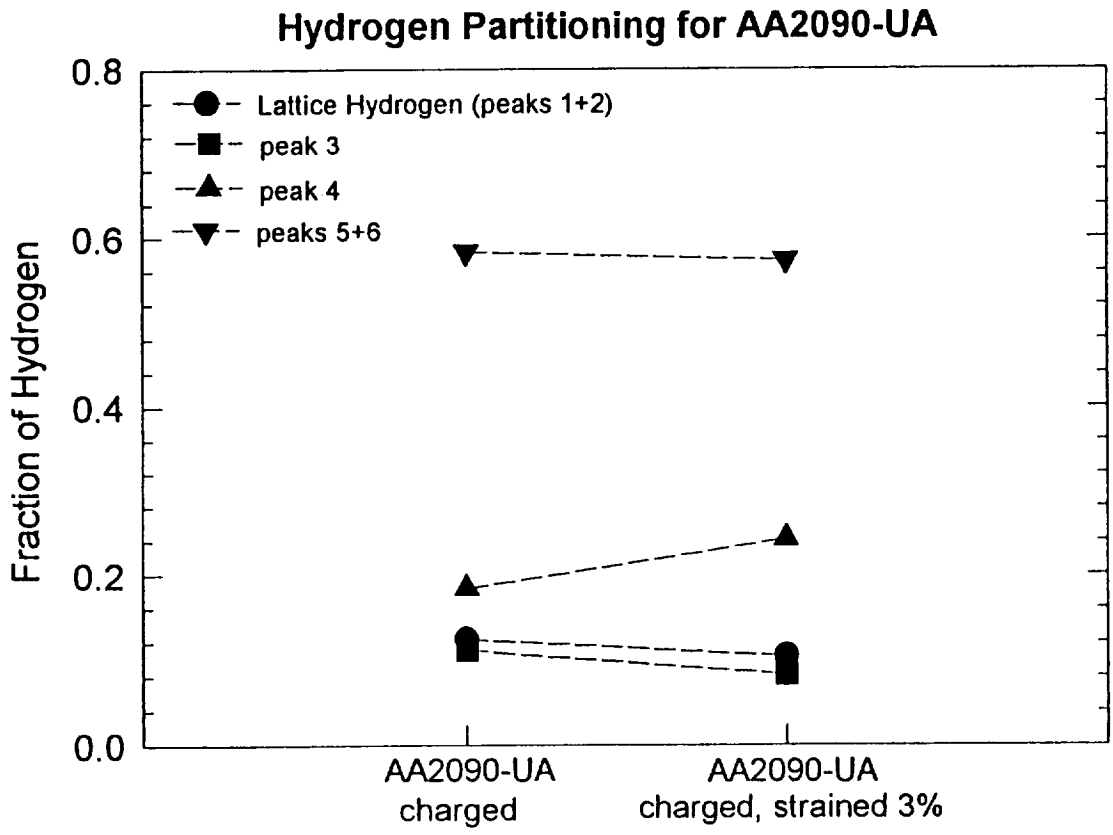
Hydrogen Partitioning for AA2090-UA
Lattice Hydrogen (peaks 1+2)
peak 3
peak 4
peaks 5+6
Fraction of Hydrogen
0.8
0.6
0.4
0.2
0.0
AA2090-UA
charged
AA2090-UA
charged, strained 3%

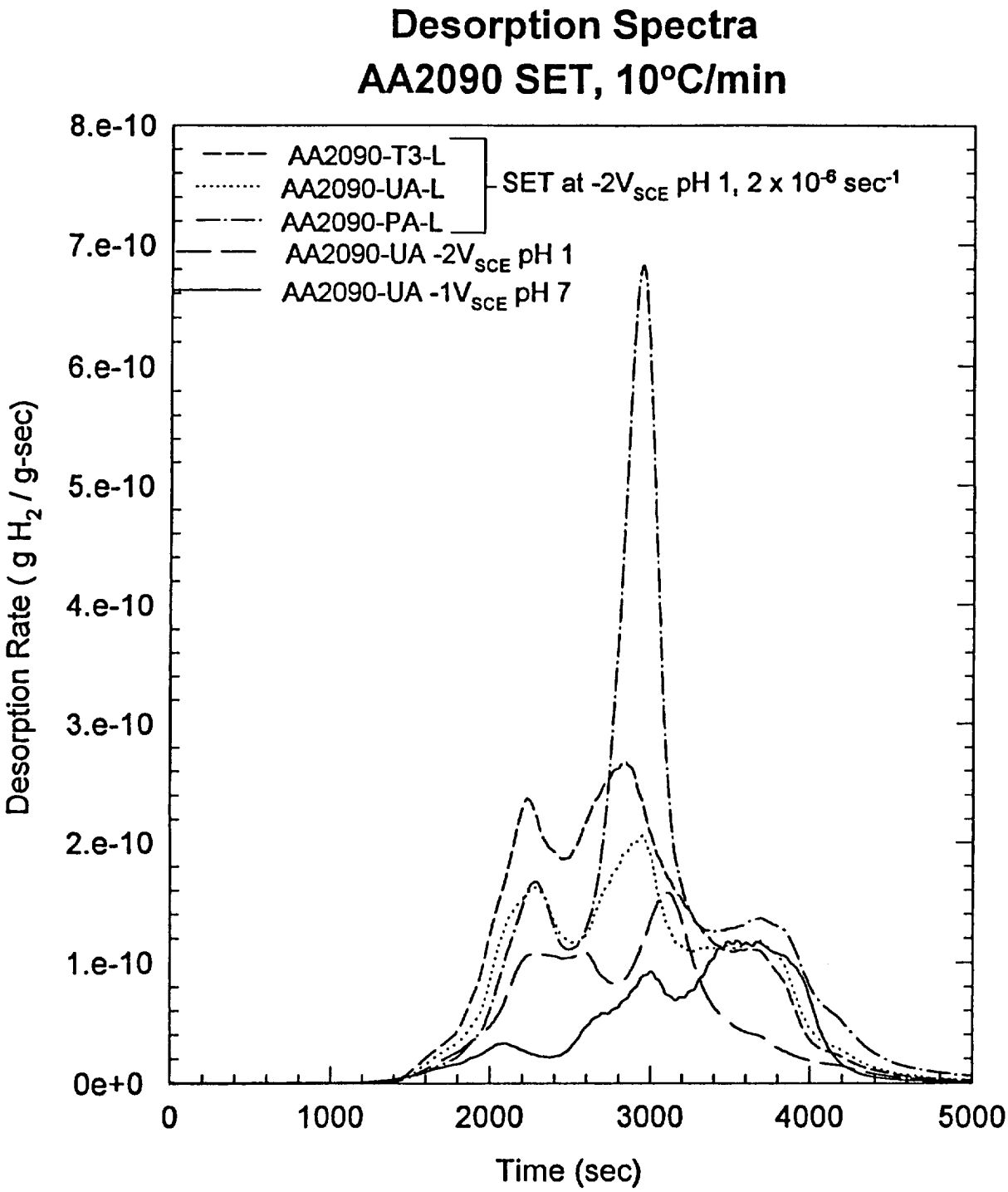
Desorption Spectra
AA2090 SET, 10°C/min
AA2090-T3-L
AA2090-UA-L
AA2090-PA-L
SET at -2V$_{SCE}$ pH 1, 2 x 10^{-6} sec^{-1}
AA2090-UA -2V$_{SCE}$ pH 1
AA2090-UA -1V$_{SCE}$ pH 7
Desorption Rate (g H$_2$ / g-sec)
8.e-10
7.e-10
6.e-10
5.e-10
4.e-10
3.e-10
2.e-10
1.e-10
0e+0
0
1000
2000
3000
4000
5000
Time (sec)

Desorption Spectra, TL Oriented AA2090, 10°C/min
Spectra of Bulk Sample Subtracted from Fracture Surface

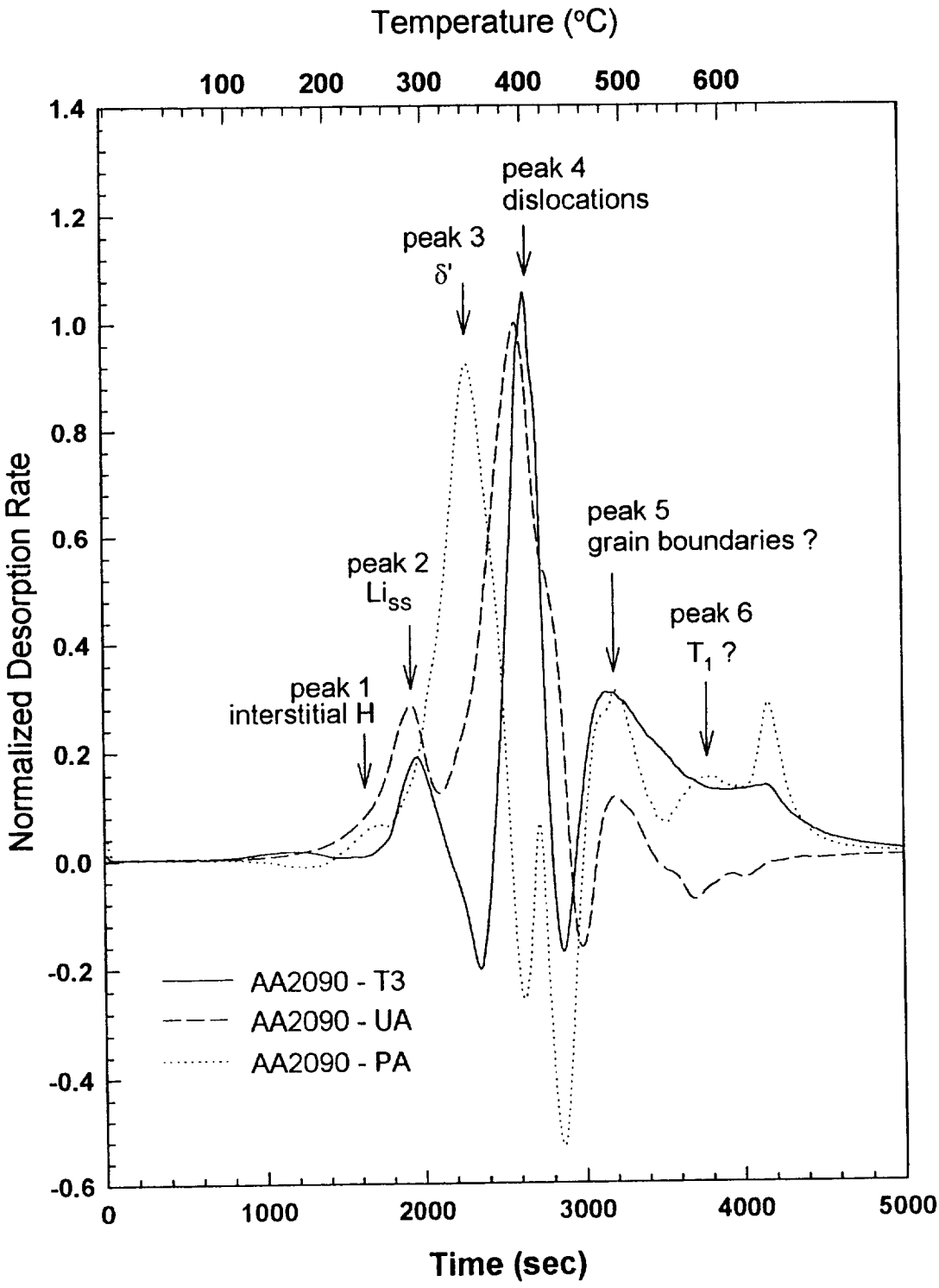

Summary: Hydrogen Transport

- Dislocations can collect trapped hydrogen from lower energy trapping states during dynamic straining.

- Hydrogen transported by dislocations can be deposited at higher energy trapping sites, such as grain boundaries, within a plastic zone.

- An increased rate of hydrogen uptake has been measured after dynamic straining in pH 1 HCl solution under cathodic polarization or in moist laboratory air. Hydrogen uptake is facilitated by dislocation transport.

Conclusions

- **Elevated levels of absorbed hydrogen results in intergranular cracking when high angle grain boundaries are oriented favorably with the tensile stress and a sufficient stress concentration is present.**

  - **FGR Al-Li-Cu-Zr, UA temper - demonstrated a change in fracture mode from TGS to IG with hydrogen pre-charging (J_i also decreased).**

  - **FGR Al-Li-Cu-Zr, PA temper - hydrogen pre-charging altered the existing IG fracture (J_i also decreased).**

  - **MGR and LGR Al-Li-Cu-Zr - Independent of temper and absorbed hydrogen level fracture was dominated by TGS.**

  - **Pre-charged TL oriented AA2090 - demonstrated more IG cracking than pre-charged LT oriented AA2090 (J_i decreased with hydrogen pre-charging for all tempers of TL oriented AA2090).**

  - **High angle grain boundaries trap hydrogen and are one of the highest energy trapping sites for hydrogen in Al-Li-Cu-Zr alloys.**

Conclusions (cont.)

- **Elevated levels of absorbed hydrogen may promote slip localization.**
  - **Dislocations are effective trapping sites for Al-Li-Cu-Zr alloys.**
  - **Enhanced deformation has been demonstrated for pre-charged AA2090 (enhanced deformation T3 > UA > PA).**
  - **Pre-charged FGR Al-Li-Cu-Zr, UA temper - possess planar slip bands on IG fracture facets.**
- **Hydrogen is implicated in the EAC of Al-Li-Cu-Zr alloys.**
  - **The rate of hydrogen absorption is increased for concurrent straining and charging.**
  - **Hydrogen is absorbed during Al aqueous exposure of AA2090.**
  - **The preferred cracking path during Al aqueous exposure and mechanical testing of specimens with pre-dissolved hydrogen is IG cracking.**
  - **The preferred cracking path correlates with a high energy trapping state.**

Conclusions

1) Elevated levels of absorbed hydrogen results in intergranular cracking when high angle grain boundaries are oriented favorably with the tensile stress and a sufficient stress concentration is present.

2) Elevated levels of absorbed hydrogen may promote slip localization.

   Elevated levels of absorbed hydrogen have been shown to affect deformation during intergranular and transgranular shear fracture processes. Dislocations have been shown to trap and transport hydrogen.

3) Hydrogen is implicated in the EAC of Al-Li-Cu-Zr alloys.

Project #5 **Metallurgical Factors Controlling Stress Corrosion Cracking in Advanced Al-Li-Cu Alloys**

Keith Eklund and John R. Scully

Objective

The objective of this new project is to characterize the stress corrosion initiation and propagation behavior of two selected advanced Al-Li-Cu alloys under chromate inhibited full immersion conditions, as well as alternate immersion conditions. We aim to correlate SCC kinetics with cracking, metallurgical variables (aging condition, orientation, composition, processing) and, to a limited extent, electrochemical variables using diagnostics such as thermal desorption trapping analysis.

Approach

The following alloys will be investigated: *C155* (approx: 3.1% Cu, 1.8% Li, 0.35% Mg, 0.16% Zr, 0.6% Mn, 0.35% Zn; max wt. pct.) and *2096* (approx. 3.0% Cu, 1.9% Li, 0.8% Mg, 0.18% Zr, 0.6% Ag, 0.25% Zn; max. wt. pct.). The approach to this new project will involve:

- Characterize SCC threshold stress intensities and stage II da/dt using conventional fatigue precracked compact tension specimens (inhibited full immersion) or double beam bolt loaded configurations (alternate immersion) for various aging treatments, specimen orientations, and/or processing variables.
- Use SEM fractography to identify crack initiation sites and cracking paths
- Correlate the above findings and metallurgical as well as compositional variables with thermal desorption analysis of trapping states. TDS analysis will be performed on specimens sectioned from the plastic zone of SCC specimens.
- Conduct other diagnostics (i.e.: dissolve δ' to change deformation mode)
- Compare threshold stress intensities and, possibly, growth rates between long cracks and short cracks to investigate differences: i.e. examine "chemical crack length" effects.

Payoff

The proposed work will provide direct correlation between metallurgical variables (Ag content at the same Cu/Li ratio) and SCC resistance, that will lead to improved mechanistic understanding of the factors controlling SCC in advanced Al-Li-Cu alloys and serve as inputs to future alloy design.

Project 5: **Localized Corrosion and Stress Corrosion Crack Initiation in Advanced Al-Li-Cu Alloys**

Glenn E. Stoner and John R. Scully

Objective

The objective of this new project is to understand localized corrosion and the factors governing the transition from localized corrosion to SCC/CF initiation. We aim to define the "windows" of susceptibility to crack initiation in terms of metallurgical (composition, aging condition and strengthening precipitate development, constituent particles, and specimen orientation), electrochemical (applied potential, localized corrosion site propagation rate), chemical (macrocell and microcell composition), and mechanical (dynamic strain rate, stress state, localized corrosion site flaw dimensions) variables.

Approach

The following alloys will be investigated: *C155* (approx: 3.1% Cu, 1.8% Li, 0.35% Mg, 0.16% Zr, 0.6% Mn, 0.35% Zn max wt. pct.) and *2096* (approx. 3.0% Cu, 1.9% Li, 0.8% Mg, 0.18% Zr, 0.6% Ag, 0.25% Zn max. wt. pct.). These alloys have approximately the same Cu/Li ratio but 2096 contains Ag. The approach to this new project will involve:

- Characterize conditions for localized corrosion behavior in precursor "macrocell" local chemistry environments and refined local environments using advanced electrochemical (current transient) and chemical diagnostics (CE).
- Superimpose mechanical variables such as dynamic strain rate, stress state, and/or cyclic strain to define windows of susceptibility to crack initiation using blunt notch specimens. Employ ex-situ crack initiation detection by metallographic and SEM techniques, and in-situ detection by use of a long focal length microscope. Characterize the critical

corrosion site flaw size necessary to initiate SCC.

- Attempt to determine threshold stress intensities and possibly growth rates from short cracks to ascertain any evidence of differences between the behaviors of short versus long cracks, i.e. a "chemical crack length" effect.

Payoff

The proposed work will provide correlations between localized corrosion and SCC initiation that will lead to improved mechanistic understanding of the factors controlling the transition to SCC. K_{th} for short cracks along with critical corrosion site flaw sizes will be obtained.

Coordination

The two projects are designed to be complimentary but not redundant. For perhaps the first time a comprehensive understanding of the *transition* from localized corrosion to SCC initiation and propagation may be achieved.

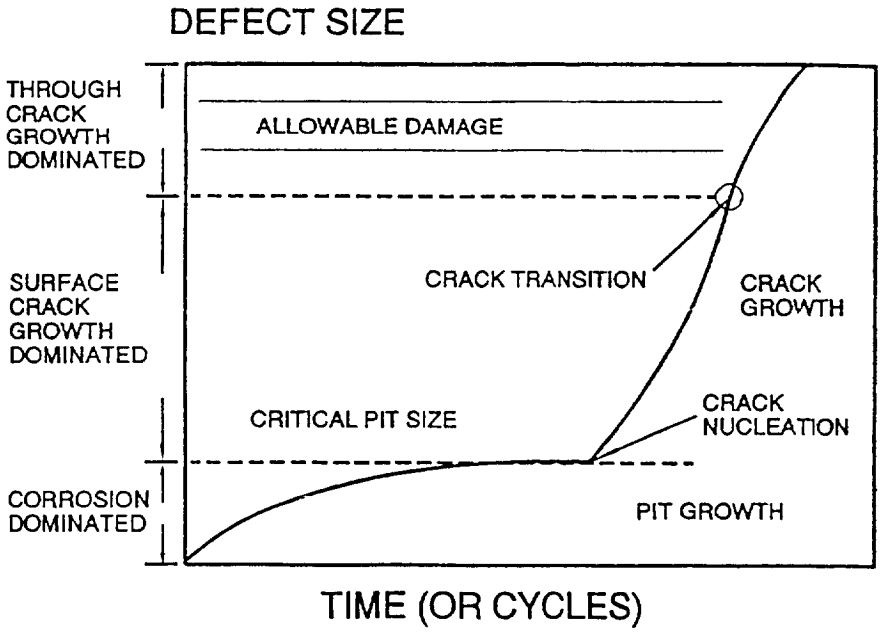

Investigation of the same two alloys will strengthen understanding of the roles of metallurgy, processing and composition: (initiation versus propagation debate). Results from each study will provide direct input to the other. Examples include:

- Characterization of local macrocell chemistry developed in an alternate immersion double beam bolt loaded configuration will provide guidance on environments for blunt notch SCC initiation experiments.
- Determination of windows of SCC initiation susceptibility will guide follow-on conventional SCC initiation and growth test conditions.
- he electrochemical activity of T, Ω or other phases with and without partitioning of Ag may be compared and contrasted to their function as hydrogen trapping states. Clear guidance on alloy design may emerge.

In summary, a coherent comprehensive picture of localized corrosion behavior and the transition to SCC initiation and growth will be developed

Project #6 **Mechanisms of Deformation and Fracture in High Strength Titanium Alloys: Effects of Temperature and Hydrogen**

Sean P. Hayes and Richard P. Gangloff

Objective

The broad objective of this research is to characterize and understand the relationships between microstructure, deformation mode, and fracture resistance of high strength titanium alloys for HSCT applications. In this project, the effects of time, temperature, and dissolved hydrogen on the precracked-fracture resistance of an advanced metastable β-titanium alloy will be characterized. The mechanisms for deformation and fracture will be physically defined and micromechanically modeled.

Current Status

The current work in this project is focusing on hydrogen-precharging and fracture toughness testing of high strength solution treated and aged (STA) Beta-21S and Low Cost Beta at temperatures ranging from 25 to 150°C. It has been observed that dissolved hydrogen decreases the plane strain initiation fracture toughness of STA Beta-21S to 30 pct of the value for the alloy without additionally added hydrogen. Fracture mode changes in concert with this reduction in toughness. These results are consistent with work by Scully and his students. Long term fracture toughness experiments with Beta-21S revealed unacceptable variability in the electrical potential signal being used to monitor crack extension during loading. Experiments were conducted to solve this problem.

Preliminary investigation of an LCB sheet provided by McDonnell Douglas has begun. Solution treated sheet was aged at 510°C for 8 hours in an argon atmosphere, and is currently being machined into four compact tension [C(T)] specimens. Two specimens will be precharged to a hydrogen concentration between 500 and 1000 wppm, while two will be tested with the as-received hydrogen concentration of 150 wppm. Charged and uncharged CT specimens will be fractured at 25 and 150°C to scope the effects of dissolved hydrogen and temperature on deformation mode and fracture resistance. A section of the sheet is being used to determine the

diffusivity of hydrogen in the solution treated condition. Metallographic techniques are being developed to characterize both the ST and STA microstructures.

A major focus of this project is on TIMETAL Low Cost Beta. Timet has recently cold rolled LCB sheet (6 pieces; 1.52 mm x 200 mm 390 mm or 0.060" x 8" x 15.3") and plate (1 piece; 10.16 mm x 152 mm x 254 mm or 0.4" x 6" x 10"). Three sheets and the plate will be solution treated in the $\alpha + \beta$ phase field, cooled to 25°C and isothermally aged at a temperature that is known to provide a balance of yield strength and fracture toughness. Three sheets will be provided in the as-cold rolled condition to heat treatment studies by Kazanjian and Starke at UVa. These materials should be delivered by August.

Recent Findings

The rising load R-curve test was used to determine the fracture toughness of hydrogen-precharged STA Beta-21S plate at 75°C with a slow load-line displacement rate of 0.22μm/min. This sample was charged at a current density of 0.30 mA/cm^2, as was a specimen previously tested at 150°C. However, the 75°C specimen surface was not masked, while the 150°C specimen had the area near the loading pin holes coated to prevent hydrogen uptake and embrittlement. As a result, hydrogen in the 150°C specimen had ample time to diffuse to the masked areas thereby lowering the hydrogen concentration immediately ahead of the precrack. Consequently, it is expected that the 75°C specimen had a hydrogen concentration between 500 and 1000 wppm while the 150°C was lower. Sections of each specimen were sent to LECO for nominal hydrogen content analysis.

The plane strain fracture toughness of the Beta-21S C(T) specimen, hydrogen-precharged and tested at 75°C, was 23.7 MPa$\sqrt{m}$ based on ASTM standard E-399 and a 95% slope-intercept method. This is significantly reduced from previously determined values of 71.9, 65.9, and 53.5 MPa$\sqrt{m}$ for uncharged specimens of Beta-21S at 150 and 25°C, and a hydrogen charged specimen at 150°C, respectively. Fractography of the specimen tested at 75°C showed several modes of fracture which were not observed previously. This indicates that hydrogen, or a hydrogen/temperature combination, degrades the fracture resistance of high strength STA Beta-21S.

Future Work

Work over the next six months will focus on: (1) completing preliminary fracture experiments with STA Beta-21S and LCB sheet provided by McDonnell Douglas, (2) beginning a systematic study of internal hydrogen embrittlement of a single STA condition of LCB sheet provided by TIMET, (3) studying the effect of fatigue precracked specimen thickness on resistance curve fracture toughness for uncharged and hydrogen-charged TIMET STA LCB plate, and (4) investigating the deformation and fracture modes in LCB of varying fracture test temperature and dissolved hydrogen concentration for fixed strength and microstructure.

Presentation Viewgraph Captions

1. Title.

2. Objectives

3. Compositions of TIMETAL Beta-21S and TIMETAL LCB.

4. Calibration curve relating applied electrochemical cathodic current and hydrogen uptake in STA Beta-21S exposed to aqueous $H_2SO_4 + Na_4P_2O_7$ at 90°C for 7 days. The majority of these results were obtained by Gaudett, Young, and Scully who are assisting with the charging of both Beta-21S and LCB.

5. C(T) specimen, buckling restraints, crack mouth opening displacement measurement by LVDT, and dcEPD probes used for determining elevated temperature fracture toughness of thin sheet alloys.

6. Load versus crack mouth opening displacement data for STA Beta-21S C(T) specimens at 25°C and 150°C, without precharged hydrogen, and at 75°C and 150°C with precharged hydrogen. A slow loading rate was employed such that each experiment required 20 to 50 hours to fracture. The deleterious embrittling effect of predissolved hydrogen at 75°C is apparent.

7. Plane strain initiation fracture toughness, defined by a loading slope secant offset method from ASTM Standard E-399, for the four specimens of STA Beta-21S at the various test temperatures and hydrogen-precharged conditions represented in Figure 6. Note the reduction in initiation toughness due to dissolved hydrogen.

8. Direct current electrical potential versus time for an unloaded C(T) specimen which shows signal variability on the order of 5 microvolts. This behavior is unacceptable and will hinder detection of the onset of cracking.

9. Direct current electrical potential versus time for an unloaded C(T) specimen which shows drift in the measured potential over time. This behavior is unacceptable and will hinder detection of the onset of cracking.

10. Measured load and electrical potential versus crack mouth opening displacement for a Beta-21S C(T) specimen (hydrogen precharged to about 700 wppm and loaded at 75°C and a slow constant load-line displacement rate of 0.2 μm/sec). This plot shows the excellent agreement in crack initiation load, resolved by either the first deviation from linearity in load *vs* displacement or the change in slope of the electrical potential *vs* displacement. For this and other experiments with high strength β-titanium alloys, small scale yielding is maintained; the contribution of the plastic component of the J-integral is small, enabling a simple elastic stress intensity analysis of fracture toughness.

11. Stress intensity *vs* crack extension R-curves for two C(T) specimens of STA Beta-21S: (1) uncharged and fractured at 25°C, and (2) hydrogen-precharged and fractured at 75°C. A slow loading rate was employed for each case. Note the strong and deleterious effect of hydrogen embrittlement. (Previous experiments represented in Figure 6 show that the R-curve for as-received STA Beta-21S is somewhat higher for loading at 150°C compared to the result here for loading at 25°C. Presumably, fracture of Beta-21S without hydrogen is similar at 75°C.)

12. Results reported by Scully and coworkers establish the reduction in initiation fracture toughness, with increasing dissolved hydrogen concentration, for precharged STA Beta-21S and STA Ti 15-3 fractured by slow loading at 25°C. The current result for precharged Beta-21S at 75°C is both consistent with the general deleterious effect of dissolved hydrogen, and shows a potentially increasingly deleterious effect of hydrogen at elevated temperature. Also note the complex fracture surface morphologies that are typical of both ductile fracture and internal hydrogen embrittlement of these high strength β-titanium alloys.

13. Scanning electron fractographs of STA Beta-21S show the change in crack surface morphology produced by dissolved hydrogen. Fracture of Beta-21S, at 150°C and without precharged hydrogen, produced a transgranular crack surface with at least two types of ductile fracture features as shown by the two fractographs on the left side of the figure. Note the fatigue precrack in the bottom portion of each fractograph. Fracture of Beta-21S, at 75°C and with precharged hydrogen, produced a mixed transgranular-intergranular surface with multiple features labelled a through f (see the two fractographs on the right side of the figure). Different fracture processes appear to be operative depending on the dissolved hydrogen concentration.

14. Higher magnification scanning electron fractographs of the hydrogen-precharged C(T) specimen of STA Beta-21S fractured at 75°C. These six areas are contained in the lower right fractograph in Figure 13. Each of these features in (a) through (f) appear to be unique to hydrogen-charged Beta-21S and internal hydrogen embrittlement, however, the cause of each feature is not understood fundamentally. For example, intergranular

cracking has been reported by others at UVa investigating the aqueous chloride stress corrosion cracking of Beta-21S, and may be traced to hydrogen trapping and decohesion of β-grain boundaries. These workers hypothesized a role of locally intense slip in nucleating boundary hydrogen embrittlement. The linear features in (b) and (e) may be indicative of this process. A substantial effort is required to understand the microscopic processes that control ductile fracture and internal hydrogen embrittlement in high strength β-titanium alloys. This work will be complicated by the fine-scale microstructures typical of cold worked and aged alloys such as LCB sheet.

15. Fracture experiments will soon be conducted on STA LCB sheet obtained from McDonnell Douglas, as a precursor to a more systematic study of LCB sheet from Timet.

16. Schematic diagram of the method employed to determine the diffusivity of hydrogen in β-titanium alloys.

17. Results of the measurement of the diffusivity of hydrogen at room temperature in annealed single phase (bcc) Beta C; after Scully and Young.

18. Conclusions.

19. Future work with TIMETAL LCB sheet and plate.

20. TIMETAL LCB will be employed for the next phase of the present study of internal hydrogen embrittlement, and will also be investigated by Kazanjian and Starke.

MECHANISMS OF DEFORMATION AND FRACTURE IN HIGH STRENGTH TITANIUM ALLOYS: EFFECTS OF TEMPERATURE AND HYDROGEN

Sean P. Hayes and Richard P. Gangloff

Funded by NASA Langley Research Center
Dennis Dicus, Grant Monitor

Objectives

- **Understand the relationships between microstructure, deformation mode, and fracture resistance of titanium alloys for HSCT applications.**

- **Characterize the effects of time, temperature, and predissolved hydrogen on the fracture resistance and growth fracture resistance of an advanced metastable β-titanium alloy.**

- **Physically define mechanisms and micromechanically model hydrogen-enhanced deformation and fracture.**

Alloy Compositions (wt. pct.)

C-3

Alloy	Ti	Mo	Fe	Al	Nb	O	H
TIMETAL LCB	Balance	6.8	4.5	1.5	---	0.09	0.015
TIMETAL 21S	Balance	15	---	3	3	0.128	0.01

Beta 21S Calibration Curve

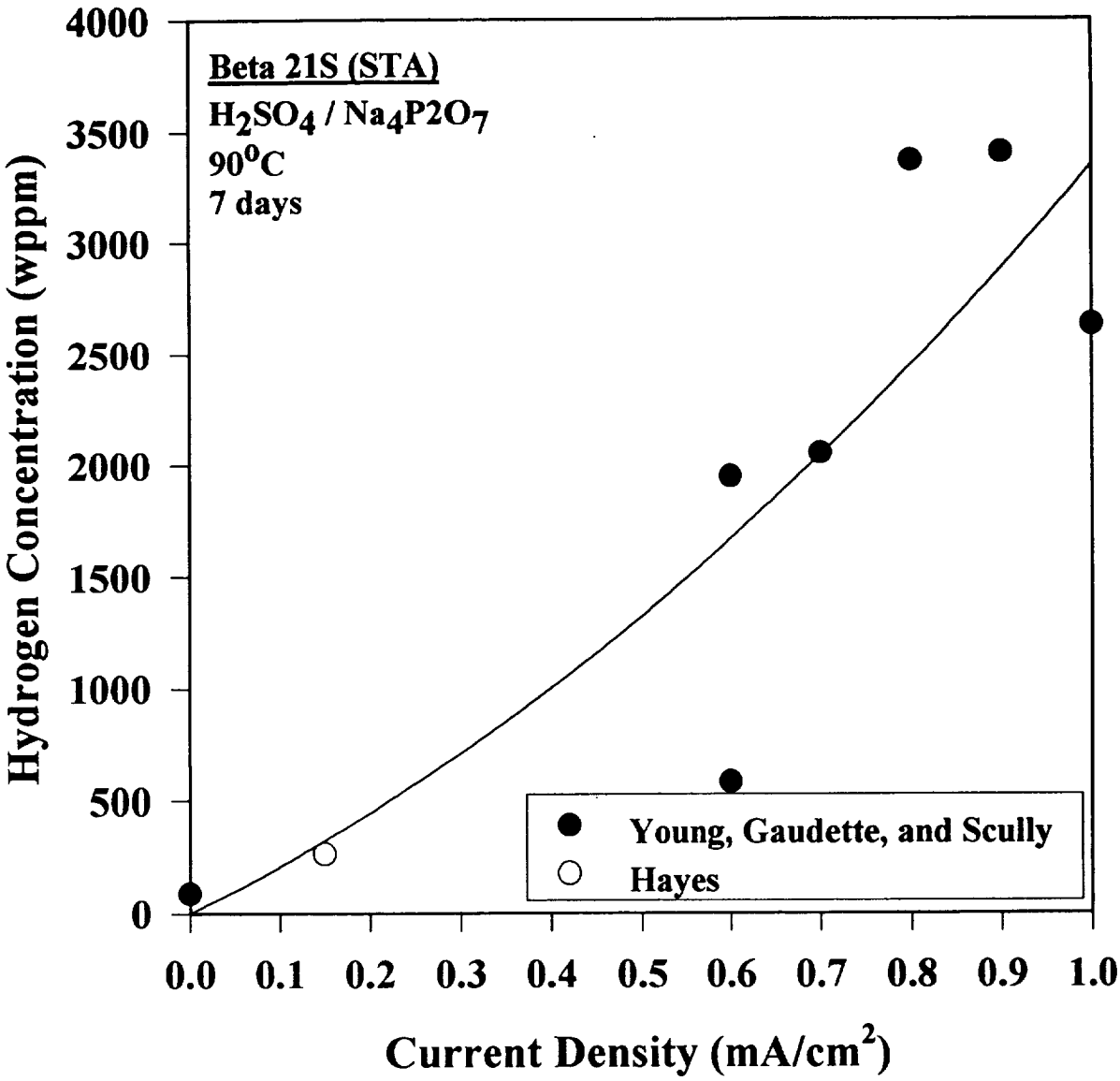

C(T) Specimen Detail for Thin Sheet J-Δa Determination

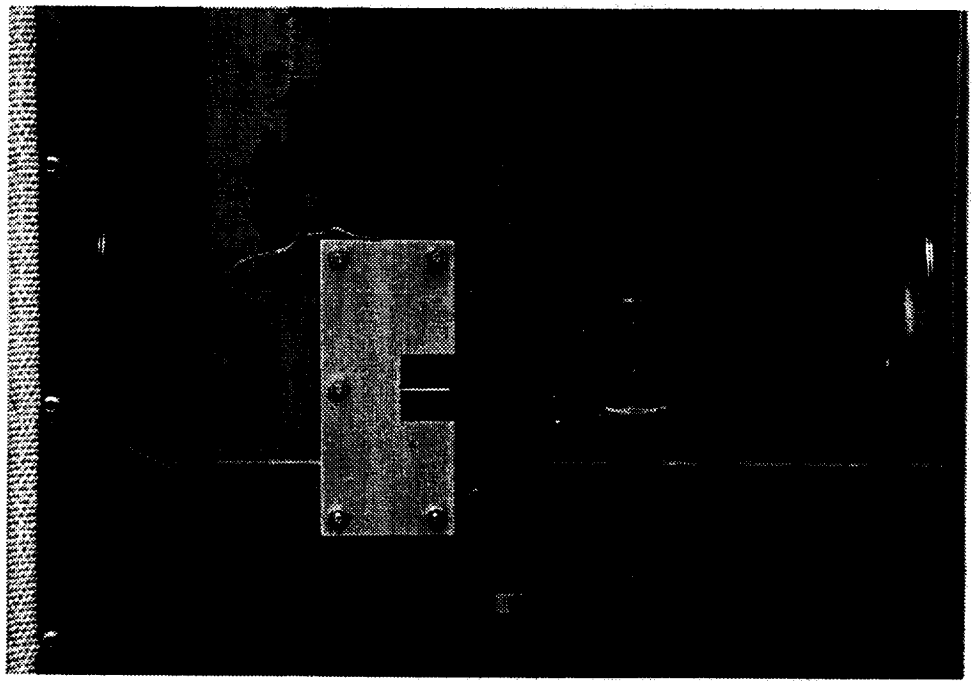

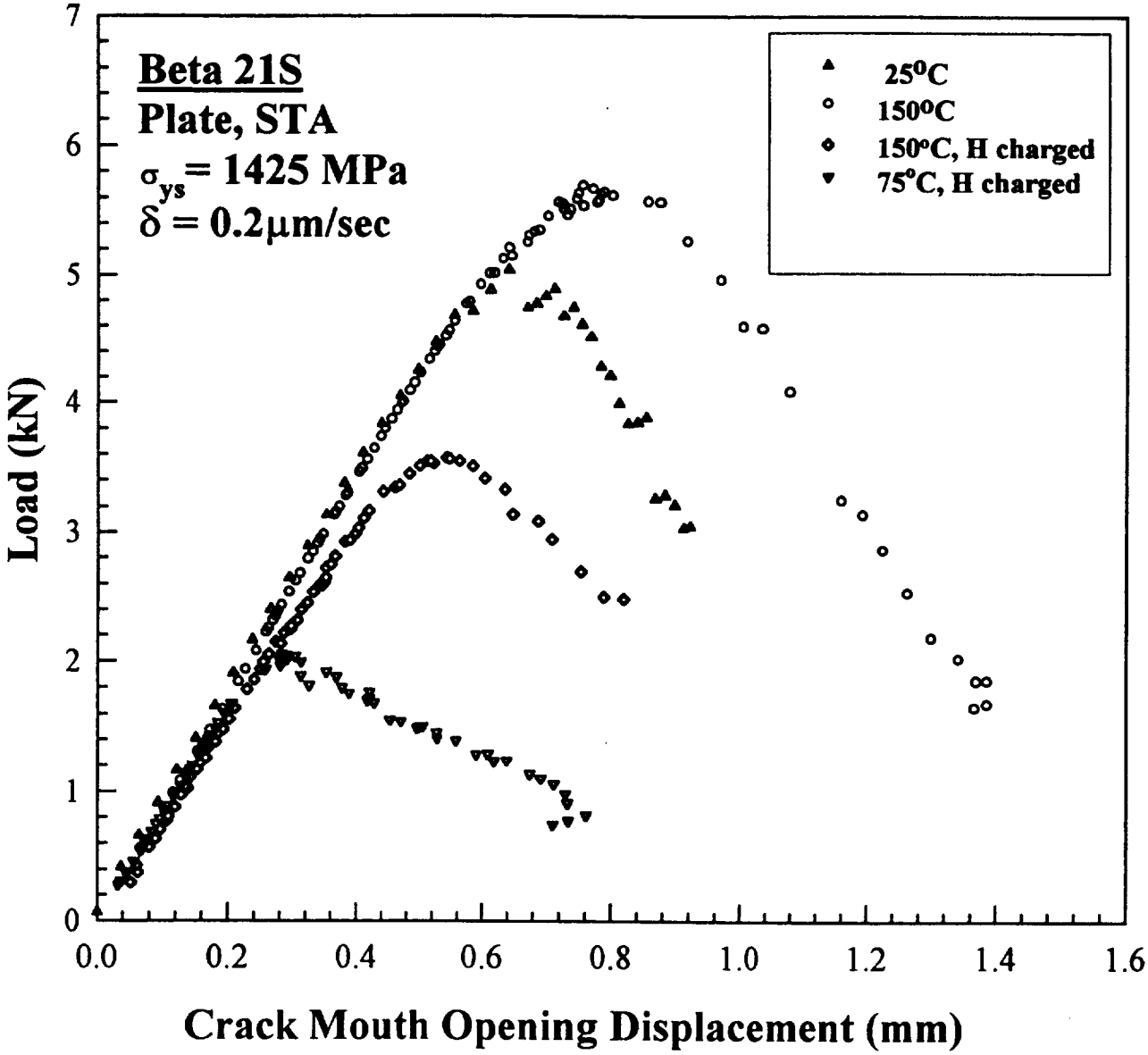
Beta 21S
Plate, STA
σ_{ys} = 1425 MPa
δ = 0.2μm/sec
25°C
150°C
150°C, H charged
75°C, H charged
Load (kN)
Crack Mouth Opening Displacement (mm)
0
1
2
3
4
5
6
7
0.0
0.2
0.4
0.6
0.8
1.0
1.2
1.4
1.6

BETA 21S FRACTURE TOUGHNESS RESULTS

Test Temperature (°C)	Estimated Hydrogen Content (wppm)	Fracture Toughness (K_{IC}-MPa$\sqrt{m}$)	Hardness (R_C)
25	100	65.9	41.4
25	100	67.9	45.2
150	100	71.9	45.2
75	750	23.7	44.5
150	< 750	53.5	44.8

K_{IC} is defined by ASTM standard E-399 and a 95% slope-intercept method

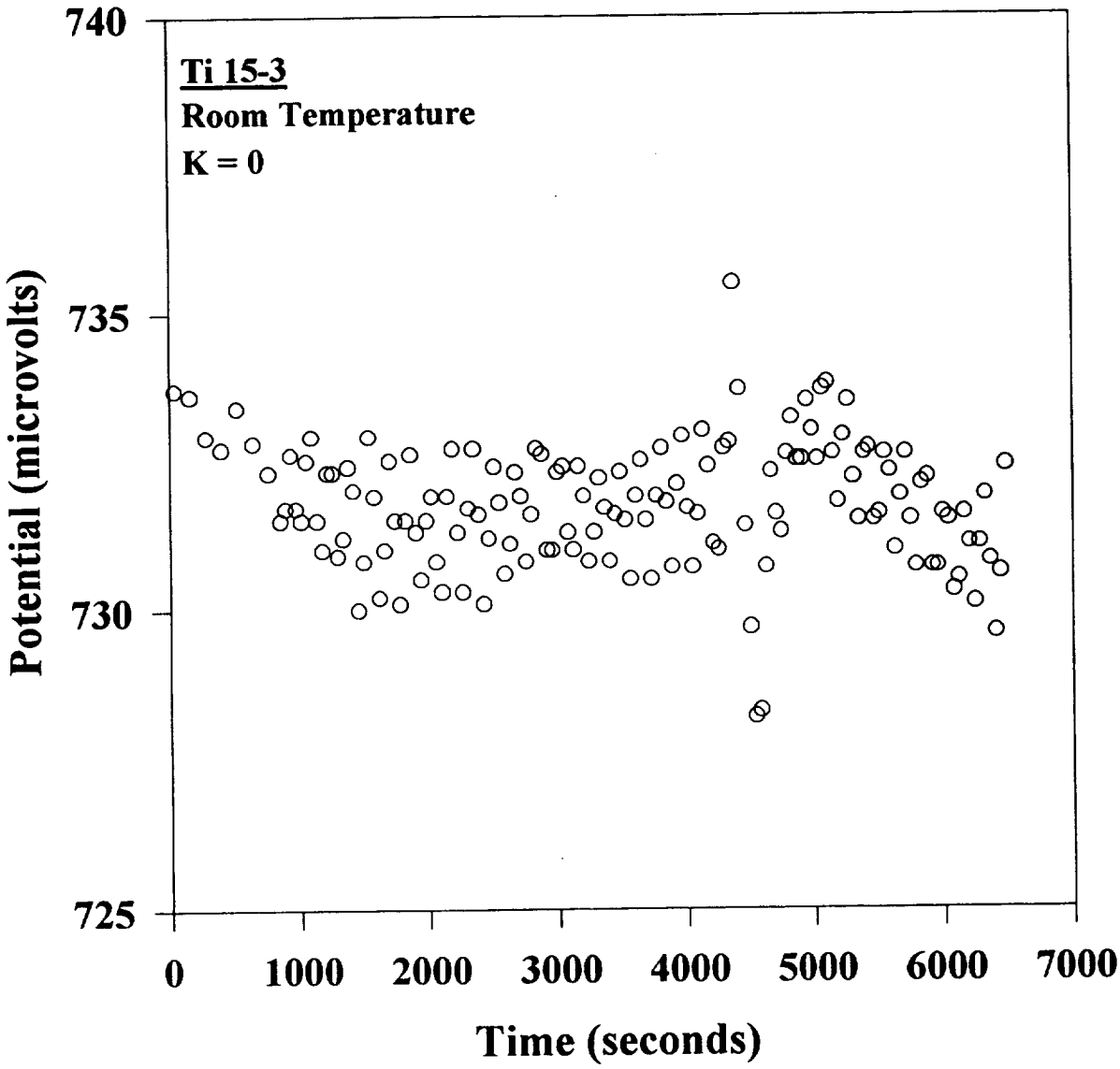
Ti 15-3
Room Temperature
K = 0
740
735
730
725
Potential (microvolts)
0
1000
2000
3000
4000
5000
6000
7000
Time (seconds)

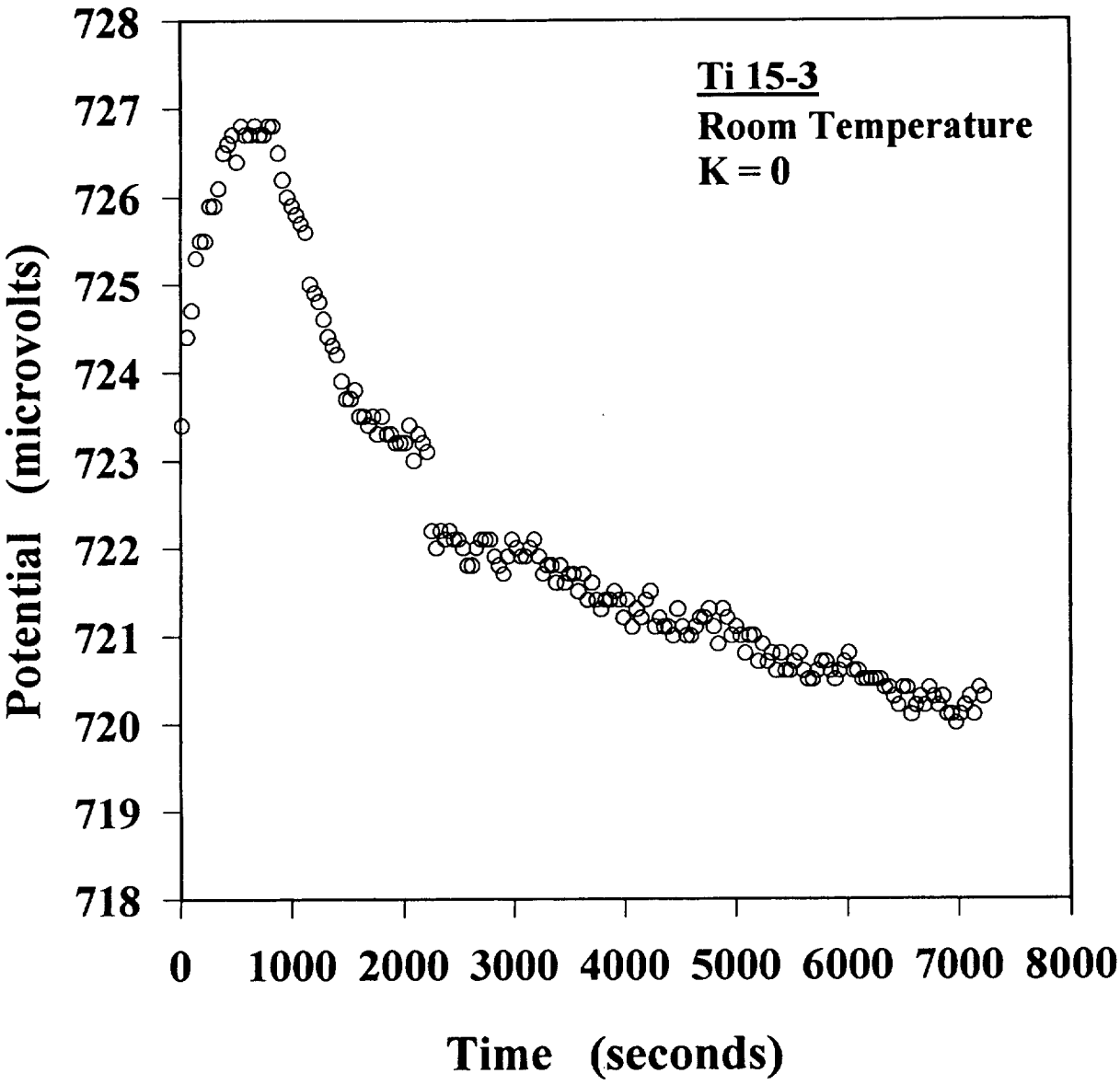
Ti 15-3
Room Temperature
K = 0
Potential (microvolts)
728
727
726
725
724
723
722
721
720
719
718
0
1000
2000
3000
4000
5000
6000
7000
8000
Time (seconds)

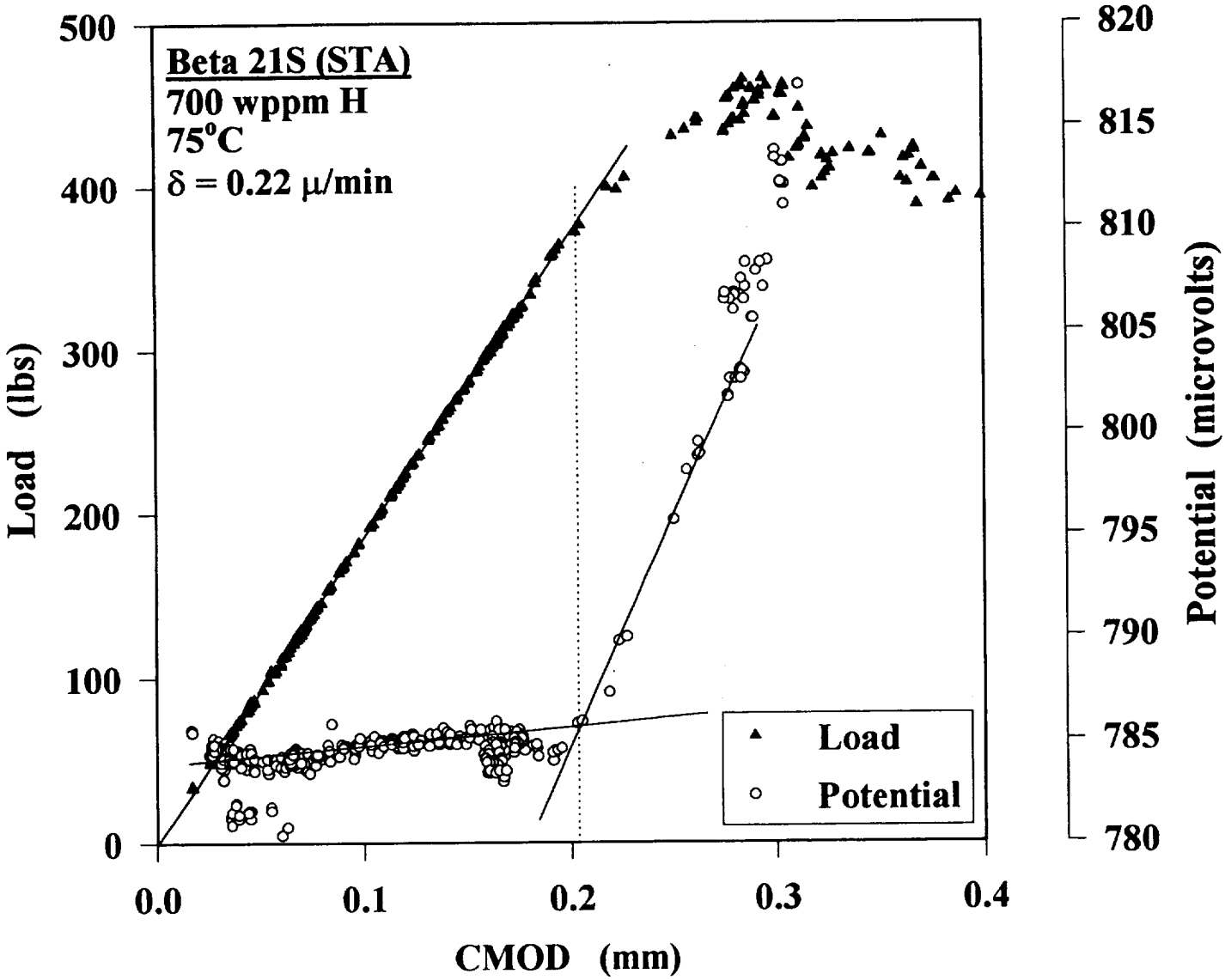
Beta 21S (STA)
700 wppm H
75°C
δ = 0.22 μ/min
Load
Potential
Load (lbs)
Potential (microvolts)
CMOD (mm)
500
400
300
200
100
0
820
815
810
805
800
795
790
785
780
0.0
0.1
0.2
0.3
0.4

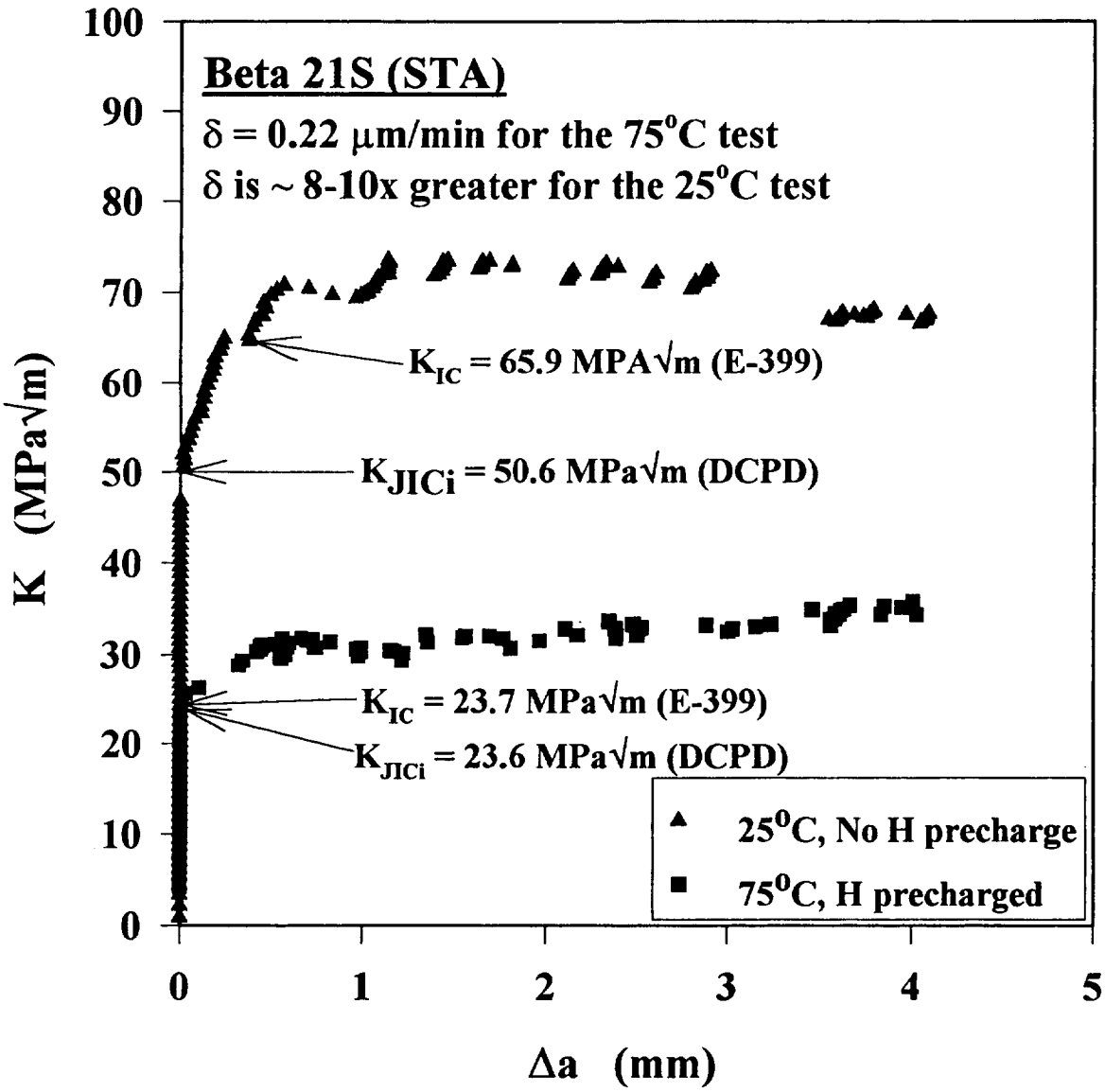
Beta 21S (STA)
δ = 0.22 μm/min for the 75°C test
δ is ~ 8-10x greater for the 25°C test
K_IC = 65.9 MPA√m (E-399)
K_JICi = 50.6 MPa√m (DCPD)
K_IC = 23.7 MPa√m (E-399)
K_JICi = 23.6 MPa√m (DCPD)
25°C, No H precharge
75°C, H precharged
K (MPa√m)
Δa (mm)
0
10
20
30
40
50
60
70
80
90
100
0
1
2
3
4
5

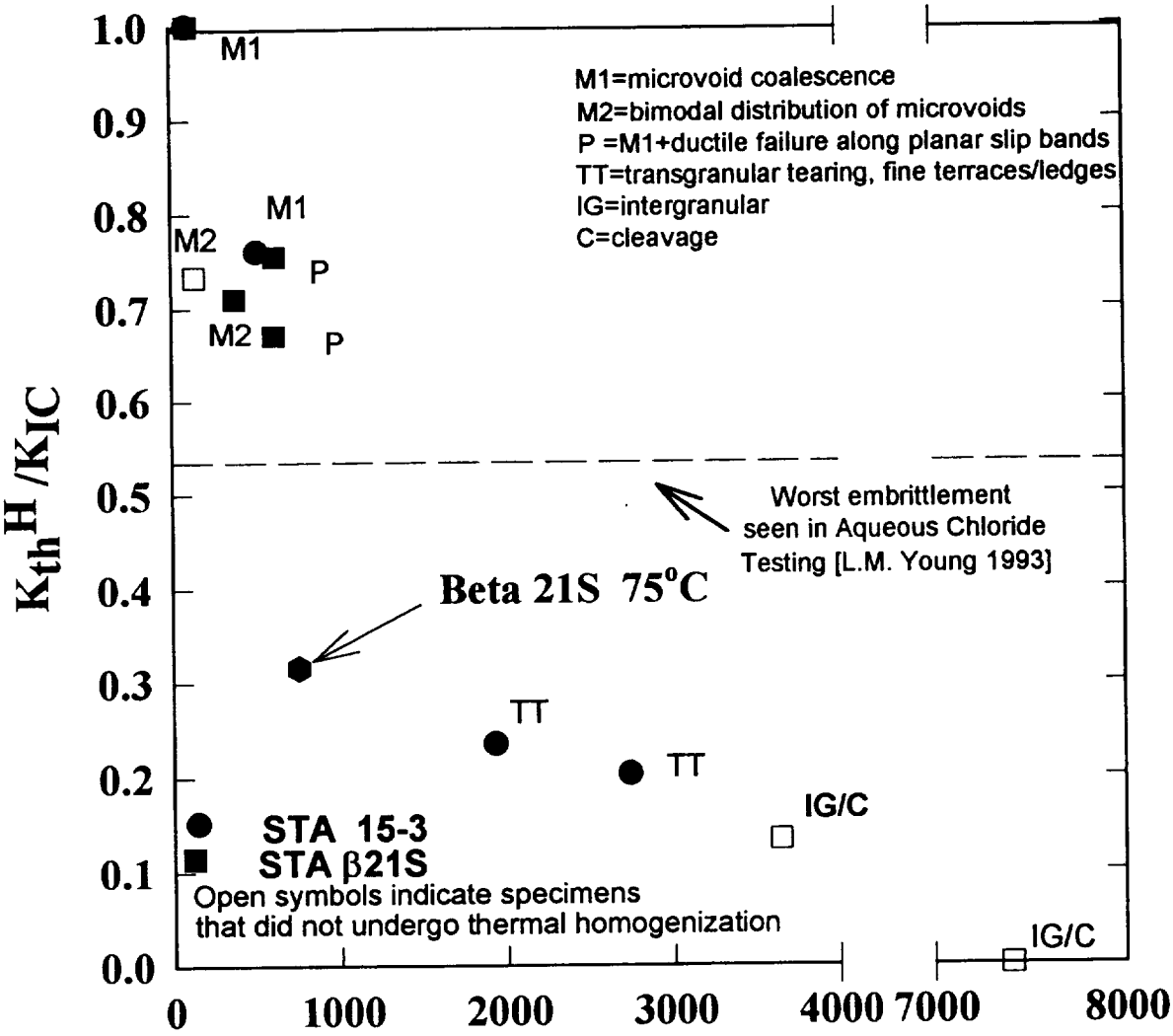

Work conducted at UVA by G. Young, L. Young, Gaudette, and Scully

Beta 21S (STA) Plate

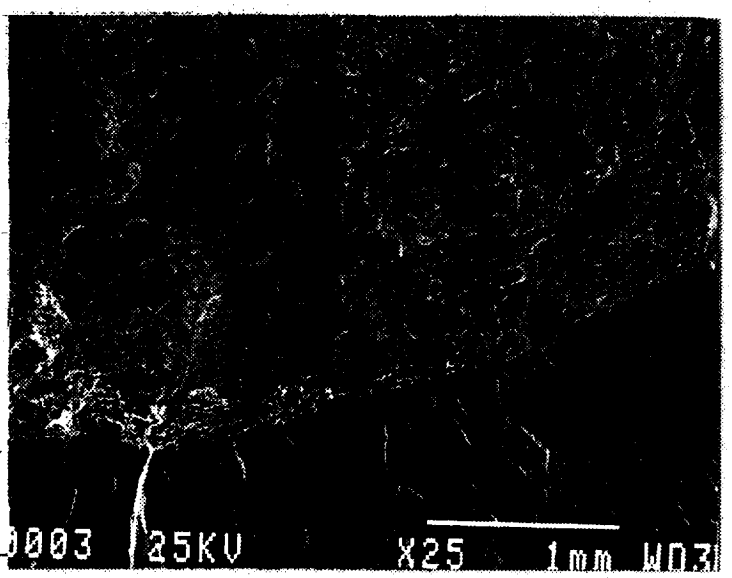

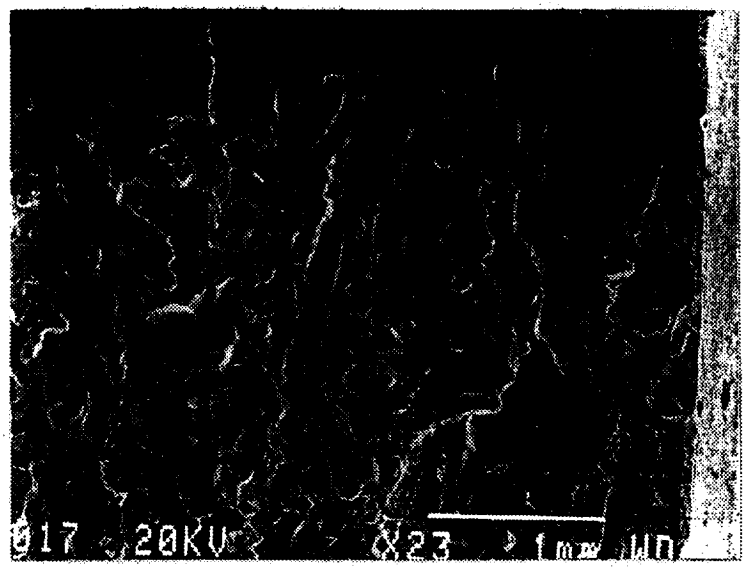

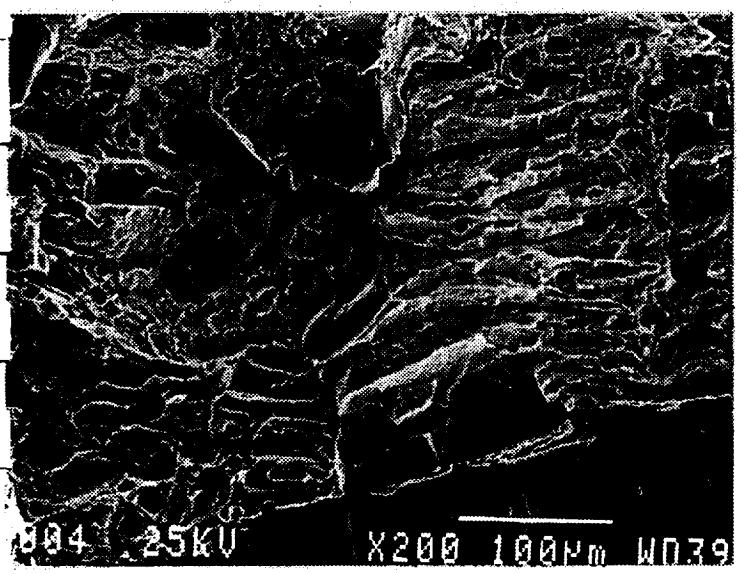

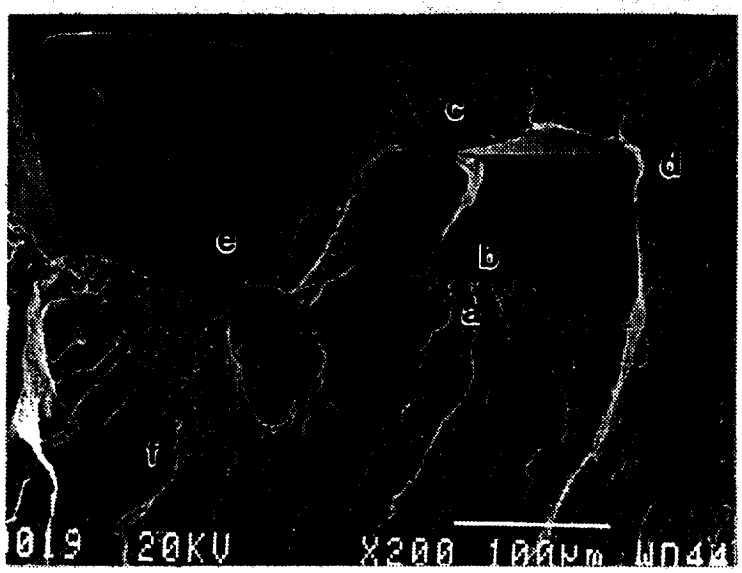

100 wppm H
150°C

700 wppm H
75°C

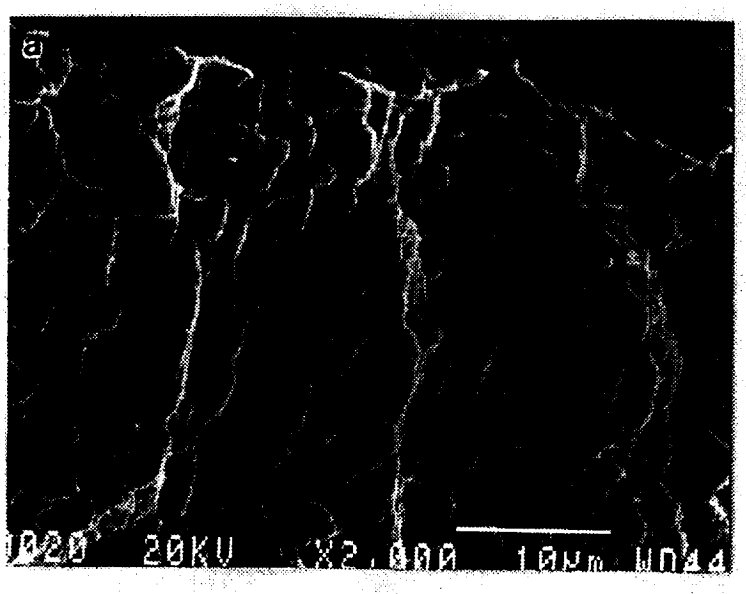
a
020 20KU X2,000 10μm WD44


b
021 20KU X2,000 10μm WD45

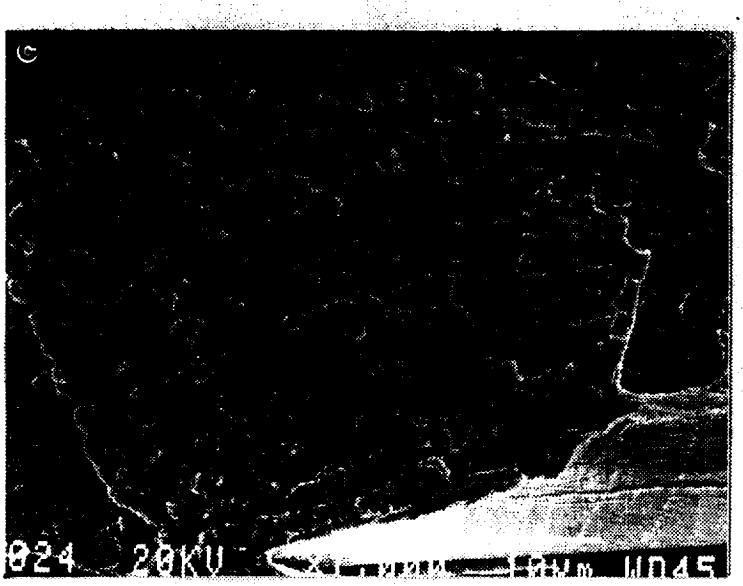
c
024 20KU 5μm WD45

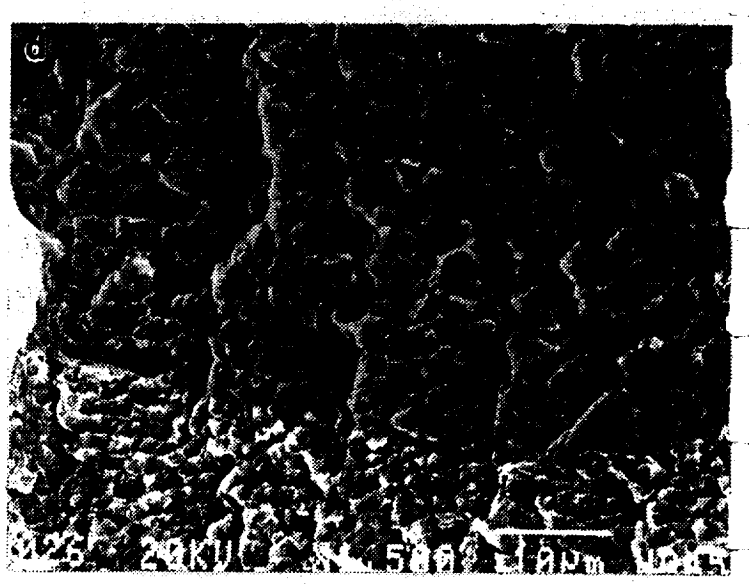
d
026 20KU 10μm

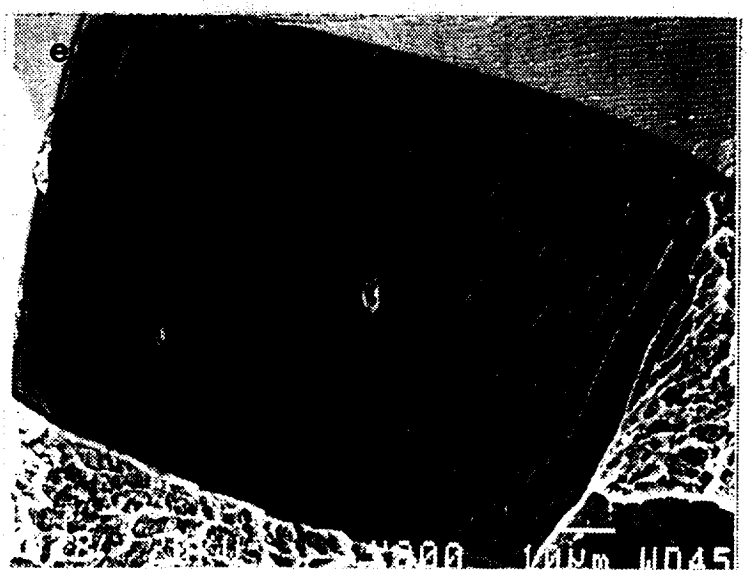
e

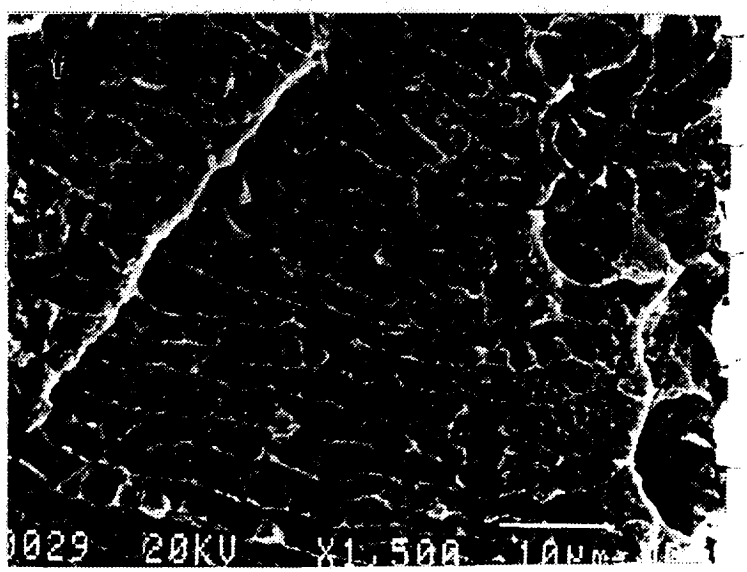
f
029 20KU X1,500 10μm

CURRENT WORK - LOW COST BETA

- **Determine the diffusivity of hydrogen in solution treated LCB.**

- **Four CT specimens of LCB sheet (McDonnell Douglas) will be tested to scope the effects of temperature and dissolved hydrogen on fracture resistance:**

STA LCB	25°C	150°C
As-received - 150 wppm H	X	X
Precharged to 500-1000 wppm H	X	X

- **Sheet and plate of LCB (ST and STA) are being provided by TIMET.**

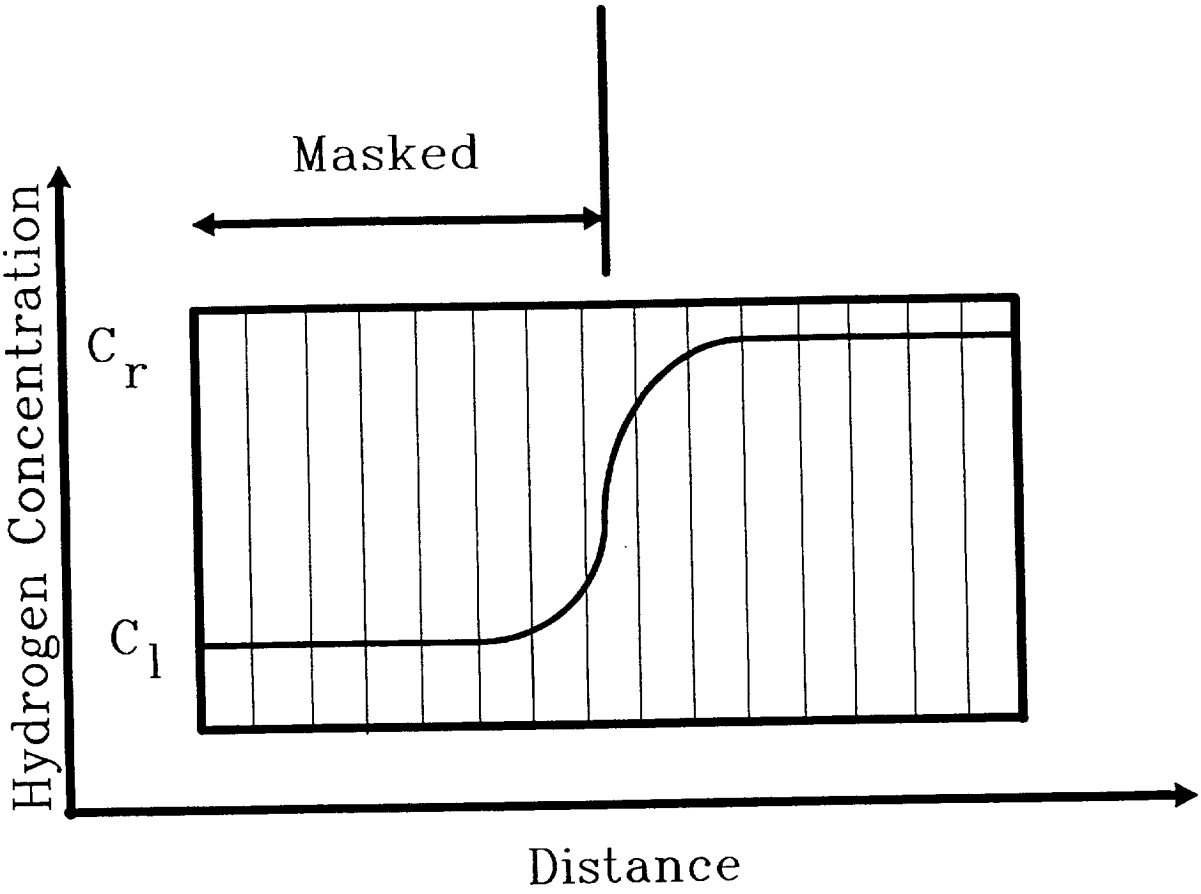

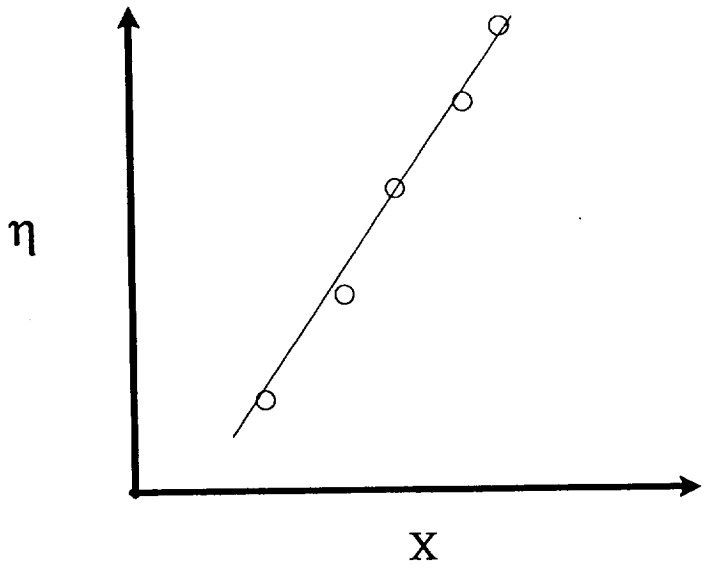

$$\eta = erf^{-1}\left[1 - \frac{2\left(C(x,t) - C_r\right)}{\left(C_l - C_r\right)}\right]$$

$$D_H = \frac{1}{\left[4t\left(\frac{d\eta}{dx}\right)^2\right]}$$

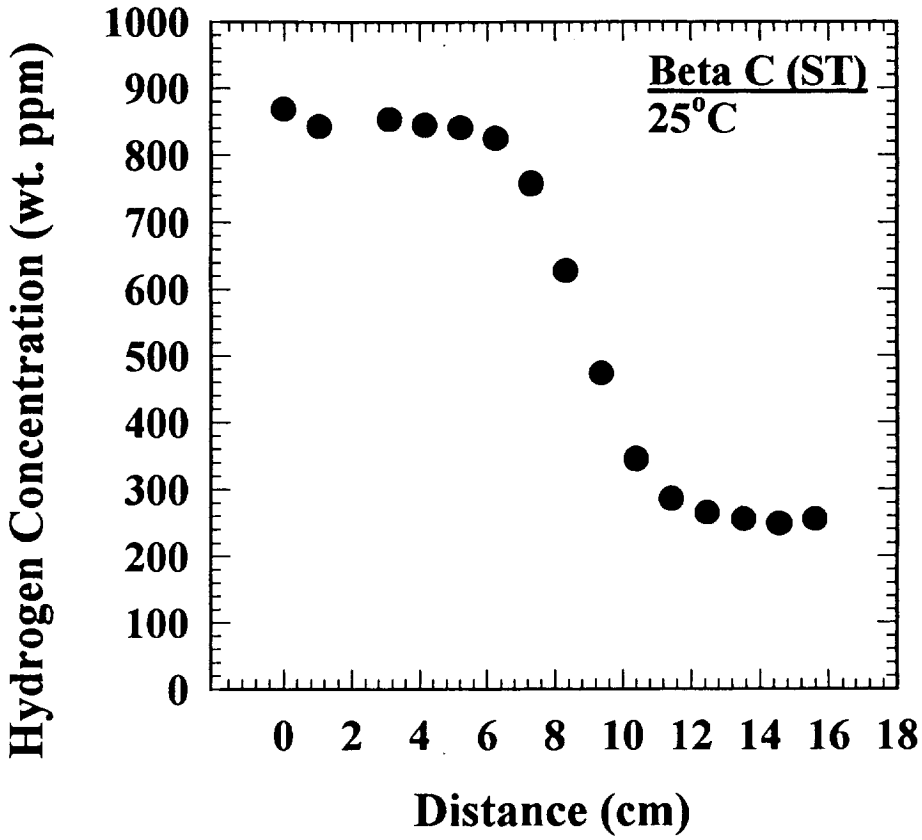

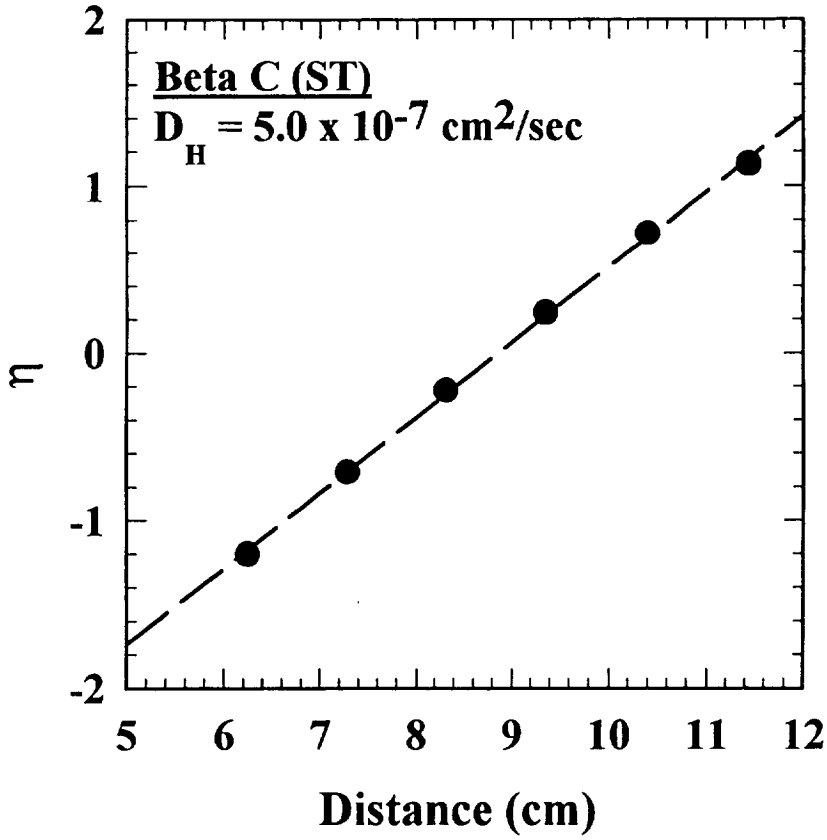

After G. Young, UVA

CONCLUSIONS

- **Dissolved hydrogen dramatically reduces the fracture toughness of high strength (STA) Beta 21S.**
  500-1000 wppm H reduces K_{IC} by 50% or more

- **Dissolved hydrogen causes a distinct change in fracture mode in STA Beta 21S plate. The morphologies of air and hydrogen fracture are complex.**

- **Problems associated with direct current potential drop (DCPD) monitoring of crack growth have been corrected.**

FUTURE WORK - LOW COST BETA

- **Determine the diffusivity of hydrogen in STA LCB at several temperatures.**
- **Establish the calibration for hydrogen charging of STA LCB in H_2SO_4 at 90°C.**
- **Characterize the effects of dissolved hydrogen and temperature on the fracture resistance (K_{TH}, K-Δa, da/dt(K)) of a single microstructure of 0.060" LCB sheet.**
- **Study the effect of fatigue precracked specimen thickness on the fracture toughness resistance curve in moist air and perhaps for IHE for STA LCB.**

TIMET LCB MATERIAL SUPPLY

- **Six LCB sheets - 0.060" x 15.25" x 8"**
  - **Three will be solution treated in the $\alpha + \beta$ region and subsequently aged**
  - **Three will be in the as-cold rolled condition**

- **One LCB plate - 0.4" x 6.75" x 13.5"**
  - **Heat treated to achieve highest possible strength with acceptable toughness**

Project #7 Evaluation of Wide-Panel Aluminum Alloy Extrusions

M.T. Lyttle and J.A. Wert

Research Objectives

The overall objective of this project is to experimentally observe and model the effects of microstructure and texture on yield strength in wide panel aluminum alloy extrusions. The modeling results will enable the prediction of locations and tensile axis orientations corresponding to minimum yield strength where localized yielding could occur in service. A generalized form of these models can be applied to any combination of microstructure and texture found in other aluminum alloys.

Progress During the Reporting Period

A model has been constructed to predict the variations in yield strength due to grain orientation, grain morphology, and precipitate plane orientation for both the plastic and elastic inclusion assumptions. Using specimen texture obtained from pole figure data, an average Taylor factor can be determined for any uniaxial stress orientation in the specimen. Combining specimen texture and precipitate plane orientation, the contribution to strengthening from precipitates with a specified habit plane orientation can be calculated.

Compression testing of different regions of the 2090 extrusion in various in-plane directions in the as-received and the overaged case has been conducted. Yield strength has been measured for the skin and cap regions in the 2090 extrusion, which contain pancake- and lath-shaped grains, respectively. Variations in yield strength are observed in Figure 8 and can be compared roughly to the typical Taylor factor variations predicted in Figure 4. The cap region (lath-shaped grains) generally exhibits a lower yield strength than the skin region (pancake-shaped grains) for all orientations tested. This is consistent with the model predictions illustrated in Figure 4. Note in particular that equal transverse strength (90°) is predicted in the cap and skin locations, precisely matching experimental observations.

To critically evaluate the significance of these predicted yield strength variations, precipitate and texture effects must be eliminated from the experimental observations. To minimize the precipitate strengthening effect, portion of the 2090 skin was overaged at 160°C for

400 hours. The resulting microstructure should contain the same volume fraction of matrix and precipitate as the usual aging procedures, but the coarsened precipitates will contribute less to strengthening and anisotropy. Figure 5 shows the correlation between the yield strength prediction of the plastic inclusion model and the experimental results for the overaged skin section of a 2090 extrusion. The correlation coefficient for the plastic inclusion model is 0.96 and the standard deviation is 9 MPa. These experimental results correspond well to the model predictions.

Refinement of the compression testing apparatus and the use of larger compression specimens has allowed more accurate and consistent yield strength data to be generated.

Recent Important Findings

A model has been developed that incorporates the effects of texture, precipitate characteristics, and grain morphology in a prediction of yield anisotropy. The effect of precipitate characteristics was addressed by consideration of the precipitate as elastic and plastic inclusions in two separate models. Both of these models predict similar behavior, so further research in this area will mainly focus on refinement of the plastic inclusion model. Grain morphology is predicted to have a measurable effect on yield anisotropy and magnitude.

Accurate predictions of yield strength anisotropy of as-received and overaged skin specimens were made. However, experimental results from the cap section deviated from the predictions of the model (standard deviation = 56 MPa). The shape of the curve correlated well with the variation in yield strength (correlation coefficient = 0.92), but the magnitude of variation was not predicted by the model. The observed variation of ~150 MPa in the cap section corresponds to about a 25% variation in yield strength as a function of stress axis orientation. For typical rolling texture, anisotropy of this magnitude is not usually predicted for Taylor factor (2.7 to 3.4) or precipitate strengthening factor (0.65 to 0.81). It is encouraging that, for all measured orientations, the current model does predict the correct trends in the anisotropy, and in most cases the magnitude of the anisotropy.

Since the yield strength predictions for the cap section specimens were the least accurate and good results were obtained for the overaged specimens, further refinement of the model appears to be necessary to correctly account for lath-shaped grains and precipitate strengthening.

Next Six Month Milestones

Development of the capability to calculate average Taylor factor and the strengthening contribution of precipitates in the plastic and elastic inclusion models for a specified uniaxial stress orientation is complete. The yield strength model consisting of grain orientation and precipitate orientation data accurately predicts the general trends of yield strength variation for the alloys tested, but to generate a more complete and exact description of the yield anisotropy, the effect of basic grain morphology effects will need further refinement.

Accurate model predictions have been made for several regions in the 2090 extrusion. Quantitative metallography will be performed on the tested regions of the 2090 extrusion to see if there is a preferred orientation of precipitates and to explicitly determine the matrix and precipitate material property inputs for the model. These results will be included in the model for 2090. To assess the general applicability and to fine tune the adjustable morphological parameters of these models, extensive yield strength testing, texture measurements and microstructural characterization will be conducted on 2096 and 2195 extrusions.

Viewgraph Captions

1. Title and Outline.

2. Approach - A brief description of the plastic inclusion model which is used to predict yield strength anisotropy given texture, grain morphology, and precipitate orientation data.

3. Dependence of Taylor Factor on Grain Shape - How Taylor factor is calculated for equiaxed and pancake-shaped grains.

4. Effect of Grain Morphology on Taylor Factor - Taylor factor variation for a rolling texture of a sample containing grains with equiaxed, pancake, and lath morphology.

5. 2090 Skin Overaged Yield Strengths - A comparison of experimental and predicted yield strengths for the 2090 skin in an overaged condition.

6. Example of Yield Strength Contribution of Texture and Precipitates for Skin of 2090 Extrusion - Taylor factor and precipitate strengthening variation for the skin of the 2090 extrusion.
7. Example of Yield Strength Prediction for Skin of 2090 Extrusion - Comparison of experimental and predicted yield strengths.

8. 2090 Skin and Cap Yield Strengths - A comparison of experimental and predicted yield strengths for the 2090 skin and cap regions.

9. Conclusions and Future Work

Effects of Texture and Microstructure on the Anisotropic Yield Strength of Wide Panel Aluminum Alloy Extrusions

M. T. Lyttle
J. A. Wert

University of Virginia
Department of Materials Science and Engineering

Objectives

- Characterize the effects of texture and microstructure on the yield strength in wide panel aluminum alloy extrusions
- Develop models which enable the prediction of locations in the extrusion and tensile axis orientations of minimum yield strength where localized yielding could occur in service

Approach

- Examine factors that influence the yield strength anisotropy of a material and construct models to predict this variation

- Models have been proposed which consider precipitate strengthening as either elastic or plastic inclusions. While the models are derived differently, similar results are predicted by both.

$$\sigma = M \tau (1 - f) + N \sigma_p f$$

1. Grain Orientation - Determines average Taylor factor for a specified stress axis orientation
   Grain Morphology - Deviation from spherical grains relaxes constraints from adjacent grains, modifying the average Taylor factor
2. Precipitate Orientation - Affects the amount of strengthening due to precipitates

- Compression tests of 2090 extrusion in the as-received and an overaged condition were conducted and validated the initial model constructions

- Using the same modeling and experimental methods in different aging conditions and on 2096 and 2195 extrusions, the role of grain morphology and precipitate orientation in influencing yield strength anisotropy will be investigated

Dependence of Taylor Factor on Grain Shape

Spherical grains

Stress State

$$\begin{bmatrix} -\sigma & 0 & 0 \\ 0 & 0 & 0 \\ 0 & 0 & 0 \end{bmatrix}$$

Strain State

$$\begin{bmatrix} -\varepsilon & 0 & 0 \\ 0 & -\varepsilon/2 & 0 \\ 0 & 0 & -\varepsilon/2 \end{bmatrix}$$

- Spherical grains are completely constrained by their neighbors
- Strain State is defined strictly by Hooke's Law
- Five slip systems are required to achieve the prescribed strain state
- Using pole figure data, generate a set of grain representative of the specimen texture
- Calculate the Taylor factor for each of these grains and average Taylor factor can be calculated directly

Pancake shaped grains

Stress State

$$\begin{bmatrix} \sigma & 0 & 0 \\ 0 & 0 & 0 \\ 0 & 0 & 0 \end{bmatrix}$$

Strain State

$$\begin{bmatrix} -\varepsilon & x & 0 \\ 0 & -\varepsilon/2 & 0 \\ 0 & 0 & -\varepsilon/2 \end{bmatrix}$$

- Deviation from equiaxed grains causes a relaxation in constraint from adjacent grains
- Surface tractions on large grain boundaries result in shear strains that can be accommodated by adjacent grains
- This accommodation enables fewer slip systems to achieve a modified strain state resulting in a lower Taylor factor

Effect of Grain Morphology on Taylor Factor

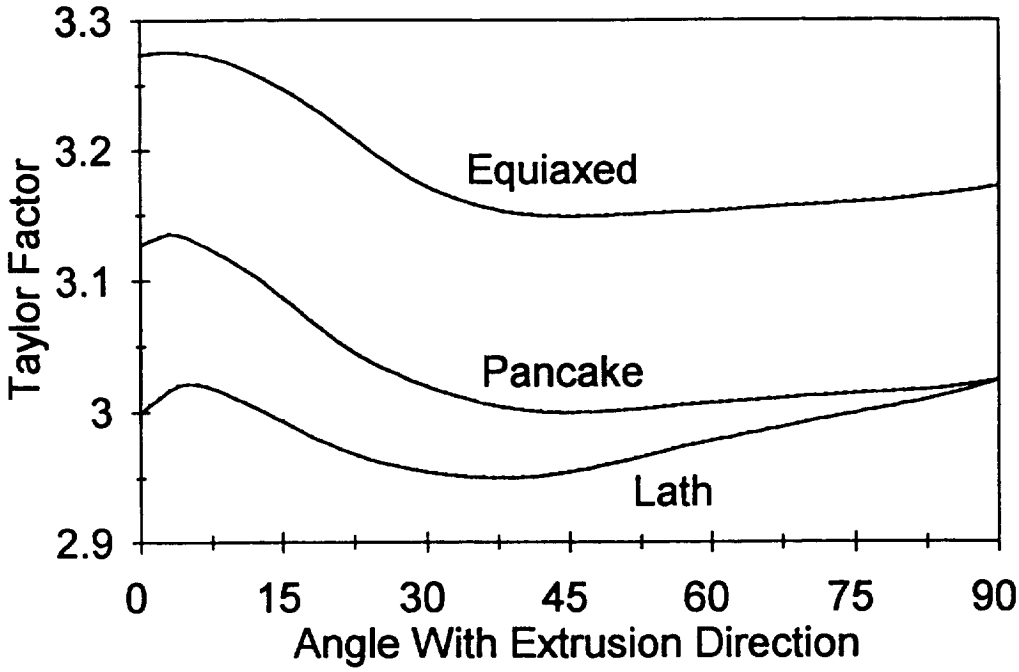

Comparison of 2090 Skin Overaged Predicted and Experimental Yield Strengths

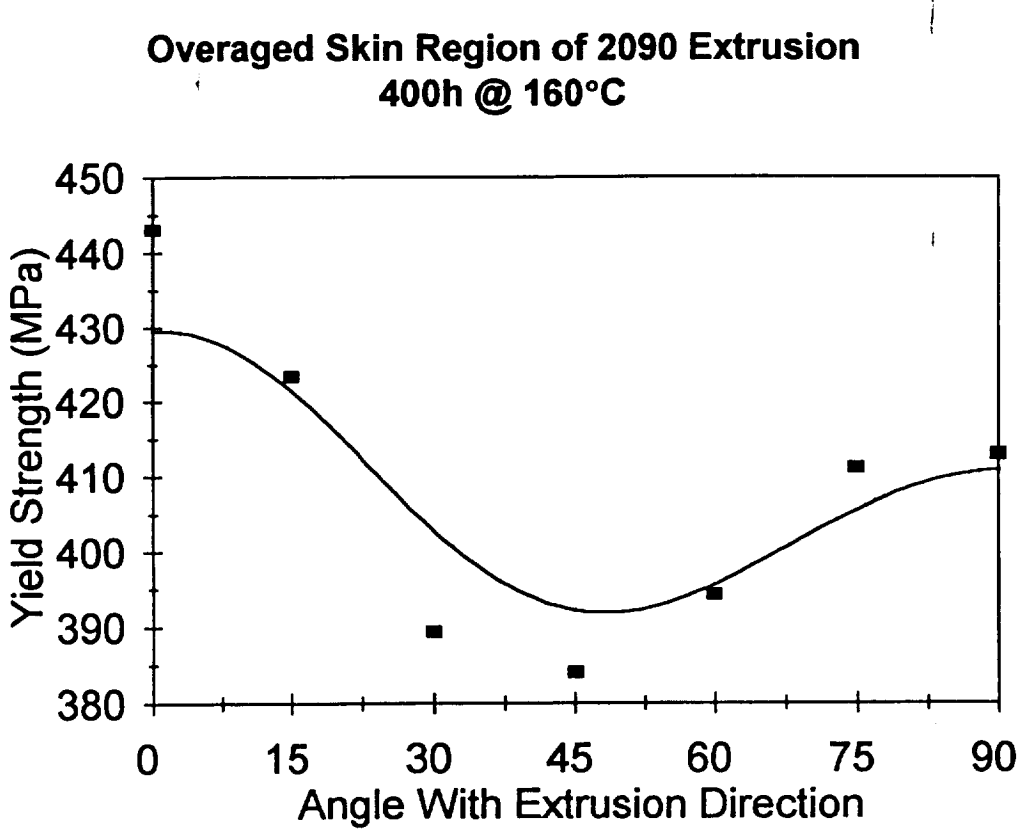

	Correlation Coefficient	Standard Deviation
Overaged Skin Region	0.96	9 MPa

Example of Yield Strength Prediction
Skin of 2090 Extrusion

Taylor Factor

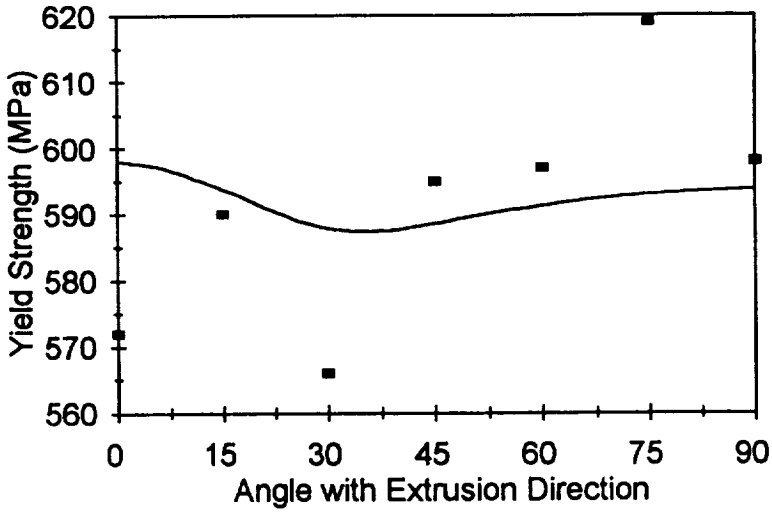

Precipitate Strengthening Ratio

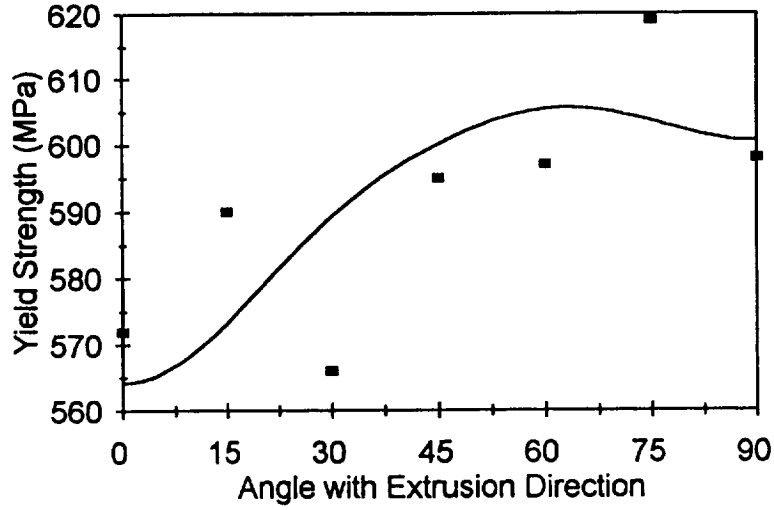

Example of Yield Strength Prediction
Skin of 2090 Extrusion

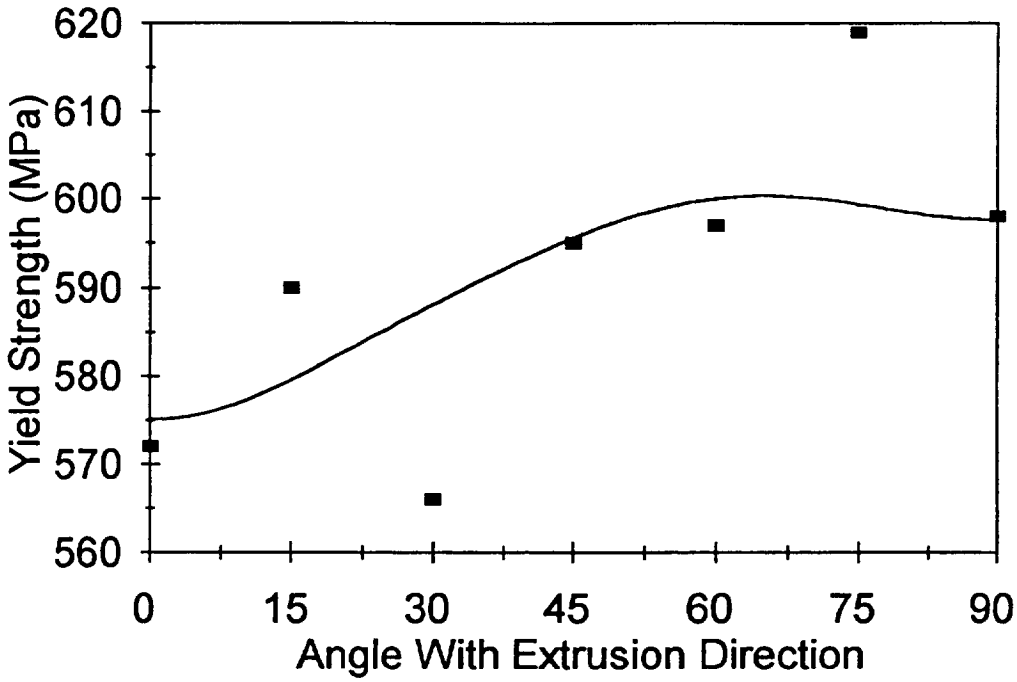

	Correlation Coefficient	Standard Deviation
Taylor Factor	0.02	18 MPa
Precipitate Strengthening	0.65	14 MPa
Yield Strength Model	0.69	13 MPa

Comparison of 2090 Skin and Cap Predicted and Experimental Yield Strengths

Skin Region of 2090 Extrusion

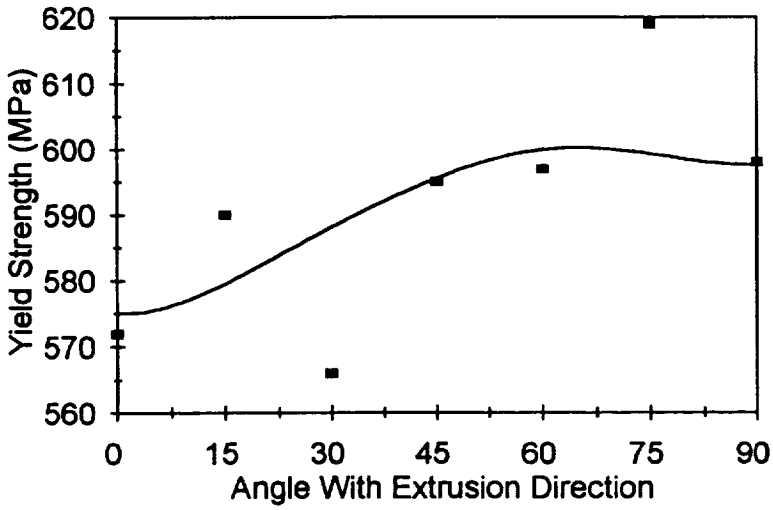

Cap Region of 2090 Extrusion

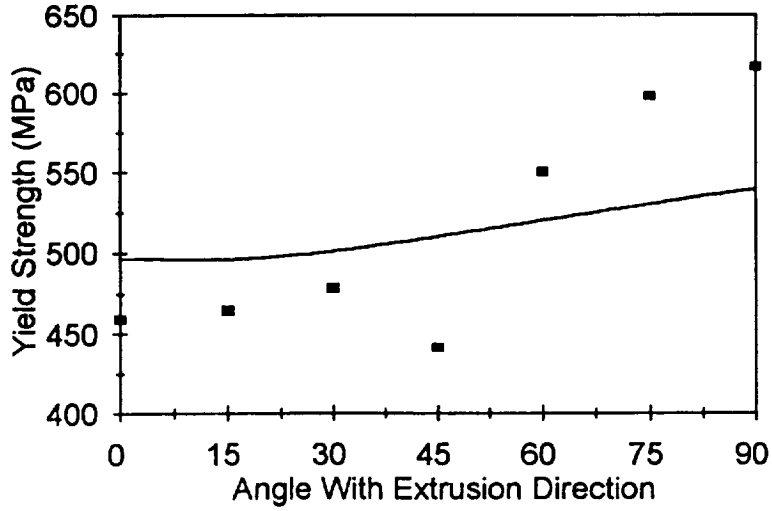

	Correlation Coefficient	Standard Deviation
Overaged Skin Region	0.96	9 MPa
Skin Region	0.69	13 MPa
Cap Region	0.92	56 MPa

Conclusions

- A model has been constructed that allows yield strength predictions based on texture, grain morphology, and precipitate plane orientation inputs.
- Accurate predictions of the trends in yield strength anisotropy in 2090 near net shape extrusions have been made.
- Refinement of compression testing techniques has allowed accurate determination of yield strength ($\pm$ 5 MPa)

Future Work

- Microstructural characterization of the 2090 extrusions and compression testing at different overaging times will allow refinement of the yield strength models.
- Similar testing will be conducted on 2096 and 2195 extrusions. Using a wide range of grain shapes and precipitate morphologies should allow a greater understanding of the role each play in the strengthening process.

Project #8 **Al-Si-Ge Alloy Development**

H.J. Koenigsmann and E.A. Starke, Jr.

Project Objective

The objective of this project is to investigate the strengthening mechanisms and the void nucleation process in a recently developed Al-0.55Si-2.02Ge (wt.%) alloy. The relationship between precipitate size and critical strain for cavity nucleation during plastic deformation is of primary interest.

Current Status

The volume fraction of the SiGe precipitates in a ternary Al-0.55Si-2.02Ge (wt.%) alloy was determined as a function of aging time using Transmission Electron Microscopy (TEM), electrical conductivity measurements, and X-ray diffraction lattice parameter measurements. The (111), (200), and (220) pole figures were determined from center sections of as-quenched samples and the results were converted into an Orientation Distribution Function (ODF) in order to calculate the Taylor factor.

Finite element calculations were performed on an IBM RS/6000 computer using the Abaqus software package. Meshes containing up to 7,000 triangular six-node elements were generated using the Patran software package. The stress and strain distributions around the SiGe precipitates were calculated for different precipitate diameters using both elasticity and plasticity models.

Recent Important Findings

The correlation between TEM measurements, electrical conductivity measurements, and lattice parameter measurements shows that there is still solute in solution in the T6 condition and that precipitation in Al-0.55Si-2.02Ge (wt.%) continues to occur up to about 100 hrs at 160°C. This observation led to a significant improvement of the theoretical yield strength prediction for this ternary alloy as a function of aging time.

Finite element calculations reveal that the maximum principal stress at the precipitate-matrix interface decreases approximately linearly with increasing precipitate diameter for both

the elasticity and plasticity models. This is consistent with the experimental observation that the volume fraction of voids decreases with increasing precipitate diameter for a given strain.

Future Work

The direct observation of voids around the SiGe precipitates will be attempted using TEM which would allow the determination of the void nucleation and void growth rates from measurements of the areal void density and the maximum void size as a function of strain for different aging times. This separation of void nucleation and void growth might provide an explanation for the experimental observation that the tensile ductility decreases with increasing aging time while the critical strain for cavity nucleation increases.

Furthermore, the quantification of the precipitate-matrix interfacial structure will be attempted using atomic resolution TEM in order to calculate the stresses associated with ledges and steps.

Presentation Viewgraphs

1. Title.
2. Outline.
3. Background.
4. Project objective.
5. Experimental procedure.
6. Experimental procedure (cont.).
7. Change of the SiGe precipitate size during aging at 160°C. The average precipitate diameter increases from 5.0nm after 1 day of aging to 14.4nm after 16 days of aging.
8. TEM microstructure. The microstructure of the ternary alloy after aging for 8 days at 160°C shows SiGe precipitates. <110> Al orientation.
9. Room temperature longitudinal tensile properties as a function of aging time at 160°C. With increasing aging time, the tensile ductility decreases significantly, whereas the decrease of both the yield strength and the tensile strength is almost negligible.

10. Prediction of the total theoretical yield strength. The total theoretical yield strength is estimated by adding the contribution of the precipitates, the yield strength of pure Al, and the contributions from grain boundary and solid solution strengthening.

11. Modified Orowan equation. This equation predicts that the contribution of the precipitates to the yield strength is proportional to the square root of the precipitate volume fraction and inversely proportional to the precipitate diameter. The ratio between the Taylor factor calculated from X-ray diffraction data and the Taylor factor calculated for fcc metals with a random distribution of grain orientations was also taken into account.

12. TEM measurements of the SiGe precipitate volume fraction as a function of aging time at 160°C. This is a direct method to determine the precipitate volume fraction, but it is associated with significant experimental errors.

13. Measurements of the electrical conductivity of the ternary alloy as a function of aging time at 160°C. These measurements are associated with very small experimental errors, but it is an indirect method and Nordheim's rule was used to estimate precipitate volume fractions based on these results.

14. Measurements of the lattice parameter of the matrix as a function of aging time at 160°C. This is a third independent approach to estimate precipitate volume fractions, but is also an indirect method and Vegard's rule was used to convert the data into precipitate volume fractions.

15. Determination of the volume fraction of the SiGe precipitates as a function of aging time at 160°C. The average value of the precipitate volume fractions determined using TEM, electrical conductivity measurements, and lattice parameter measurements was used in the modified Orowan equation to estimate the contribution of the precipitates to the yield strength for each aging time.

16. Size distribution of the SiGe precipitates during aging at 160°C. The precipitate diameter used in the modified Orowan equation was based on the precipitate size distribution for each aging time shown here for the shortest and the longest aging times.

17. SEM fracture surface of the peak-aged ternary alloy after performing a room temperature tensile test in longitudinal direction. The micrographs reveal that fracture occurred as dimpled rupture.

18. Determination of the volume fraction of voids as a function of strain and precipitate diameter. The volume fraction of voids was determined through a pycnometer by measuring densities of the deformed gage section and the grip part. All measurements were performed before necking occurred. The volume fraction of voids decreases with increasing precipitate diameter at a given true strain value. The critical strain to nucleate cavities (ϵ_c) was determined from the experimental data by linear regression.

19. Energy criterion for cavity nucleation. This criterion predicts that the critical strain to nucleate cavities is independent of the precipitate size.

20. Geometrical correction factor used in the energy criterion. This correction factor takes into account that cavities nucleate at particle poles in the direction of the tensile axis.

21. Coarsening theory developed by Lifshitz and Wagner. This theory predicts that, when the rate of coarsening is controlled by the diffusion of the solute species through the matrix, the cube of the average precipitate radius increases linearly with aging time.

22. Determination of the precipitate-matrix interfacial free energy. The precipitate-matrix interfacial free energy (γ) is a parameter in the energy criterion for cavity nucleation. This parameter was estimated from coarsening data using the theory developed by Lifshitz and Wagner. Note that the graph is only drawn for longer aging times when the precipitate volume fraction stays approximately constant.

23. Evaluation of the energy criterion for cavity nucleation. The experimental results agree approximately with the prediction of the energy criterion, but the critical strain clearly depends on the precipitate size contrary to the prediction of this criterion.

24. Stress Criterion for cavity nucleation. This criterion predicts that the critical strain to nucleate cavities depends linearly on the precipitate size.

25. Evaluation of the stress criterion for cavity nucleation. The experimental results agree well with the prediction of the stress criterion if the critical stress is chosen as 1/40 of the shear modulus of the matrix and if the numerical parameter α is chosen as 1/7.

26. Typical finite element mesh used for the calculations of the elastic stress and strain distributions around two quarter precipitates. This mesh contains 6,570 triangular six-node elements. Based on symmetry considerations, the boundary conditions were chosen in such a way that the displacements are zero in the vertical direction along the horizontal lower edge and in the horizontal direction along the two vertical edges. A uniform load based on the experimental tensile data was applied in the vertical direction along the horizontal upper edge.

27. Typical distribution of the maximum principal elastic stresses around two quarter precipitates. This stress distribution reveals that the stresses associated with the smaller (left) precipitate are larger than those associated with the larger (right) precipitate. This is consistent with the experimental observation that the volume fraction of voids decreases with increasing precipitate diameter.

28. Ramberg-Osgood relationship. This relationship describes the mechanical behavior of the material as nonlinear at all stress levels, but, for commonly used values of the stress exponent ($n>5$), the nonlinearity only becomes significant at stress magnitudes exceeding the yield strength.

29. Typical finite element mesh used for the calculations of the total stress and strain distributions around a quarter precipitate. This mesh contains 3,570 triangular six-node elements. The boundary conditions and the load were chosen as described above.

30. Typical distribution of the maximum principal total stresses around a quarter precipitate. The total stresses were calculated using the deformation plasticity model based on the Ramberg-Osgood relationship described above. Only one quarter precipitate was considered since no overlap of the stress fields of the precipitates occurs.

31. Dependence of the maximum principal stress at the precipitate-matrix interface on the precipitate diameter using the elasticity and the deformation plasticity models. The stress decreases approximately linearly with increasing precipitate diameter for both models. The stresses predicted by the deformation plasticity model are always smaller than those predicted by the elasticity model as should be expected.

32. Conclusions.

33. Future work.

Al-Si-Ge Alloy Development

H.J. Koenigsmann and E.A. Starke, Jr.
Department of Materials Science and Engineering
University of Virginia

Sponsor: NASA LaRC

Outline

- Background and project objective
- Experimental procedure
- Tensile properties
  - Experimental results
  - Strengthening mechanisms
- Cavity nucleation
  - Experimental void volume fractions
  - Cavity nucleation models
  - Finite element calculations
- Conclusions and future work

Background

- Uniform distribution of very small SiGe precipitates
  - Diamond structure
  - Looped by dislocations
- High degree of hardening for a small volume fraction of precipitates
- Precipitate density in Al-Si-Ge alloys is one order of magnitude higher than in Al-Si and Al-Ge alloys
  - Si has smaller and Ge has larger atomic diameter than Al
  - Atomic size misfit can be compensated by pair formation
  - Similarities in electronic structure between Si and Ge

Project Objective

- Investigate strengthening mechanisms and void nucleation process in recently developed Al-0.55Si-2.02Ge (wt.%)
- Study relationship between precipitate size and critical strain for cavity nucleation during plastic deformation

Experimental Procedure

- Al-0.55Si-2.02Ge (wt.%) provided by Alcoa
  - Compensation of atomic size misfit
- Homogenization
  - 30hrs at 500°C (based on DSC)
- Hot rolling
- Solution heat treatment
  - 1hr at 490°C
- Cold water quenching
- Aging
  - Up to 16 days at 160°C

Experimental Procedure (cont.)

- Tensile tests as function of aging time
- Electron microscopy
  - TEM (quantitative stereology, CBED) and SEM
- Determination of precipitate volume fractions
  - TEM micrographs, electrical conductivity, lattice parameter
- Determination of Taylor factor
  - (111), (200), (220) pole figures, ODF
- Cavity nucleation measurements
  - Void volume fraction measurements (pycnometer)
  - Ultrasonic velocity measurements (SiGe shear modulus)

Change of Precipitate Size during Aging

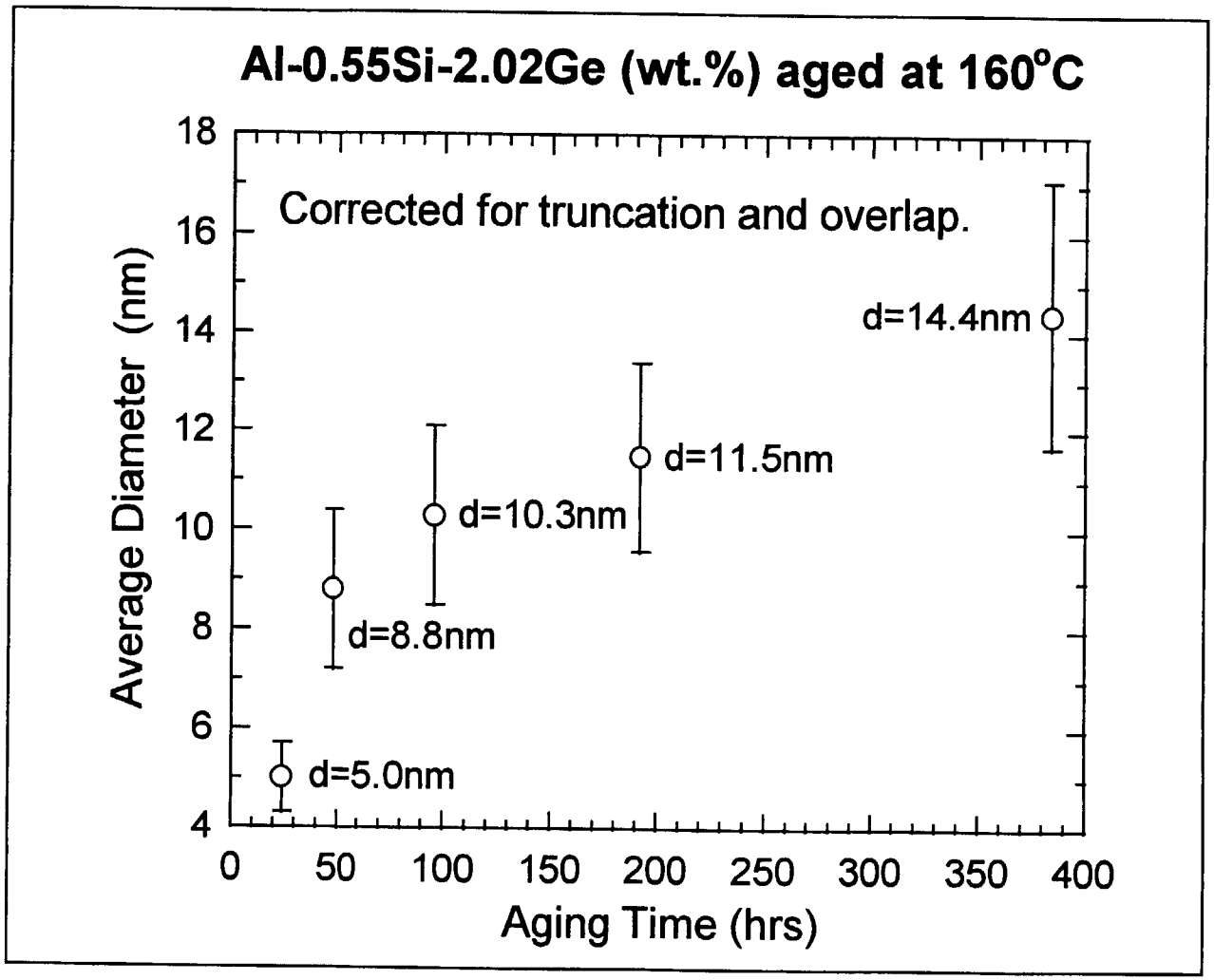

Microstructure (TEM)

Al-0.55Si-2.02Ge (wt.%) aged 8 days at 160°C

($[110]_{Al}$ zone axis)

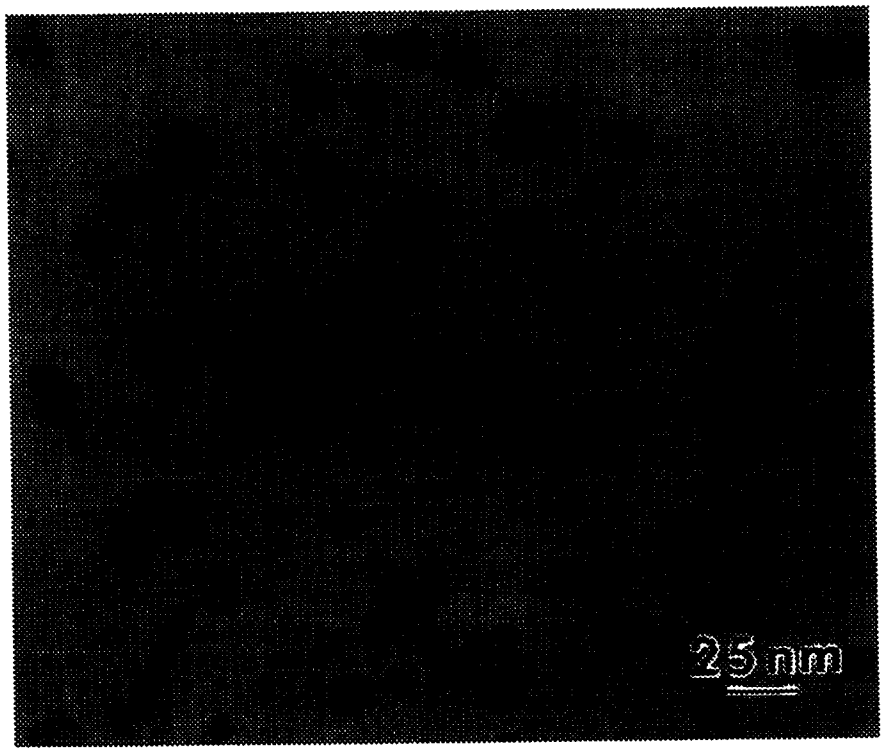

Tensile Properties after Aging at 160°C

t_a (d)	σ_{th} (MPa)	σ_Y (MPa)	σ_{TS} (MPa)	ε_f (%)
1	107	105	164	17
2	90	103	162	16
4	80	100	158	13
8	75	100	155	9
16	67	94	153	9

Theoretical Yield Strength

- $\sigma_{th} = \Delta\sigma_p + \sigma_{Al} + \Delta\sigma_b + \Delta\sigma_s$
  - Total theoretical yield strength: σ_{th}
  - Contribution of SiGe precipitates to the yield strength: $\Delta\sigma_p$
    - Decreases from 81MPa (1 day) to 42MPa (16 days)
  - Yield strength of pure Al: σ_{Al}
    - 20MPa
  - Contribution from grain boundary strengthening: $\Delta\sigma_b$
    - 5MPa (for a grain size of 200μm)
  - Contribution from solid solution strengthening: $\Delta\sigma_s$
    - 1MPa (Fleischer's approach)

Modified Orowan Equation

- $\Delta\sigma_p = M'\mu b\sqrt{f}/d$
  - Contribution of SiGe precipitates to the yield strength: $\Delta\sigma_p$
  - Ratio between Taylor factor calculated from X-ray diffraction data (2.86) and Taylor factor calculated for f.c.c. metals with a random distribution of grain orientations (3.06): M'
  - Shear modulus of the matrix: μ
    - 26GPa
  - Burgers vector: b
    - 0.284nm
  - Volume fraction of SiGe precipitates: f
  - Diameter of SiGe precipitates: d

TEM Volume Fraction Measurements

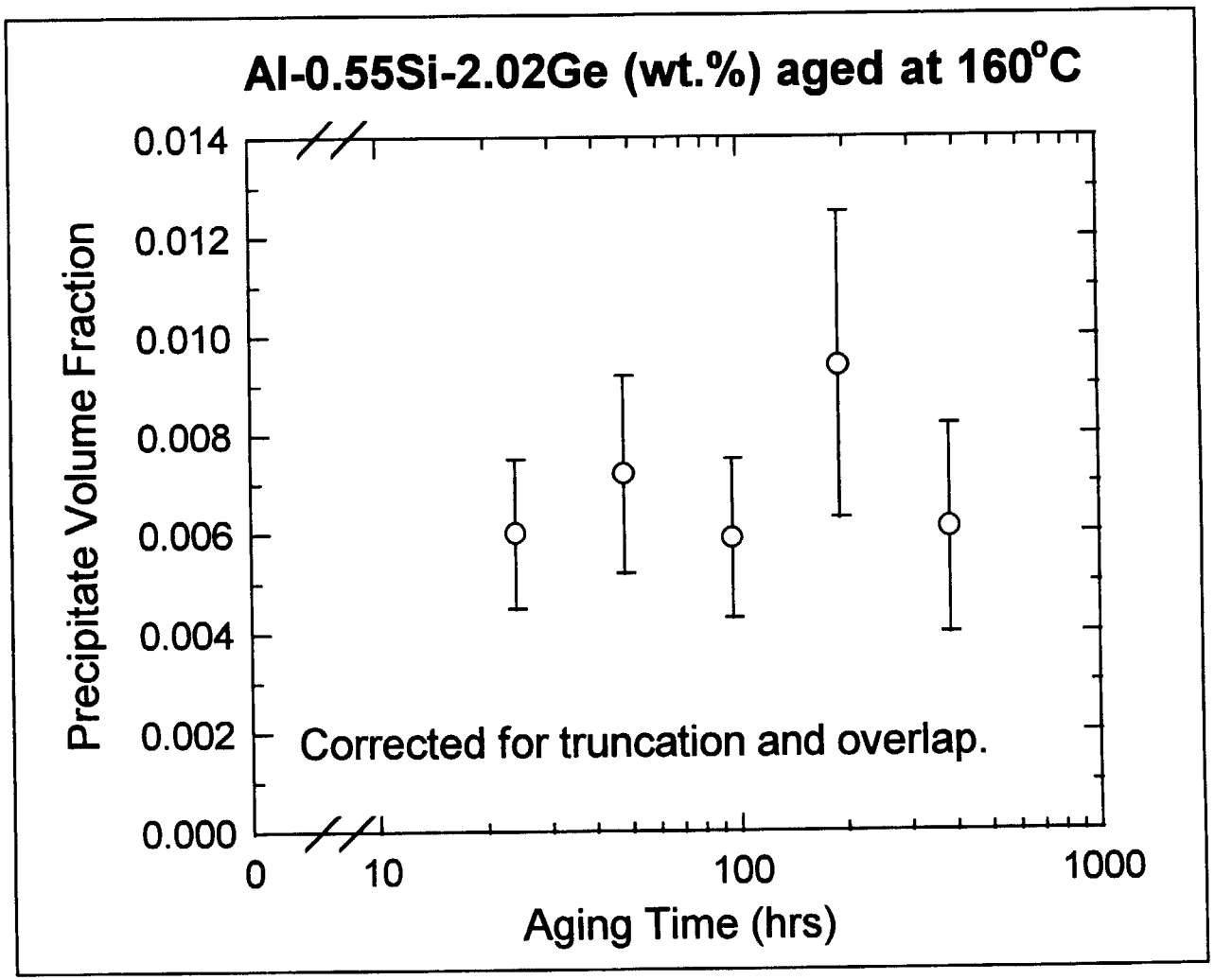

Electrical Conductivity Measurements

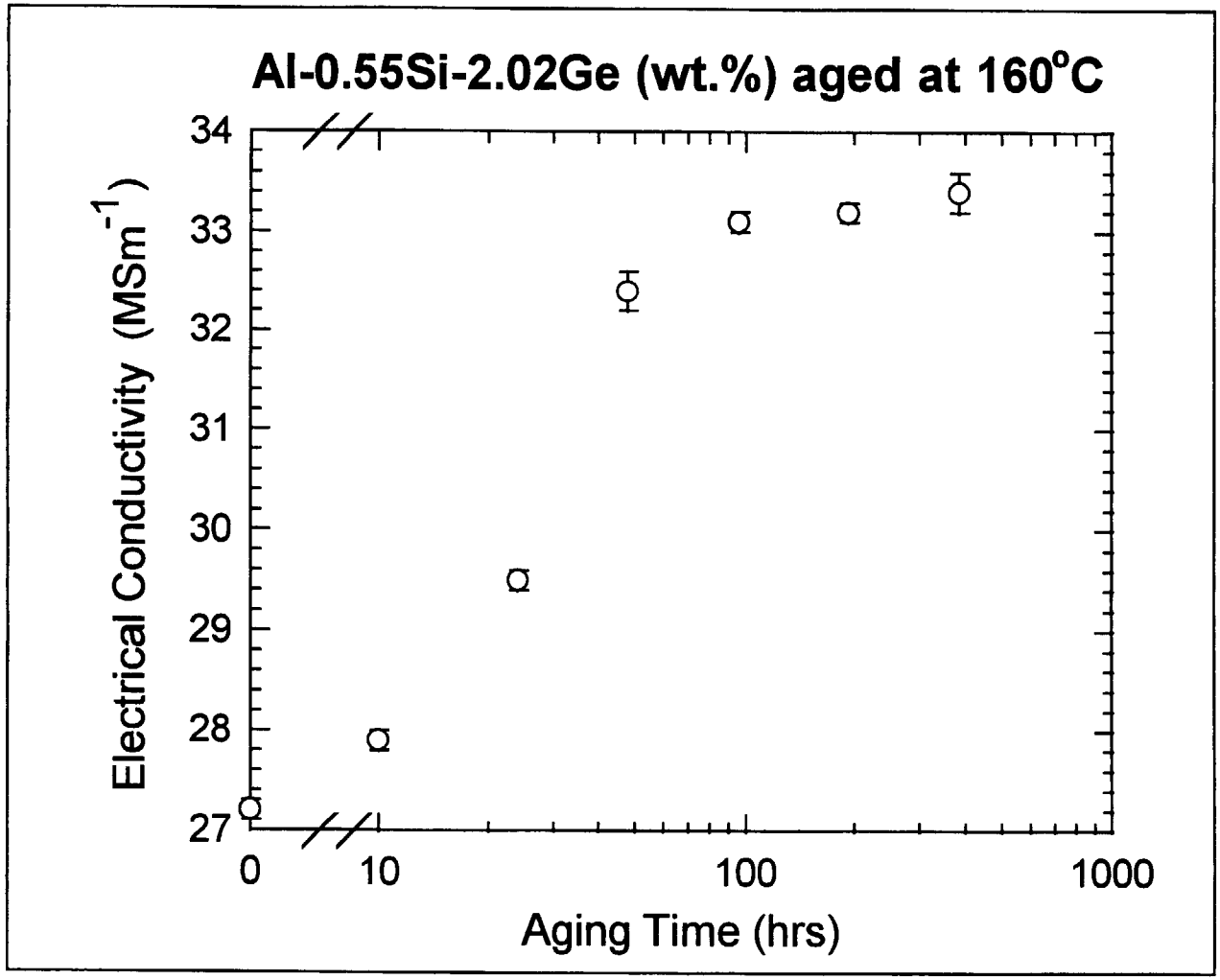

Lattice Parameter Measurements

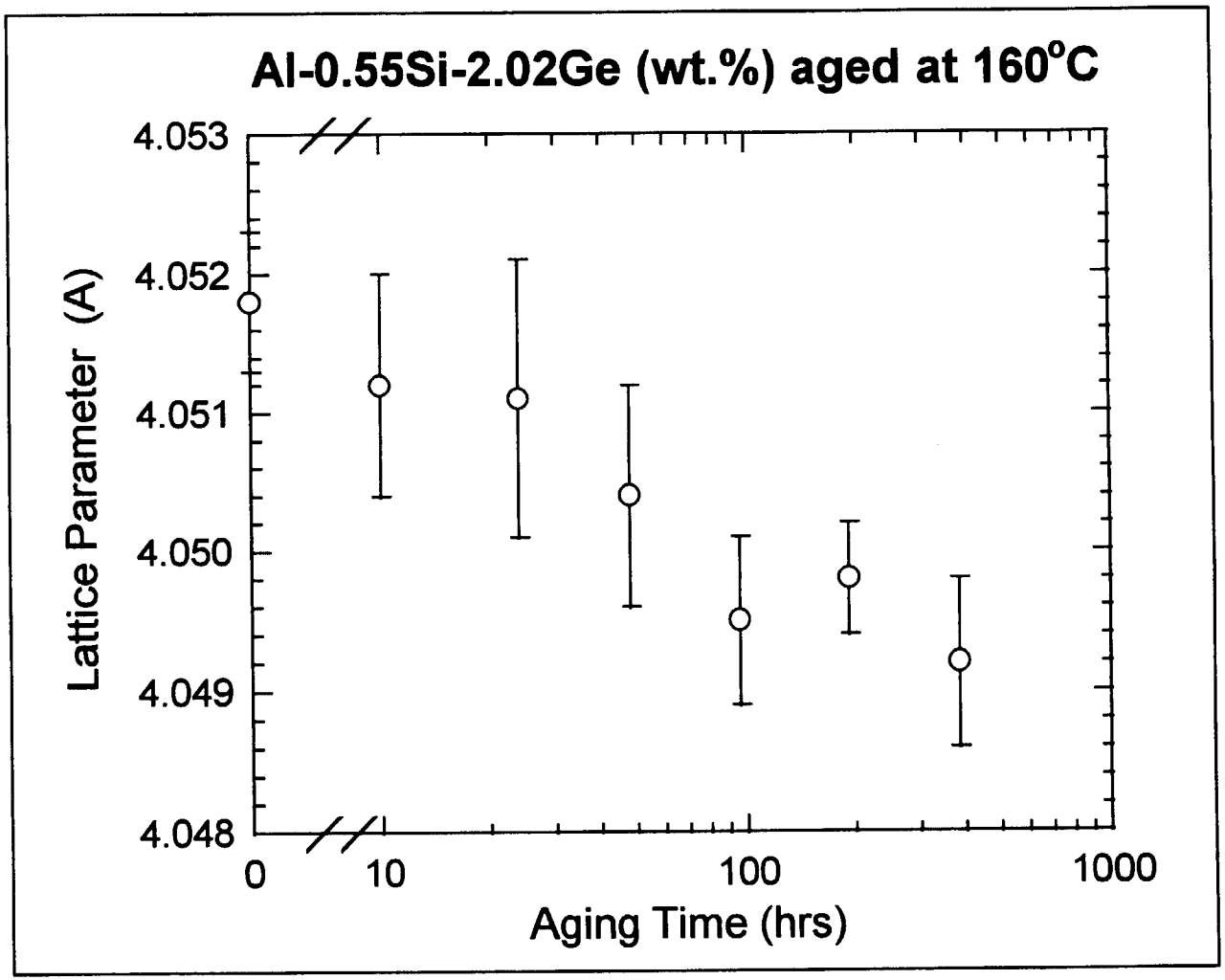

SiGe Volume Fraction Determination

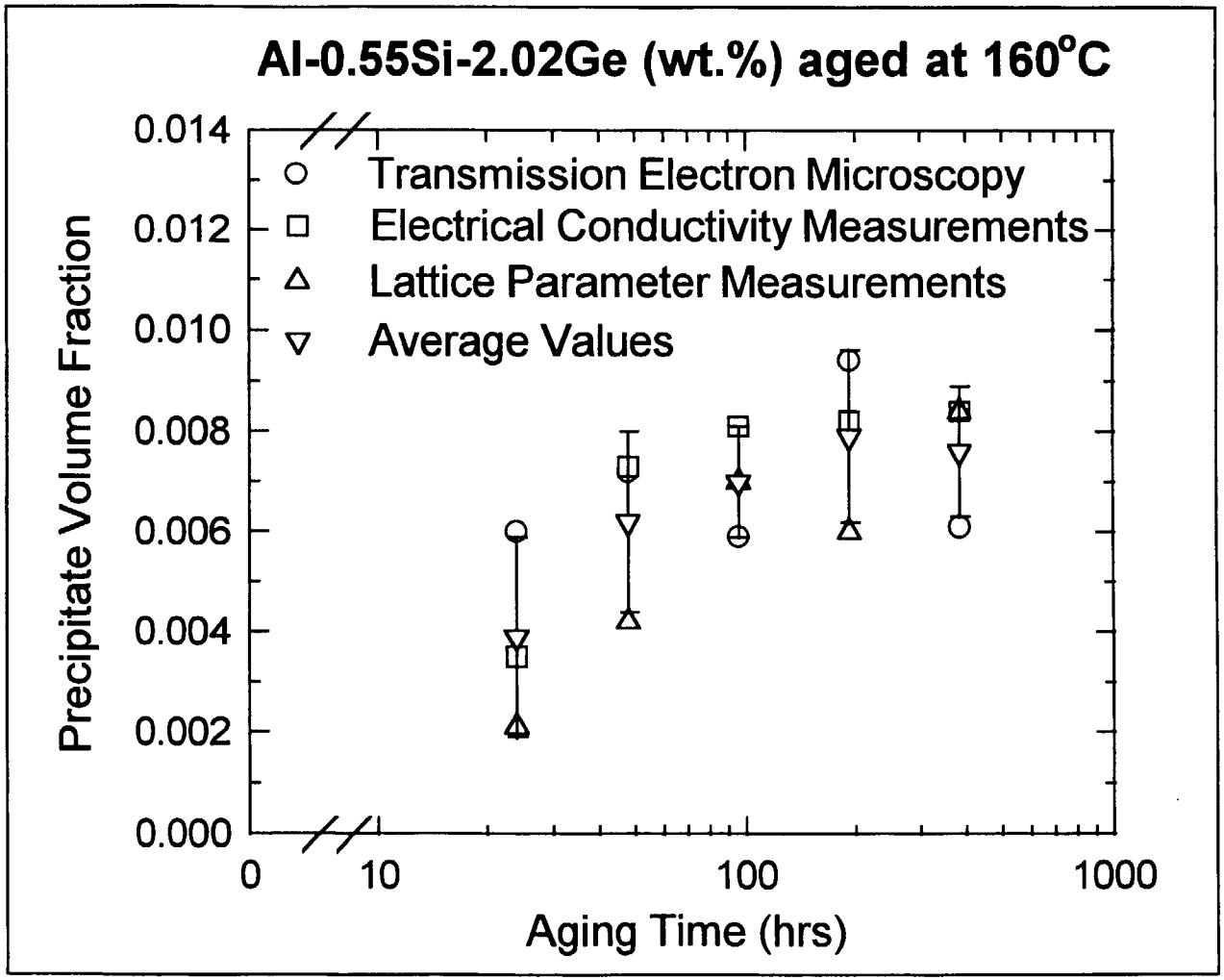

SiGe Precipitate Size Distribution

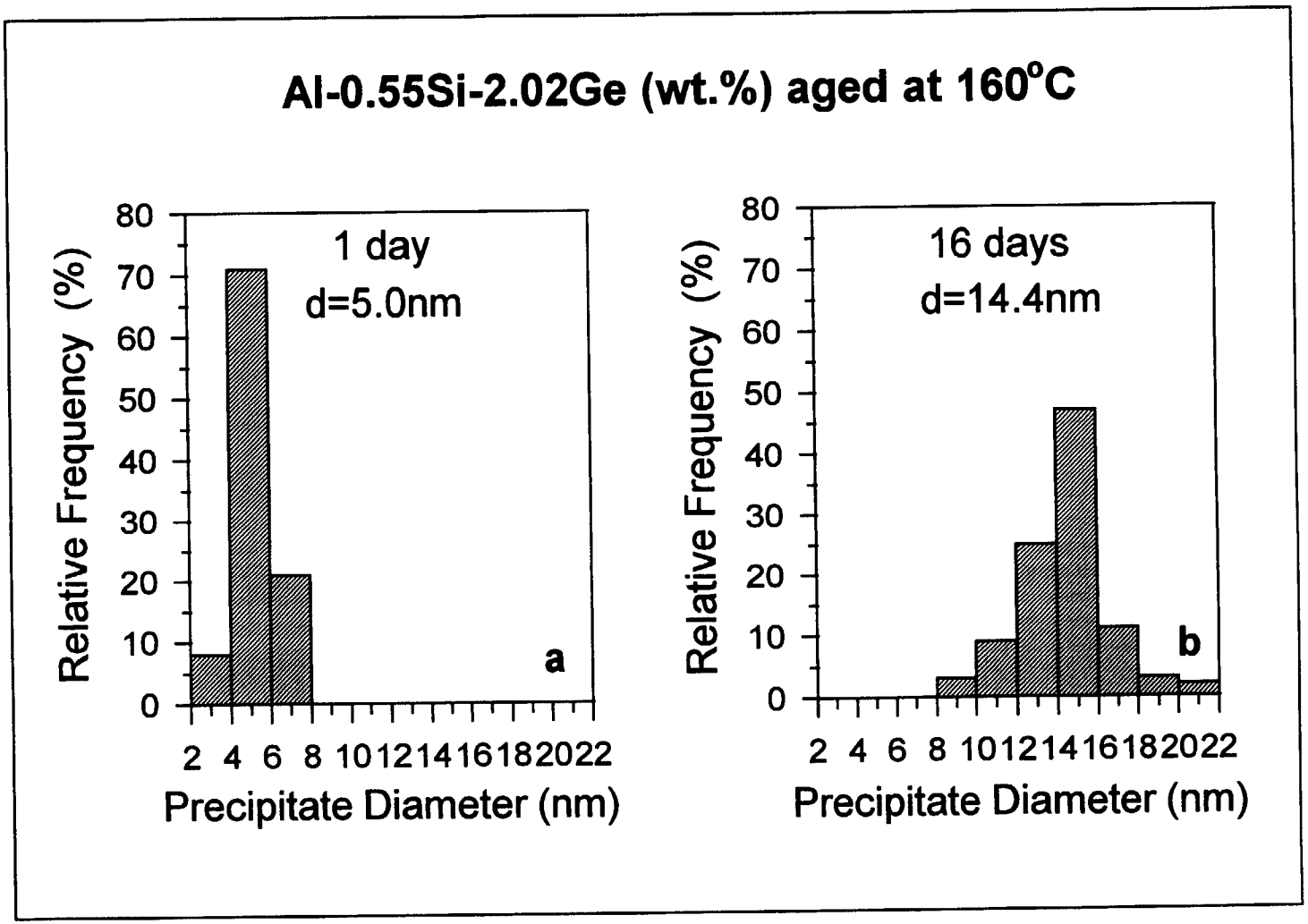

Fracture Surface (SEM)

Room temperature tensile test performed with Al-0.55Si-2.02Ge (wt.%) in longitudinal direction after peak-aging at 160°C

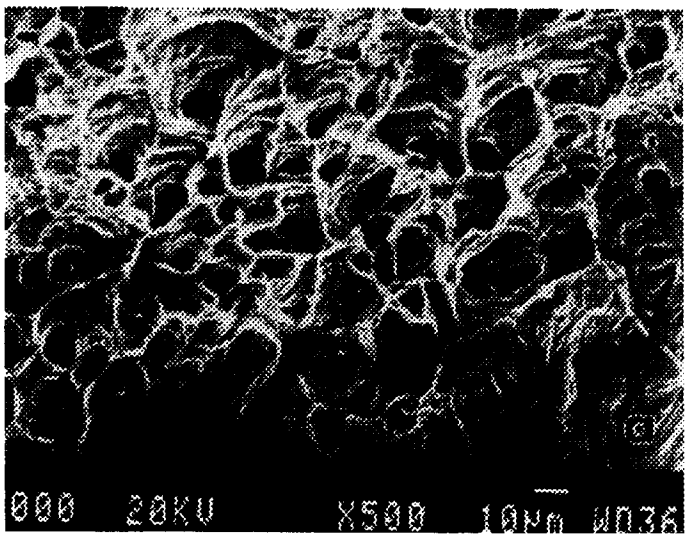

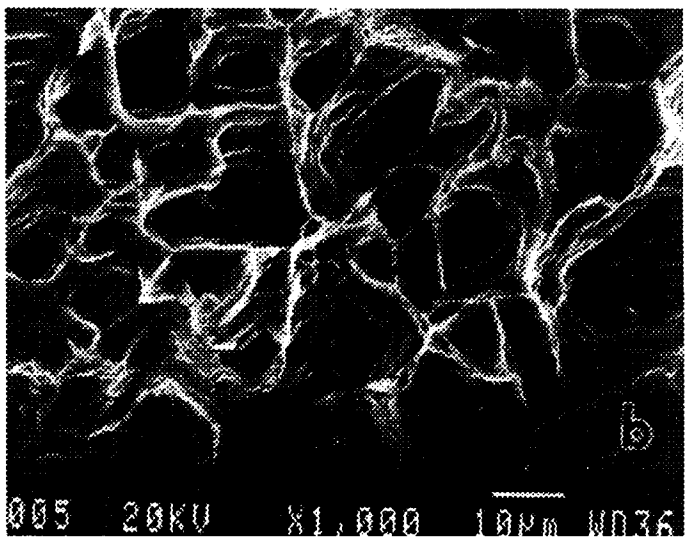

Determination of Void Volume Fraction

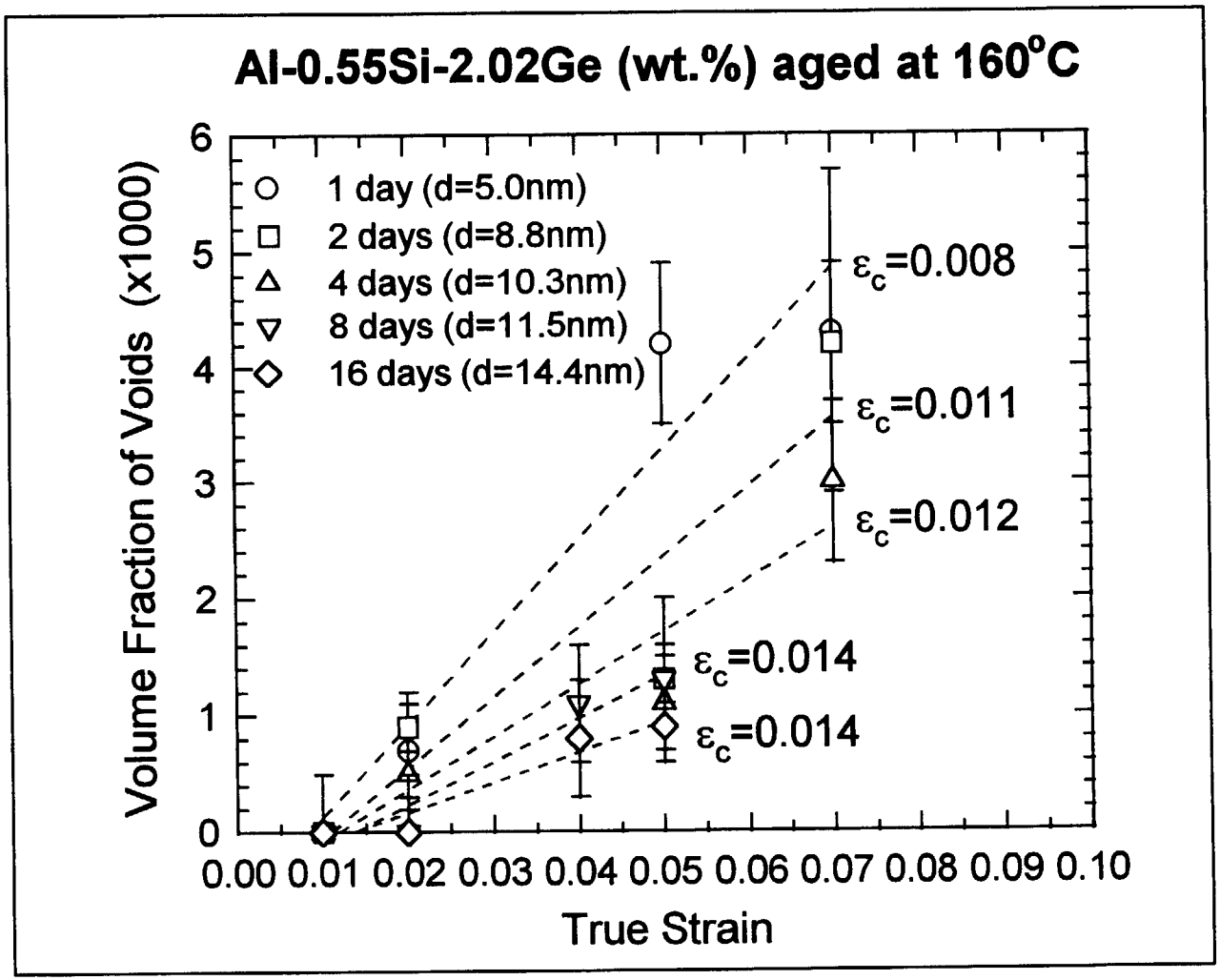

Cavity Nucleation: Energy Criterion

- $\Delta E_{el} + \Delta E_s \leq 0$
  - Internal elastic energy of the precipitates: ΔE_{el}
  - Energy increase in forming new surfaces: ΔE_s

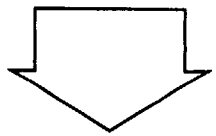

- $\varepsilon_c \geq \gamma(1-\cos\Theta)/2\mu_p b\sin^2\Theta$
  - Critical strain for cavity nucleation: ε_c
  - Precipitate-matrix interfacial free energy: γ
  - Geometrical correction factor: Θ
  - Shear modulus of the precipitates: μ_p
  - Burgers vector: b

Geometrical Correction Factor

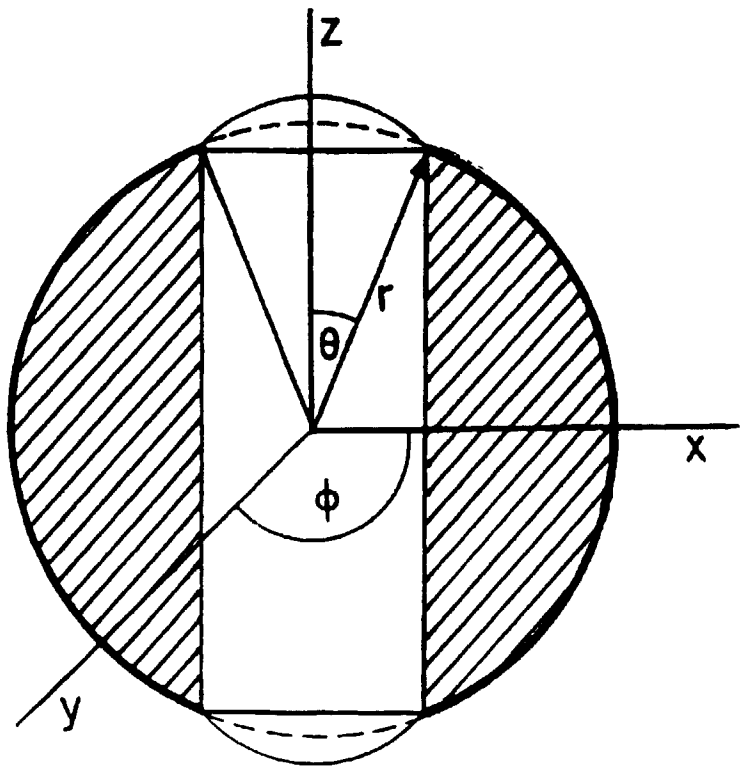

- Internal surfaces are formed from only a small fraction of the particle-matrix interface
- Elastic energy release occurs from the cylinder bounded by the cavity caps
- Resulting correction factor: $(1-\cos\Theta)/4\sin^2\Theta$

Coarsening Theory (Lifshitz & Wagner)

- $r^3 - r_o^3 = 8\gamma D c_o V_m^2 (t - t_o)/9RT$
  - Average precipitate radius: r
  - Initial average precipitate radius: r_o
  - Precipitate-matrix interfacial free energy: γ
  - Diffusivity of the solute species in the matrix: D
  - Equilibrium concentration of the solute species: c_o
  - Molar volume of the precipitate: V_m
  - Time: t
  - Time when coarsening commences: t_o
  - Gas constant: R
  - Temperature: T

Precipitate-Matrix Interfacial Energy

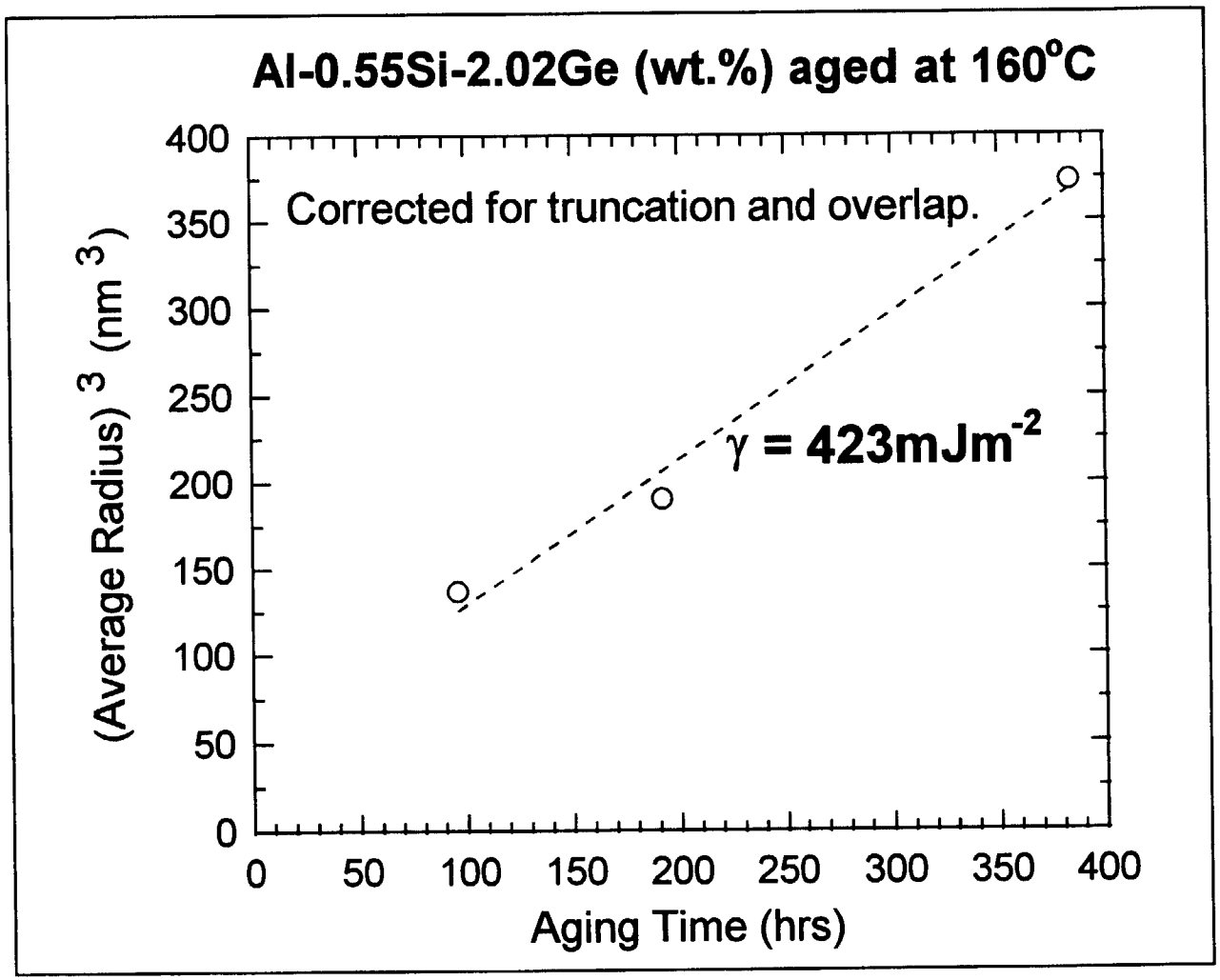

Evaluation of Energy Criterion

- $\varepsilon_c \geq 0.008$ independent of precipitate size
  - Precipitate-matrix interfacial free energy: 423mJm^{-2}
    - Estimated from coarsening data
  - Geometrical correction factor: 35°
    - Estimated from finite element calculations
  - Shear modulus of the SiGe precipitates: 49GPa
    - Determined through ultrasonic velocity measurements in the ternary alloy and in pure Al
  - Burgers vector: 0.284nm
- Experimental data between 0.008 and 0.014, but not independent of precipitate size

Cavity Nucleation: Stress Criterion

- $\sigma_c = 4.2\alpha\mu b\sqrt{\rho}$, $\rho = 5.1\varepsilon_c/db$
  - Critical stress: σ_c
  - Numerical parameter: α
  - Shear modulus of the matrix: μ
  - Burgers vector: b
  - Local dislocation density: ρ
  - Critical strain: ε_c
  - Precipitate diameter: d

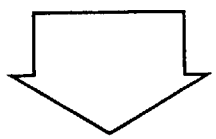

- $\varepsilon_c \geq \sigma_c^2 d/90\alpha^2\mu^2 b$

Evaluation of Stress Criterion

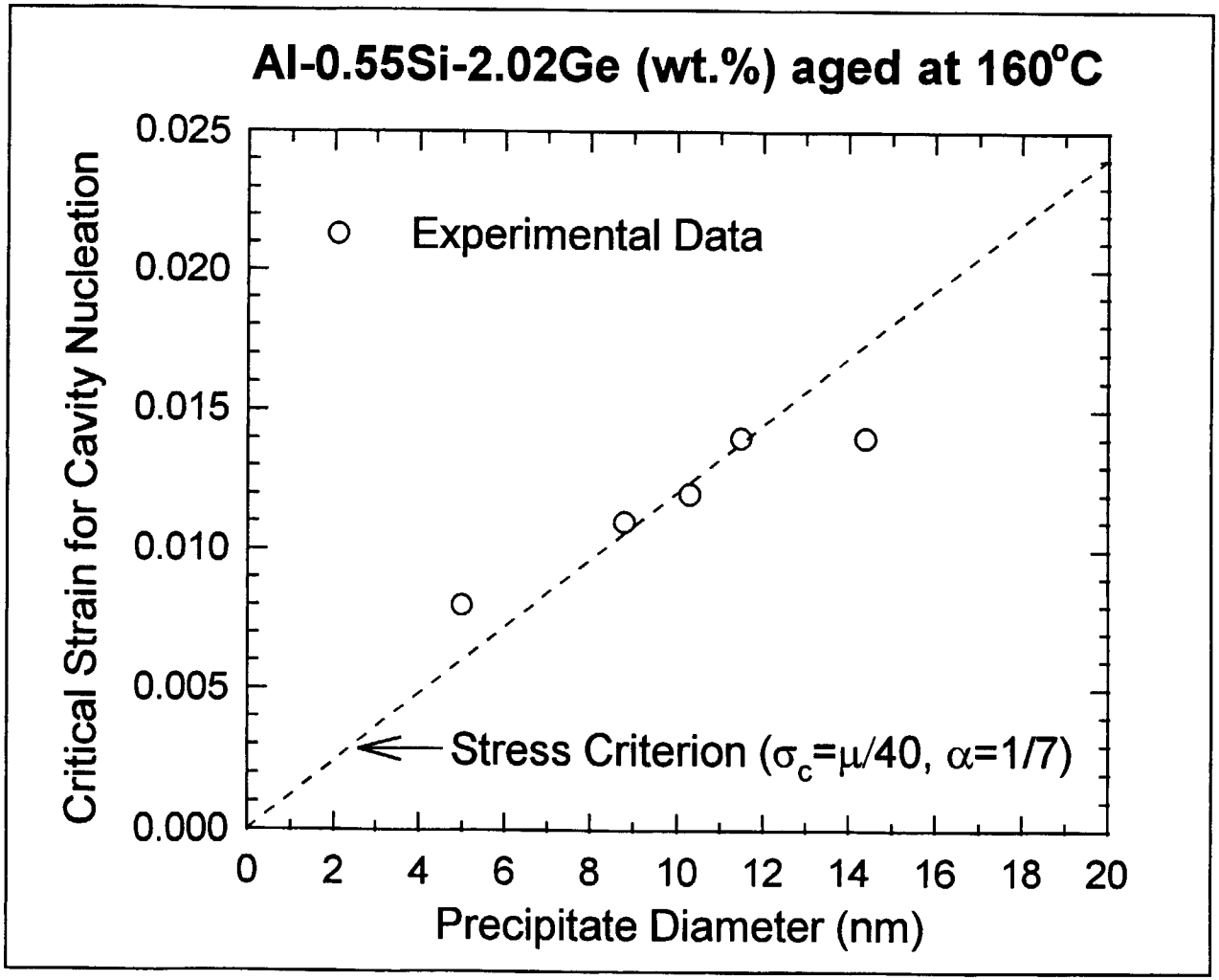

Mesh for Calculation of Elastic Stresses

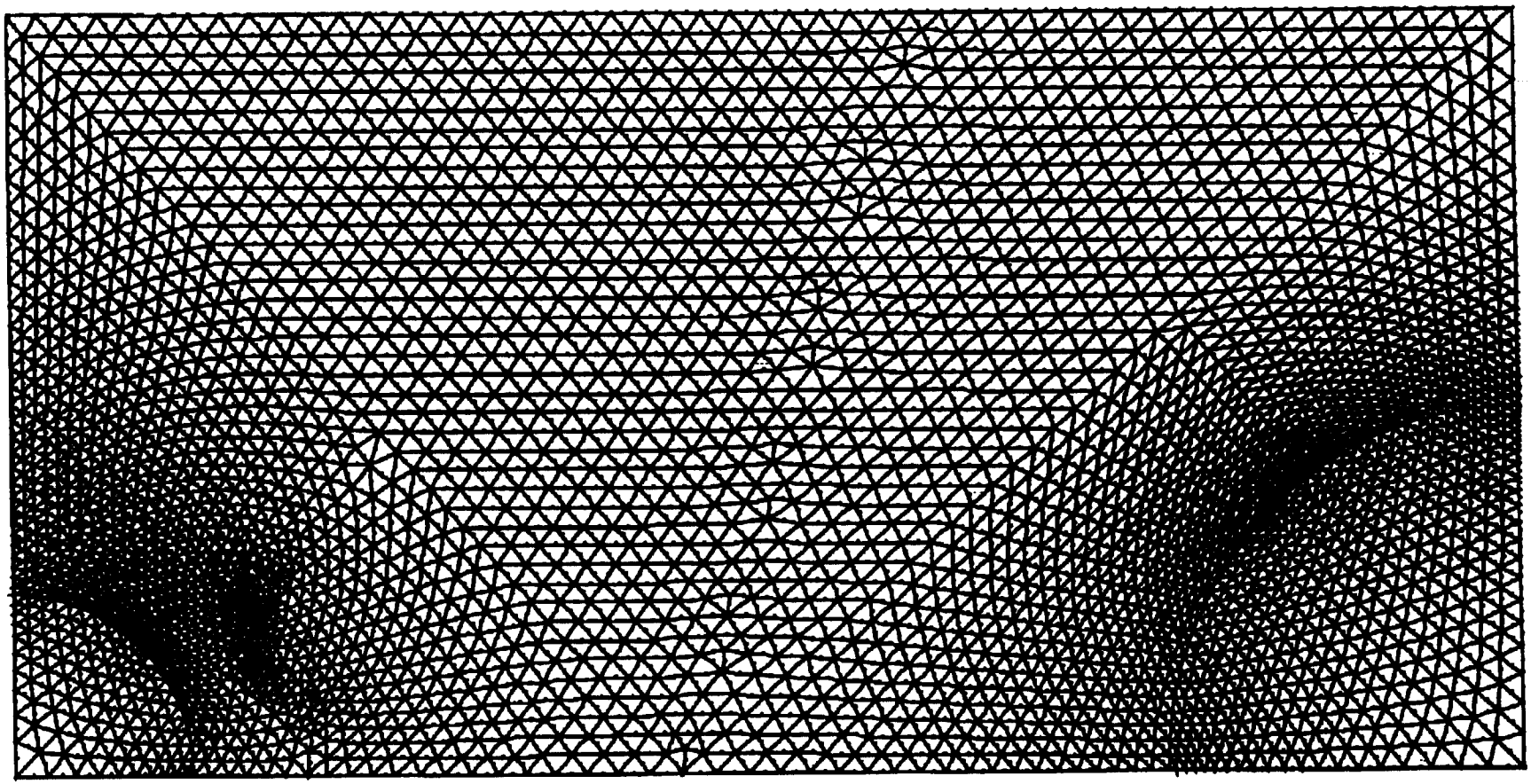

Elastic Stress Distribution around SiGe

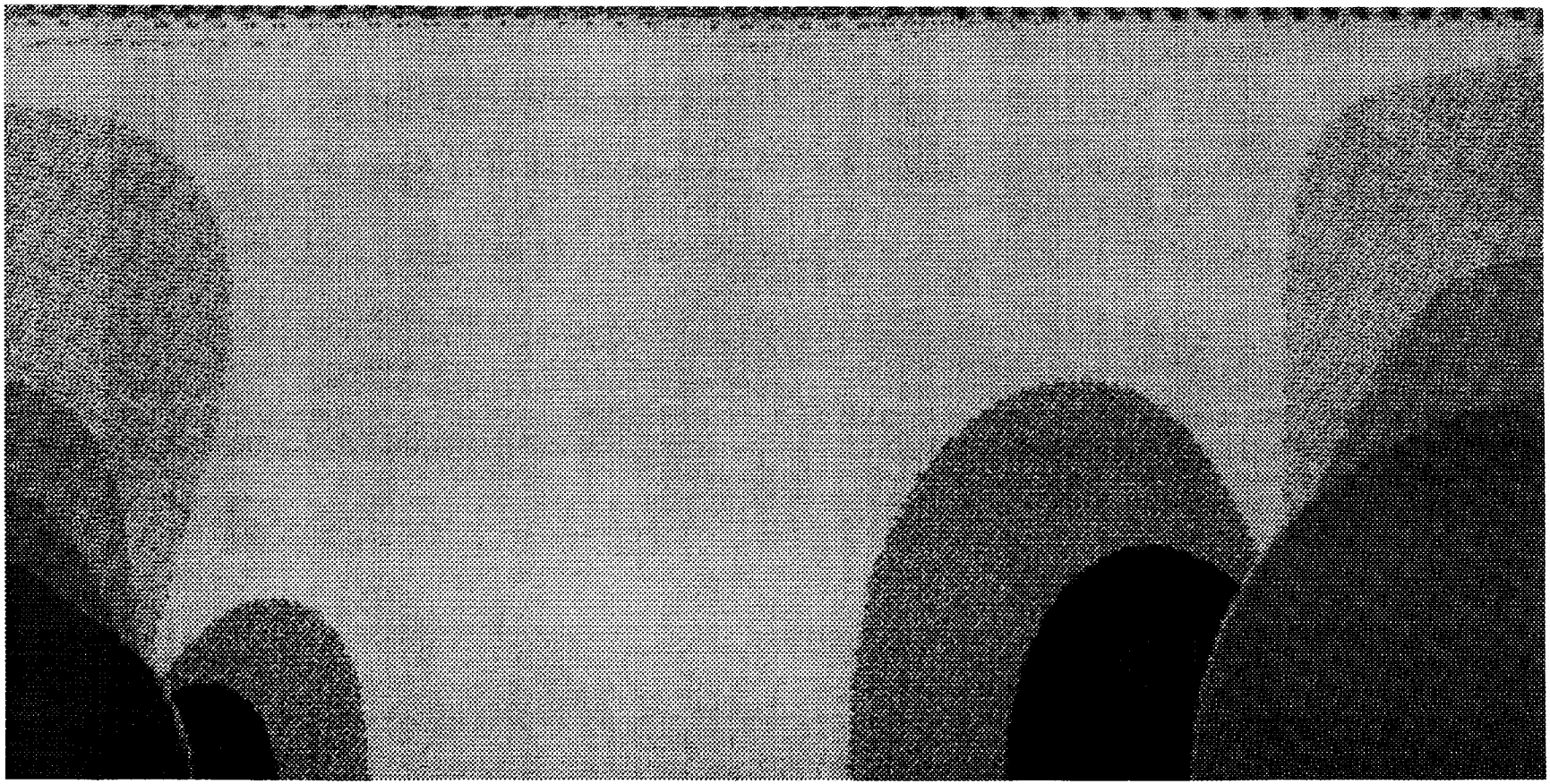

Ramberg-Osgood Relationship

- $E\varepsilon = \sigma + \alpha\,(|\sigma| / \sigma_Y)^{n-1}\,\sigma$
  - Young's modulus: E
  - Strain: ε
  - Stress: σ
  - Yield offset: α , defined in such a way that, when

    $\sigma = \sigma_Y,\ \varepsilon = (1 + \alpha)\,\sigma_Y / E$
  - Hardening exponent: n ($n \geq 1$)

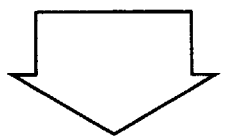

- Nonlinearity significant for $\sigma > \sigma_Y$ (if $n > 5$)

Mesh for Calculation of Total Stresses

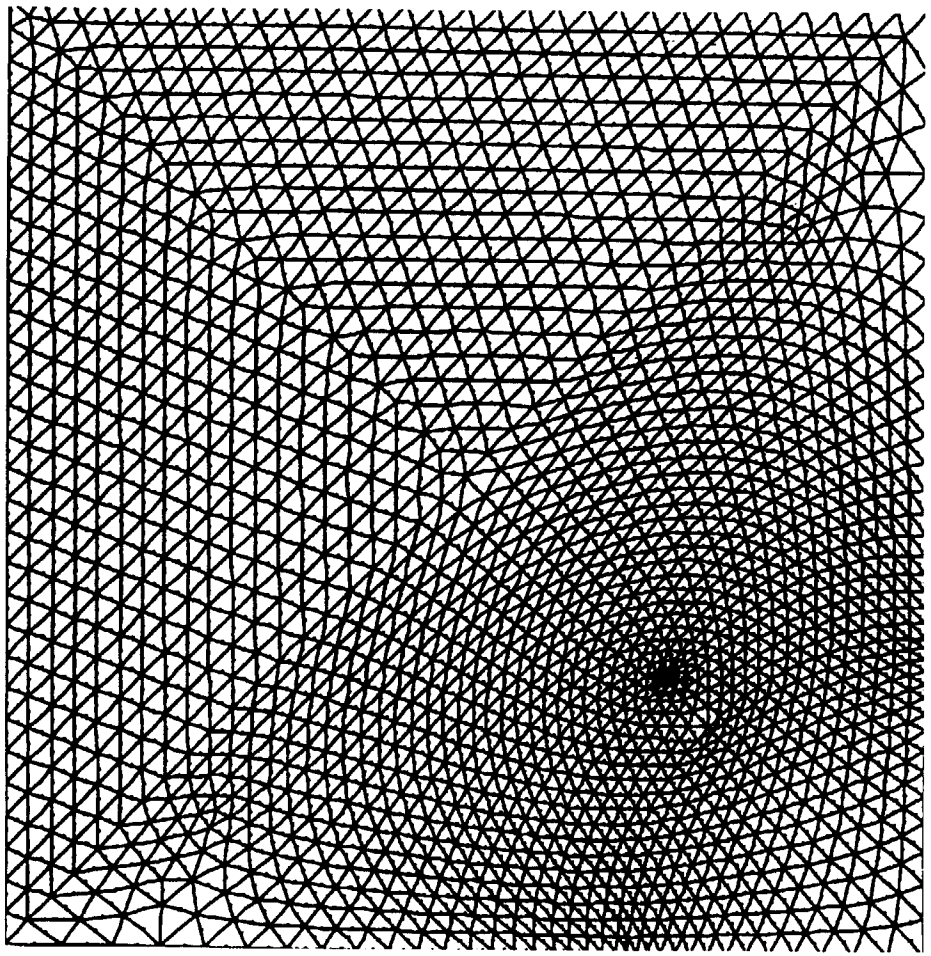

Total Stress Distribution around SiGe

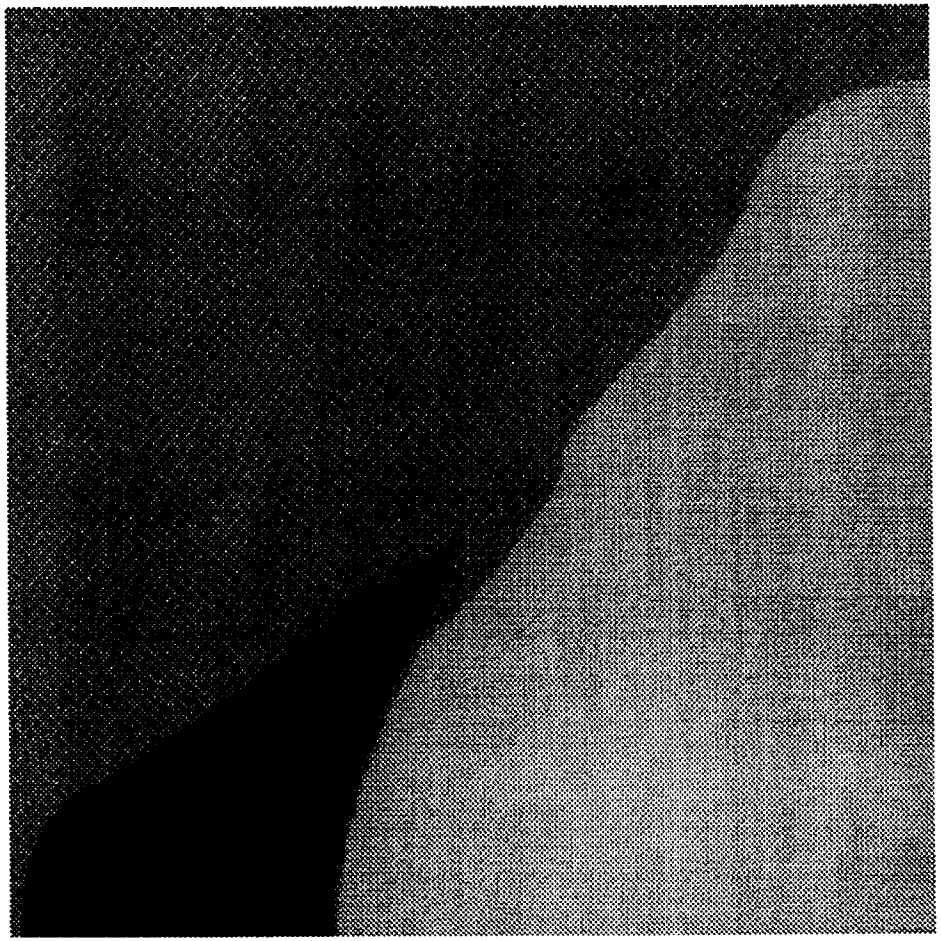

Finite Element Calculations

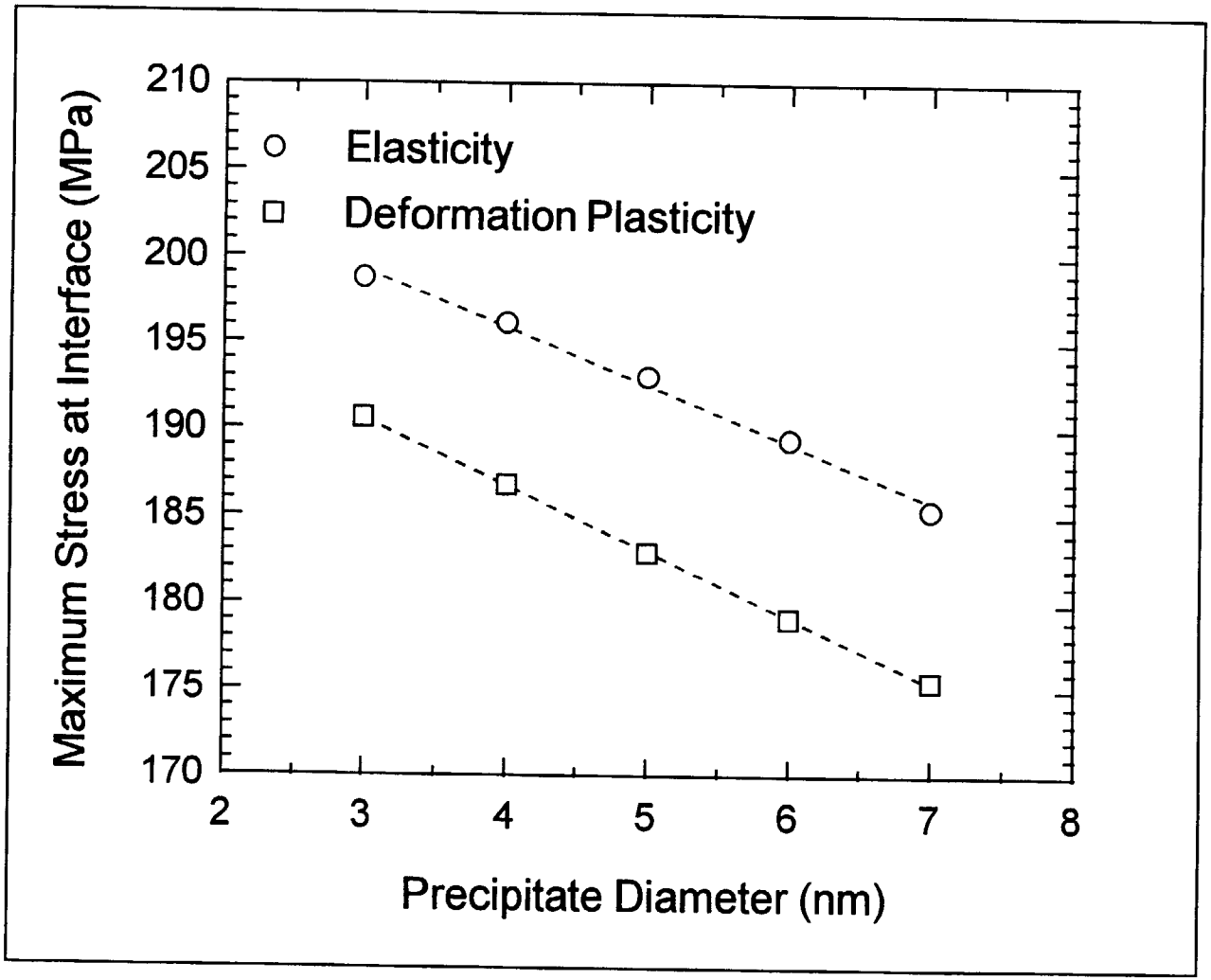

Conclusions

- Precipitation in Al-0.55Si-2.02Ge (wt.%) continues to occur up to 100hrs at 160°C
- Improvement of the yield strength prediction for this ternary alloy as a function of aging time
- Volume fraction of voids determined in this ternary alloy decreases with increasing diameter of the SiGe precipitates at a given true strain value
- Critical strain to nucleate cavities increases linearly with precipitate size in agreement with the stress criterion by Brown & Stobbs
- Finite element calculations are consistent with experimentally determined void volume fractions

Future Work

- Direct observation of voids around SiGe precipitates using TEM
  - Determination of void nucleation and void growth rates from measurements of areal void density and maximum void size as a function of strain for different aging times
  - Explanation of decreasing tensile ductility but increasing critical strain for cavity nucleation with increasing aging time
- Quantification of precipitate-matrix interfacial structure using atomic resolution TEM in order to calculate stresses associated with ledges and steps

Project #9 **Effect of Texture and Precipitates on Mechanical Property Anisotropy of Al-Cu-Mg-X Alloys**

Birgit Skrotzki, Gary J. Shiflet and Edgar A. Starke, Jr.

Objective

The objective of this study is to determine the effect of texture in unrecrystallized and recrystallized modified 2519 on the precipitation of the Ω and Θ' phases in the T6 and T8 conditions, and the associated relationship with anisotropy of the mechanical properties. In addition, the effect of an applied stress (both elastic and plastic) on nucleation and growth of the strengthening precipitates will be examined.

Current Status

Solution heat treated and T6 samples of the Al-Cu-Mg-Ag alloy were aged under stress to study the effect on nucleation and growth of precipitates. Solutionized binary Al - 5 wt.% Cu samples were also aged under stress to study the effect in greater detail. This alloy was used as a model system because its microstructure is less complicated than that of the quaternary alloy. The microstructure was characterized by TEM and the volume fraction, number density and size of precipitates were measured.

Recent Findings

Quantitative microstructure analysis was carried out to investigate whether preferential nucleation or growth on certain habit planes occurs when aging is done under stress. Therefore, the volume fraction was determined separately for every precipitate habit plane and the angle between the precipitate and the direction of the applied load was measured. The value of the measured angle, α, between precipitate and the stress direction is subtracted from 90°. This means that precipitates with $|90° - \alpha| = 0°$ are perpendicular and those with $|90° - \alpha| = 90°$ are parallel to the stress direction. For solution heat treated samples it was found that the higher volume fractions of Θ' are parallel and the lower volume fractions are perpendicular to the stress direction when the applied stress is 40% of the room temperature yield stress. For Ω, the values

are randomly scattered over the whole spectrum of angles when the same amount of stress was applied.

It was supposed that there might be a threshold stress which has to be exceeded before a similar effect can be observed for Ω. Therefore, samples were aged under a higher stress. After aging under a stress equivalent to the room temperature yield stress, the higher volume fractions are observed parallel to the stress axis for both type of precipitates. The threshold stress for Ω in this alloy is found to be between 119 and 142 MPa for solution heat treated samples. No comparable effect was found for samples in the T6 condition at this stress, neither for the volume fractions, nor for the number density or the size of the precipitates. Samples of the solutionized binary Al - Cu alloy were also aged under a different stress to study the observed effect in greater detail. A similar effect was observed. The Θ' phase precipitates preferentially parallel to the stress axis. The threshold stress for Θ' is found to be between 16 and 19 MPa.

The following discussion will focus on the Al-Cu system because there are more data available on precipitation of Θ' than for Ω, but may also apply to the more complicated alloy. An externally applied stress during aging can affect nucleation of precipitates or their growth (coarsening) or both. If nucleation is affected, the number of particles perpendicular to the stress axis should be dramatically different than the number parallel to the axis. Likewise, if growth is affected, the precipitate length/thickness should be different parallel and perpendicular to the applied stress axis. A large effect on nucleation was observed since most of the Θ' precipitates are parallel to the stress axis. The following discussion will also argue that the growth and coarsening behavior should be affected, as well because of the presumed growth ledges on the plates.

A model developed by Dahmen and Westmacott suggests that the smallest Θ' precipitate (critical nucleus) is 2 unit cells and has a vacancy misfit (negative). Stobbs and Purdy have experimentally shown that 2 unit cells (or smaller) indeed have a vacancy-type misfit. A 2 unit cell Θ' precipitate fits into 3 unit cells of the Al-matrix with a misfit of - 4.5 % (calculated from the lattice parameters). Based on previous work (i.e. δ' in Al-Li) a negative misfit with the matrix will result in nucleation of the precipitate in the compressed region of the matrix. Therefore, it is concluded that the plate shaped Θ' nuclei should preferentially nucleate parallel to the tensile stress axis, because it is this direction that is under compression. This contradicts

the results of Hosford and Agrawal. They found a higher density of Θ' precipitates perpendicular to the tensile stress axis. (Nevertheless, it has to be noted that their single published micrograph (in a [310] orientation) is not conclusive and they did not carry out any quantitative analysis.) In contrast to their findings, Eto, et al., observed preferential precipitation parallel to the stress axis which is in agreement with our observations. Is has to be noted that different aging temperatures were used.

Calculations from the lattice parameters indicate that Ω nuclei probably have an even larger vacancy type misfit and are therefore affected in the same way. The growth and coarsening behavior is probably affected as well because of the mechanism of thickening of a precipitate plate is by the movement of ledges. This has not been observed in the T6 samples so far but might show if the aging is carried out under a higher stress which exceeds the threshold stress for this condition.

Milestones

DSC measurements are planned to get more information about the sequence of precipitation and what type of precipitation stage is affected by the external stress. The question arises if precursor phases of Θ' form during heat-up. Preliminary results of DSC experiments show no dissolution of any phase before precipitation starts at 188°C in the Al-Cu-Mg-Ag alloy (no stress applied). This might be different if aging is done under stress. More TEM investigations need to be done to find out how the misfit is affected by stress aging. The approach first used by Ashby and Brown will be applied.

TEM work will be done on the new material (C415 and C416). Creep samples were sent by Alcoa and the microstructure will be characterized concerning grain boundary precipitation and coarsening of the precipitate phases.

Presentation Viewgraphs

1. Title.
2. Objective.
3. Subtitle.

4. Background: Effect of external and internal stresses associated with second phase particles.

5. Background: Reason for preferential nucleation and consequences of preferential precipitation.

6. Alloy composition and processing.

7. Precipitate phases and morphology.

8. Mechanical properties at room temperature and elevated temperature in solution heat treated and T6 condition for different orientations.

9. Parameters used for heat treatment, aging and stress aging.

10. Creep sample geometry used for stress aging experiments.

11. Experimental procedure for microstructure characterization.

12. Volume fractions of precipitates in Al-Cu-Mg-Ag measured for T6, T8, solution heat treated and stress aged and T6 and stress aged. Higher volume fractions of Ω and Θ' are present in prestrained samples than in T6. Further nucleation of Ω occurs in stress aged T6 samples than in T6 alone. Higher volume fraction of Θ' form after aging of solution heat treated samples under higher stress (SHT*) compared to lower stress.

13. Number density of precipitates in Al-Cu-Mg-Ag measured for T6, T8, solution heat treated and stress aged and T6 and stress aged. A high number density of Ω and Θ' formed after aging under stress. A high number density of Θ' formed after aging of solution heat treated samples under higher stress (SHT*) compared to lower stress.

14. Precipitate diameter and thickness in Al-Cu-Mg-Ag were measured for T6, T8, solution heat treated and stress aged and T6 and stress aged. Ω shows higher thermal stability than Θ'. Θ' starts to grow very early, but considerable growth of Ω occurs after 1000 h aging.

15. Volume fractions were measured separately for each variant in Al-Cu-Mg-Ag, and the angle α between the precipitate and the stress axis was measured. α was subtracted from 90°. $|90° - \alpha| = 0°$ is perpendicular to the stress axis. $|90° - \alpha| = 90°$ is parallel to the stress axis. In solution heat treated and stress aged samples, preferential precipitation of Θ' occurs parallel to the stress axis. No effect was observed for Ω.

16. For higher stresses, preferential precipitation of both kinds of precipitates parallel to the stress axis was observed for solution heat treated Al-Cu-Mg-Ag samples.

17. In binary Al-Cu preferential precipitation of Θ' was also observed for solution heat treated and stress aged samples.

18. Microstructure of stress aged Al-Cu in TEM. Stress direction is indicated by arrows. Almost all precipitates are parallel to the stress axis.

19. The threshold stress for preferential precipitation in solution heat treated samples was determined. No effect was observed in T6 samples.

20. Microstructure of Al-Cu in TEM. Sample was heated with applied stress to 160°C in about 70 min. Precipitates are Θ" and randomly distributed.

21. DSC curves show precipitation at temperatures higher than 160°C.

22. Schematic drawing showing the observed effect on microstructure in solution heat treated samples.

23. Definition of vacancy and interstitial type of misfit. Misfit predicted and observed for Θ' precipitates.

24. Crystallographic model for Θ' nucleus in Al-matrix. Note the properly oriented cube-cube relationship.

25. Due to the negative (vacancy) misfit, Θ' should nucleate in the compressed region of the matrix which is parallel to the external tensile stress axis. Growth should also be affected by an external stress because the elastic accommodation strain can be minimized by growth ledge heights which have the requisite number of Θ' subunits.

26. Ω precipitate in HRTEM. Growth of plate shaped precipitates occurs by moving of the growth ledges.

27. Conclusions.

Effect of Texture and Precipitates on Mechanical Property Anisotropy of Al-Cu-Mg-X Alloys

B. Skrotzki, E. A. Starke, G. J. Shiflet

LA²ST Grant Review Meeting
NASA Langley Research Center
July 17-18, 1995

UVA Dept. of Materials Science

Objective

Determine the effect of texture in unrecrystallized and recrystallized modified 2519 on the precipitation of the Ω and Θ' phases in T6 and T8 conditions and the associated relationship with anisotropy of mechanical properties.

In addition, the effect of an applied stress on nucleation and growth of the strengthening precipitates will be examined.

The Effect of Stress on Nucleation and Growth of Precipitates in Al-Cu-Mg-X Alloys

UVA Dept. of Materials Science

Background

- Externally applied stresses and internal stresses associated with second phase particles can affect both nucleation of the precipitates and their growth
- Coherency strains
  - ➤ usually stabilize single phase field
- Externally imposed strains
  - ➤ may change stability of a phase
  - ➤ may move solvus line either into the single phase or two phase region

Background

- Normal aging conditions (no applied or residual stresses) => equal number of platelets on all habit planes
- A strong texture results in anisotropy of properties and this can be enhanced or decreased by precipitates
- Preferential precipitation could produce anisotropy of strength properties => texture strengthening effect
- Preferential nucleation
  - ➤ precipitates have large coherency strains
  - ➤ strains being produced in the matrix due to volume difference between precipitate and matrix

Alloy System

Chemical Composition [wt.%]

Alloy	Cu	Mg	Mn	Ag	Zr	V	Fe	Si	Al
1*	5.00								bal.
2	5.75	0.52	0.30	0.49	0.16	0.09	0.06	0.05	bal.

* high purity

Alloy 1: cast at Reynolds Metals Co. and rolled to 0.25" (6.3 mm) sheet

Alloy 2: cast at Alcoa Technical Center and rolled to 0.125" (3.2 mm) sheet

Precipitate Phases

- Strengthening Phases
  - Alloy 1: Θ", Θ', Θ
  - Alloy 2: Θ", Θ', Θ, Ω, (S')

- Morphology
  - Θ': $\{100\}_{Al}$, plate shaped, Al_2Cu
  - Ω: $\{111\}_{Al}$, plate shaped, Al_2Cu
  - S': $\{210\}_{Al}$, lath shaped, Al_2CuMg

Mechanical Properties

(completely recrystallized; random texture)

Alloy	Condition	Orientation	T [℃]	σ_y [MPa]	UTS [MPa]	A〔%〕
1	SHT	RD	RT	120.1	274.5	30.8
1	SHT	RD	163	168.8	-	-
2	SHT	RD	RT	167.0	408.8	24.3
2	SHT	45°	RT	181.2	405.2	24.2
2	SHT	TD	RT	169.5	402.8	24.2
2	SHT	RD	163	244.4	-	-
2	T6	RD	RT	480.0	535.4	12.1
2	T6	45°	RT	471.1	520.5	13.3
2	T6	TD	RT	481.4	526.7	12.0
2	T6	RD	163	366.7	-	-

Heat Treatment

- SHT (#1: 1h/540˚C, #2: 1h/520˚C)
- T6 (T8) @ 163˚C
- Stress aging* @ 160˚C
  - ➤ 40% of $R_{p0.2}$(RT)
    - – 69 MPa for #2 (SHT)
    - – 191 MPa for #2 (T6)
  - ➤ tapered samples
    - – various stresses in one sample

* load was applied to SHT samples before heating

Sample Geometry

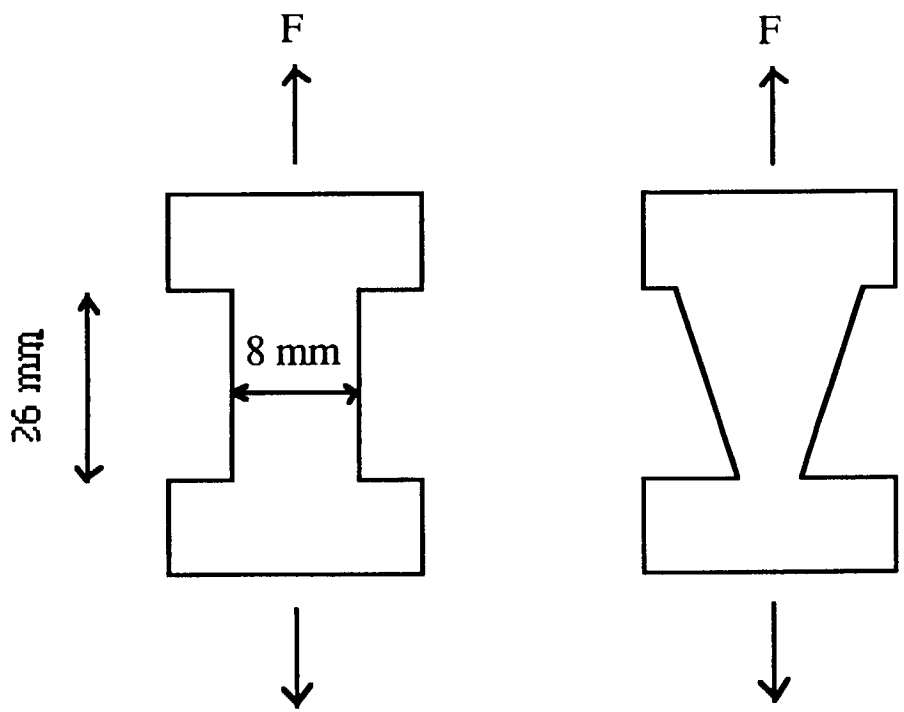

t = sheet thickness

Microstructure Characterization

- TEM (Philips EM 400T, U = 120 kV)
- HRTEM (JEOL 4000 EX, U = 400 kV)
- Volume fraction, number density and size of precipitates
- CBED => foil thickness

Stereology

- Higher volume fractions of Ω and Θ' in prestrained samples
- Further nucleation of Ω after aging of T6 samples
- Higher volume fraction of Θ' after aging of SHT samples under higher stress

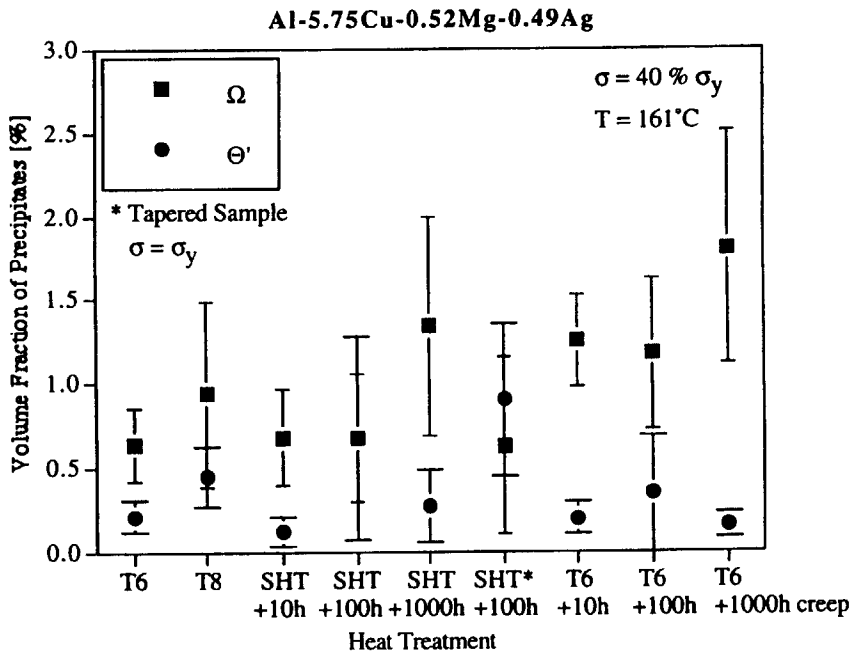

Stereology

- High number density of Ω and Θ' after SHT and T6 and aging under stress
- High number density of Θ' in SHT samples after aging under higher stress

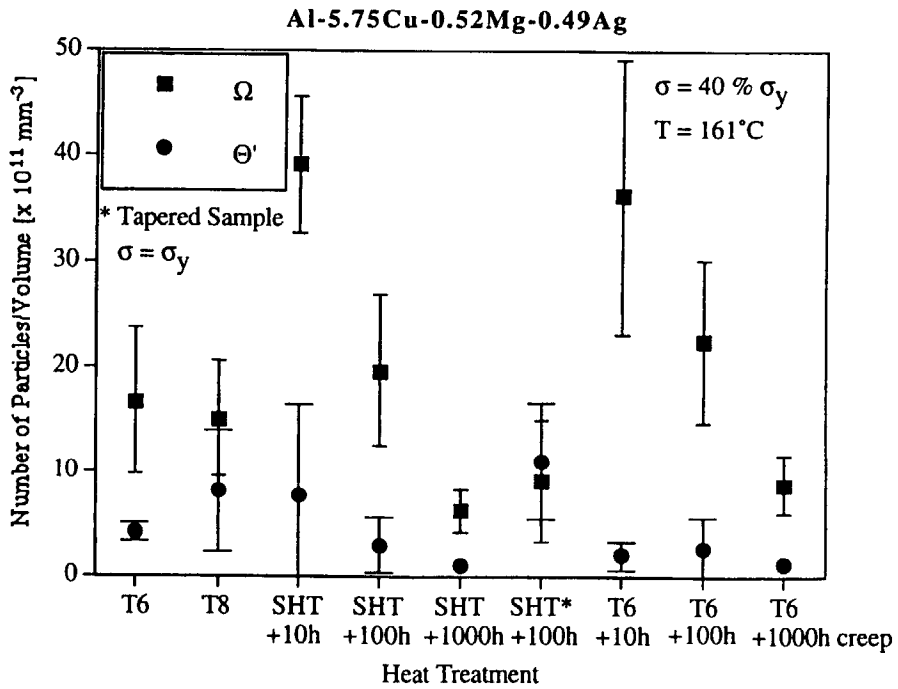

Stereology

- Ω shows higher thermal stability than Θ'
- Θ' starts to grow early
- considerable growth of Ω occurs after 1000 h aging

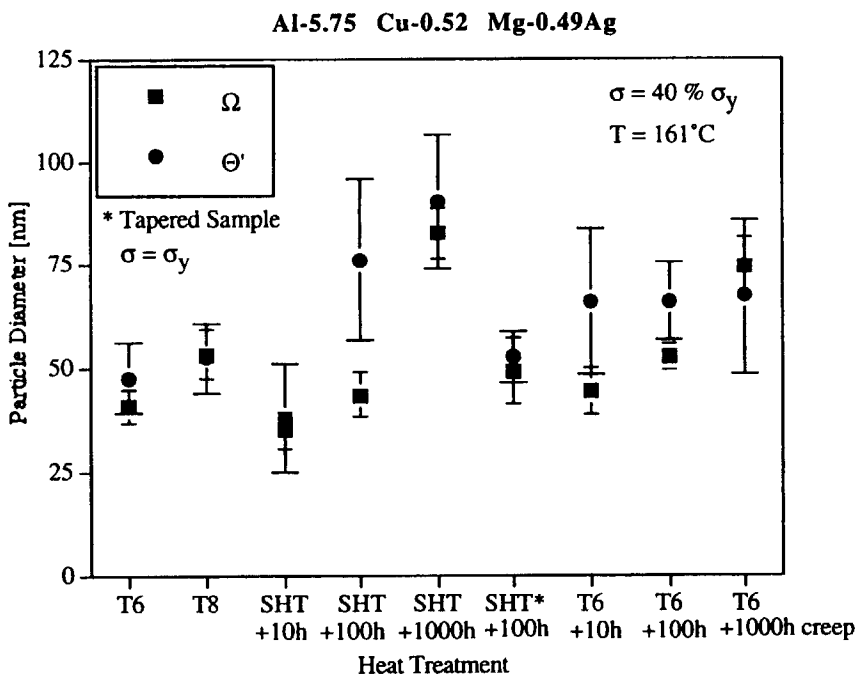

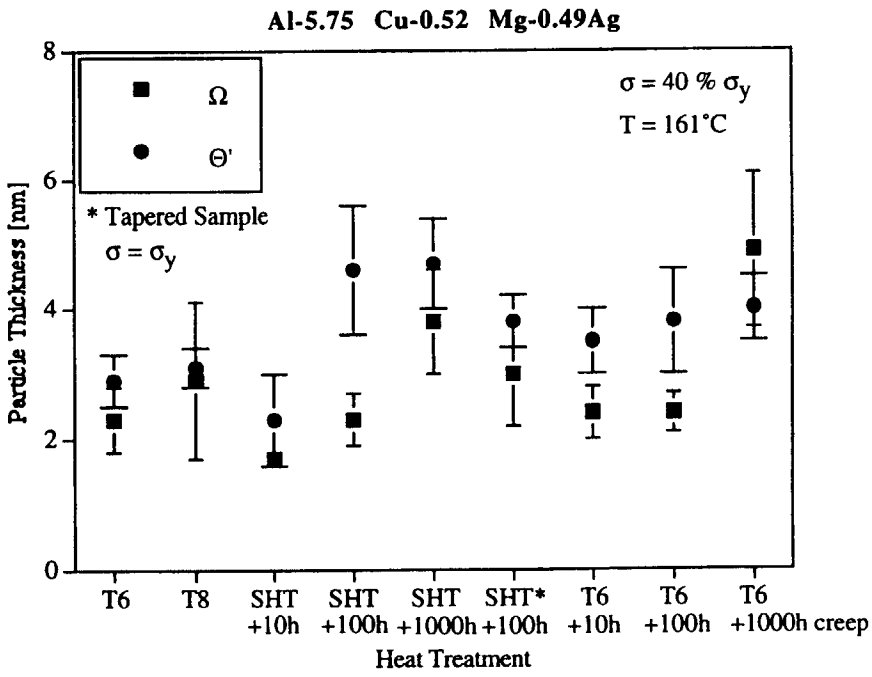

Stereology

- Preferential precipitation of Θ' parallel to stress axis after SHT and aging under stress

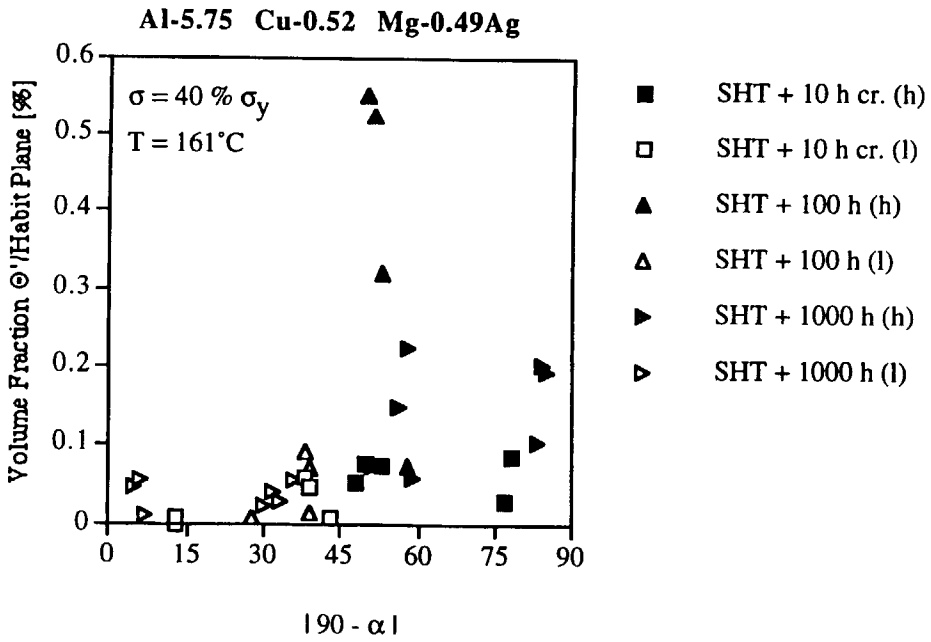

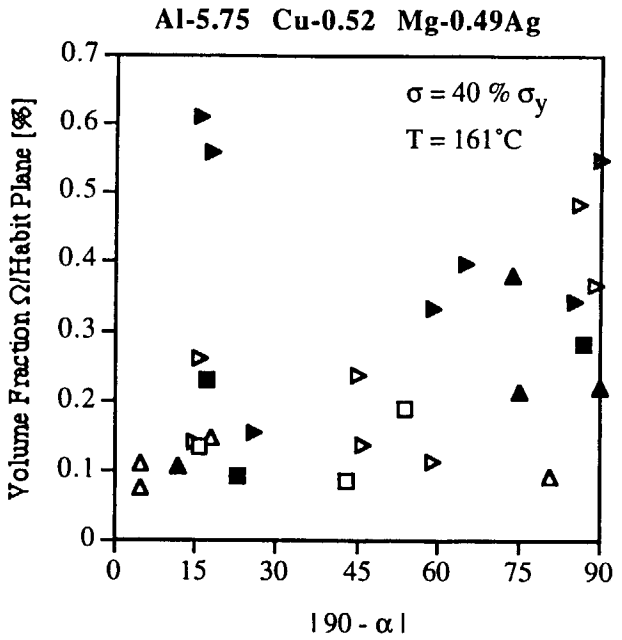

Stereology

- Preferential precipitation of Ω and Θ' parallel to stress axis after SHT and aging under higher stress => threshold stress

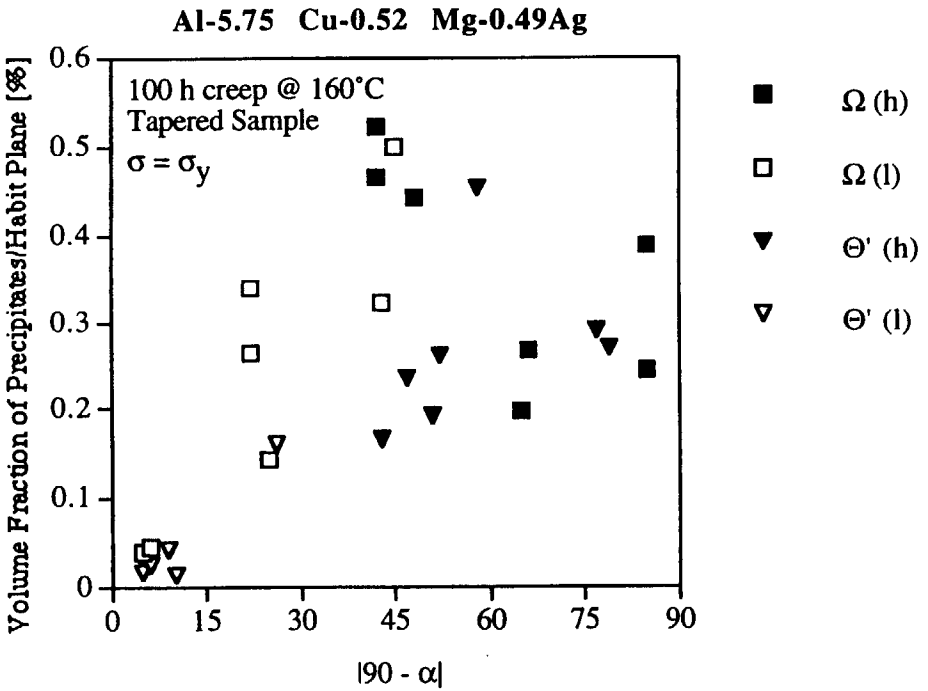

Al - 5 wt.% Cu

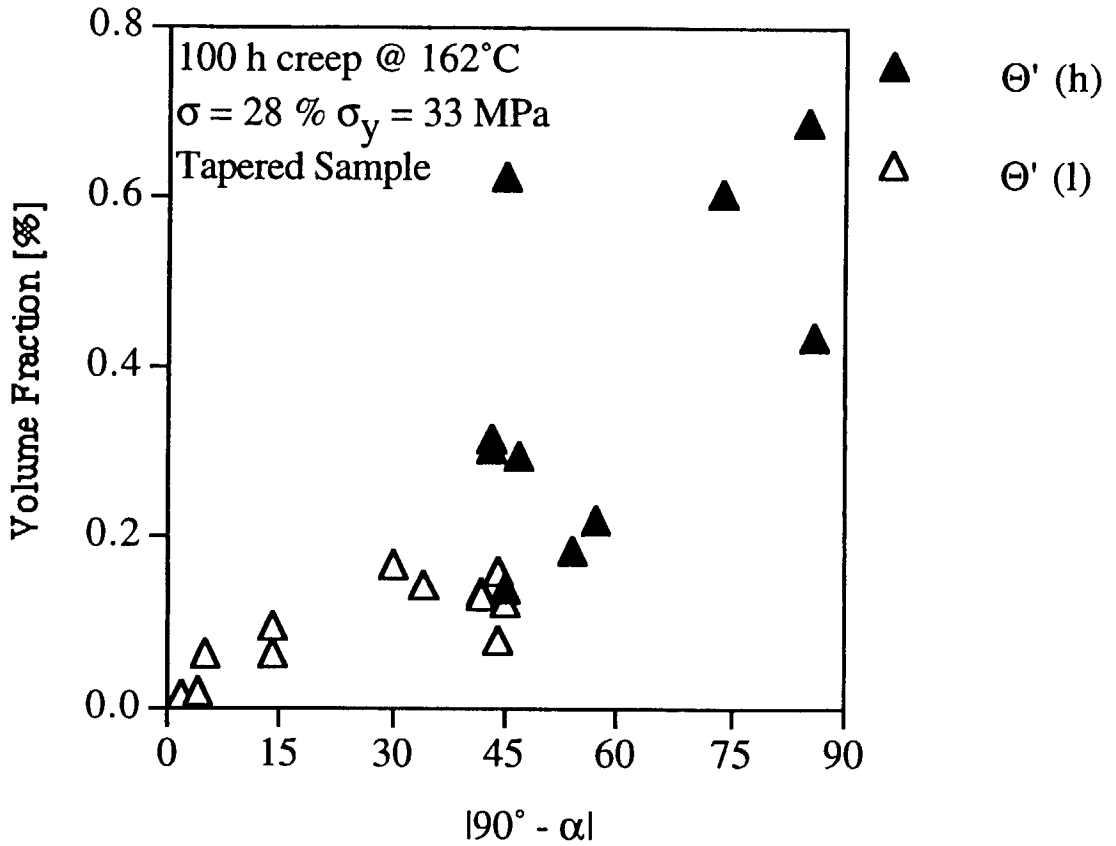
100 h creep @ 162°C
σ = 28 % σy = 33 MPa
Tapered Sample
Θ' (h)
Θ' (l)
Volume Fraction [%]
0.0
0.2
0.4
0.6
0.8
0
15
30
45
60
75
90
|90° - α|

Al - 5 wt.% Cu

- SHT + 100 h @ 162°C, 33.4 MPa (= 28 % $R_{p0.2}$)

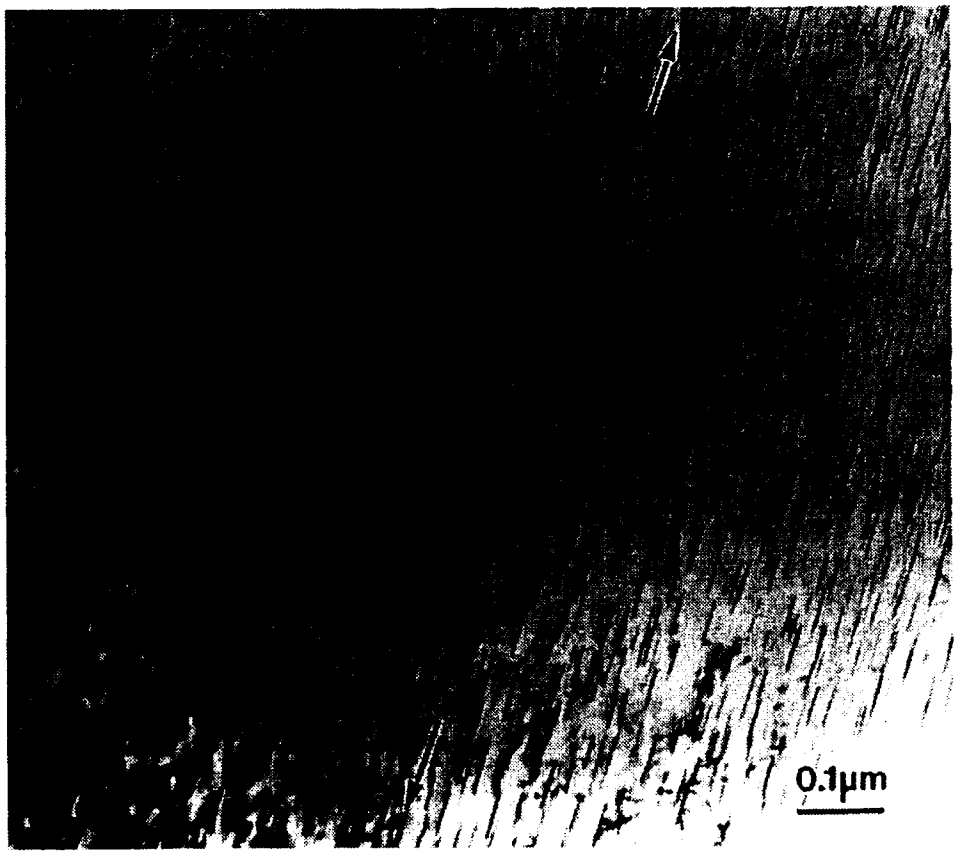

$[001]_{\alpha}$

Threshold Stress

- Critical stress for SHT samples:
  - Ω : $120 < \sigma_c < 140$ MPa
  - Θ': $16 < \sigma_c < 19$ MPa
- No effect observed in T6 samples

Al - 5 wt.% Cu

- Creep sample heated with applied stress (σ = 75.4 MPa) from 20°C to 160°C in ~70 min.

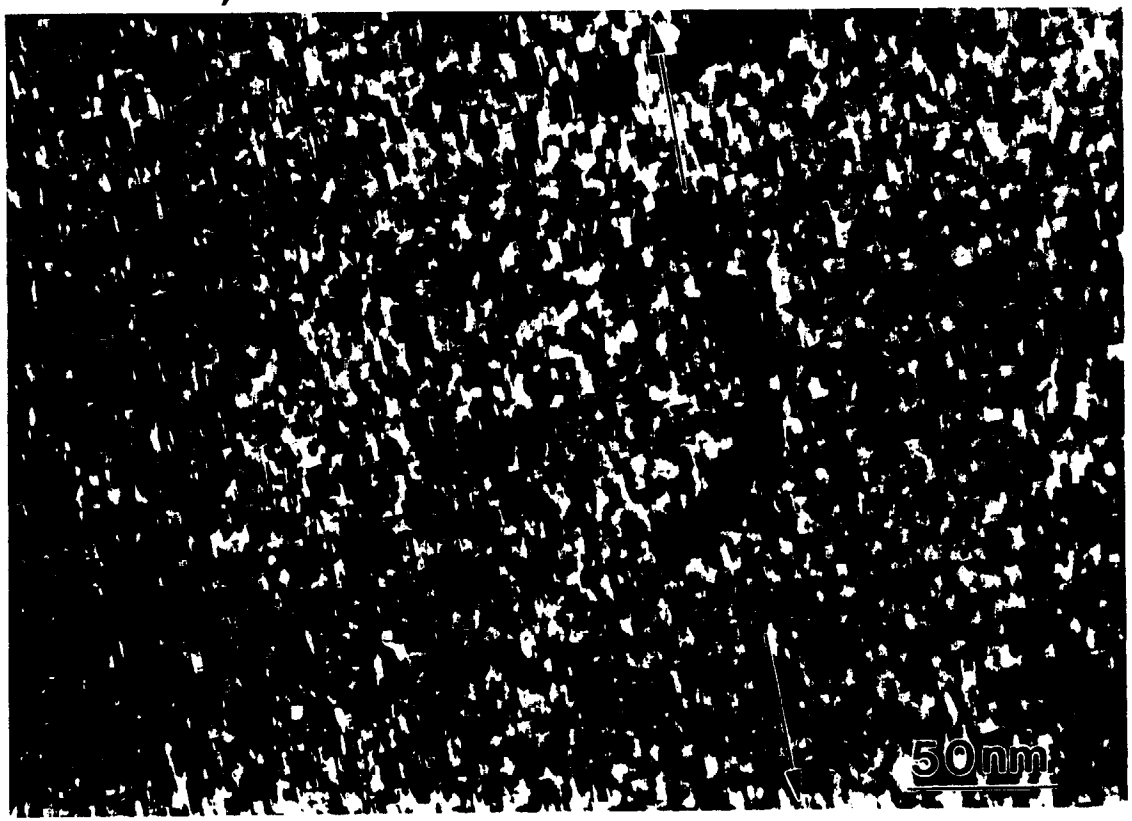

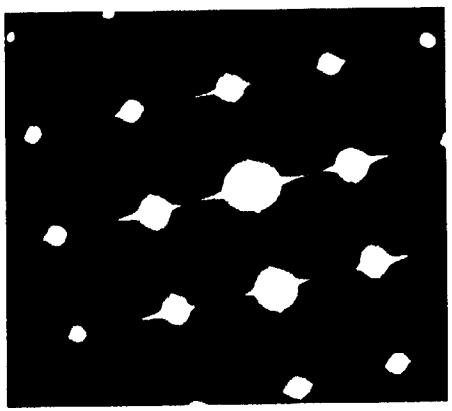

$[001]_{\alpha}$

Al - Cu - Mg - Ag

Curve 1: DSC
File info: ACMA-2 Tue Jun 27 15:57:29 1995
Sample Weight: 27.420 mg
AlCuMgAg repeat

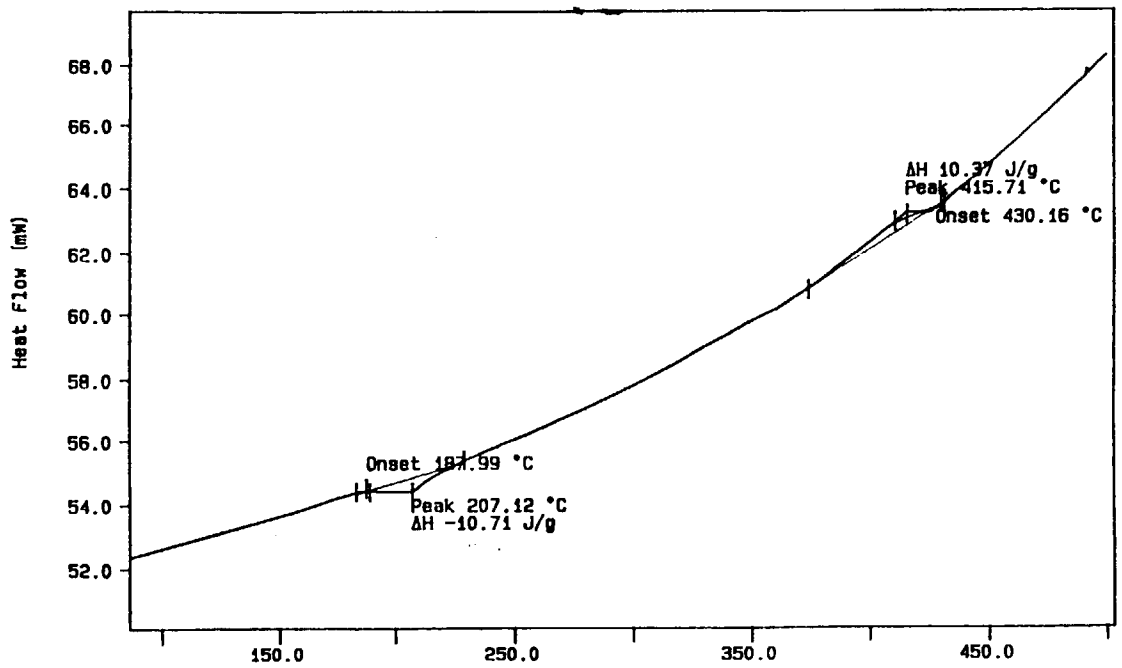

from 20 to 500
TEMP1: 20.0 C TIME1: 0.0 min RATE1: 5.0 C/min
TEMP2: 500.0 C

Dongjian Li
PERKIN-ELMER
7 Series Thermal Analysis System
Tue Jun 27 16:13:35 1995

Al - Cu

- Large effect on nucleation
- Precipitates are parallel to applied stress

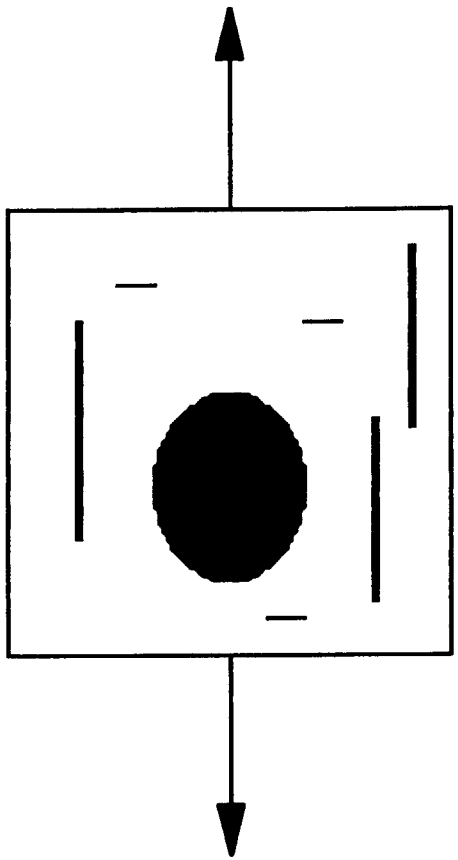

Discussion

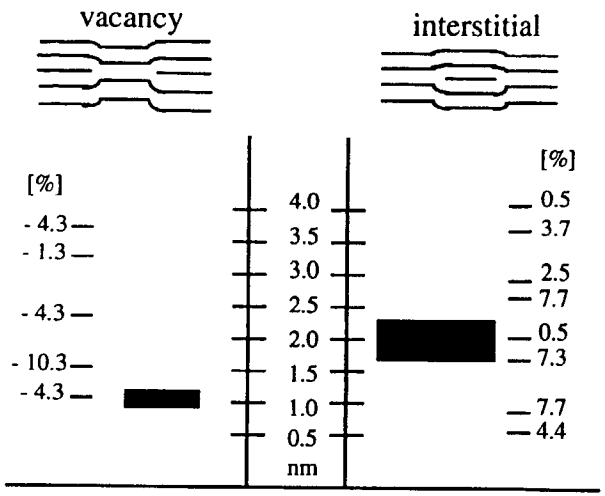

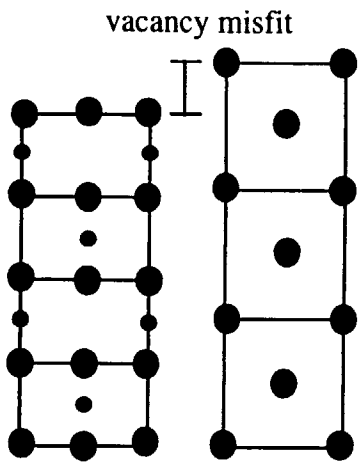

- Model by Dahmen and Westmacott suggests that smallest Θ' precipitate (critical nucleus) is 2 unit cells which would have vacancy misfit (negative). Stobbs and Purdy have experimentally shown that 2 unit cells or smaller have vacancy-type misfit.
- Based on previous work (e.g. δ') a negative misfit with the matrix will result in nucleation in compressed region of the matrix.

Crystallographic Model

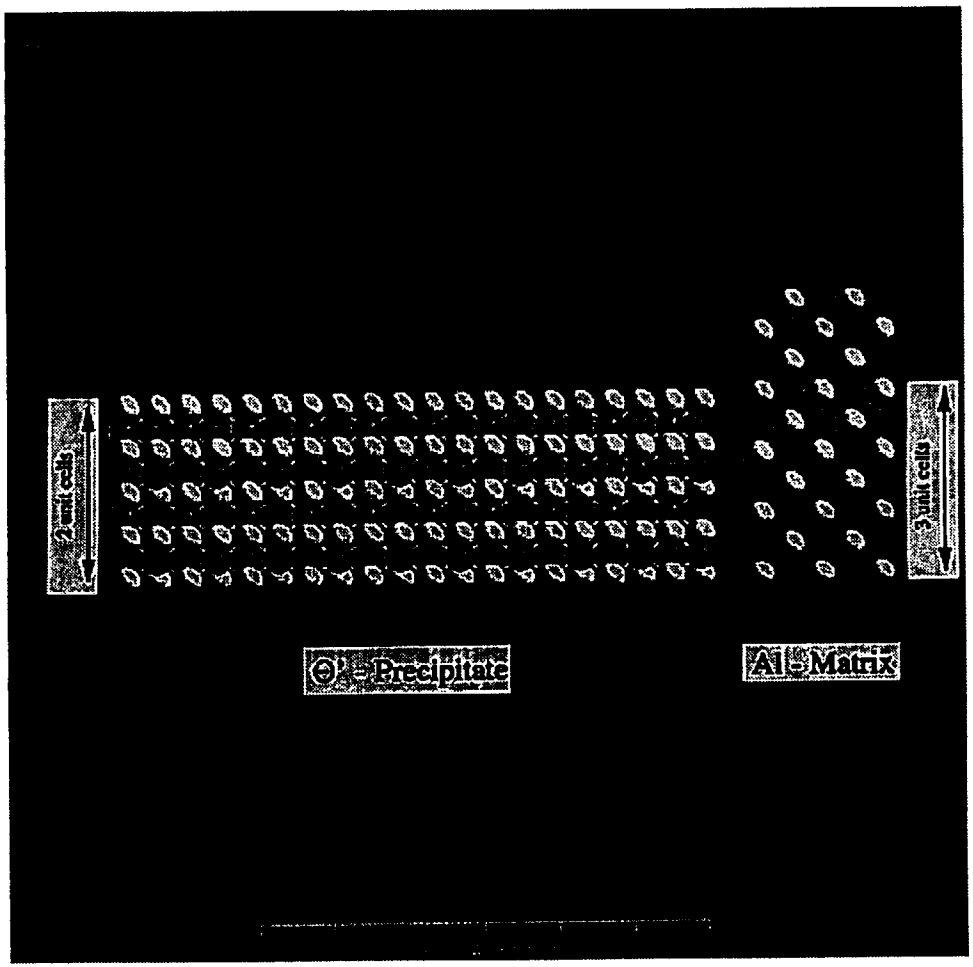

Discussion

- Plate shaped Θ' nuclei should preferentially nucleate parallel to stress axis.
- Contradicts results (tensile stress) of Hosford and Agrawal (Met. Trans. 6A (1975) 487) but is in agreement with results of Eto, et al. (Acta Metall. 26 (1978) 499)
- During growth the growth ledge height should have the requisite number of Θ' subunits (half unit cells) to minimize the elastic accommodation strain.

Al - 5.75 Cu - 0.52 Mg - 0.49 Ag

- SHT + 1000 h @ 161°C/ 69 MPa (= 40 % $R_{p0.2}$)

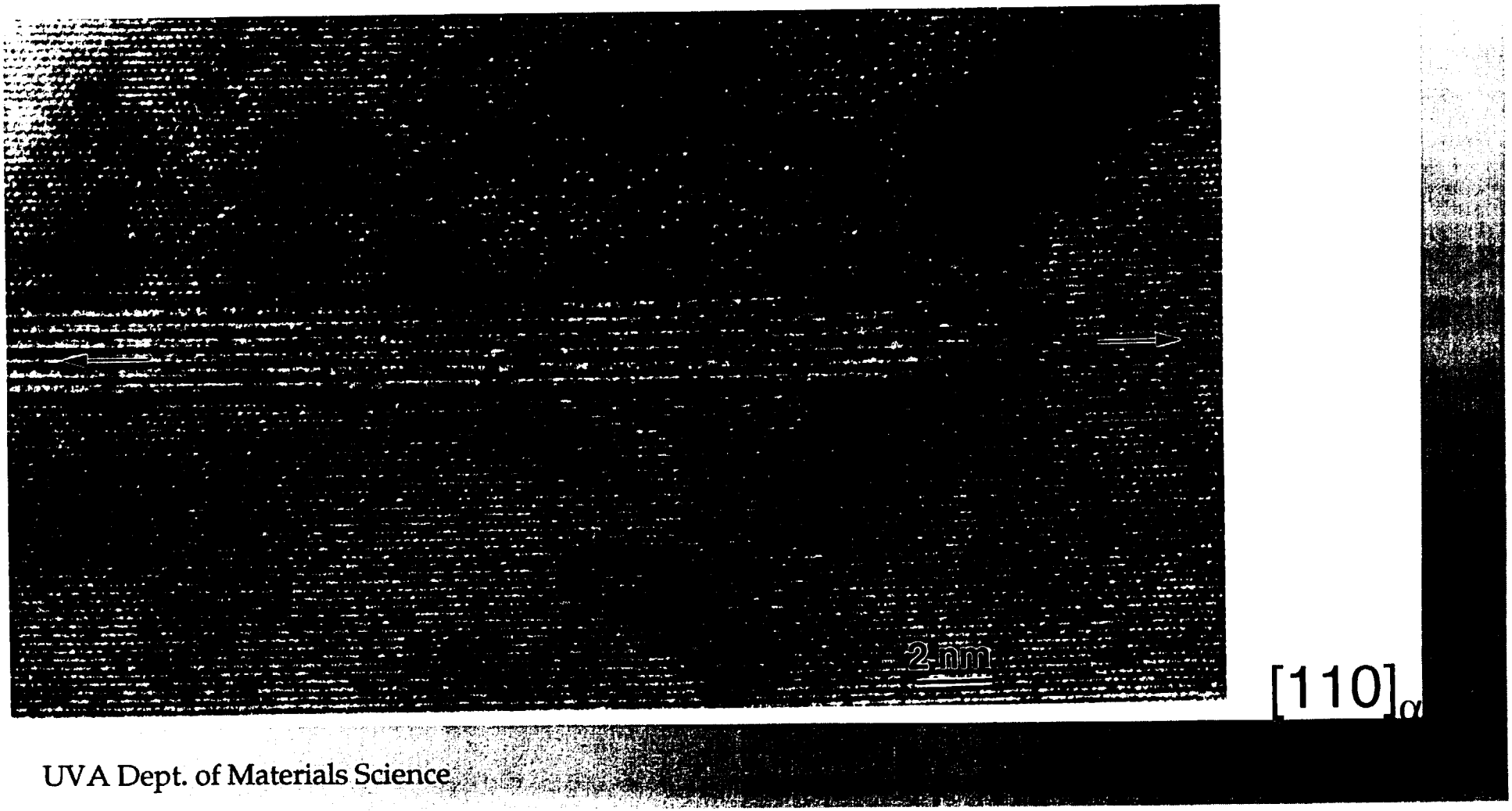

Conclusion

- Ω and Θ' are preferentially oriented parallel to the applied stress.
- Large effect on nucleation. Θ' nuclei have negative misfit which is accommodated in compressed matrix.
- Growth ledge height minimize the elastic accommodation strain.

Project #10 **Damage Evolution in Polymeric Composites**

R. D. Schroedter III and C. T. Herakovich

Progress achieved in this project will be reported elsewhere.

Project #11 **Computer Modeling Environment Enhanced Fatigue Crack Propagation in Light Aerospace Alloys**

Edward Richey III and Richard P. Gangloff

Objective

The objective of this research is to develop the methods and understanding needed to incorporate time and loading wave-form dependent environmental effects on fatigue crack propagation (FCP) in NASA FLAGRO. The research seeks to test the Wei and Landes linear superposition model and an interpolative model, and to suggest improvements to these models based on an improved understanding of the time dependencies which affect environmental fatigue crack propagation (EFCP) in structural alloys. In particular Ti-6Al-4V is studied in the mill annealed (MA), extra low interstitial (ELI) condition due to its complex, time-dependent environmental fatigue behavior.

Current Status

The experimental work for Ti-6Al-4V (MA,ELI) in NaCl was completed during this reporting period. Computer-automated constant ΔK and ΔK decreasing experiments were employed to determine the effect of frequency on da/dN. Monotonically rising load tests were conducted to determine the stress corrosion cracking (SCC) susceptibility of the alloy. These data were employed to assess computer models of EFCP rates developed in previous reporting periods. The graduate student, Mr. Edward Richey III, has completed and defended his Master's of Science thesis, and is beginning his doctoral studies in the Department of Materials Science and Engineering at UVa. A paper reporting the complete findings of this research is planned for journal publication. A computer program and documentation will be provided to Dr. R.G. Forman (NASA-Johnson Space Center) for possible incorporation into NASA-FLAGRO.

Recent Results

Monotonic loading experiments were conducted in order to determine the stress corrosion cracking susceptibility of Ti-6Al-4V (MA,ELI) in a 3.5% NaCl solution. ELI grade Ti-6Al-4V

exhibits a much greater resistance to SCC than standard grade Ti-6Al-4V. The threshold stress intensity for crack initiation in 3.5% NaCl solution (K_{TH}) is between 48 and 55 MPa$\sqrt{m}$ depending on loading rate. For moist air, K_{JIC} was found to be 78 MPa$\sqrt{m}$, slightly higher than the value for standard grade Ti-6Al-4V. ELI grade Ti-6Al-4V exhibits a much slower da/dt than the standard grade, of order 10^{-5} mm/sec or less. ELI grade Ti-6Al-4V exhibits environment assisted cracking (EAC), albeit at a very high K level.

Corrosion fatigue experiments were conducted on Ti-6Al-4V (MA,ELI) in moist air and a 3.5% NaCl solution for ΔK values in the range of 5 to 25 MPa$\sqrt{m}$, frequencies in the range of 0.03 to 40 Hz, and a stress ratio of 0.1. A 3.5% NaCl solution is detrimental, and enhances fatigue crack growth rate two to four fold compared to cracking in moist air. The ELI grade alloy does not exhibit the same frequency dependence as standard grade Ti-6Al-4V. The ELI grade alloy does not exhibit the frequency "crossover" effect exhibited by the standard grade. Instead, da/dN increases as frequency increases; da/dN is proportional to $f^{0.1 \text{ to } 0.2}$.

Nominal crack closure levels were recorded during all fatigue experiments. Crack closure levels were consistent with plasticity induced closure and the Forman Equation with closure. Crack closure levels were independent of environment. For ΔK value below 10 MPa$\sqrt{m}$, closure levels increased as ΔK decreased. This could be due to roughness or oxide induced closure. For ΔK levels above 10 MPa$\sqrt{m}$, there is no roughness or oxide induced closure.

Both linear superposition and interpolative models were utilized to represent EFCP rates in standard and ELI grade Ti-6Al-4V in 3.5% NaCl. The linear superposition model proved effective for standard grade Ti-6Al-4V for ΔK values where K_{max} exceeds K_{TH} (23 MPa$\sqrt{m}$) and frequencies greater than 1 Hz. The linear superposition model is not effective for ELI grade Ti-6Al-4V due to the increased SCC resistance of this alloy. The interpolative model was effective in modeling the effect of frequency in both standard and ELI grade Ti-6Al-4V when the frequencies where data were interpolated are within the establishing data base.

The computer models developed during this research are reasonably effective in representing EFCP rates, and can be incorporated in NASA FLAGRO. The programs are available on a FORTRAN 77 program disk in executable form, along with the source code. Given the complexity of EFCP in a variety of aluminum, iron, nickel and titanium-based alloys,

this program is only a first step in developing the necessary interpolative and predictive capabilities in NASA-FLAGRO; substantial additional work is required.

Presentation Viewgraph Captions

1. Title.

2. Problem Statement. The problem is that coupling an aggressive environment with cyclic plastic deformation can significantly reduce the fatigue life of an aerospace structure; these environmental effects, however, have not been incorporated in NASA FLAGRO.

3. Objective and current work. The general objective of the research is to develop an effective method for estimating environmental effects on fatigue crack propagation for use in NASA FLAGRO.

4. Da/dN versus ΔK data for Ti-6Al-4V in moist air and a 3.5% NaCl solution for a frequency of 5 Hz, and R = 0.1. In moist air da/dN is a function only of ΔK and R. In an aggressive environment such as NaCl, da/dN is a function not only of ΔK and R, but also loading frequency and hold time.

5. Summary of equation used by the computer programs to relate da/dN to ΔK. Five different crack growth rate equations are available including the Forman Equation with and without crack closure, the Paris Equation, the Hyperbolic Sine Equation, and the Sigmoidal Equation.

6. Summary of the method proposed to interpolate trends in environmental fatigue behavior using an approach similar to that reported by Haritos et al. Trends are interpolated by relating equation constants to load-time characteristics using empirical relationships. The form of these relationships is selected based on interpolative models discussed in the literature, and experimental results generated for Ti-6Al-4V (MA,ELI).

7. Summary of equations used to interpolate crack growth rate-equation constants based on load characteristics. The load characteristics are stress ratio, hold time and frequency. The form of the relationships depends on the number of data sets fit to a crack growth rate equation, and the form of the basic crack growth rate equation.

8. Summary of the multiple power law model developed during this research. The purpose of the multiple power law model is to develop a computer program which allows the user to fit a multiple power law equation to da/dN versus ΔK data.

9. Plot of da/dN versus ΔK for Ti-6Al-4V (MA,ELI) in moist air and a 1.0% NaCl solution for R = 0.4 and a frequency of 5 Hz. The alloy exhibits a complex da/dN versus ΔK behavior in both moist air and aqueous chloride, as exhibited by the multiple slope transitions. The power law segments were determined using the multiple power law model developed during this research.

10. Chemical composition and mechanical properties for Ti-6Al-4V (MA,ELI). In all environment assisted cracking experiments, compact tensions specimens machined in the L-T orientations were utilized. A 3.5% NaCl solution served as the corrosive environment, and specimens were held at a fixed electrode potential of -500 mV_{SCE}.

11. Summary of the method utilized during the constant CMOD rate tests which were conducted to determine the stress corrosion cracking susceptibility of Ti-6Al-4V (MA,ELI). All experiments were conducted in CMOD control with crack length calculated using the DCPD method, and CMOD measured by a clip gauge. Also shown in a schematic of the environmental cell utilized during the experiments.

12. Summary of the results for the constant CMOD rate experiments conducted for Ti-6Al-4V (MA,ELI). K_{JIC} was found to be 78 MPa$\sqrt{m}$, slightly higher than K_{IC} for standard grade Ti-6Al-4V. ELI grade Ti-6Al-4V exhibits a greater resistance to stress corrosion cracking than standard grade Ti-6Al-4V, with a K_{TH} between 48 and 55 MPa$\sqrt{m}$ depending on loading rate. ELI grade Ti-6Al-4V also exhibits a slower da/dt than standard grade.

13. Plot of load versus CMOD for Ti-6Al-4V (MA,ELI) in a 3.5% NaCl solution. The specimen was loaded monotonically to a stress intensity level of 40 MPa$\sqrt{m}$ in 65 minutes. The load was then held constant for 140 hours at this level. A load drop of 0.1 kN would have been noticeable, and corresponded to 0.2 mm of crack extensions. The load did not drop, thus da/dt is less than 5×10^{-7} mm/sec. Shown on the graph is the literature-reported K_{TH} value for standard grade Ti-6Al-4V.

14. Plot of load versus CMOD for Ti-6Al-4V(MA,ELI) in moist air and 3.5% NaCl for various loading rates. Notice that there are small sharp decreases in the load at a constant CMOD for the NaCl experiments. The air data do not show decreases in load at a constant CMOD. Since for two of the experiments, the loading rates were identical and only the environment varies, environment assisted cracking occurs in Ti-6Al-4V (MA,ELI), but only at high stress intensities. (Note that the fatigue precrack length was longer for the experiment represented by o, compared to the two experiments with equal and shorter crack lengths, represented by □ and +.)

15. Conclusions for environmental fatigue experiments conducted on Ti-6Al-4V (MA,ELI). 3.5% NaCl is detrimental, enhancing fatigue crack growth rates two to fourfold compared to moist air. ELI grade Ti-6Al-4V does not exhibit the frequency "crossover" effect for the range of frequencies and ΔK levels utilized during this research (0.03 to 40 Hz and 5 to 25 MPa$\sqrt{m}$, respectively) due to the increased stress corrosion cracking resistance of

the alloy. Instead, ELI grade Ti-6Al-4V exhibits a mild frequency dependence for ΔK values between 12.5 and 25 MPa$\sqrt{m}$ where da/dN is proportional to $f^{0.1 \text{ to } 0.2}$. The closure levels exhibited by Ti-6Al-4V (MA,ELI) are consistent with plasticity induced closure.

16. Description of the frequency "crossover" effect exhibited by $\alpha + \beta$ titanium alloys in aqueous chloride solutions. The "crossover" is a change in the ordering of da/dN as a function of frequency at a transition ΔK level (ΔK_{SCC}) associated with the onset of "cyclic" stress corrosion cracking. Below ΔK_{SCC}, da/dN decreases as frequency decreases perhaps due to passive film stability. Above ΔK_{SCC}, da/dN increases as frequency decreases perhaps due to hydrogen embrittlement mechanisms.

17. Da/dN versus ΔK for Ti-6Al-4V (MA,ELI) in moist air, 1.0% NaCl and 3.5% NaCl for various frequencies and a stress ratio of 0.1. Fatigue crack growth rates are enhanced in the aqueous chloride compared to moist air, and are only mildly frequency dependent.

18. Plot of da/dN versus frequency for Ti-6Al-4V (MA,ELI) for constant ΔK values of 12.5 and 25 MPa$\sqrt{m}$. For both constant ΔK values, da/dN generally increases mildly as frequency increases for frequencies in the range 0.03 to 40 Hz. For both ΔK levels where K_{max} was less than K_{TH}, da/dN was proportional to $f^{0.1 \text{ to } 0.2}$. The dashed line indicates the type of trend that would be observed if the alloy/environment system exhibited the frequency crossover effect.

19. Plot of ΔK_{SCC} versus frequency for standard and ELI grade Ti-6Al-4V. The literature data shown for standard grade Ti-6Al-4V are consistent with a K_{TH} of 23 MPa$\sqrt{m}$. Since the ELI grade alloy exhibits a much higher K_{TH} value, the EFCP data for standard grade Ti-6Al-4V were linearly scaled to generate the trend lines shown for the ELI grade Ti-6Al-4V. "Cyclic" stress corrosion cracking does not occur in the ELI grade Ti-6Al-4V for the range of frequencies and applied stress intensity ranges used during this study due to the increased SCC resistance. Since "cyclic" SCC did not occur, the alloy did not exhibit the frequency "crossover" effect. For example, for applied ΔK values below 25 MPa$\sqrt{m}$, "cyclic" SCC should not occur for frequencies below 200 Hz, five times faster than the fastest frequency where data were collected during this research, 40 Hz.

20. Plot of K_{cl} / K_{max} versus crack length for Ti-6Al-4V (MA,ELI) in moist air and a 3.5% NaCl solution for a constant ΔK value of 15 MPa$\sqrt{m}$, stress ratio of 0.1, and frequency of 5 Hz. Crack closure levels exhibited by Ti-6Al-4V (MA,ELI) were independent of environment. The closure levels are consistent with plasticity induced closure modeling, and the associated Forman Equation with closure. For ΔK values less than 10 MPa$\sqrt{m}$, crack closure increased as ΔK decreased. This could be due to roughness or oxide induced closure. For ΔK values greater than 10 MPa$\sqrt{m}$, there is apparently no contribution from roughness or corrosion debris/oxide induced closure.

21. Summary of conclusions for the computer models developed during this research. Linear superposition is effective in modeling environment enhanced FCP rates for material/environment systems where the alloy is extremely sensitive to stress corrosion

cracking. For standard grade Ti-6Al-4V, linear superposition is effective for ΔK values where K_{max} exceeds K_{TH}. Linear superposition is not effective for ELI grade Ti-6Al-4V due to the increased SCC cracking resistance of the alloy. The interpolative model is effective in modeling FCP rates when the load characteristics where data are interpolated are within the establishing data base. Specifically, the effects of frequency and stress ratio are reasonably modeled in standard and ELI grade Ti-6Al-4V.

22. Linear superposition predictions of literature-reported corrosion fatigue crack growth rates in standard grade Ti-6Al-4V in 3.5% NaCl. The linear superposition model is effective for ΔK values where K_{max} exceeds K_{TH} (23 MPa$\sqrt{m}$) and loading frequencies greater than 1 Hz.

23. Fitted and interpolated data for standard grade Ti-6Al-4V in a 3.5% NaCl solutions using the Forman Equation with closure. The logarithmic form of the frequency dependence was selected.

24. Fitted and interpolated data for ELI grade Ti-6Al-4V in a 3.5% NaCl solution using the Forman Equation with closure. The crack growth rate equation constants were related to the frequency using the f^{α} dependence. α was specified as 0.1.

25. Summary of the University of Virginia Fatigue Analysis Software. The linear superposition, interpolative, and multiple power law models are each contained in the DOS executable program UVAFAS.EXE. The source code is also included on the disk. The program was written using FORTRAN 77. This program will be provided to Dr. R.G. Forman at the NASA-Johnson Space Center.

26. Summary of future work required to improve and generalize the linear superposition model. The question has been posed: Can one calculate da/dt *vs* K from measured da/dN *vs* ΔK data; this issue will be investigated. This calculation can be completed currently using linear regression, provided that da/dt is well represented by a simple Paris equation, and the fatigue load-wave form is a simple square function. Saff et al. advocate this approach. The problem of calculating da/dt becomes nonlinear when other functions are necessary. It is erroneous to assume that da/dt is necessarily independent of loading frequency, because frequency affects crack tip strain rate and crack tip strain rate may affect da/dt, for example, as predicted by film rupture modeling.

27. Schematic diagram showing typical dependencies of EFCP rate (da/dN *vs* ΔK) on loading frequency. For the NaCl solution case, steels often exhibit da/dN proportional to the inverse square root of frequency above a critical stress intensity range, while aluminum and titanium alloys often exhibit da/dN proportional to frequency raised to a power on the order of -0.1 for aluminum alloys and both +0.1 and -0.8 for titanium alloys. The exact exponent depends on frequency and ΔK, as discussed with regard to the crossover effect. The simple linear superposition predicts that this power is -1.0, if a frequency independent value of da/dt exists at a given applied K level.

28. Summary of the feasibility and usefulness of calculating da/dt from da/dN. The model, if developed with sufficient mathematical sophistication, should be able to calculate a set of da/dt *vs* K data from da/dN *vs* ΔK, however, the model will always predict da/dN proportional to $f^{-1.0}$ if da/dt is assumed to be frequency-independent. This result is not broadly accurate for aluminum, titanium alloys and even steels. These various frequency-dependent da/dN data sets will produce a nonunique da/dt *vs* K relationship. That is, frequency-dependent da/dN *vs* ΔK data may produce a unique set of frequency-dependent da/dt *vs* K. This result may be mechanistically meaningful and should be pursued.

29. Summary of the method proposed to express da/dt, derived from $(da/dN)_{SCC}$ *vs* ΔK data, as a function of frequency for use in superposition modeling.

Computer Modeling Environment Enhanced Fatigue Crack Propagation in Light Aerospace Alloys

Edward Richey, III and Richard P. Gangloff

LA^{2}ST Program Review

NASA Langley Research Center

July 18, 1995

Problem Statement

- Coupling an aggressive environment with cyclic plastic deformation can reduce fatigue life of an aerospace alloy.

- Environmental effects have not been incorporated in computer life prediction codes such as NASA FLAGRO.

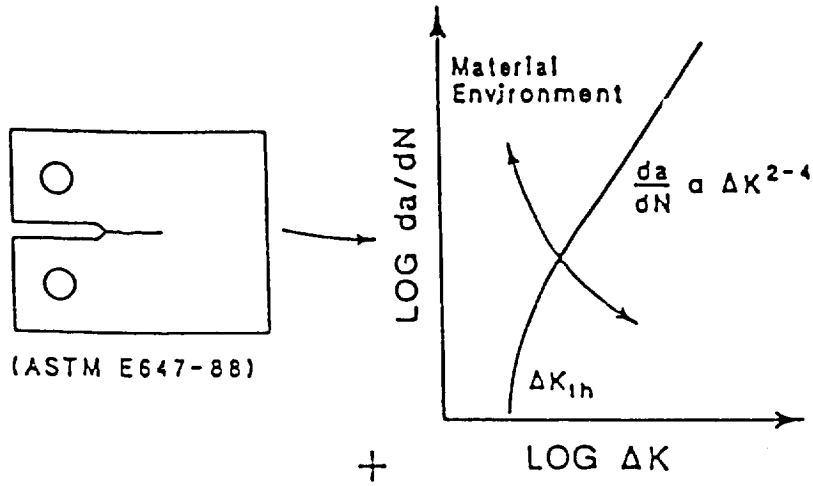

+

$$\Delta K_{COMPONENT} = f\ (\text{Loading, Flaw size , Geometry})$$

$$N,\ N_f = \int_{a_{INIT}}^{a_{LIM}} (\text{Crack Growth Law})(\Delta K_{COMPONENT})\ da$$

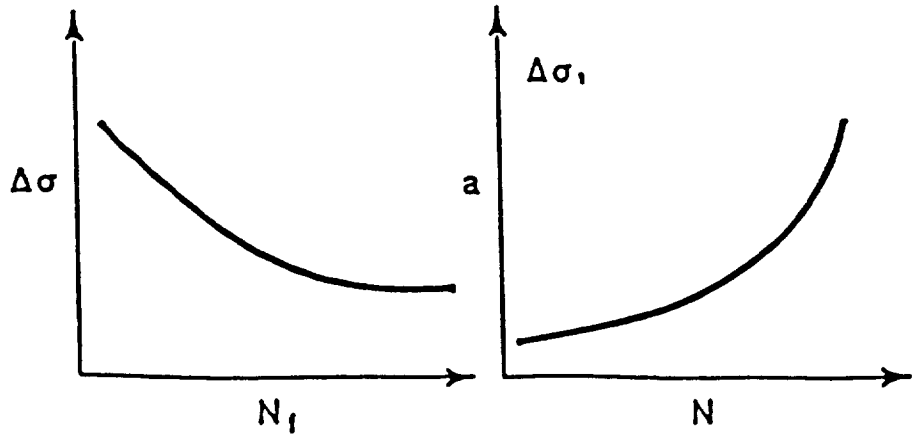

General Objective

Develop an effective method to estimate environmental effects on fatigue crack propagation in light aerospace alloys for use in NASA FLAGRO.

Computer Modeling Goals

- **Develop program implementing Wei and Landes linear superposition model.**
- **Develop curve-fitting based interpolative model extending approach used in NASA FLAGRO.**
- **Develop computer program to fit multiple power laws to fatigue data.**
- **Apply models to titanium alloys.**

Environment Assisted Cracking (EAC) of Ti-6Al-4V

- **Literature analysis for standard grade Ti-6Al-4V.**
- **Determine stress corrosion susceptibility of Ti-6Al-4V in 3.5% NaCl solution.**
- **Determine effect of loading frequency on fatigue crack propagation in Ti-6Al-4V in 3.5% NaCl.**

Output

- **Program for NASA.**
- **Understanding of corrosion fatigue behavior of Ti-6Al-4V.**

Fatigue Crack Propagation in Ti-6Al-4V (MA,ELI)

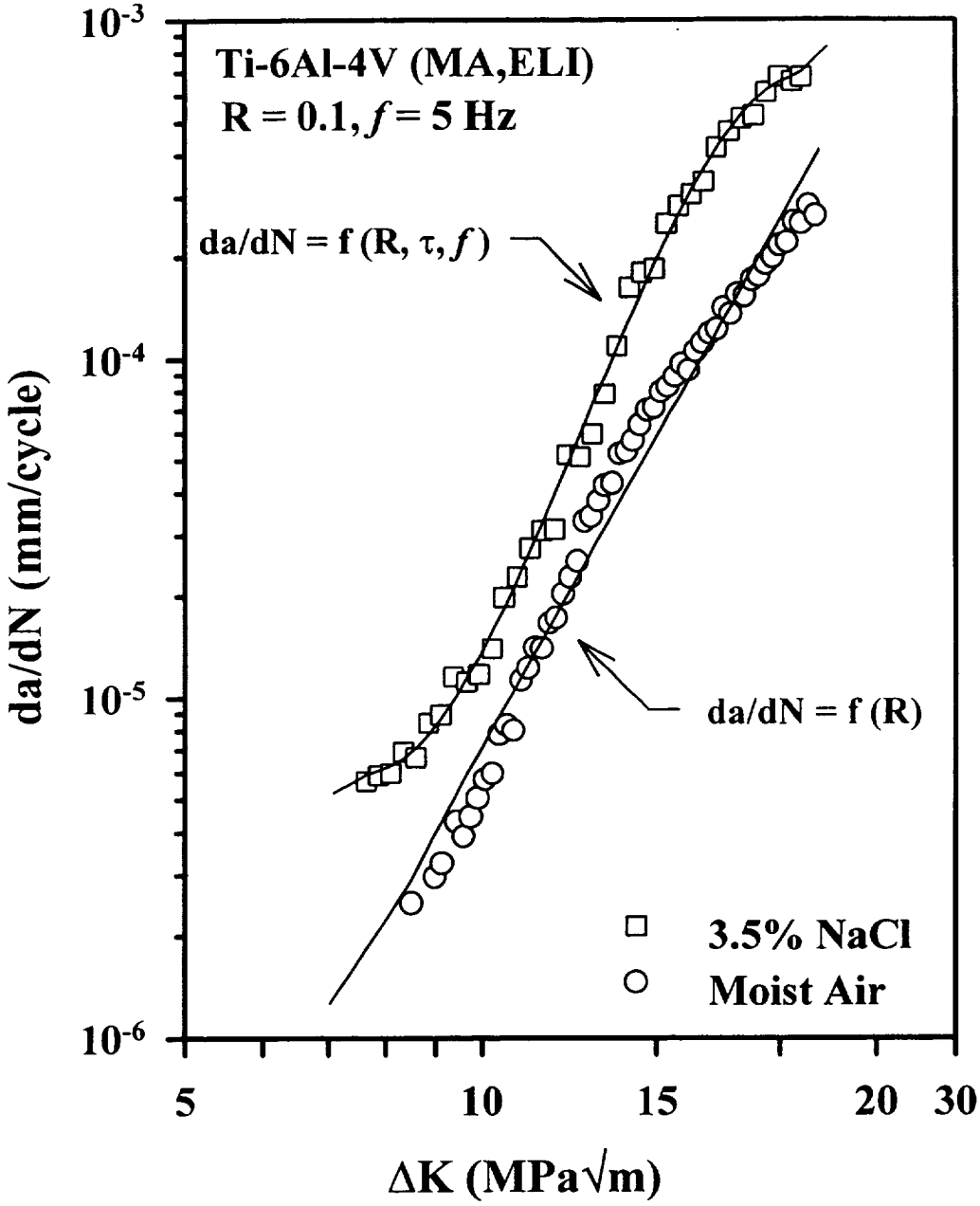

- In moist air, da/dN is a function of ΔK and R.
- In NaCl, da/dN is a function of ΔK, R, τ, *f*.

Crack Growth Rate Equations

- **Forman With Closure**

$$\frac{da}{dN} = \frac{C\ (1 - f\ )^n\ \Delta K^n \left(1 - \frac{\Delta K_{th}}{\Delta K} \right)^p}{(1 - R)^n \left(1 - \frac{\Delta K}{(1 - R)\ K_C} \right)^q}$$

- **Forman Without Closure**

$$\frac{da}{dN} = \frac{C\ \Delta K^n\ (1 - R)^m \left(1 - \frac{\Delta K_{th}}{\Delta K} \right)^p}{\left(1 - R - \frac{\Delta K}{K_C} \right)^q}$$

- **Paris**

$$\frac{da}{dN} = C\ \Delta K^n$$

- **Hyperbolic Sine (SINH)**

$$\log \left(\frac{da}{dN} \right) = C_1\ \sinh\ (\ C_2\ [\ \log\ (\Delta K) + C_3\ ]\ ) + C_4$$

- **Sigmoidal**

$$\frac{da}{dN} = e^B \left(\frac{\Delta K}{\Delta K_{th}} \right)^P \left[\ln \left(\frac{\Delta K}{\Delta K_{th}} \right) \right]^Q \left[\ln \left(\frac{\Delta K_C}{\Delta K} \right) \right]^D$$

Interpolative Model

- FLAGRO is primarily accurate for fatigue in moist air.
- Need: estimate time and load-wave form-dependent trends in fatigue behavior for corrosive environments.
- Interpolate trends by relating equation constants to load time characteristics.
- If η is an equation constant then: $\eta = f(f, \tau, R)$
  - f = frequency
  - τ = hold time
  - R = stress ratio
- Form of relationships based on interpolative models discussed in literature and results generated for Ti-6Al-4V (MA,ELI).
- Interpolation function are empirical, not based on mechanistic understanding.

Interpolation Functions

- **If one data set entered:**

$$\eta = a_1 \log\left[\left(\frac{1}{f}\right) + 1\right]$$

- **If two data sets entered using Forman Equation:**

$$\eta = a_1 \log\left[\left(\frac{1}{f}\right) + 1\right] + a_2 \log\left[\frac{\tau + 1}{0.1}\right]$$

- **If three data sets entered using Paris, SINH, or Sigmoidal:**

$$\eta = a_1 \log\left[\left(\frac{1}{f}\right) + 1\right] + a_2 \log(1 - R) + a_3 \log\left[\frac{\tau + 1}{0.1}\right]$$

- **Log [(1/f)+1] dependence can be replaced with f^{α}, α is a user specified constant defined by experiment or theory.**

Multiple Power Law Model

- **Goal: Develop computer program to fit a multiple power law equation to da/dN vs. ΔK data.**
- **User has three methods for fitting equation to data:**
  - **Define slope offset between two successive segments.**
  - **Define number of segments.**
  - **Define desired number of segments and approximate ΔK transitions.**
- **Current methods of fitting equation are subjective.**

Ti-6Al-4V (MA,ELI) in Moist Air and 1.0% NaCl, R = 0.4, f = 5 Hz

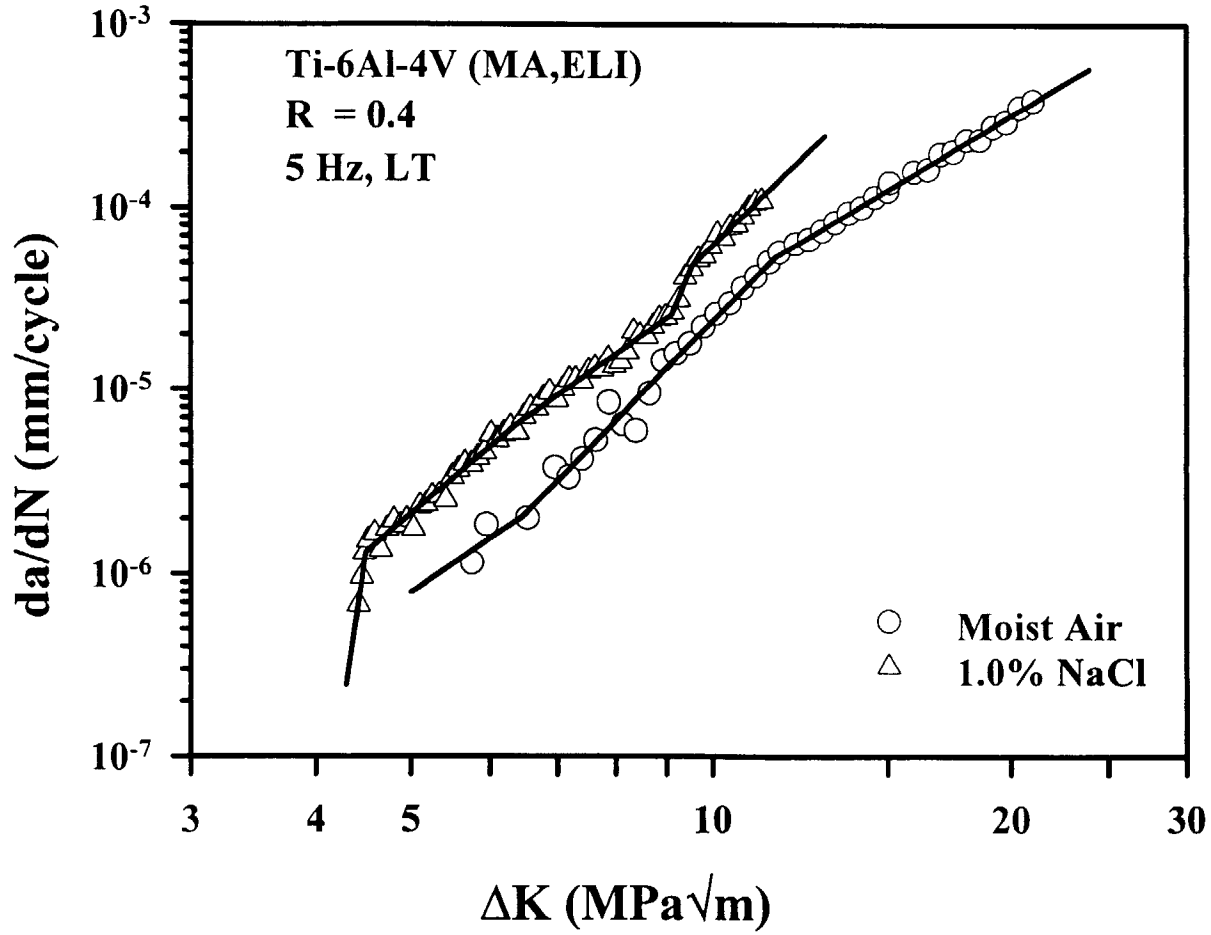

Materials Specifications for Ti-6Al-4V (MA,ELI)

Chemical Composition (wt. %)

Al	V	C	N	Fe	O	H	Y	Ti
6.17	4.33	. 0.025	0.011	0.19	0.12	0.0055	0.0005	balance

Mechanical Properties

Yield Strength MPa (ksi)	Tensile Strength MPa (ksi)	Elongation Percent (%)	Reduction in Area (%)
940 (136)	982 (142)	13	30.2

EAC Experiments

- Compact tension (CT) specimens machined in L-T orientation.
- 3.5% NaCl solution used, specimen held at fixed electrode potential of -500 mV_{SCE}.

Constant CMOD Rate EAC Tests

- Constant CMOD rate experiments conducted to determine stress corrosion susceptibility of Ti-6Al-4V (MA,ELI).
- All tests conducted in CMOD control, crack length calculated by DCPD, CMOD measured with clip gage.

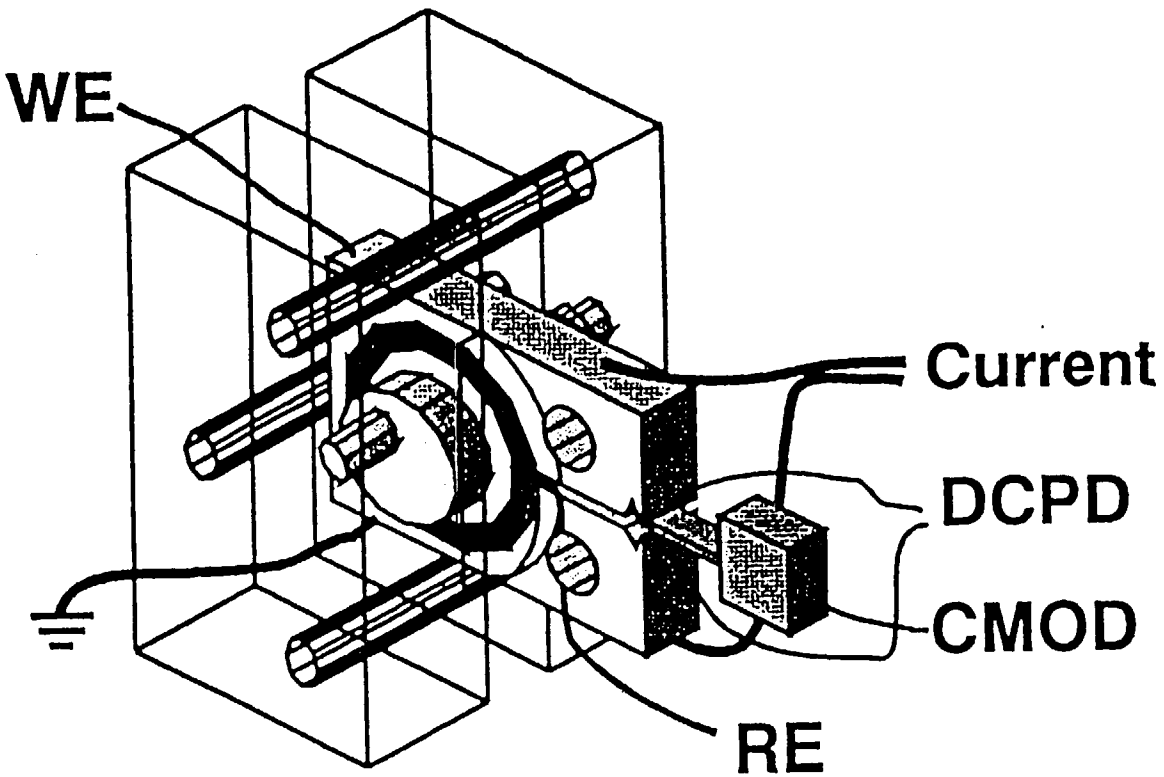

Results and Conclusions for Constant CMOD Rate Tests

- K_{JIC} is 78 MPa$\sqrt{m}$, slightly higher than standard Ti-6Al-4V.
- K_{TH} for Ti-6Al-4V (MA,ELI) is between 48 and 55 MPa$\sqrt{m}$ in 3.5% NaCl depending on loading rate.
  - K_{TH} = 55 MPa$\sqrt{m}$ (CMOD Rate = 3 x 10^{-5} mm/sec)
  - K_{TH} = 48 MPa$\sqrt{m}$ (CMOD Rate = 4.7 x 10^{-5} mm/sec)
- Ti-6Al-4V (MA,ELI) exhibits a greater resistance to SCC than standard grade Ti-6Al-4V (MA).
- ELI Ti-6Al-4V exhibits a slower (da/dt) than standard Ti-6Al-4V (of order 10^{-5} mm/sec or less).

Static Load Test

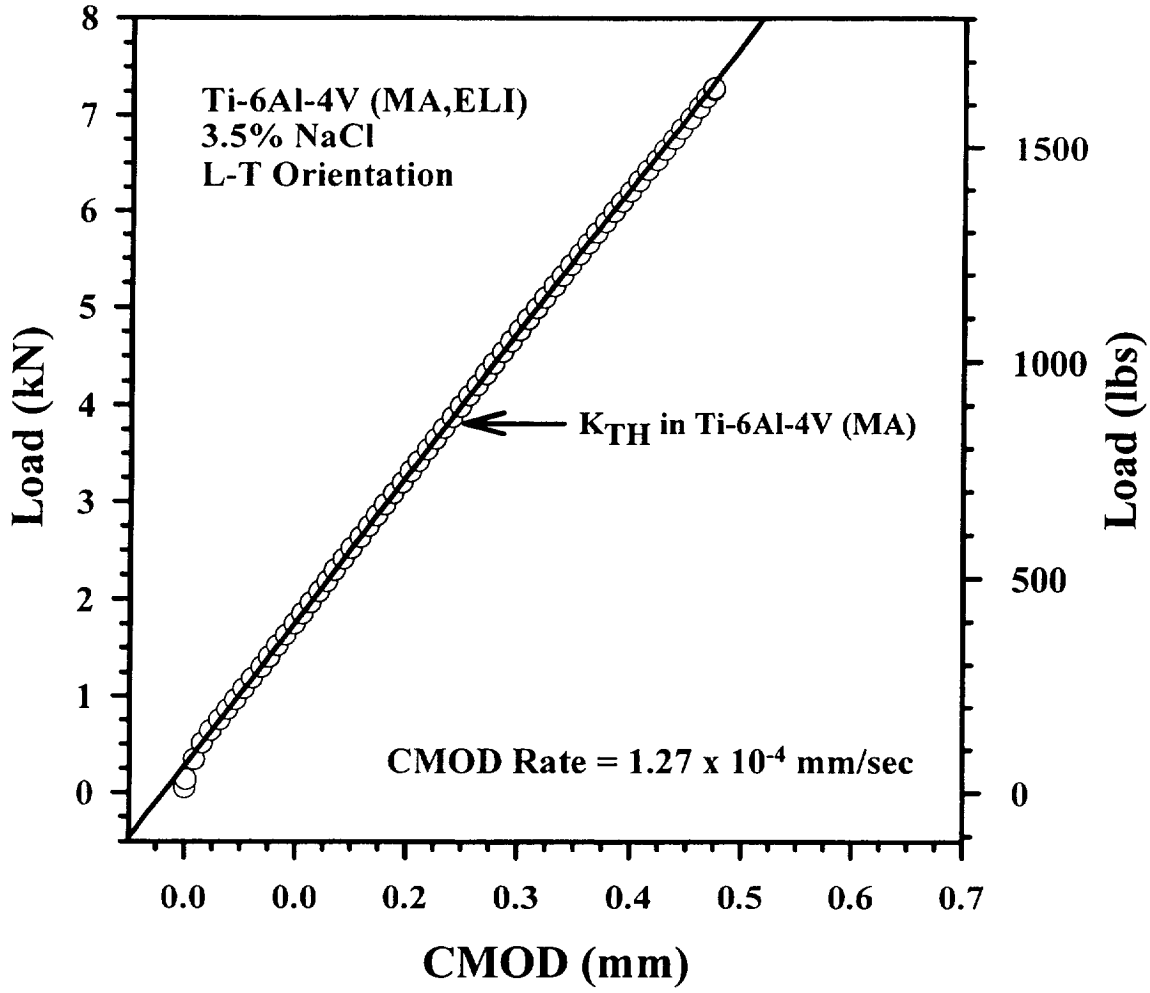

- Load increased monotonically to stress intensity level of 40 MPa$\sqrt{m}$ in 65 minutes, held for 140 hours.
- Load drop of 0.1 kN (25 lbs) would have been noticeable and corresponded to 0.2 mm of crack growth.
- Load did not drop, thus da/dt is less than 5 x 10^{-7} mm/sec.

Results for Constant CMOD Rate Tests

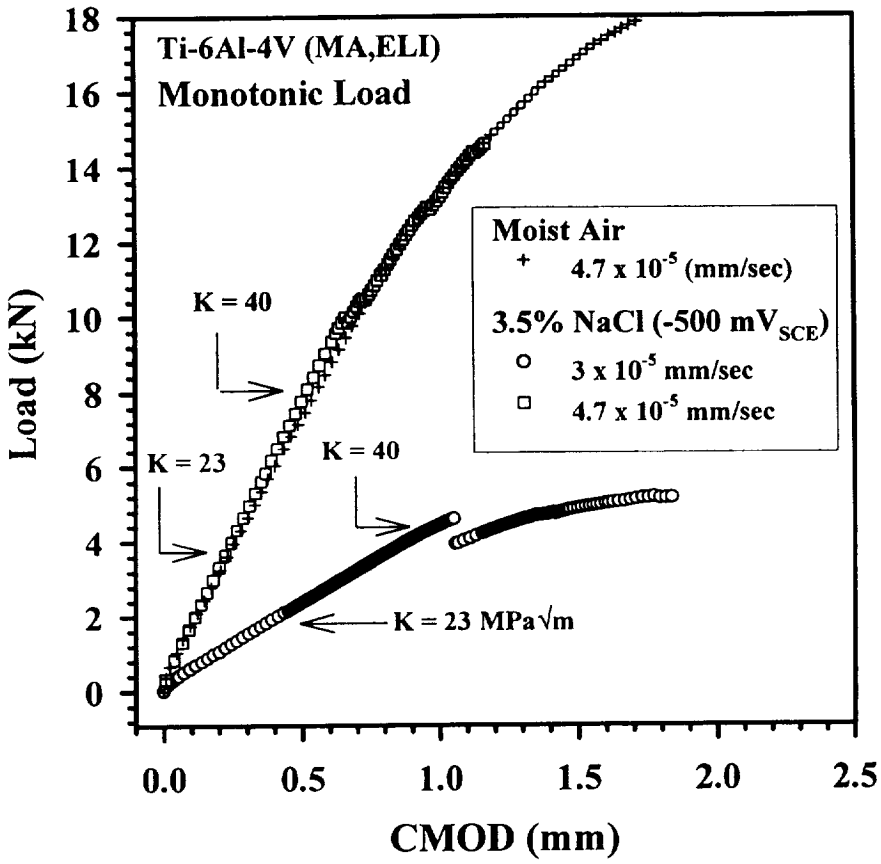

- There are sharp decreases in load at constant CMOD for NaCl experiments.
- Air data do not show sharp decreases in load at constant CMOD.
- Since loading rates were identical and only environment changed, EAC does occur in Ti-6Al-4V (MA,ELI), only at high K.

Conclusions: Environmental Fatigue Behavior of Ti-6Al-4V (MA,ELI)

- 3.5% NaCl solution is detrimental and enhances fatigue crack propagation (FCP) rates two to four fold compared to moist air.
- ELI Ti-6Al-4V does not exhibit the frequency "crossover" effect for ΔK value less than 25 MPa$\sqrt{m}$ for frequencies between 0.03 and 40 Hz due to increased SCC resistance.
- ELI Ti-6Al-4V exhibits a mild frequency dependence for ΔK values 12.5 and 25 MPa$\sqrt{m}$; da/dN is proportional to $f^{0.1 \text{ to } 0.2}$.
- Closure levels exhibited by ELI Ti-6Al-4V are consistent with plasticity induced closure, and are independent of environment.

Frequency "Crossover" in α + β Titanium Alloys

- α + β titanium alloys in aqueous chloride solutions exhibit frequency "crossover".

- "Crossover" is a change in ordering of da/dN as a function of frequency at a transition ΔK level.

- Transition ΔK level (ΔK_{SCC}) is associated with onset of "cyclic" SCC.

- Below ΔK_{SCC}, da/dN decreases as frequency decreases perhaps due to passive film stability.

- Above ΔK_{SCC}, da/dN increases as frequency decreases perhaps due to hydrogen embrittlement mechanisms.

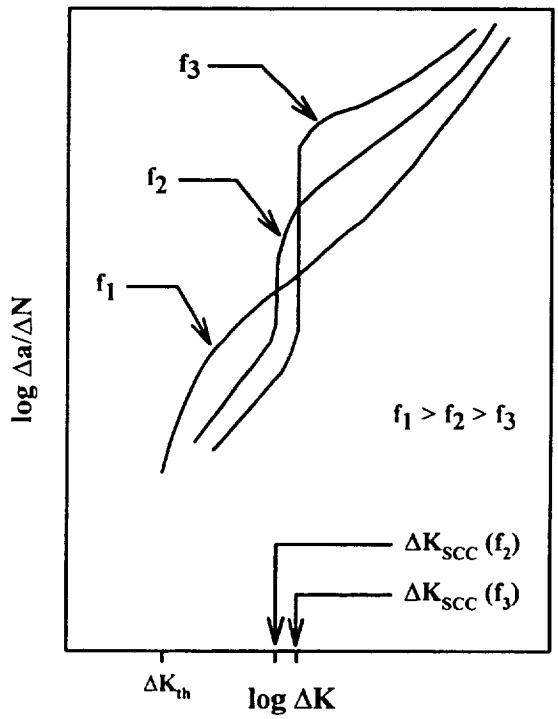

Fatigue Results for Ti-6Al-4V (MA,ELI)

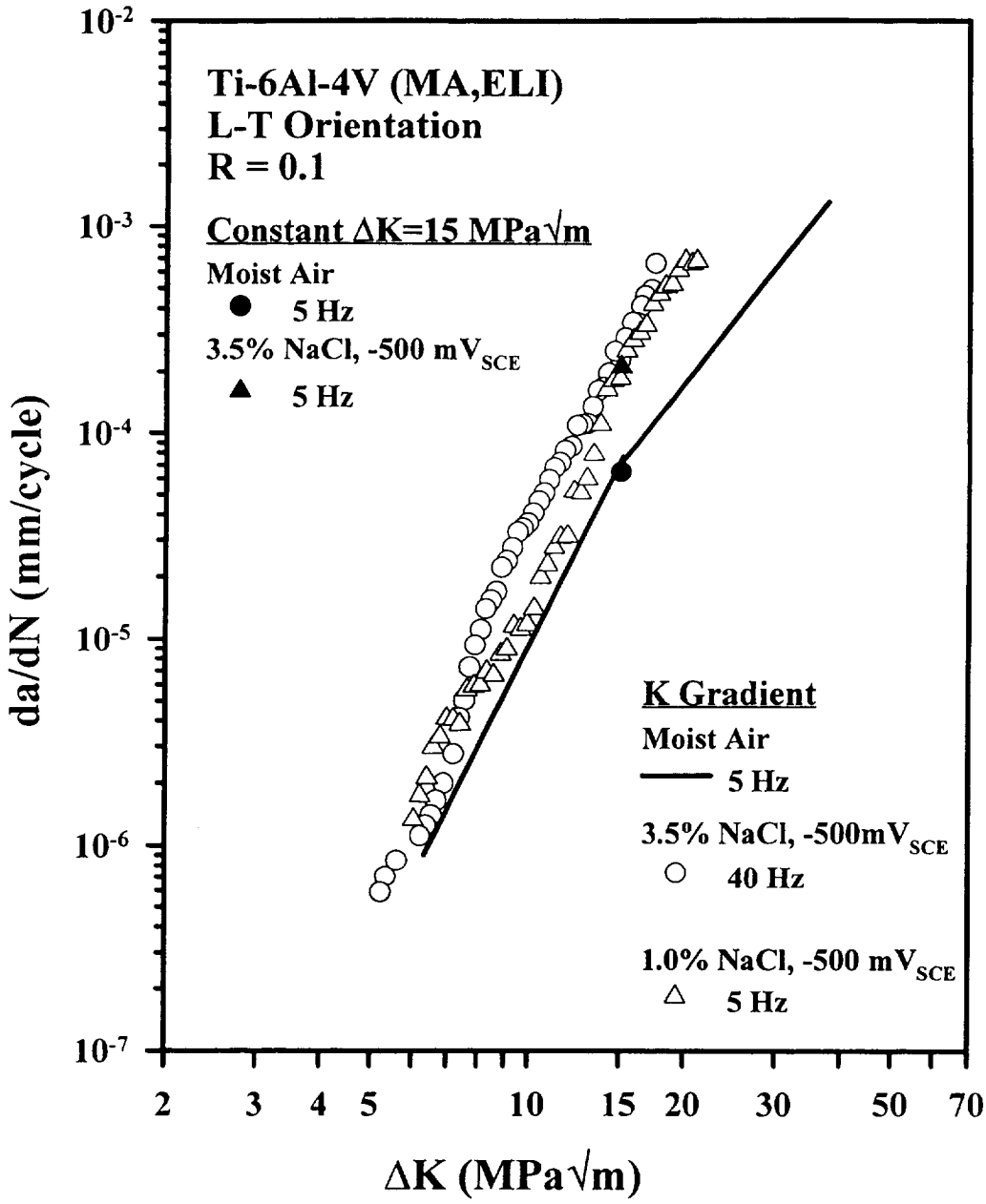

Frequency Response of Ti-6Al-4V (MA,ELI)

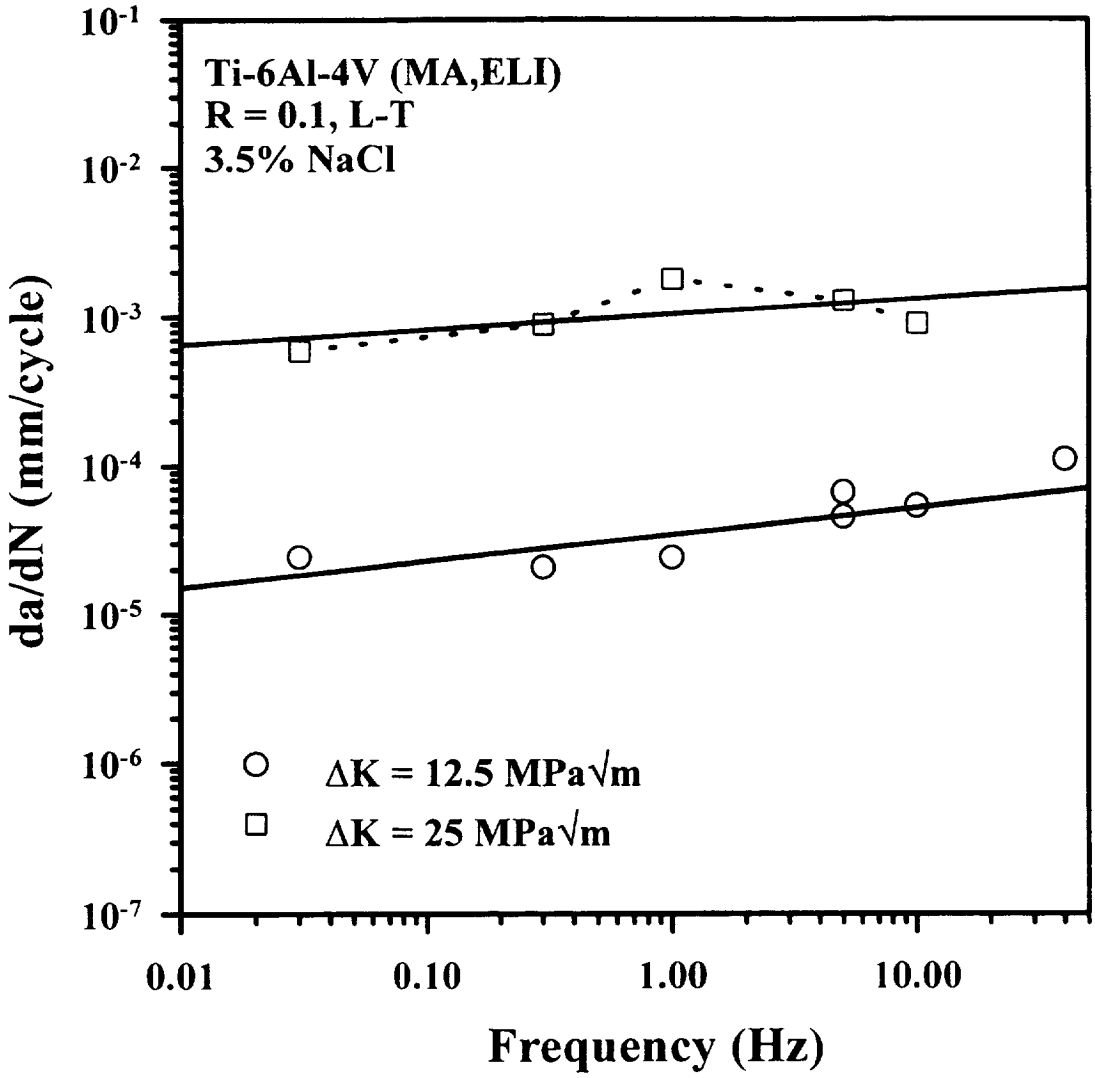

- Results do not exhibit frequency "crossover" effect.
- Da/dN increases as frequency increases for $0.03 < f < 40$ Hz.
- Da/dN is proportional to $f^{0.1 \text{ to } 0.2}$ for each ΔK where $K_{max} < K_{TH}$.

Frequency "Crossover" In Ti-6Al-4V (MA,ELI)

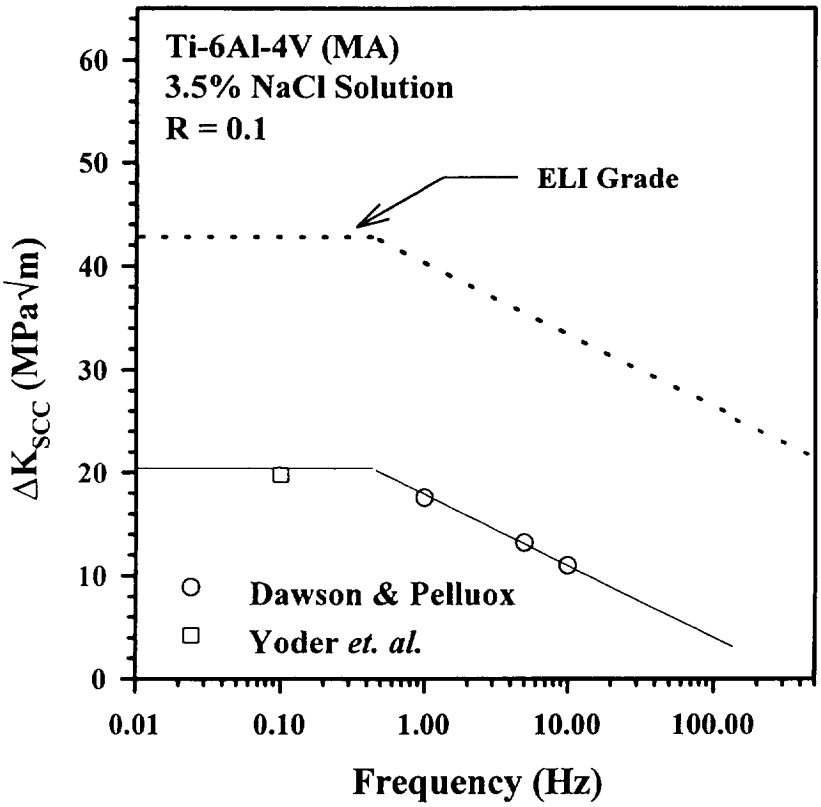

- "Cyclic" SCC does not occur in ELI grade for the range of frequencies tested due to increased SCC resistance.
- Since "cyclic" SCC does not occur, frequency "crossover" effect is not exhibited.
- For ΔK values below 25 MPa$\sqrt{m}$, "cyclic" SCC does not occur for frequencies below 200 Hz.
- Fastest frequency where data were collected during this study is 40 Hz.

Crack Closure in Ti-6Al-4V (MA,ELI)

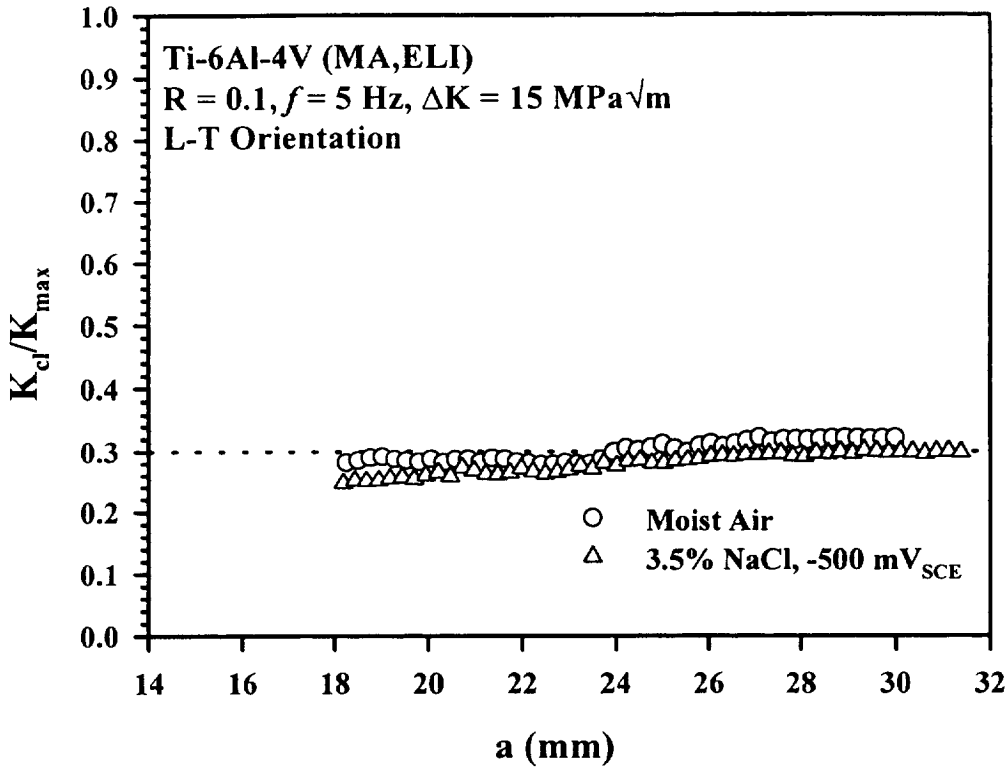

- Crack closure levels are independent of environment.
- Closure levels are consistent with plasticity induced closure (K_{cl}/K_{max} = 0.3) and with Forman Equation.
- Crack closure levels increase as ΔK decreases for ΔK values less than 10 MPa$\sqrt{m}$, could be due to roughness or oxide induced closure.
- At ΔK values > 10 MPa$\sqrt{m}$, there is no roughness or oxide induced closure.

Conclusions for Computer Modeling

- Linear superposition is effective in modeling environment enhanced FCP rates for material/environment systems where the alloy is sensitive to SCC.
- Linear superposition is effective for standard Ti-6Al-4V for ΔK values where K_{max} exceeds K_{TH}.
- Linear superposition does not work for ELI Ti-6Al-4V due to SCC resistance of alloy.
- Interpolative model effectively models FCP rates when the load characteristics are within the establishing data base.
- Interpolative model effectively models the effect of *f* and R in standard and ELI grade Ti-6Al-4V.
- Models contained in the program UVAFAS.EXE are effective in modeling environment enhanced FCP rates, and can be incorporated in NASA FLAGRO.

Application of Linear Superposition to Ti-6Al-4V

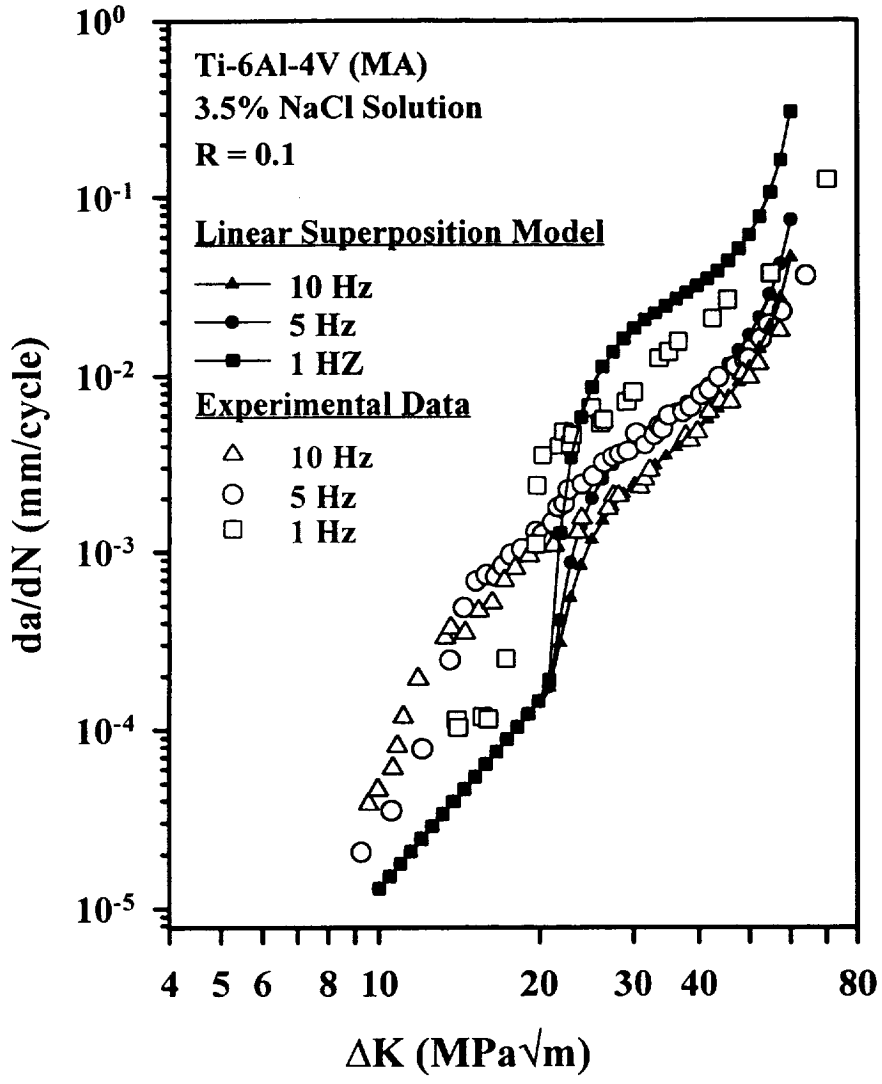

- Superposition is effective for ΔK values where K_{max} is greater than K_{TH} (~23 MPa$\sqrt{m}$) and f > 1 Hz.

- Superposition is not effective for ELI Ti-6Al-4V due to increased SCC resistance (K_{TH} ~ 48 to 55 MPa$\sqrt{m}$).

Application of Interpolative Model to Standard Ti-6Al-4V

Forman Equation With Closure

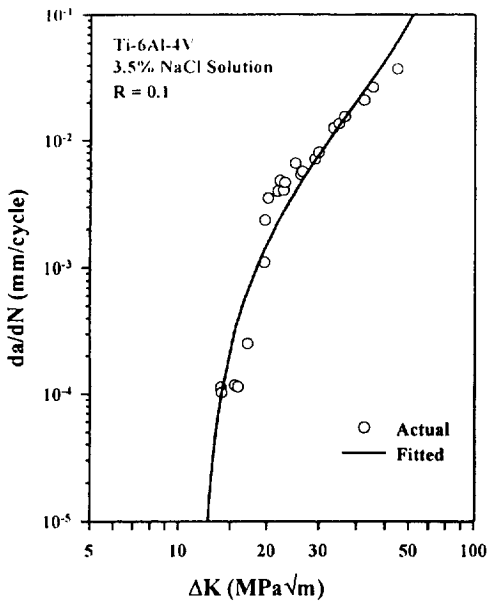

Actual and fitted data for $f = 1$ Hz.

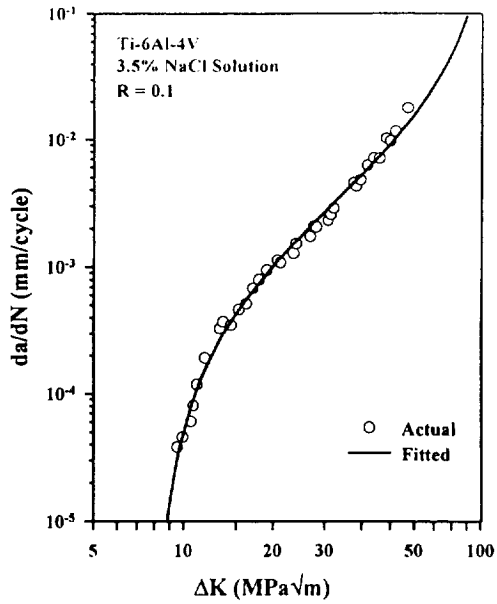

Actual and fitted data for $f = 10$ Hz.

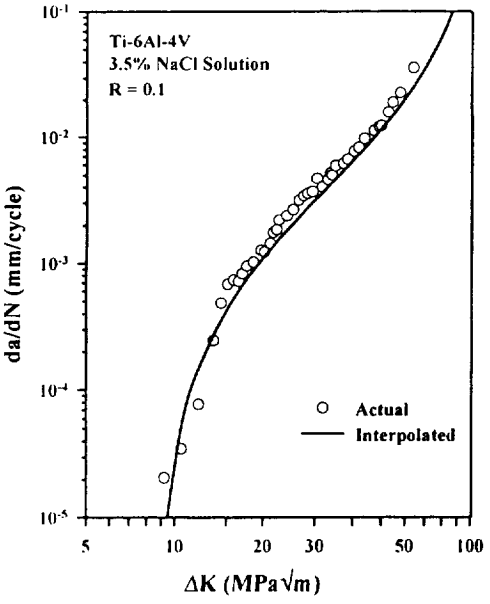

Actual and interpolated data, $f = 5$ Hz.

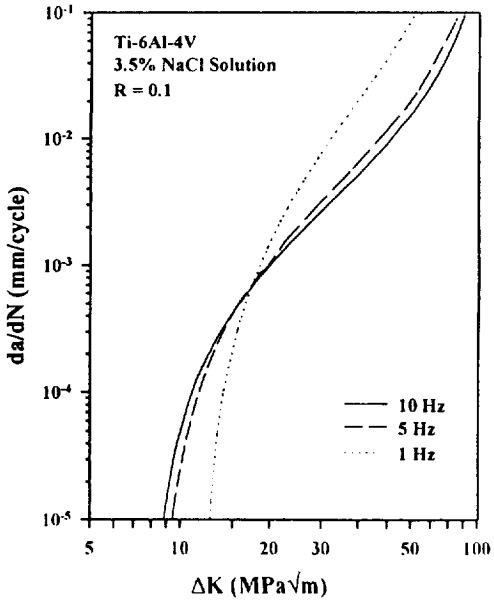

Effect of frequency on da/dN.

Application of Interpolative Model to ELI Ti-6Al-4V

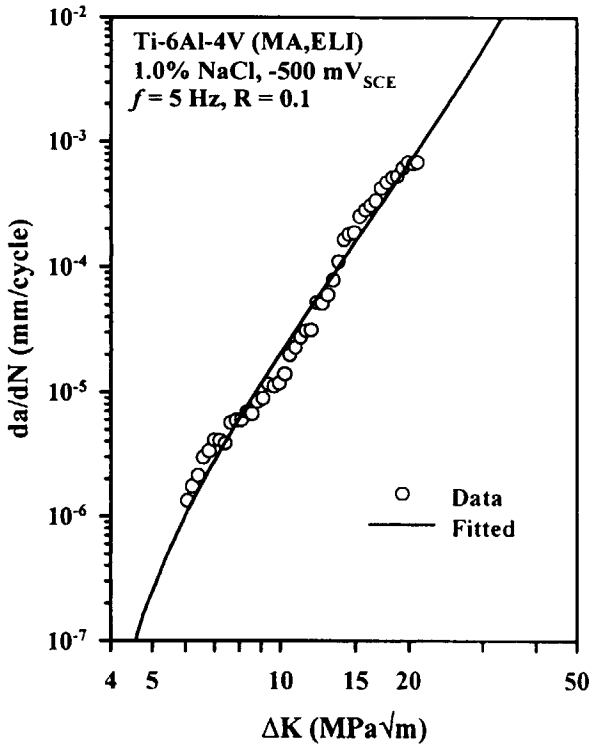

Actual and fitted data for f = 5 Hz.

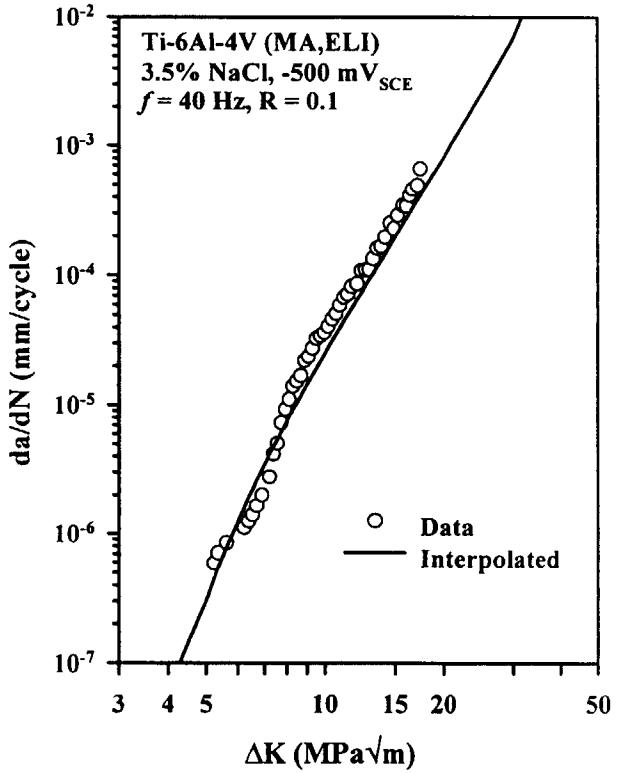

Actual and interpolated data for f = 40 Hz.

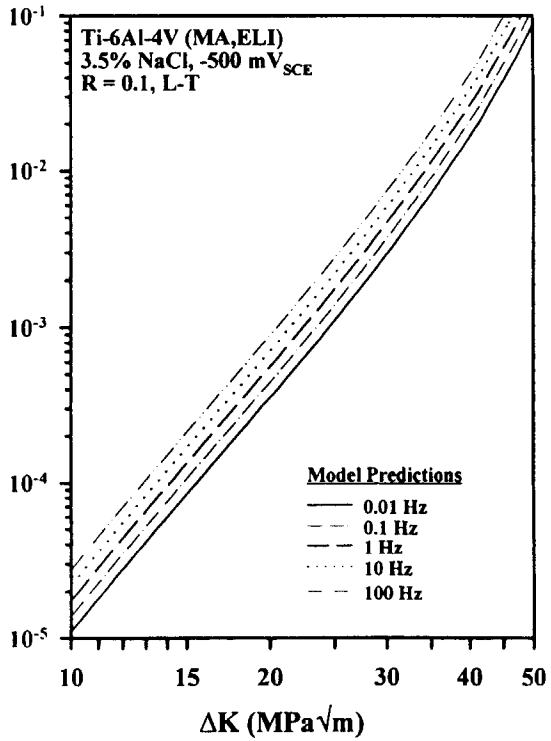

Predicted da/dN for 0.01 < f < 100 Hz.

University of Virginia Fatigue Analysis Software

University of Virginia
Fatigue Analysis Software

Edward Richey, III
Allen W. Wilson
Richard P. Gangloff
Department of Materials Science and Engineering
University of Virginia

Future Work Regarding Linear Superposition Model

- **Include capability to calculate da/dt (K) from da/dN versus ΔK.**
- **May improve model by generating a set of da/dt data more reflective of crack tip strain rates during fatigue.**
- **Solve for da/dt in following equation:**

$$\frac{da}{dN} = \int_{\tau} \frac{da}{dt}[K(t)]\ dt$$

- **Linear regression utilized if da/dt is represented by Paris Equation and K(t) is represented by square wave with R= 0.**

$$\frac{da}{dt} = C\ K^n$$

$$\left(\frac{da}{dN}\right)_{SCC} = C\ \tau\ K_{max}^n\ (1 - \alpha)$$

τ = period of loading cycle
α = fraction of load cycle at K_{max}

- **Problem is complicated and non-linear when other wave forms and equations are used.**

Relationship between da/dN and Frequency

- da/dN $\propto f^{-0.5}$ (Steel in NaCl)

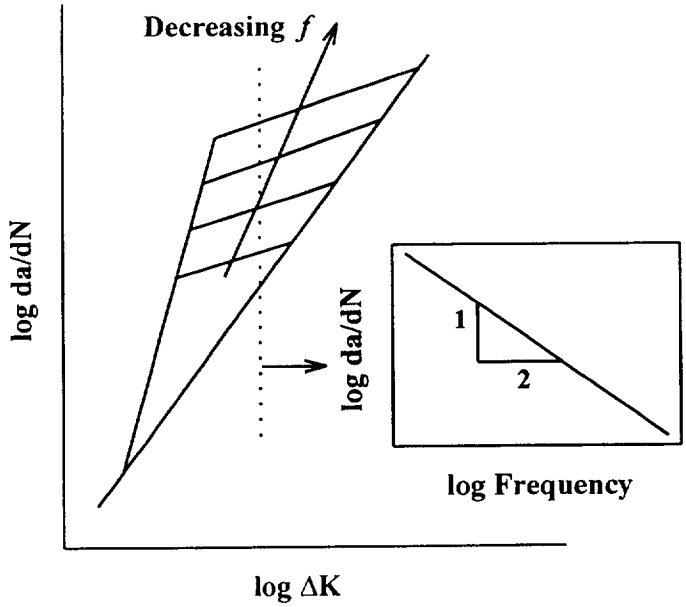

- da/dN $\propto f^{-0.1}$ (Ti in NaCl)

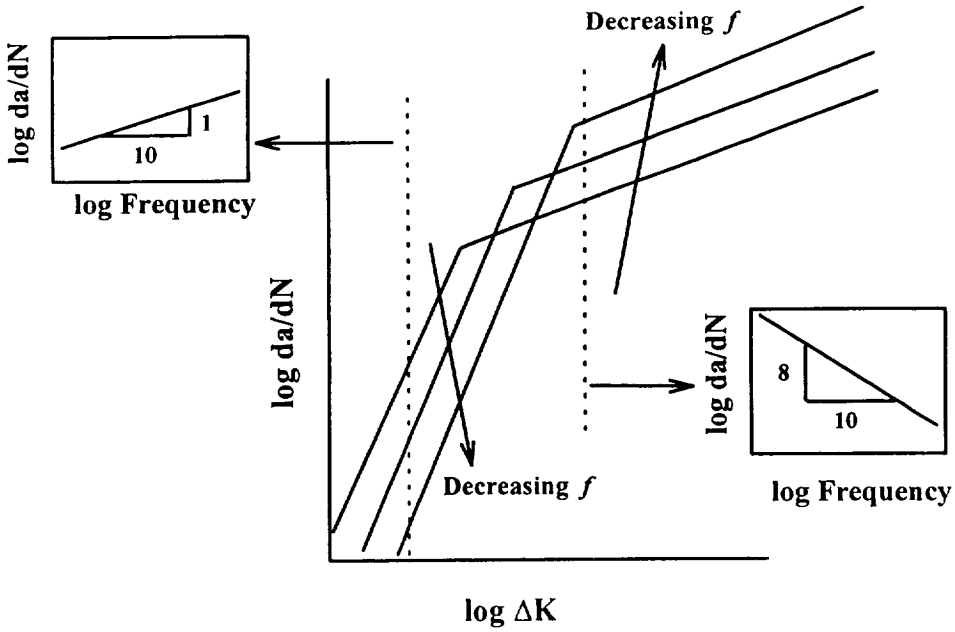

- Linear Superposition predicts da/dN $\propto f^{-1}$

Feasibility of Calculating da/dt From da/dN

- Assume $da/dN \propto f^{\alpha}$, $-1.0 < \alpha < 0.1$

- Will da/dt calculated from da/dN be physically meaningful and useful ?

  - Model will predict da/dN proportional to f^{-1}, with da/dt not dependent on frequency.

  - Model may be effective if da/dt is treated as a function of frequency.

  - Model not effective for material/environment systems where the dependence of da/dN on frequency changes at a critical frequency or ΔK level.

Relating da/dt to Frequency

- **Dimensional analysis shows:**

$$\frac{da}{dN} = \frac{da}{dt} f^{-1}$$

- **If da/dt is independent of frequency:**

$$\frac{da}{dN} \propto f^{-1}$$

as predicted by simple linear superposition model.

- **If da/dt is a function of frequency:**

$$\frac{da}{dt} \propto f^{\alpha} \qquad 0 < \alpha < 1.5$$

$$\frac{da}{dN} \propto \frac{da}{dt} f^{-1} \propto f^{(\alpha - 1)}$$

- **Must define frequency dependence of da/dt:**

$$\frac{da}{dt} = C\ K^{n} f^{\alpha}$$

Film rupture modeling:

$$\frac{da}{dt} \propto f^{m} \qquad where\ m \sim 0.5$$

APPENDIX I: GRANT PUBLICATIONS (January 1 to June 30, 1995)

1. H.J. Koenigsmann and E.A. Starke, Jr., "Fracture Behavior in Al-Si-Ge Alloys", in Proceedings of the 2nd International Conference on Microstructures and Mechanical Properties of Aging Materials, TMS-AIME, Warrendale, PA, in press (1995).

2. R.G. Buchheit, F.D. Wall, G.E. Stoner and J.P. Moran, "Anodic Dissolution-Based Mechanism for the Rapid Cracking, Preexposure Phenomenon Demonstrated by Aluminum-Lithium-Copper Alloys", Corrosion, Vol. 51, pp. 417-428 (1995).

3. Donald C. Slavik and Richard P. Gangloff, "Environment and Microstructure Effects on Fatigue Crack Facet Orientation in an Al-Li-Cu-Zr Alloy", Acta Metallurgica et Materialia, in review (1995).

4. P.N. Kalu and J.A. Wagner, " A Microtexture Investigation of the Fracture Behavior of Al-Li Alloy 2090", Lightweight Alloys for Aerospace Applications III, TMS-AIME, Warrendale, PA, in press (1995).

5. B. Skrotzki, E. A. Starke and G. J. Shiflet, "The Effect of Stress on Nucleation and Growth of Precipitates in Al-Cu-Mg-X Alloys", Proc. of the 2nd International Conference on Microstructure and Mechanical Properties of Aging Materials, TMS-AIME, Warrendale, PA, in press (1995).

6. B. Skrotzki, E. A. Starke and G. J. Shiflet, "Effect of Texture and Precipitates on Mechanical Property Anisotropy of Al-Cu-Mg-X Alloys", Proc. of the 4th Int. Conf. on Aluminum Alloys, Vol. II, EMAS, Warley Heath, UK p. 40 (1994).

APPENDIX II: GRANT PRESENTATIONS (January 1 to June 30, 1995)

1. H.J. Koenigsmann and E.A. Starke, Jr., "Fracture Behavior in Al-Si-Ge Alloys", 2nd International Conference on Microstructures and Mechanical Properties of Aging Materials, Las Vegas, NV, February, 1995.

2. H.J. Koenigsmann and E.A. Starke, Jr., "Fracture Behavior in Al-Si-Ge Alloys", Beijing University of Aeronautics and Astronautics, Beijing, China, June , 1995.

3. M.J. Haynes, B.P. Somerday, C.L. Lach and R.P. Gangloff, "Characterization and Micromechanical Modeling of Elevated Temperature Fracture in Advanced Aluminum Alloys", 27th National Symposium on Fatigue and Fracture Mechanics, Williamsburg, VA, June 1995.

4. R.P. Gangloff, "Elevated Temperature Fracture of Advanced Aluminum Alloys", Albany, Schenectady, Troy Chapters of ASM International and TMS-AIME, Troy, NY, May, 1995.

5. R.P. Gangloff, ""Elevated Temperature Fracture of Advanced Aluminum Alloys", Washington Chapter of ASM International, Washington, DC, January, 1995.

6. P.N. Kalu and J.A. Wagner, "A Microtexture Investigation of the Fracture Behavior of Al-Li Alloy 2090", 1995 TMS Annual Meeting, Las Vegas, NV, February, 1995.

7. B. Skrotzki, E. A. Starke and G. J. Shiflet, "Alterung einer Al-Cu-Mg-Ag Legierung unter aeusserer Spannung", Annual Meeting of the German Materials Society, Bochum, Germany, June, 1995.

8. B. Skrotzki, E. A. Starke and G. J. Shiflet, "The Effect of Stress on Nucleation and Growth of Precipitates in Al-Cu-Mg-X Alloys", 124th TMS Annual Meeting, 2nd International Conference on Microstructure and Mechanical Properties of Aging Materials, Las Vegas, Nev., February, 1995.

9. B. Skrotzki, E. A. Starke and G. J. Shiflet, "Effect of Texture and Precipitates on Mechanical Property Anisotropy of Al-Cu-Mg-X Alloys", 4th International Conference on Aluminum Alloys, Atlanta, Ga, September, 1994. (Not listed in a previous progress report.)

APPENDIX III: GRANT PROGRESS REPORTS (January, 1988 to June, 1995)

1. R.P. Gangloff, G.E. Stoner and R.E. Swanson, "Environment Assisted Degradation Mechanisms in Al-Li Alloys", University of Virginia, Report No. UVA/528266/MS88/101, January, 1988.

2. R.P. Gangloff, G.E. Stoner and R.E. Swanson, "Environment Assisted Degradation Mechanisms in Advanced Light Metals", University of Virginia, Report No. UVA/528266/MS88/102, June, 1988.

3. R.P. Gangloff, G.E. Stoner and R.E. Swanson, "Environment Assisted Degradation Mechanisms in Advanced Light Metals", University of Virginia, Report No. UVA/528266/MS89/103, January, 1989.

4. R.P. Gangloff, "NASA-UVa Light Aerospace Alloy and Structures Technology Program", UVa Report No. UVA/528266/MS90/104, August, 1989.

5. R.P. Gangloff, "NASA-UVa Light Aerospace Alloy and Structures Technology Program", UVa Report No. UVA/528266/MS90/105, December, 1989.

6. R.P. Gangloff, "NASA-UVa Light Aerospace Alloy and Structures Technology Program", UVa Report No. UVA/528266/MS90/106, June, 1990.

7. R.P. Gangloff, "NASA-UVa Light Aerospace Alloy and Structures Technology Program", UVa Report No. UVA/528266/MS91/107, January, 1991.

8. R.P. Gangloff, "NASA-UVa Light Aerospace Alloy and Structures Technology Program", UVa Report No. UVA/528266/MS91/108, July, 1991.

9. R.P. Gangloff, "NASA-UVa Light Aerospace Alloy and Structures Technology Program", UVa Report No. UVA/528266/MS92/109, January, 1992.

10. R.P. Gangloff, "NASA-UVa Light Aerospace Alloy and Structures Technology Program", UVa Report No. UVA/528266/MS93/111, July, 1992.

11. R.P. Gangloff, "NASA-UVa Light Aerospace Alloy and Structures Technology Program", UVa Report No. UVA/528266/MSE93/112, March, 1993.

12. R.P. Gangloff, "NASA-UVa Light Aerospace Alloy and Structures Technology Program", UVa Report No. UVA/528266/MSE93/113, July, 1993.

13. R.P. Gangloff, "NASA-UVa Light Aerospace Alloy and Structures Technology Program", UVa Report No. UVA/528266/MSE93/114, March, 1994.

14. R.P. Gangloff, "NASA-UVa Light Aerospace Alloy and Structures Technology Program", UVa Report No. UVA/528266/MSE94/116, July, 1994.

15. E.A. Starke, Jr. and R.P. Gangloff, "NASA-UVa Light Aerospace Alloy and Structures Technology Program", UVa Report No. UVA/528266/MSE94/117, March, 1995.

APPENDIX IV: LA^{2}ST GRANT REVIEW MEETING AGENDA

FINAL AGENDA

SIXTH ANNUAL NASA-UVa LA^{2}ST MEETING

NASA-Langley Research Center
Hampton, Virginia

Day 1: Monday, July 17, 1995

1:00-1:15 pm	Dennis L. Dicus: Welcome. Edgar A. Starke and Richard P. Gangloff: LA^{2}ST program status.
1:15-2:00	"Al-Si-Ge Alloy Development"; Holger Koenigsmann and E.A. Starke.
2:00-2:45	"Effects of Texture and Microstructure on the Anisotropic Yield Strength of Wide Panel Aluminum Alloy Extrusions"; Mark T. Lyttle and John A. Wert
2:45-3:00	Break
3:00-3:40	"Effect of Texture and Precipitates on Mechanical Property Anisotropy of Al-Cu-Mg-X Alloys"; Birgit Skrotzki, G.J. Shiflet and E.A. Starke.
3:40-4:20	"Elevated Temperature Fracture of AA2519 with Ag"; Michael J. Haynes and R.P. Gangloff.
4:20-4:50	"Microtexture and Temperature-Dependent Fracture of AA2090" John A. Wagner and R.P. Gangloff.
4:50-5:20	"Effects of Aging and Temperature on the Ductile Fracture of AA2095 and AA2195", Cynthia L. Lach and R.P. Gangloff.

Day 2: Tuesday, July 18, 1995

8:30-9:15 am	"Modeling Time-Dependent Environmental Fatigue Crack Propagation in Aluminum and Titanium Alloys for NASA-FLAGRO"; Edward Richey, M.E. Mason and R.P. Gangloff.
9:15-10:00	"Mechanisms of Localized Corrosion in Alloys 2090 and 2095"; F. Douglas Wall and G.E. Stoner.
10:00-10:15	Break
10:15-11:00	"Hydrogen Interactions and Their Correlation to the Hydrogen Embrittlement Susceptibility of Al-Li-Cu-Zr Alloys"; Stephen W. Smith and J.R. Scully.
11:00-11:20	"SCC Initiation in Advanced Al-Li-Cu Alloys; J.R. Scully and G.E. Stoner.
11:20-11:50	"Internal Hydrogen Embrittlement of Low Cost Beta"; Sean P. Hayes, R.P. Gangloff, S.M. Kazanjian and E.A. Starke.
11:50-1:15 pm	Lunch
1:15-2:15	Group discussion between UVa and LaRC participants on the health of the LA^{2}ST Grant, the LA^{2}ST-HSCT program merger, and directions for future NASA/UVa research.

DISTRIBUTION LIST

1-4 Mr. D. L. Dicus
Contract Monitor
Metallic Materials Branch, MS 188A
NASA Langley Research Center
Hampton, VA 23681-0001

5-6* NASA Scientific and Technical Information Facility
P. O. Box 8757
Baltimore/Washington International Airport
Baltimore, MD 21240

7 Mr. Neil Price
Grants Officer, M/S 126
NASA Langley Research Center
Hampton, VA 23681-0001

8 Dr. Darrel R. Tenney
Materials Division
NASA Langley Research Center
Hampton, VA 23681-0001

9 Dr. Charles E. Harris
Mechanics of Materials Branch
NASA Langley Research Center
Hampton, VA 23681-0001

10 Mr. W. Barry Lisagor
Metallic Materials Branch
NASA Langley Research Center
Hampton, VA 23681-0001

11 Mr. T.W. Crooker
Code RM
NASA Headquarters
Washington, DC 20546

12 Dr. Robert S. Piascik
Mechanics of Materials Branch
NASA Langley Research Center
Hampton, VA 23681-0001

13 Mr. W. Brewer
Metallic Materials Branch, MS 188A
NASA Langley Research Center
Hampton, VA 23681-0001

14 Mr. Thomas T. Bales
Metallic Materials Branch, MS 188A
NASA Langley Research Center
Hampton, VA 23681-0001

15 Mr. John Wagner/Ms. Cynthia Lach
Metallic Materials Branch, MS 188A
NASA Langley Research Center
Hampton, VA 23681-0001

16 Dr. William F. Bates
Lockheed Aeronautical Systems Co.
86 South Cobb Drive
Marietta, GA 30063-0648

17 Dr. Alex Cho
Reynolds Metals Co.
4th and Canal Street
Richmond, VA 23261

18 Mr. E.A. Colvin
Alcoa Technical Center
Route 780, 7th Street Road
Alcoa Center, PA 15069

19 Dr. L.M. Karabin
Alcoa Technical Center
Route 780, 7th Street Road
Alcoa Center, PA 15069

20 Dr. Ravi Kahandal
McDonnell Douglas Aerospace
Mail Stop 36-90
3855 Lakewood Blvd.
Long Beach, CA 90846

21 Mr. Fred Casey
Space Transportation Systems Division
Rockwell International
Dept. 289 MC/AC56
12214 Lakewood Blvd.
Downey, CA 90241

22-23 E.A. Starke, Jr.; MS&E

24-25 R.P. Gangloff; MS&E

26 G. J. Shiflet; MS&E

27 G.E. Stoner; MS&E

28 J.A. Wert; MS&E

29 J.R. Scully; MS&E

30 C.T. Herakovich; CE and AM

31-32 S.S. Kerbel; Clark Hall

33 SEAS Preaward Administration Files

34 Mr. Gwyn Faile
Code ED 24
Marshall Space Flight Center
Huntsville, AL 35812

35 Mr. Brian McPherson
Code ED 24
Marshall Space Flight Center
Huntsville, AL 35812

36 Dr. William E. Quist
Boeing Aerospace and Electronics
Aerospace Group
Mail Stop GH-CJ
P.O. Box 3707
Seattle, WA 98124

37 Dr. Howard G. Nelson
NASA-Ames Research Center
EEM: 213-3
Moffett Field, CA 94035

38 Dr. R.G. Forman
Mail Code ES-5
NASA-L.B. Johnson Space Flight Center
Houston, TX 77058

39 Professor A.K. Noor
Center for Computational Structures Technology
NASA Langley Research Center
Hampton, VA 23681-0001

40 Prof. A.K. Ghosh
Department of Materials Science and Engineering
University of Michigan
2102 Dow Building
Ann Arbor, MI 48109-2136

41 Dr. D. Ferton
Pechiney Centre de Recherches
De Voreppe
B.P. 27 -- 38340 Voreppe
FRANCE

42 Dr. John Papazian
Grumman Aerospace & Electronics
Mail Stop A02-026
Bethpage, NY 11714-3582

43 Dr. Richard Lederich
McDonnell Douglas Aircraft Company
Mail Stop 111-1041
P.O. Box 516
St. Louis, MO 36166

44 Dr. Alan Hopkins
Senior Research Metallurgist
Research Institute
The University of Dayton
300 College Park
Dayton, OH 45469-0172

45 Dr. Frances Hurwitz
Ceramic Composites
NASA Lewis Research Center
21000 Brookpark Road
Cleveland, OH 44135

46 Dr. Malcolm Ozelton
Manager, Metallic & Ceramic Materials
B-2 Division
Northrop Corporation
8900 E. Washington Blvd.
T241/GK
Pico Rivera, CA 90660-3737

47 Dr. S. Sampath
Technical Center
Federal Aviation Administration
Atlantic City International Airport,
NJ 08405

48 Dr. James Staley
Alcoa Laboratories
Alcoa Center, PA 15069

49 Dr. Jeffrey Waldman
Code 6063
Naval Air Development Center
Warminster, PA 18974

*One reproducible copy

Updated: July, 1995